

Diss. ETH No. 16709 and
ETHZ-IPP Internal Report 2006-04



Diffractive ρ^0 photoproduction at HERA

A dissertation submitted to the
Swiss Federal Institute of Technology Zurich
for the degree of
Doctor of Natural Sciences

presented by
Ronald M. Weber

Dipl. Phys. ETH
born on November 28, 1974
citizen of Basel (BS)

accepted on the recommendation of
Prof. Dr. Ralph Eichler, examiner and
Prof. Dr. Urs Langenegger, co-examiner

June 2006

Abstract

From a sample of over 989'000 events taken at the experiment H1 using the new Fast Track Trigger (FTT), a new measurement of the differential cross section for diffractive ρ^0 photoproduction is performed in the kinematic range $20 < W_{\gamma p} < 90 \text{ GeV}$ and $|t| < 3 \text{ GeV}^2$.

The large data sample allows for a measurement of the cross section double differentially in $W_{\gamma p}$ and t and thus the energy dependence of this process for eight t values in a single experiment. From this data, the pomeron trajectory in elastic ρ^0 photoproduction is determined to be

$$\alpha_{\mathbb{P}}(t) = 1.097 \pm 0.004 (stat)_{-0.008}^{+0.008} (sys) + (0.133 \pm 0.027 (stat)_{-0.046}^{+0.033} (sys)) \text{ GeV}^{-2} \cdot t.$$

In 2002 the first complete readout chip (PSI43) for the pixel detector at the Compact Muon Solenoid (CMS) became available at the Paul Scherrer Institut (PSI), Villigen. After extensive tests of the single readout chip, the first prototype modules were assembled and tested electrically. The experience obtained from these modules was used to optimize the next generation of modules and to establish an efficient and simple assembly line for mass production of these modules for the CMS experiment at the Large Hadron Collider (LHC).

Zusammenfassung

Eine neue Messung des differentiellen Wirkungsquerschnittes für diffraktive ρ^0 Photoproduktion im kinematischen Bereich $20 < W_{\gamma p} < 90 \text{ GeV}$ und $|t| < 3 \text{ GeV}^2$ wird präsentiert. Das zu Grunde liegende Daten Sample umfasst über 989'000 Ereignisse welche am H1 Experiment mit Hilfe des neuen schnellen Spurtriggers aufgezeichnet wurden.

Das Daten Sample ist gross genug, um die Messung doppelt differentiell in $W_{\gamma p}$ and t zu machen und somit auch die Energieabhängigkeit bei acht Werten von t in nur einem einzigen Experiment zu messen. Aus diesen Daten wird die Pomeron Trajektorie extrahiert mit den Werten

$$\alpha_{\mathbb{P}}(t) = 1.097 \pm 0.004 (stat)_{-0.008}^{+0.008} (sys) + (0.133 \pm 0.027 (stat)_{-0.046}^{+0.033} (sys)) \text{ GeV}^{-2} \cdot t.$$

Der erste komplette Prototyp des Auslesechips PSI43 für den Pixel Detektor des Compact Muon Solenoid (CMS) Experimentes traf 2002 am Paul Scherrer Institut (PSI) in Villigen ein. Nach ausführlichen Test zur Funktionalität des Chips wurden die ersten Prototyp Module gebaut und ihre elektrischen Eigenschaften getestet. Die erworbenen Erfahrungen wurden einerseits dazu verwendet um die nächste Generation von Modulen zu verbessern und andererseits um eine einfache und effiziente Produktionslinie zu erstellen mit der die Massenproduktion der Module für das CMS Experiment am Large Hadron Collider (LHC) bewältigt werden kann.

Contents

I	Analysis	1
1	Introduction	2
2	An Introduction to High Energy Particle Diffraction	5
2.1	Kinematics	5
2.1.1	Two Body Processes	5
2.1.2	Electron - Proton Scattering	6
2.1.3	Vector Meson Production	7
2.2	Equivalent Photon Approximation and Vector Meson Dominance Model	7
2.3	Diffraction: A Definition	10
2.4	An Introduction to REGGE Theory	12
2.4.1	REGGE Trajectories	12
2.4.2	Shrinkage	14
2.4.3	Pomeron	15
2.5	pQCD Models	16
3	Monte Carlo Modelling	19
3.1	The diffVM Generator	19
3.2	Kinematical Distributions	21
4	Experimental Setup	25
4.1	The HERA Collider	25
4.2	The H1 Detector	27
4.2.1	Tracking Detectors	30
4.2.2	Liquid Argon Calorimeter (LAr)	34
4.2.3	Forward Region	35
4.2.4	Superconducting Coil and Iron Yoke	37
4.2.5	Trigger System and Reconstruction	37
4.2.6	Luminosity System	38
5	The Fast Track Trigger	39
5.1	General Introduction	39
5.1.1	Level 1	41
5.1.2	Level 2	42
5.1.3	Level 3	42

5.2	FTT Tracks compared to Offline Reconstructed Tracks	43
6	Data Selection	47
6.1	The ρ^0 Photoproduction Trigger	47
6.2	Run Selection	48
6.2.1	CJC Gain	49
6.2.2	Event Yield	50
6.2.3	Final Run Selection	51
6.3	Reconstruction of Kinematic Quantities	52
6.4	Event Selection	59
6.5	Invariant Mass Distribution	66
6.6	Forward Tagging	70
6.6.1	Tagging Probability	74
6.7	Background	75
7	Acceptance and Efficiency	77
7.1	Visible Cross Section Definition	77
7.2	Acceptance	78
7.3	Efficiency	80
7.3.1	Reconstruction Efficiency	80
7.3.2	Trigger Efficiency	82
7.4	Overall Correction	89
8	Cross Section Determination	91
8.1	Fitting the Invariant Mass Distribution	91
8.2	Elastic Production vs. Proton-Dissociation	93
8.3	Differential Cross Sections	98
8.4	Systematic Uncertainties	100
9	Results	107
9.1	Systematic Uncertainties for the $W_{\gamma p}$ Slopes and the Pomeron Trajectory	115
10	Conclusion	119
II	Hardware	121
11	Development of the Pixel Barrel Module for the CMS Detector	122
11.1	Introduction	122
11.1.1	Secondary Vertex Detection	122
11.2	The Pixel Detector	124
11.2.1	Pixel Barrel Module	125
11.2.2	Description of all Components	126
11.3	ROC Testing	142
11.4	Module Assembly	145

11.5	Module Test Setup	152
11.5.1	Impedance Matching	152
11.6	Results	156
11.6.1	Assembly Line	156
11.6.2	Sensor Leakage Current	156
A	Cross Section Tables	159
	Danksagung	177
	Curriculum Vitae	179

Part I

Analysis

Chapter 1

Introduction

Hadronic processes can be classified in two distinct classes: *soft processes* and *hard processes*.

Soft processes, such as diffractive light vector meson production, have only one typical energy scale which is of the order of the hadron size R (~ 1 fm). The momentum transfer squared t is usually small ($|t| \sim 1/R^2 \sim$ a few 100 MeV^2) and the dependence of the cross section on t is characterized by an exponential fall-off ($d\sigma^{\gamma p}/dt \sim \exp(-R^2 \cdot |t|)$). The large length scale R makes these processes intrinsically non-perturbative and therefore perturbative quantum chromodynamics (pQCD) cannot describe them adequately. A proper description of soft processes can be achieved by the approach of the REGGE theory, where the soft hadronic phenomena are assumed to be dominated by the exchange of a quaint object, the *pomeron*.

Hard processes on the other hand, have besides the soft energy scale (which is still of the order of the hadron size) at least one further 'hard' scale which determines the order of magnitude of the momentum transfer squared t ($\gtrsim 1 \text{ GeV}^2$). The t dependence of the cross section is usually given by a power law. Deep inelastic scattering (DIS) and large p_T jet production are typical examples for hard processes, which can be described by the use of pQCD.

The study of diffraction in hadronic physics began in the 1960ies with the startup of the first high-energy accelerators. The characteristic features of hadronic diffraction were found to be

- steep momentum transfer distributions
- a slow increase with energy of the cross section (total and elastic)
- a narrowing of the forward peak with increasing energy called 'shrinkage'

With the commissioning of the accelerators HERA and Tevatron in the '90ies, the experimentalists observed unexpectedly high rates of diffractive physics in DIS at HERA as well as in jet physics at the Tevatron. Thus the field of diffractive physics could be studied from a different perspective and gave hope to a more complete understanding of the high energy diffraction than hitherto achieved, i.e. to close the gap between soft and hard processes.

With the new colliders also new energy frontiers became accessible. At the HERA collider electrons (or positrons¹) and protons are collided head on. A large fraction of the collisions can be interpreted as photon-proton (γp) interactions² where a virtual photon is radiated off the electron. The elastic photoproduction of vector mesons is such a process:

$$\gamma^* p \longrightarrow V p \quad \text{with } V = \rho, \omega, \phi, \dots \quad (1.1)$$

Vector meson production was already studied in fixed target experiments with center of mass energies up to $W_{\gamma p} \approx 20$ GeV in the early years of diffractive physics. With HERA it was possible to reach center of mass energies of up to $W_{\gamma p} \approx 200$ GeV.

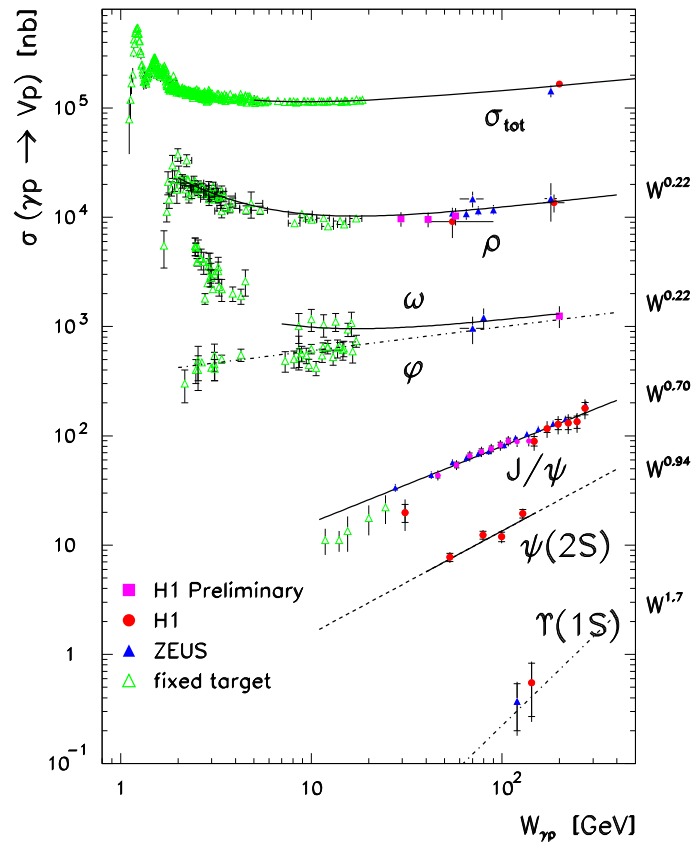


Figure 1.1: The total γp cross section $\sigma_{\gamma p}^{\text{tot}}$ and $\sigma_{\gamma p}$ for various vector mesons. The full lines are fits to the photoproduction cross section while the dashed lines indicate a power law energy dependence as stated on the right hand side.

Elastic photoproduction of light vector mesons at high energies exhibits the typical features of a soft diffractive process, namely a weak energy dependence of the cross section and an exponential

¹Most data at HERA were taken using positrons (e^+) instead of electrons (e^-), from now on 'electron' refers to both particles.

²Also referred to as photoproduction processes.

dependence on the squared four momentum transfer at the proton vertex (t). Those dependencies are also typical for elastic hadron-hadron scattering and are consistent with the vector meson dominance model (VDM) where the photon is assumed to fluctuate into a virtual vector meson before interacting with the proton.

Even though elastic photoproduction of ρ^0 mesons has been studied in many experiments and analyses also at HERA [1–19], many aspects in the high energy domain remain uncertain, in particular the energy dependence of the cross section with increasing $W_{\gamma p}$ (Fig. 1.1). The previous measurements extracted the cross sections differentially in t for a fixed $W_{\gamma p}$ and combined their results with other experiments (different $W_{\gamma p}$) to extract this energy dependence.

This thesis presents an analysis done at the H1 experiment, where the cross section is determined double differentially in $W_{\gamma p}$ and t and the energy dependence is extracted from a measurement at a single experiment differentially in t .

During a major upgrade project at the HERA collider, the H1 experiment was equipped with a new highly selective track trigger which allows for a very efficient triggering of vector mesons and thus provides a large enough data sample to extract the cross section double differentially.

Chapter 2

An Introduction to High Energy Particle Diffraction

2.1 Kinematics

2.1.1 Two Body Processes

All relevant processes in this thesis are two body reactions $A + B \longrightarrow C + D$ as illustrated in Fig. 2.1.

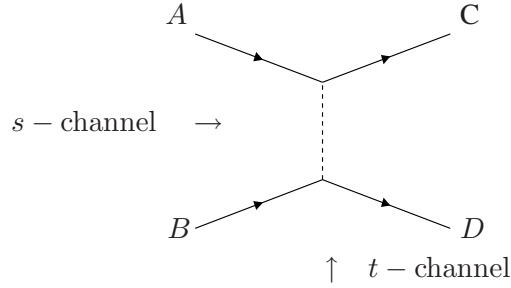


Figure 2.1: The two body reaction $A + B \longrightarrow C + D$ can be viewed in the s -channel or the t -channel.

Denoting p_i as the four vector of particle i , the two Lorentz invariant variables s and t are then defined as:

$$s = (p_A + p_B)^2 = (p_B - p_{\bar{A}})^2 = (p_C + p_D)^2 = (p_C - p_{\bar{D}})^2 \quad (2.1)$$

$$t = (p_C - p_A)^2 = (p_C + p_{\bar{A}})^2 = (p_B - p_D)^2 = (p_B + p_{\bar{D}})^2 \quad (2.2)$$

An important feature of such reactions is the crossing symmetry: For the reaction $A+B \longrightarrow C+D$ the square of the center of mass energy is given by s while t is the squared four momentum transfer.

For the crossed reaction $A + \bar{C} \longrightarrow \bar{B} + D$ the two variables are interchanged; t is the square of the center of mass energy and s the squared four momentum transfer. Two body reactions can therefore be looked at either in the s -channel or the t -channel.

2.1.2 Electron - Proton Scattering

A schematic diagram of the reaction $e + p \longrightarrow e' + Y$ is shown in Fig. 2.2. Within the electroweak theory the exchanged gauge boson for neutral current (NC) interactions can either be a photon (γ) or a neutral weak vector boson (Z^0)¹.

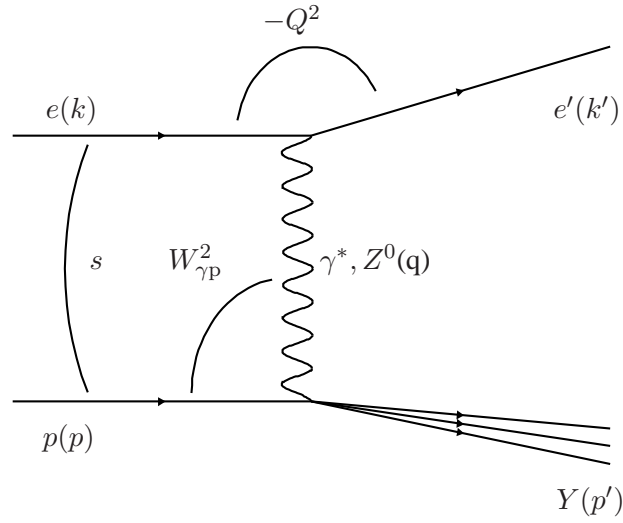


Figure 2.2: Generic ep scattering event with the kinematic variables. The electron interacts via a photon exchange with the proton.

The kinematics of such an event can be described by the following variables

$$s \equiv (k + p)^2 \approx 4 \cdot E_p \cdot E_e \quad (2.3)$$

$$Q^2 \equiv -q^2 \equiv -(k - k')^2 \quad (2.4)$$

$$W_{\gamma p}^2 \equiv (q + p)^2 \quad (2.5)$$

with s being the square of the ep center of mass energy, $E_{e(p)}$ the energy of the incoming electron (proton) beam, Q^2 the momentum transfer at the electron vertex and $W_{\gamma p}^2$ the γp center of mass energy squared.

¹The Z^0 exchange is suppressed by a factor $\sim Q^2/(Q^2 + M_Z^2)$ and can be neglected for the kinematic phase space considered in this thesis ($Q^2 < 4 \text{ GeV}^2$).

Further kinematical variables in ep -scattering are

$$y \equiv \frac{q \cdot p}{k \cdot p} \quad (2.6)$$

$$x \equiv \frac{Q^2}{2 \cdot q \cdot p} \quad (2.7)$$

where y is the fraction of the beam electron energy carried by the photon in the proton rest frame, commonly called the inelasticity, and x is the Bjorken Scaling variable denoting the fraction of the beam-proton energy carried by the struck quark in the infinite momentum frame.

The following relations between the kinematical variables are useful

$$Q^2 = x \cdot y \cdot s \quad (2.8)$$

$$W_{\gamma p}^2 = y \cdot s - Q^2 + m_p^2 \quad (2.9)$$

2.1.3 Vector Meson Production

The diffractive production of vector mesons ($V = \rho, \phi, \omega, \dots$) can either be elastic

$$ep \longrightarrow epV \quad (2.10)$$

or inelastic

$$ep \longrightarrow eYV \quad (2.11)$$

where the proton dissociates. The latter process is often referred to as *proton dissociation*. The two diagrams for the production processes are given in Fig. 2.3.

2.2 Equivalent Photon Approximation and Vector Meson Dominance Model

The incoming electron emits a virtual photon which then interacts with the proton. Therefore it is appropriate to consider the interaction as photon-proton interaction.

For such events the Lorentz invariant variable t can be expressed as

$$|t| = (p - p')^2 \quad (2.12)$$

with p and p' the four-momenta of the incoming and scattered proton.

The ep cross sections at the HERA collider are related to the virtual γp cross sections by the photon flux from the electron which can be modeled by the improved Weizsäcker-Williams Approximation (WWA) [20–23], also referred to as equivalent photon approximation². The ep cross section factorises into the γp cross section and the transverse photon flux Γ_T :

²WWA describes the incoming particle as beam of photons with the same energy spectrum as the field of the particle, namely transverse components.

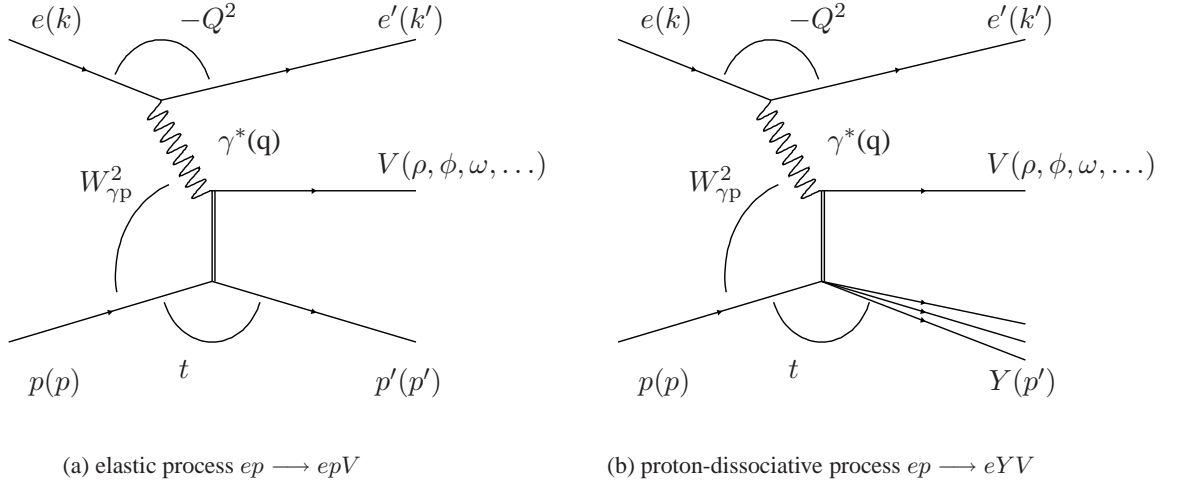


Figure 2.3: The diffractive production processes for ρ^0 . In (a) the proton scatters elastically while in (b) the proton dissociates. The latter case is called inelastic or proton dissociative process.

$$\sigma_{ep} = \int_{y_{\min}}^{y_{\max}} dy \int_{Q_{\min}^2}^{Q_{\max}^2} dQ^2 \cdot \Gamma_T(y, Q^2) \cdot \sigma_{\gamma p}(y, Q^2) \quad (2.13)$$

$$\text{with} \quad \Gamma_T(y, Q^2) = \frac{\alpha_{\text{em}}}{2\pi y Q^2} \left(1 + (1-y)^2 - 2m_e^2 \frac{y^2}{Q^2} \right) \quad (2.14)$$

where α_{em} is the fine structure constant and m_e the electron mass. The integrated flux of transversely polarized photons Φ can be defined as

$$\Phi = \int_{y_{\min}}^{y_{\max}} dy \int_{Q_{\min}^2}^{Q_{\max}^2} dQ^2 \cdot \Gamma_T(y, Q^2) \quad (2.15)$$

Relating y and W , the ep cross section for a bin extending from $W_{\min} < W < W_{\max}$, $Q_{\min}^2 < Q^2 < Q_{\max}^2$ can be related to the γp cross section by:

$$\sigma_{ep} = \Phi \cdot \sigma_{\gamma p}(\langle W_{\gamma p} \rangle, \langle Q^2 \rangle) \quad (2.16)$$

From the measurement one gets the ep cross section whereas the theoretical predictions are calculated for the γp cross section. With Eq. (2.16) it is possible to extract the γp cross section from the measured ep cross section for comparisons.

Photon-hadron collisions have similar properties and behavior as hadron-hadron collisions. The uncertainty principle allows the photon to fluctuate into a $q\bar{q}$ pair with the same quantum numbers as the photon ($J^{PC} = 1^{--}$; $Q = S = B = 0$), namely vector mesons. If the fluctuation happens long before the interaction, it can be assumed that the vector meson interacts with the proton (Fig. 2.4).

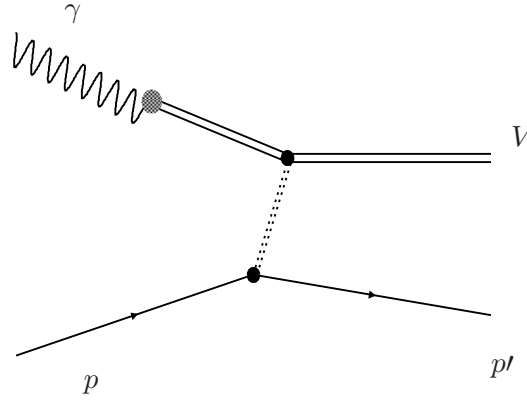


Figure 2.4: Vector meson production in the vector meson dominance model (VDM). The photon fluctuates into a light vector meson and interacts elastically with the proton.

The vector meson dominance model (VDM) [24–28] describes the photon therefore as superposition of a bare QED³ photon $|\gamma_{\text{QED}}\rangle$ and an hadronic part $|h\rangle$

$$|\gamma\rangle = N|\gamma_{\text{QED}}\rangle + \sum_h \frac{e}{\gamma_h} |h\rangle \quad (2.17)$$

where N is a normalization factor, e is the electron charge and γ_h denotes the VDM coupling constants [29]:

$$\frac{4\pi}{\gamma_h^2} = \frac{3\Gamma_{ee}}{\alpha_{\text{em}}^2 m_h} \quad (2.18)$$

with α_{em} being the fine structure constant and m_h and Γ_{ee} the mass and partial width $\Gamma(e^+e^-)$ of the vector meson respectively.

While VDM allows only light vector mesons (ρ^0 , ω and ϕ) as hadronic components of $|h\rangle$, further contributions to the hadronic part are considered in the generalized vector meson dominance model (GVD). A more detailed description of these models can be found in [27, 30, 31].

³Quantum ElectroDynamics

2.3 Diffraction: A Definition

The term diffraction was first used by Francesco Maria Grimaldi (1618 - 1663) who collected his optical observations and speculations in his book 'Physico-Mathesis de lumine, coloribus, et iride'.

In nuclear high energy physics the term was introduced in the 1950ies by Landau and his school [32, 33]. It is used in strict analogy with the optical phenomenon of diffraction where the intensity of the diffracted light at small angles ϑ and large wave numbers k is given by

$$I(\vartheta) \simeq I(0)(1 - bk^2\vartheta^2), \quad (2.19)$$

where $b \sim R^2$, the squared radius of the obstacle or the hole in the screen and $q \sim k\vartheta$ is the momentum transfer. The intensity has a forward peak and a rapid decrease. The same behavior is observed for diffractive hadronic processes where the differential cross sections can be expressed as

$$\frac{d\sigma}{dt} = \left. \frac{d\sigma}{dt} \right|_{t=0} e^{-b|t|} \simeq \left. \frac{d\sigma}{dt} \right|_{t=0} (1 - b|t|) \quad (2.20)$$

for small values of t^4 . Despite these similarities, the optical analogy is not fully applicable, i.e. the observed shrinkage of the forward peak with increasing energy is seen solely in hadronic diffraction but not in optics.

Classes of Diffractive Processes

The diffractive hadronic processes can be grouped in three classes: elastic scattering, single and double diffraction.

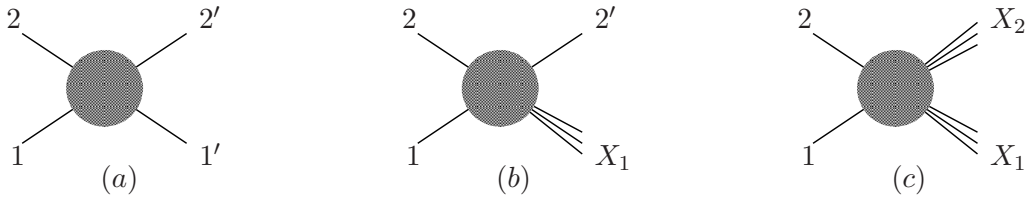


Figure 2.5: The three classes of diffractive hadronic processes: Elastic scattering (a), single diffraction (b) and double diffraction (c).

⁴At high energies the squared momentum transfer is proportional to the scattering angle: $|t| \propto \vartheta^2$.

- elastic scattering

The incident particles emerge after the collision

$$1 + 2 \longrightarrow 1' + 2' \quad (2.21)$$

This interaction is the process of interest for this analysis.

- single diffraction

Here one of the incident particles dissociates into a higher mass state with the same quantum numbers while the other particle emerges unscathed

$$1 + 2 \longrightarrow X_1 + 2' \quad (2.22)$$

- double diffraction

Both incident particles dissociate into a higher mass state with the same quantum numbers

$$1 + 2 \longrightarrow X_1 + X_2 \quad (2.23)$$

A definition of diffraction in purely particle physics terms can be stated as follows [34]:

1. *A reaction in which no quantum numbers are exchanged between the colliding particles is, at high energies, a diffractive reaction.*

As only the vacuum quantum numbers can be exchanged, the emerging particles have to have the same quantum numbers as the incident particles. Diffraction then is the phenomenon taking place asymptotically with increasing energies.

For an elastic scattering like Eq. (2.21) it is trivial to recognize it as diffractive process defined as above. In the case where the final state is not fully reconstructed, i.e. Eq. (2.23), this definition is not very useful. Therefore a more applicable definition of diffraction can be formulated [34]:

2. *A reaction is characterized by a large, non-exponentially suppressed, rapidity gap⁵ in the final state.*

From this definition a reaction such as Eq. (2.23) would be diffractive if the observed rapidity gap (angular separation) between X_1 and X_2 is large.

The phenomenology of diffraction is successfully described within the theoretical framework of REGGE theory. It models the hadronic reactions at high energies as exchange of objects called REGGE trajectories characterized according to the exchanged quantum numbers. The trajectory with the vacuum quantum numbers dominating the high energy domain is called pomeron trajectory.

⁵See Sect. 4.2 for the definition of rapidity.

2.4 An Introduction to REGGE Theory

...Regge theory remains one of the great truths in particle physics...

DONNACHIE & LANDSHOFF [35]

2.4.1 REGGE Trajectories

REGGE theory [36] investigates the dynamics of hadrons by studying the two particle scattering $A+B \longrightarrow C+D$ in the t -channel and the use of the crossing symmetry (Sect. 2.1.1). The quantum numbers for the exchanged object are the same in both the s -channel and the t -channel. The two channels are assumed to share a common scattering amplitude $A(t, s)$ as given in Eq. (2.24), but involve different regions of s and t .

$$A(t, s) \propto A_\ell(t) \cdot P_\ell(\cos \vartheta_t) \quad (2.24)$$

with $A_\ell(t)$ being the partial wave amplitudes, P_ℓ the Legendre polynomials and ϑ_t the scattering angles in the center of mass system of the t -channel reaction. The partial wave amplitude can be identified with a propagator-like term for the exchanged particle of mass M

$$A_\ell(t) \propto \frac{\Gamma_\ell(t)}{t - M^2}. \quad (2.25)$$

Assuming all incident particles have the same mass⁶ m , the scattering angle can be expressed as

$$\cos \vartheta_t = 1 + \frac{2s}{t - 4m^2}. \quad (2.26)$$

The poles of $A_\ell(t)$ from Eq. (2.25) are identified with bound states with respective masses m_ℓ and correspond to the exchanged particles.

Regge's idea [37, 38] was to continue $A(t, s)$ to complex angular momentum ℓ and thus obtain an interpolating function $A(\ell, t)$, which reduces to $A_\ell(t)$ for $\ell = 0, 1, 2, \dots$ and is defined for complex angular momentum ℓ .

The sequence of poles for $\ell = L_1$ at $t = t_1$, $\ell = L_2$ at $t = t_2$, \dots is interpreted as single moving REGGE pole at $\ell = \alpha(t)$, where $\alpha(t)$ is called *REGGE trajectory*.

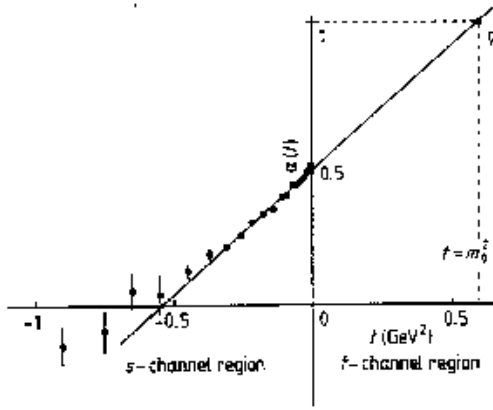
When $\alpha(t)$ is equal to an integer value L for a certain energy t , this corresponds to a resonance or a bound state with $\ell = L$ and mass and width given by $t_\ell = m_L^2 - im_L\Gamma$. The same trajectory also has a pole at the real value $t = m_L^2$ for a complex $\ell = L + \text{Im } \alpha(t)$. These real values t_R with $\text{Re}(\alpha(t_R)) = L$ correspond to particles with masses $m_L^2 = t_R$ and spin L . In Fig. 2.6(a) the ρ trajectory is plotted as determined from the charge exchange reaction $\pi^- p \rightarrow \pi^0 n$ [39, 40]. For $t = m_\rho^2$ the trajectory takes the value of the spin of the ρ : $\alpha(m_\rho^2) = 1$.

For different processes, in general, other vector mesons can mediate the interaction where the mediating particles are determined by quantum number conservation. The masses and spins of

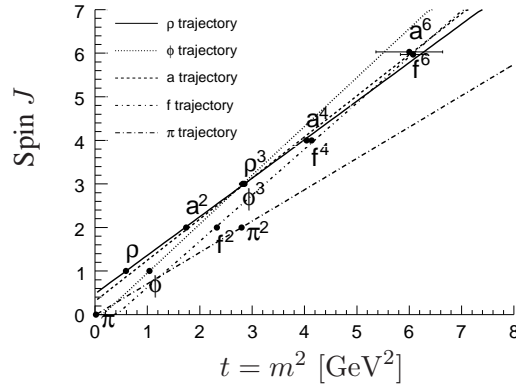
⁶Basically this is only true in the case of elastic scattering of identical particles, but as long as all incident particles are on their mass shell, the mass differences become negligible in the considered high energy limit.

these particles plotted against each other in the spin- t -plane, the so called Chew-Frautschi plot [41], lie almost on a straight line as shown in Fig. 2.6(b). Each of these lines represents a REGGE trajectory of the form

$$\alpha(t) = \alpha_0 + \alpha' \cdot t. \quad (2.27)$$



(a) The ρ trajectory as extracted from the reaction $\pi^- p \rightarrow \pi^0 n$ [39, 40].



(b) Various vector meson trajectories plotted in the Chew-Frautschi plane. Each trajectory can be parametrized as straight line as in Eq. (2.27).

Figure 2.6: A single REGGE trajectory (a) with the interpolation between the s and t channel, and leading mesonic trajectories (b).

Originally, Regge used the function $A(\ell, t)$ to obtain the asymptotic behavior of the scattering amplitude in the t -channel for the unphysical limit $\cos \vartheta_t \rightarrow -\infty$:

$$A(t, s) \underset{\cos \vartheta_t \rightarrow -\infty}{\sim} (\cos \vartheta_t)^{\alpha(t)} \quad (2.28)$$

where $\alpha(t)$ is the leading trajectory with the largest real part for a fixed t . Using the crossing symmetry where $A(t, s) = A(s, t)$, the t -channel limit corresponds to the limit $s \rightarrow \infty$ for the crossed s -channel reaction and yields for a fixed t value:

$$A(s, t) \underset{s \rightarrow \infty}{\sim} s^{\alpha(t)} \quad (2.29)$$

The imaginary part of the forward amplitude $A(s, t = 0)$ is related to the total cross section by the optical theorem

$$\sigma_{\text{tot}} = \frac{1}{s} \text{Im} A(s, t = 0) \underset{s \rightarrow \infty}{\sim} s^{\alpha(0)-1}. \quad (2.30)$$

In REGGE theory one or more trajectories are exchanged instead of exchanging single particles and one talks about a reggeon \mathbb{R} exchange as shown in Fig. 2.7. Exchanging reggeons will not

violate the Froissart-Martin [42,43] bound if $\alpha(0) < 1$. The Froissart-Martin bound limits the rate of growth with energy of any cross section to

$$\sigma_{\text{tot}} < \frac{\pi}{m_\pi^2} \cdot \ln^2 s \simeq (60 \text{ mb}) \ln^2 s \quad (2.31)$$

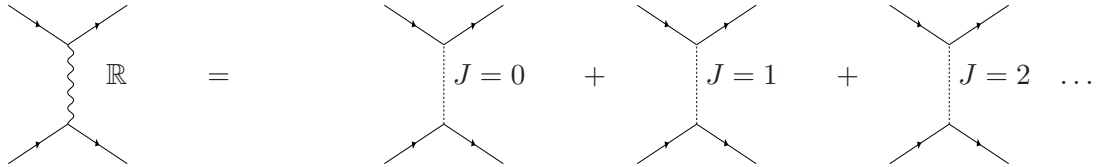


Figure 2.7: Reggeon exchange as formulated within the framework of REGGE theory. Instead of exchanging a single particle with definite spin, a whole family of resonances, so called REGGE trajectory, is exchanged in the t channel.

REGGE theory predicts, that the properties of t -channel reactions (left side of the spin- t plane, $t < 0$) are fixed by the properties of the REGGE trajectory formed by the exchanged particles on the right side ($t > 0$, s -channel) of the spin- t plane.

2.4.2 Shrinkage

The differential cross section is related to the scattering amplitude by

$$\frac{d\sigma}{dt} \simeq \frac{1}{s^2} |A(s, t)|^2 \quad (2.32)$$

for large energies s . Inserting Eq. (2.29) yields

$$\frac{d\sigma}{dt} \simeq \left(\frac{s}{s_0} \right)^{2(\alpha(t)-1)} \quad (2.33)$$

where s_0 is a scaling factor. For a single reggeon exchange with a trajectory given by Eq. (2.27) the differential cross section can be written as

$$\frac{d\sigma}{dt} \simeq \left(\frac{s}{s_0} \right)^{2(\alpha(0)-1)} \cdot e^{-f(t)} \quad (2.34)$$

where $f(t)$ describes the functional dependence of the fall off of the cross section. REGGE theory models $f(t)$ in case of vector meson production as:

$$f(t) = |t| \cdot (b_0 + 2\alpha'_{\mathbb{P}} \cdot \ln(s/s_0)) \quad (2.35)$$

with b_0 and W_0 being free parameters. For increasing energies s the fall off $f(t)$ rises which corresponds to the shrinkage of the forward peak mentioned in Sect. 2.3.

Altogether the differential cross section for elastic vector meson production within the framework of REGGE theory can be expressed as

$$\frac{d\sigma}{dt}(t, W_{\gamma p}) = \left. \frac{d\sigma}{dt} \right|_{t=0, W_{\gamma p}=W_0} \cdot \left(\frac{W_{\gamma p}}{W_0} \right)^{4(\alpha(0)-1)} \cdot e^{-b_0 \cdot |t|} \cdot \left(\frac{W_{\gamma p}}{W_0} \right)^{-4\alpha'_p \cdot |t|}, \quad (2.36)$$

where s has been replaced by $W_{\gamma p}^2$, the squared center of mass energy for photon-proton interactions.

2.4.3 Pomeron

The REGGE trajectories from Fig. 2.6(b) have intercepts $\alpha(0)$ which are less than 0.5 and their exchange would lead to a total cross section (Eq. (2.30)) decreasing with increasing energy s . Experimentally the opposite is observed as can be seen in Fig. 1.1: While for low center of mass energies a decreasing σ_{tot} is observed, it starts to rise toward higher energies.

To preserve REGGE theory the existence of a trajectory with intercept $\alpha_0 \gtrsim 1$ had to be introduced. Gell-Mann named it 'Pomeranchukon trajectory' after Pomeranchuk, who derived his theorems about the asymptotic behavior of the differences of cross sections in 1958 [44]. For simplicity, the name was later on abbreviated to pomeron trajectory.

Studies by Donnachie and Landshoff [35] showed that the use of only two main trajectories is sufficient to describe the data of total hadron-hadron cross sections: An effective meson trajectory and the pomeron trajectory. The parameters of the trajectories are given in Table 2.1.

Parameters of the two main trajectories		
Trajectory	Intercept α_0	Slope α'
Effective meson	0.4525	0.9 GeV ⁻²
Pomeron	1.0808	0.25 GeV ⁻²

Table 2.1: The parameters of the two main REGGE trajectories by Donnachie and Landshoff.

Since the intercept for the effective meson trajectory is smaller than 1, only the pomeron trajectory contributes to the total cross section (Eq. (2.30)) at high energies. The pomeron trajectory is therefore responsible for the rise of the total cross section with increasing center of mass energy squared s . Most processes contributing to the total cross section have very small p_T which led to the term *soft pomeron* for the interaction.

The recurrences of the pomeron trajectory do not correspond to any known particle and are expected to be glueballs. A 2^{++} candidate from [45] is compatible with the parameters of the pomeron trajectory from Donnachie and Landshoff and is shown in Fig. 2.8.

Early measurements of the total hadronic γp cross section at HERA [16, 18] are in agreement with the Donnachie and Landshoff parametrizations. Therefore also at HERA the rise of the total hadronic γp cross section with the center of mass can be described by the soft pomeron.

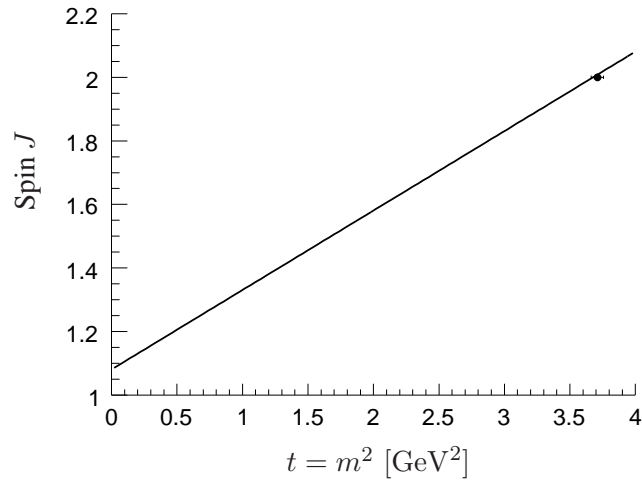


Figure 2.8: The pomeron trajectory with the parameters from Donnachie and Landshoff [35] with a glueball candidate [45].

2.5 pQCD Models

In perturbative QCD (pQCD) diffractive vector meson production is described by the exchange of a colorless two-gluon system. This can either be a simple two-gluon pomeron or a gluon ladder. For the latter, the leading logarithmic approximation (LLA) is applied, which encompasses the whole system of LLA ladder diagrams. The corresponding diagrams are given in Fig. 2.9.

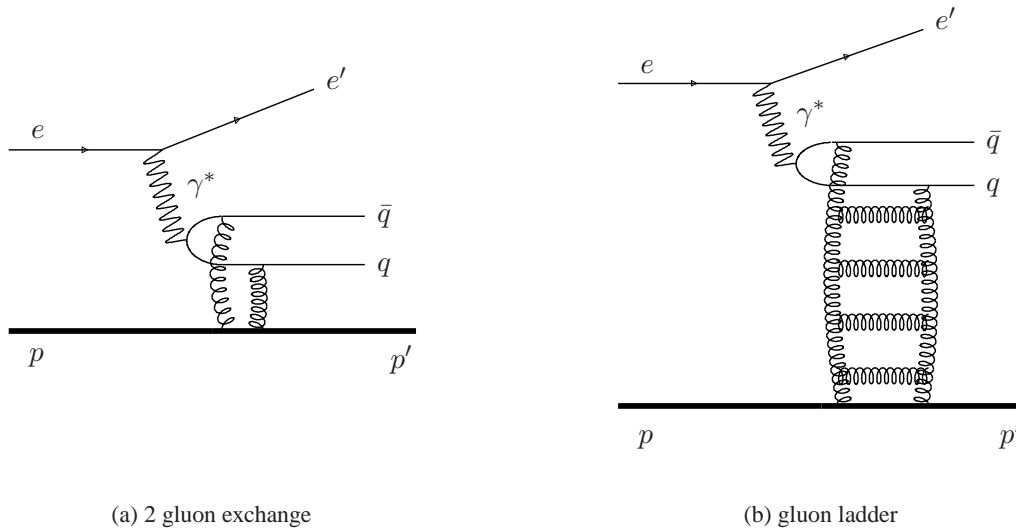


Figure 2.9: The 2 gluon and gluon-ladder pQCD leading order diagrams for the Pomeron exchange. In total are all four combinations of the two gluons coupling to the two quarks considered.

A pQCD equivalent of the pomeron is postulated within the framework of the BFKL formalism [46]. It is an asymptotic ($x \rightarrow 0$) of the scattering amplitude in pQCD in a kinematic region, where the logarithmic scale is large, $\alpha_s \ln(1/x) \gg 1$, and the virtualities of the incoming particles are more or less the same.

The highest eigenvalue of the BFKL equation is related to the intercept of the pomeron. In leading order (LO) it turns out to be rather large, $\alpha_{0,\text{BFKL}} = 1 + 12 \ln(1\alpha_s/\pi) \simeq 1.55$ for $\alpha_s = 0.2$. Since the running of the QCD coupling constant α_s is not included and the allowed kinematic range of LO BFKL is not known, next-to-leading order (NLO) calculations are important. NLO corrections to the BFKL resummation of energy logarithms were found to be large [47, 48] and the resulting NLO BFKL pomeron intercept is about $\alpha_{0,\text{BFKL}} \simeq 1.165$. No information on the slope is given in [46] and it is assumed to be zero. The resulting BFKL pomeron trajectory would then be

$$\alpha_{\text{BFKL}} \simeq 1.165 \tag{2.37}$$

Chapter 3

Monte Carlo Modelling

The *Monte Carlo methods* (MC) are a class of computational algorithms for simulating the behavior of various physical and mathematical systems. They are distinguished from other simulation methods by being stochastic, using mostly random numbers as opposed to deterministic algorithms.

In particle physics these methods are embedded in *Monte Carlo Generators* which randomly compute the 4-vectors of particles on parton level within the physical context of the generator. These generated four vectors are further processed by dedicated simulation routines (H1SIM, GEANT) to simulate the detector response. The output of the simulation routines is used as input for the reconstruction mechanism (H1REC) of the detector. This assures that the generated processes undergo the identical reconstruction and analysis chain as the actual data.

3.1 The diffVM Generator

All MC simulations used in this analysis are based on the diffVM Generator [49]. It was written to simulate diffractive vector meson production in ep scattering at HERA using the framework of REGGE theory and the VDM. Both elastic and proton dissociative vector meson production can be generated.

The virtual photon emission from the incident electron is generated using the equivalent photon approximation. Angle and energy are calculated depending on y and Q^2 . The helicity of the emitted photon is also generated and relevant for angular distributions of the vector meson decay particles and the Q^2 dependence of the cross section. Additional photon emissions from initial or final state radiation are not implemented.

Within the VDM, the photon fluctuates into a virtual vector meson prior to the interaction. The cross section for transversely polarized photons is parametrized as

$$\sigma_{\gamma^*p}^T = \sigma_{\gamma p} \left(\frac{1}{1 + \frac{Q^2}{\Lambda^2}} \right)^n \quad (3.1)$$

with $\Lambda = m_V$ the mass of the vector meson produced in the reaction. The cross section ratio for longitudinally to transversely polarized photons is implemented as follows

$$R(Q^2) = \frac{\sigma_{\gamma^*p}^L}{\sigma_{\gamma^*p}^T} = \frac{\xi \frac{Q^2}{\Lambda^2}}{1 + \chi \xi \frac{Q^2}{\Lambda^2}}, \quad (3.2)$$

with ξ a constant parameter of the Q^2 dependence of R and χ a purely phenomenological parameter limiting $R(Q^2)$ to $\frac{1}{\chi}$ for $Q^2 \gg \Lambda^2$. For $\Lambda = m_V$ and $\chi = 0$ Eq. (3.2) reduces to

$$R(Q^2) = \xi \frac{Q^2}{m_V^2} \quad (3.3)$$

giving $\sigma_{\gamma^*p}^L \rightarrow 0$ for $Q^2 \rightarrow 0$ since real photons are transversely polarized.

As mentioned, diffVM uses the framework of REGGE theory to describe the $W_{\gamma p}$ and t dependence of the γp cross section for vector meson production. According to Eq. (2.36) the cross section for elastic scattering of the vector meson V and a proton within that framework can be written as

$$\frac{d\sigma}{dt} = \left. \frac{d\sigma}{dt} \right|_{t=0, W_{\gamma p}=W_0} \cdot e^{-b|t|} \cdot \left(\frac{W_{\gamma p}}{W_0} \right)^{4\varepsilon} \quad (3.4)$$

with

$$b(W_{\gamma p}) = b(W_0) + \alpha' \ln \left(\frac{W_{\gamma p}}{W_0} \right)^4 \quad (3.5)$$

for a fixed center-of-mass energy $W_{\gamma p}$ and momentum transfer squared t . Free input parameters are the slope parameter $b(W_0)$ at a fixed value of $W_{\gamma p}$, the intercept of the exchanged pomeron trajectory $1 + \varepsilon$ and its slope α' . The mass of the vector meson is generated according to a non-relativistic Breit-Wigner distribution.

For the inelastic scattering, the diffractive dissociation of the proton is modelled according to

$$\frac{d^2\sigma}{dt dM_Y^2} \propto \frac{f(M_Y)}{M_Y^{2(1+\varepsilon)}} \quad (3.6)$$

with M_Y being the mass of the dissociated system and $\varepsilon = 0.0808$. For the low mass region $M_Y < 1.9$ GeV the deviations from a pure $1/(M^2)^{1+\varepsilon}$ behavior are parametrized by the function $f(M_Y)$ which was fitted to experimental data [50]. In this mass region, the dissociating system is treated as one of the N^{*+} nucleon resonances (N(1440), N(1520), N(1680) and N(1700)) which decay according to the measured branching ratios [51]. For the mass region $M_Y > 1.9$ GeV, the system is modeled as a quark-diquark system, where the quark is assumed to be scattered out of the proton, and the hadronization is performed using the Lund fragmentation as implemented in JETSET [52].

For both elastic and dissociative simulations, 10 million events were generated and reconstructed with the total γp cross section $\sigma_{\gamma p,0} = 13.8 \text{ mb}$ corresponding to a simulated integrated Luminosity for the elastic (dissociative) simulation of 3.928 pb^{-1} (4.418 pb^{-1}). The free parameters used for the elastic and proton dissociative simulation are summarized in Table 3.1.

diffVM Generator Settings									
process	$\sigma_{\gamma p,0}$ [μb]	n	Λ	ξ [GeV]	χ	ε^{gen}	α'^{gen} [GeV $^{-2}$]	W_0^{gen} [GeV]	b^{gen} [GeV $^{-2}$]
elastic	13.8	2.4	0.770	0.42	1.11	0.0808	0.0	90	5
proton-dissociative	13.8	2.4	0.770	0.42	1.11	0.0808	0.0	90	2

Table 3.1: diffVM Generator Settings of free input parameters for elastic and proton dissociative simulation.

3.2 Kinematical Distributions

The distributions of the kinematic variables in the MC simulation vary often from the actual distributions observed in the data. Therefore the MC events are reweighted in the corresponding kinematic variables to get the best possible description of the experimentally observed distributions. For this analysis the relevant kinematic variables are $W_{\gamma p}$, t and $m_{\pi\pi}$.

- $W_{\gamma p}$ and t

The differential cross section in t depends not only on t but also on $W_{\gamma p}$ as can be seen from Eq. (3.4). The MC generator models a purely exponential behavior in t , $d\sigma^{\gamma p}/dt = \exp(b_0 t)$ while the data shows an exponential decrease of the form $d\sigma^{\gamma p}/dt \propto \exp(b_0 t + b_0^2 t^2/2a)$ at low values of $|t|$. For larger $|t|$ values the decrease is dominated by a power law behavior $d\sigma^{\gamma p}/dt \propto |t|^{-a}$. The MC events are therefore reweighted to the form

$$\frac{d\sigma^{\gamma p}}{dt} \propto e^{(a \ln(1-b_0 t/a))} \quad (3.7)$$

which smoothly interpolates between the two $|t|$ regions. The parameter values are $b_0 = 11.5$ (6.2) GeV $^{-2}$ at $W_0 = 90$ GeV and $a = 23$ (6.0) for elastic (proton-dissociative) ρ^0 production. The coefficient a has been determined from fits of the form $d\sigma^{\gamma p}/dt \propto \exp(b_0 t + c_0 t^2)$ for elastic production and fits to large $|t|$ data for the proton-dissociative production [53]. For the generation of the elastic (proton-dissociative) sample, the b_0^{gen} parameter was set to 5 (2) (Table 3.1) to enhance the statistics at large $|t|$ values. Altogether, the applied weight $w(W_{\gamma p}, t)$ then takes the form

$$w(W_{\gamma p}, t) = \frac{\sigma_{\gamma p,0} \cdot e^{a \ln(1-b_0 t/a)} \cdot b_0 \cdot \left(\frac{W_{\gamma p}}{W_0}\right)^{4(\varepsilon+\alpha' t)}}{\sigma_{\gamma p,0}^{\text{gen}} \cdot e^{b_0^{\text{gen}} t} \cdot b_0^{\text{gen}} \cdot \left(\frac{W_{\gamma p}}{W_0^{\text{gen}}}\right)^{4(\varepsilon^{\text{gen}}+\alpha'^{\text{gen}} t)}} \quad (3.8)$$

with $\sigma_{\gamma p,0} = \sigma_{\gamma p}(W_0)$ and $\sigma_{\gamma p,0}^{\text{gen}} = \sigma_{\gamma p}^{\text{gen}}(W_0)$.

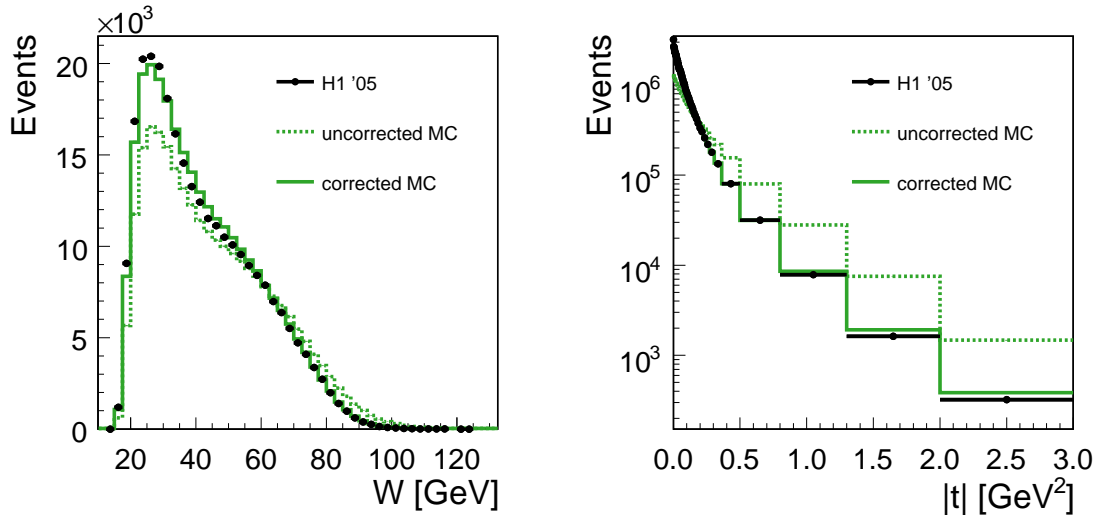


Figure 3.1: The $W_{\gamma p}$ and t distributions for data (dots) and MC events. The MC distributions are shown before (dashed) and after (solid) the reweighting.

- Di-pion Mass $m_{\pi\pi}$

The vector meson mass is generated according to a non-relativistic Breit-Wigner ($nrBW$) distribution

$$nrBW(m_{\pi\pi}) = \frac{0.25 \cdot \Gamma_{\rho,0}^2}{(m_{\pi\pi} - m_\rho)^2 + 0.25 \cdot \Gamma_{\rho,0}^2} \quad (3.9)$$

with $m_\rho = 0.770$ GeV and $\Gamma_{\rho,0} = 0.150$ GeV, in the mass range between $m_{\text{low}}^{\text{gen}} = 2m_\pi$ and $m_{\text{high}}^{\text{gen}} = 2.27$ GeV. For the presented analysis the visible cross section is defined within the mass range of $m_{\text{low}} = 2m_\pi$ to $m_{\text{high}} = m_\rho + 5 \cdot \Gamma_\rho$ (see also Sect. 7.1). The MC events are re-weighted to a skewed relativistic Breit-Wigner (rBW) distribution as it is implemented in the model by Ross and Stodolsky [54] (see Sect. 6.5 for details)

$$rBW(m_{\pi\pi}, n) = \frac{m_\rho m_{\pi\pi} \Gamma_\rho}{(m_\rho^2 - m_{\pi\pi}^2)^2 + (m_\rho \Gamma_\rho)^2} \cdot \left(\frac{m_\rho}{m_{\pi\pi}}\right)^n \quad (3.10)$$

with the momentum dependent width Γ_ρ defined in Eq. (6.14) on page (67) and the skewing parameter n given by [53,55]

$$n(t) = 6.1 \cdot \exp(-1.95 \text{ GeV}^{-2} \cdot |t|). \quad (3.11)$$

The resulting weight function can be expressed as

$$w(m_{\pi\pi}) = \frac{\frac{rBW(m_{\pi\pi}, n)}{\int_{m_{\text{low}}}^{m_{\text{high}}} rBW(m, n=0) dm}}{\frac{nrBW(m_{\pi\pi})}{\int_{m_{\text{low}}^{\text{gen}}}^{m_{\text{high}}^{\text{gen}}} nrBW(m) dm}} \quad (3.12)$$

Additionally to the kinematic variables, the distribution of the reconstructed z-vertex is reweighted as well. As the position of the z-vertex heavily depends on the running conditions and beam settings of the data taking period, the generated distribution in the MC events is broad. This allows for a reweighting of the distribution to describe the experimentally observed distribution without applying large weight factors. The distributions are adequately described by a gaussian function with a linear background term:

$$f(z) = N \cdot e^{-0.5 \left(\frac{z-\mu}{\sqrt{2\nu}} \right)^2} + p \cdot z + q \quad (3.13)$$

where N is a normalization factor, μ and ν are the mean and width of the gaussian and p and q are the slope and intercept of the linear background term respectively. The weight is obtained from the ratio

$$w(z) = \frac{f(z)}{f^{\text{gen}}(z)} \quad (3.14)$$

where $f(z)$ represents the fit result from the real data and $f^{\text{gen}}(z)$ was fitted to the simulated events.

All numerical values of the applied parameters are summarized in Table 3.2. The parameters labeled with 'gen' are either used as input settings for the diffVM generator or obtained from fits to the simulated events.

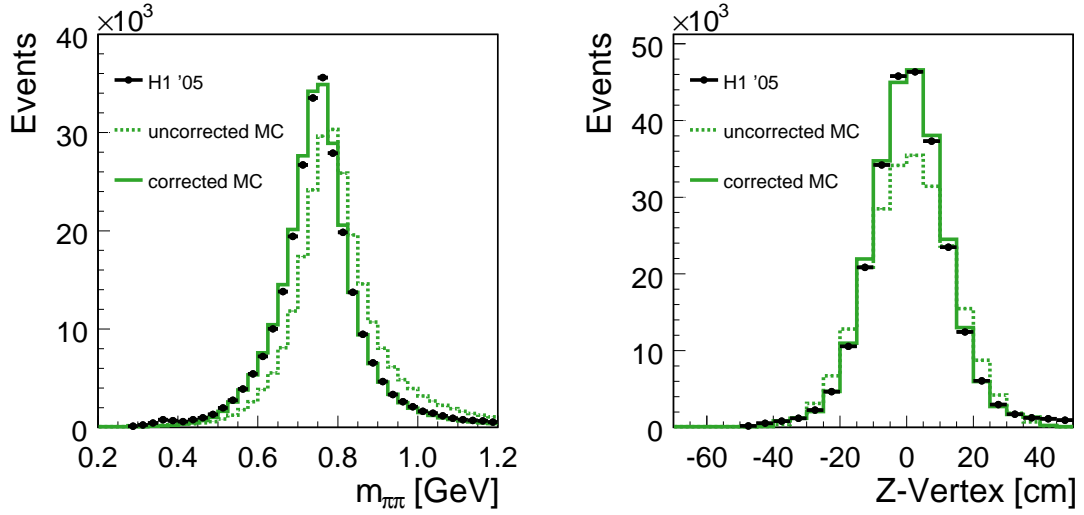


Figure 3.2: The $m_{\pi\pi}$ and Z-Vertex distributions before (dashed) and after (solid) the reweighting.

Reweight Settings						
	$W_{\gamma p}$ and t		Dipion mass $m_{\pi\pi}$		Z-Vertex	
	elastic	proton-dissociative				
σ_0 [μb]	11.5	9.78	m_{low} [GeV]	0.27	N	76106.4
a	23	6	m_{high} [GeV]	1.52	μ	0.436325
b_0 [GeV^{-2}]	11.5	6.0			ν	10.5415
W_0 [GeV]	90	90			p	18.9412
ε	0.08	0.04			q	1948.25
α' [GeV^{-2}]	0.125	0.0				
σ_0^{gen} [μb]	23	6	$m_{\text{low}}^{\text{gen}}$ [GeV]	0.27	N^{gen}	74776.3
b_0^{gen} [GeV^{-2}]	5	2	$m_{\text{high}}^{\text{gen}}$ [GeV]	2.27	μ^{gen}	0.938633
W_0^{gen} [GeV]	90	90			ν^{gen}	12.9119
ε^{gen}	0.0808	0.0808			p^{gen}	0.821527
α'_{gen} [GeV^{-2}]	0	0			q^{gen}	-11.0188

Table 3.2: Reweight Settings used to obtain the best possible description of the data in the MC simulation.

Chapter 4

Experimental Setup

4.1 The HERA Collider

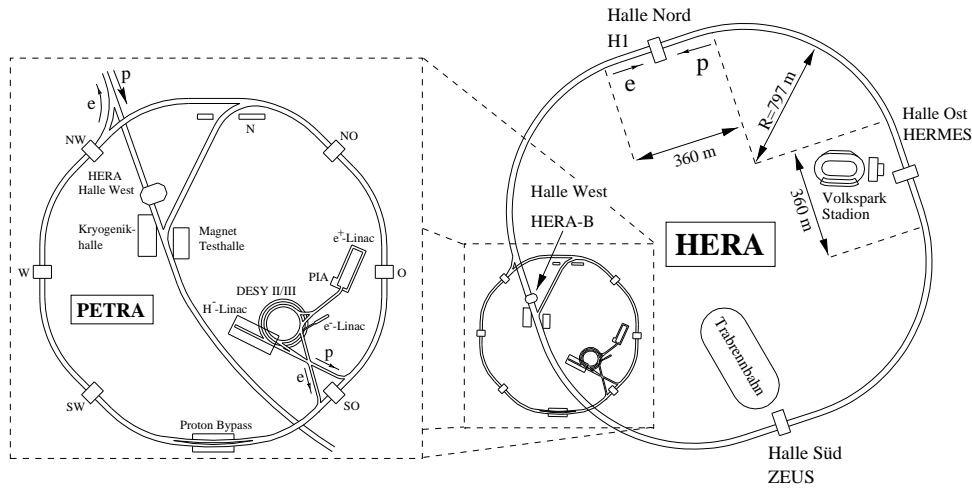


Figure 4.1: The HERA collider with the storage ring and the preaccelerators. The experiment H1 is situated in the northern hall.

The HERA (**H**adron **E**lektron **R**ing**A**nlage) accelerator is located at the DESY laboratories in Hamburg, Germany. HERA accelerates and stores electrons and protons and provides a unique opportunity to study lepton - quark interactions at highest center of mass energies. The two particle types are gathered in bunches with up to 10^{11} particles per bunch. During normal operation roughly 180 bunches of e and p each in 96 ns time intervals circulate in the storage rings. The two storage rings are 6.3 km long and are roughly 20 m below the surface.

HERA is in operation since 1992. The electrons and protons are preaccelerated with various linear accelerators (LINACs) and two storage rings (DESY, PETRA) and then fed to the large HERA rings where the particles reach their final energies of 27.6 GeV and 920 GeV, respectively, leading to a center of mass energy of $\sqrt{s} = 319 \text{ GeV}$ (see Eq. (2.3)). An overview of the preaccelerators

and the HERA rings is given in Fig. 4.1.

Located along the storage rings of HERA there are 4 large experimental halls. The northern hall houses the experiment H1, built and operated by an international collaboration of about 400 scientists from 42 institutes of 15 countries throughout the world. Here the electron and proton beams are collided head-on and the resulting particles of the collisions are detected with the general purpose H1 detector. The main interest of research of the H1 collaboration is to measure the structure of the proton, to study the fundamental interactions between particles, and to search for physics beyond the Standard Model of the elementary particles. The three other halls are occupied by the experiments HERMES, ZEUS and HERA-B.

HERA II Design Parameters		
	e-beam	p-beam
Energy	27.6 GeV	920 GeV
Number of bunches total/colliding	180/174	180/174
Particles per bunch	$4.2 \cdot 10^{10}$	$10 \cdot 10^{10}$
Beam current	58 mA	140 mA
Beam size $\sigma_x \times \sigma_y$	$118 \mu\text{m} \times 32 \mu\text{m}$	$118 \mu\text{m} \times 32 \mu\text{m}$
Collision rate	10.4 MHz	
Luminosity	$7.36 \cdot 10^{31} \text{ cm}^{-2} \text{ s}^{-1}$	
Specific luminosity	$1.64 \cdot 10^{30} \text{ cm}^{-2} \text{ s}^{-1} \text{ mA}^{-2}$	

Table 4.1: Design parameters of HERA II (from [56]).

After the successful running period in the years 1992 - 2000 called HERA I, the accelerator went through a major upgrade project [56, 57] with the goal to raise the luminosity provided by the accelerator. The final energies of the beam particles were not changed, but the beam spot sizes were reduced to increase the luminosity. Therefore the interaction regions¹ had to be completely redesigned and new, superconducting final focussing magnets were placed very close to the interaction points of H1 and ZEUS.

¹The zone where the beams are collided at H1

4.2 The H1 Detector

Unlike most other colliding beam detectors, the H1 detector is not symmetric with respect to the nominal interaction point² (IP); this is due to the different energies of the two beam particles. The proton has more energy (momentum) than the electron and the greater momentum along the beam axis causes the particles from the collision to be boosted in flight direction of the proton beam.

The *reference frame* at H1 is defined as follows: The positive z axis is along the proton beam and is called the forward direction, perpendicular to it is the *xy* plane (where the x-axis points toward the center of the ring and the y-axis points upward), also referred to as the *transverse plane*. The origin of the coordinate system is in the nominal interaction point.

There are further two angles of importance: θ is the *polar angle* between the trajectory and the z-axis (scattering angle) and ϕ the *azimuthal angle* in the transverse plane with $\phi = 0$ corresponding to the positive x-axis.

Another frequently used variable is the *rapidity* \hat{y} :

$$\hat{y} = \frac{1}{2} \ln \frac{E + p_z}{E - p_z} \quad (4.1)$$

with E being the energy of the particle and p_z the longitudinal momentum. With this definition, the rapidity transforms additively under a Lorentz boost along the z-axis and thus any rapidity difference is invariant under longitudinal boosts. In most cases the relevant parameter is the *pseudo-rapidity* η which is an approximation of \hat{y} , neglecting the masses of the particles ($m = 0$). The pseudo-rapidity is correlated with the polar angle θ by

$$\eta \equiv \hat{y}|_{m=0} = -\ln \left(\tan \frac{\theta}{2} \right). \quad (4.2)$$

The H1 detector is divided into three major regions, the forward, central and backward part as listed in Table 4.2. The present analysis concentrates on particles detected in the central area.

Angular Regions of the H1 Detector			
Region	forward	central	backward
Angular coverage	$7^\circ < \theta < 20^\circ$	$20^\circ < \theta < 160^\circ$	$160^\circ < \theta < 175^\circ$

Table 4.2: The three angular regions of the H1 detector, for the polar angle θ , where $\theta = 0^\circ$ corresponds to the proton beam flight direction.

During the HERA upgrade project (2001-2003) the H1 detector was also upgraded. The forward region of the H1 detector was equipped with new detectors. The luminosity system, various sub-detectors and the data acquisition were adapted to the new running conditions. Also the trigger

²The nominal interaction point is the point where the electron and proton beams should collide

system was adjusted as well as extended by new triggers.

Fig. 4.2 shows the H1 detector with the reference frame and the asymmetric structure. A detailed description of the H1 detector is available in [58, 59]. The important elements of the detector are shortly summarized in the following.

Components of the H1 Detector		
	Detector component	Abbreviation
1	Nominal interaction point	IP
<i>Tracking detectors</i>		
2	Central silicon tracker	CST
(3	Backward silicon tracker	BST)
(4	Forward silicon tracker	FST)
5	Central inner proportional chamber	CIP
6	Central outer proportional chamber	COP
	Central outer z chamber	COZ
7	Inner central jet chamber	CJC1
8	Outer central jet chamber	CJC2
9	Forward tracking detectors	FTD
10	Backward proportional chamber	BPC
<i>Calorimeters</i>		
11	Liquid argon container	LAr elm. LAr hadr.
12	Liquid argon electromagnetic calorimeter	
13	Liquid argon hadronic calorimeter	
14	Liquid argon cryogenics system	SpaCal elm. SpaCal hadr.
15	Electromagnetic spaghetti calorimeter	
16	Hadronic spaghetti calorimeter	
17	Superconducting solenoid	
<i>Muon detectors</i>		
18	Instrumented iron (central muon / tail catcher)	CMD/TC
19	Forward muon detector (incl. toroid magnet)	FMD
20	Veto wall / time of flight system	ToF
21	New superconducting focusing magnets	GO/GG
22	Concrete shielding	

Table 4.3: The main components of the H1 detector - legend to Fig. 4.2. The two silicon trackers FST and BST were not inserted in the 2005 running period.

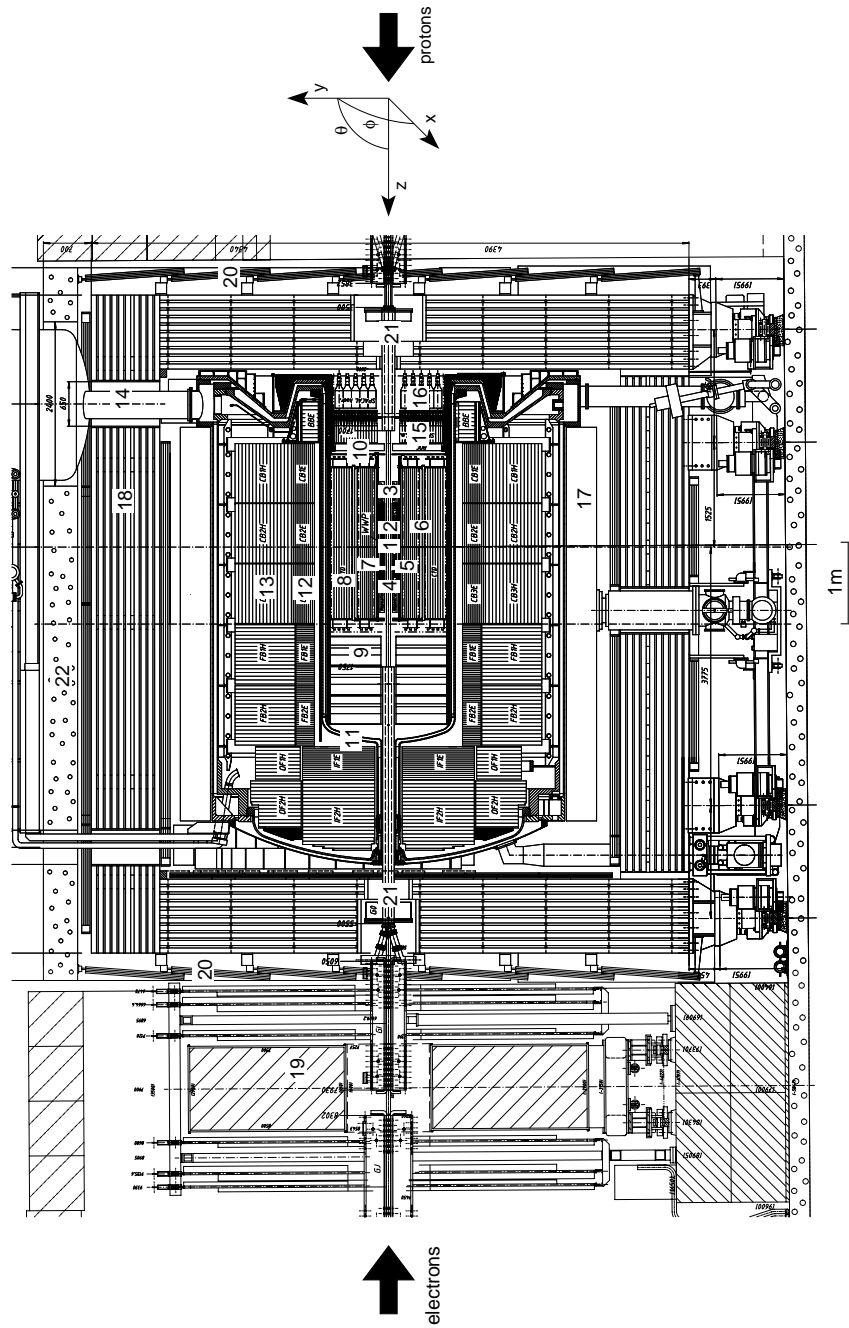


Figure 4.2: A cut through the H1 detector as it appears after the luminosity upgrade; see Table 4.3 for the various subdetectors. The coordinate system used in H1 is shown together with the two angles θ and ϕ .

4.2.1 Tracking Detectors

The innermost part of the detector is responsible for measuring the trajectories of the charged particles and the primary vertex³ location. A charged particle penetrating the tracking chamber will leave a trace in the chamber, this trace forms the trajectory of the particle and is called *track*. According to the three regions along the z -axis, three tracking devices exist: The *Forward Tracking Detector* (FTD), the *Central Tracking Detector* (CTD) and the *Backward Proportional Chamber* (BPC). Fig. 4.3 shows the H1 tracking system in r - z view. One can clearly see the three angular regions from Table 4.2.

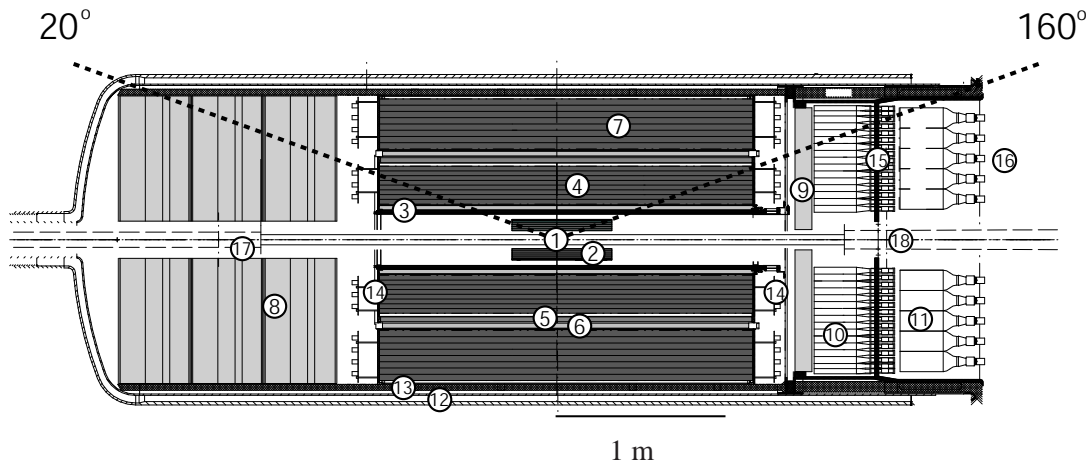


Figure 4.3: The H1 Tracking system in r - z view as it was implemented in the 2005 running period. The central region is given by $20^\circ < \theta < 160^\circ$, Table 4.2.

The CTD is based on two concentric drift chambers, the *Central Jet Chambers* CJC1 and CJC2, the central silicon tracker CST, two proportional chambers CIP and COP (inner and outer, respectively), and the z chamber COZ. See Fig. 4.4.

The tracks are described by five parameters $= (\kappa, \vartheta, \varphi, d, z)$. The transverse momentum p_T is measured with a magnetic field (1.2 Tesla) provided by the superconducting coil (Sect. 4.2.4). The trajectory of a particle with momentum p and electric charge z in a constant magnetic field \vec{B} is a helix with curvature R and pitch angle λ . The momentum can be calculated by the equation

$$p \cos(\lambda) = c_0 \cdot z \cdot e \cdot B \cdot R. \quad (4.3)$$

with c_0 being the speed of light in vacuum. At H1 the relation for the transverse momentum is

$$p_T[\text{GeV}] = 0.345 \cdot R[\text{m}]. \quad (4.4)$$

³the primary vertex is the real interaction point

Components of the H1 Tracker					
1	Nominal interaction point	IP		<i>Calorimeters</i>	
	<i>Central tracking detectors</i>		10	Elm. spaghetti calorimeter	SpaCal elm.
2	Central silicon tracker	CST	11	Hadr. spaghetti calorimeter	SpaCal hadr.
3	Central inner prop. chamber	CIP		<i>Electronics, support and beam magnets</i>	
4	Inner central jet chamber	CJC1	12	CJC electronics	GO GG
5	Central outer prop. chamber	COP	13	Cables	
6	Central outer z chamber	COZ	14	LAr cryostat inner wall	
7	Outer central jet chamber	CJC2	15	SpaCal elm. Photomultipliers	
	<i>Forward tracking detectors</i>		16	SpaCal hadr. Photomultipliers	
8	Forward tracking detectors	FTD	17	Final focussing magnet	
	<i>Backward tracking detectors</i>		18	Final focussing magnet	
9	Backward prop. chamber	BPC			

Table 4.4: The main components of the H1 tracker - legend to Fig. 4.3.

The determination of the curvature R is based on the signals recorded from the CJC1 and CJC2 devices and is correlated to κ by

$$R = \frac{1}{\kappa}. \quad (4.5)$$

Since this analysis is mainly based on information from the CTD, the two main contributors are described in more detail.

Central Jet Chamber (CJC)

The Central Jet Chamber [59] consists of two large drift chambers, the inner CJC1 and the outer CJC2 covering a z range from -112.5 cm to +107.5 cm. The parameters of the two chambers are listed in Table 4.5. They are segmented azimuthally in 30 (60) cells for CJC1 (CJC2) centered around the sense wires. The cells are tilted by 30° so that most tracks will cross the sense wire planes once to correct for the Lorentz angle.

If operated in a magnetic field, the ionization electrons drift approximately perpendicular to the high momentum tracks. It is impossible to determine from which side of the wire plane the drift charge came resulting in a left-right ambiguity. This adds a mirror image of each track to the reconstruction, which can be resolved by the cell tilt and a vertex assumption or the use of both CJC rings.

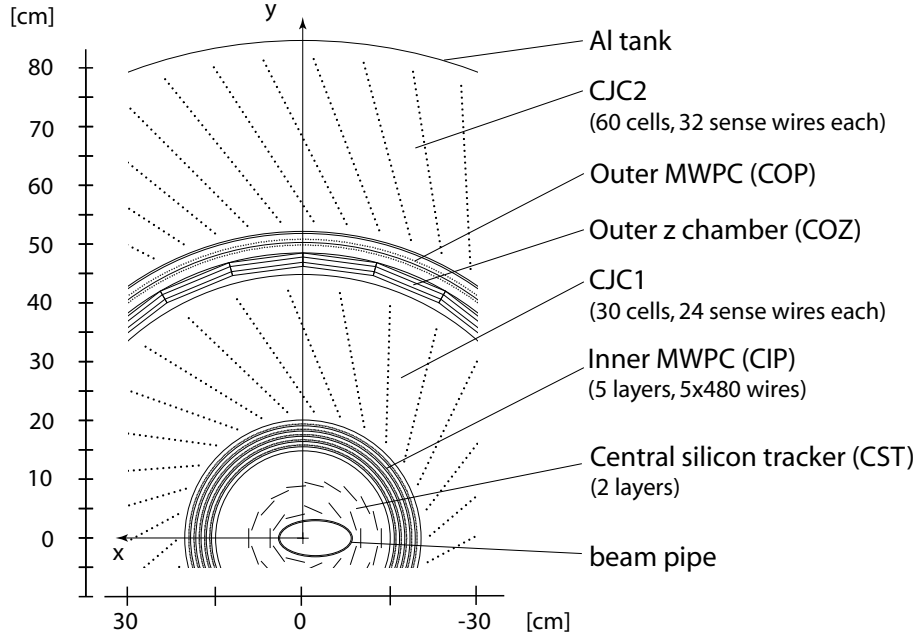


Figure 4.4: An r - ϕ view of the CTD. the presented analysis uses information from the CJC and the CIP only.

The sense wires are read out on both sides and the hit position is reconstructed from the pulse-integral (Q) and the timing (t) in the Qt -analysis. The CJC HV parameters control the electric field applied in the drift chamber and hence the gas amplification. A higher voltage translates to a larger gas amplification, a higher pulse-integral Q and finally in a higher single hit finding efficiency. On the other hand a large gas amplification can cause more frequent overcurrents (trips) on the sense wires in case of high track densities, mainly due to background. A too large gas amplification can result in a lasting damage of the drift chamber due to aging. The single hit resolution in $r - \phi$ is $140 \mu\text{m}$ and for the z coordinate $6 - 10 \text{ cm}$ which is measured by charge division.

CJC Parameters		
	CJC1	CJC2
Number of cells	30	60
Number of sense wires per cell	24	32
inner radius [cm]	20.3	53.0
outer radius [cm]	42.6	84.4
active radius [cm]	22.5	29.6

Table 4.5: CJC Parameters.

Central Inner Proportional Chamber (CIP)

During the upgrade, the old 2-layer-CIP [60] and the CIZ were replaced by a new 5-layer-CIP [61, 62]. It is positioned between the central silicon detector (CST) and the central drift chamber (CJC) covering a z range from $z = -112.7$ cm to $z = +104.3$ cm. Radially, it extends from the innermost layer at $r = 15.7$ cm to $r = 19.3$ cm for the outermost layer. Each radial layer has 480 anode wires with a nominal high voltage during operation of 2250 – 2500 V, depending on the layer.

The cathode of each layer is segmented into pads; there are 16 ϕ sectors covering 22.5° in azimuth. The number of pads in z -direction depends on the layer and is summarized in Table 4.6.

All 5 layers of the CIP are also used to provide trigger information for the first trigger level (see Sect. 4.2.5). With a time resolution around 75 ns the chambers are well below the 96 ns from the HERA bunch crossing frequency and the CIP is able to provide timing information t_0 . This is needed as starting time for the trigger and determines the bunch crossing of the event.

The space points from the cathode pads are combined to track candidates (masks) from which the vertex position can be determined. Depending on the z coordinate of the determined vertex position, the mask will either be added to the central masks or the backward masks, corresponding to a vertex position inside or outside the interaction area of H1. For events resulting from ep collisions, the sum of central masks will exceed the sum of backward masks significantly. The ratio of the sums of central over backward masks can therefore be used to suppress background events with interaction vertices outside the H1 detector [62].

CIP Parameters			
z-range [cm]		-112.7 - +104.3	
radial-range [cm]		15.7 - 20.2	
θ -range		11° - 169°	
Layer	Radius [cm]	Pad length [cm]	Number of Pads / ϕ sector
0	15.7	1.8250	119
1	16.6	1.9322	112
2	17.5	2.0531	106
3	18.4	2.1900	99
4	19.3	2.3464	93

Table 4.6: CIP design parameters (from [62]).

4.2.2 Liquid Argon Calorimeter (LAr)

In the central and forward region of the detector the *Liquid Argon Calorimeter* (LAr) covers an angular range from $4^\circ < \theta < 153^\circ$. It is divided in an electromagnetic (ECAL) and a hadronic (HCAL) part measuring the energies of electrons, photons and hadrons by absorption. These particles will shower up in the calorimeter and deposit their energy while muons deposit only a small amount of energy in both parts of the LAr by ionization. The precision of the measured energy for electromagnetic showers is $\sigma(E)/E = 12\%/\sqrt{E/\text{GeV}} \oplus 1\%$ and for hadronic showers $\sigma(E)/E = 55\%/\sqrt{E/\text{GeV}} \oplus 2\%$ [63].

Fig. 4.5 shows the individual parts and the segmentation of ECAL and HCAL. One can see the central (CB 1 - 3) and the forward barrels (FB 1 - 2, IF, OF), which are divided into the ECAL and the HCAL sections.

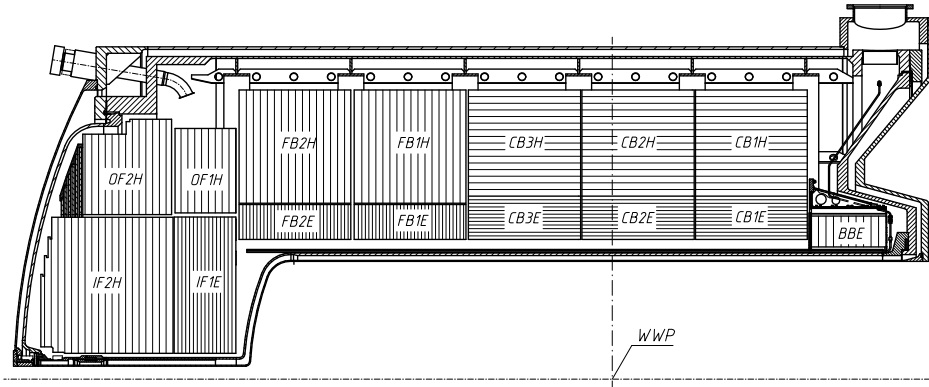


Figure 4.5: LAr calorimeter in r-z view showing the division into individual parts. The ending 'E' stands for the ECAL and 'H' for the HCAL. One can clearly see the partitioning of the LAr calorimeter in central barrels (CB 1 - 3) and forward barrels (FB 1 - 2, IF, OF).

The LAr is highly segmented in cells, which collect the charges from the ionization by the shower particle. The calorimeter reconstruction program converts the charges to energies in the calorimeter cells for electromagnetic and hadronic showers. Each cell passing the cell level reconstruction is subject to clustering. The cluster algorithms are tuned so that the cells containing energy depositions from electromagnetic showers are most probably merged into one cluster whereas for the hadronic showers the energy depositions are often split into several clusters.

Further calorimeters complement the detector in backward (SpaCal) and forward (PLUG) direction.

4.2.3 Forward Region

Due to the asymmetry of the interactions at HERA, the forward region needs a dedicated system of subdetectors to complement the central part of the H1 detector. For geometrical reasons, particles emerging very close to the beampipe cannot be detected within the H1 detector. Therefore most forward detectors are located further along the positive beam axis.

In the frame of this analysis these detectors are used to detect the proton remnant from proton-dissociative events and hence separate the elastic and proton-dissociative processes.

FMD

The Forward Muon Detector (FMD) [64] is located at the very front of the H1 detector. It detects high energy muons within an angular range $3^\circ \leq \theta \leq 18^\circ$ shown in Fig. 4.6. It is built of six drift chamber planes with a toroidal magnet in between. Each drift chamber plane is divided into octants which are formed from individual double-layer drift cells. The two layers are displaced w.r.t. each other to resolve ambiguities and determine the timing t_0 . The orientation of the drift cells in four planes (1, 3, 4 and 6) is such that the polar angle θ can be measured, whereas the other two planes (2, 5) are measuring the azimuthal angle ϕ .

The toroidal magnet is 1.2 m thick and provides a magnetic field of about 1.75 Tesla at the inner radius and roughly 1.5 Tesla at the outer radius.

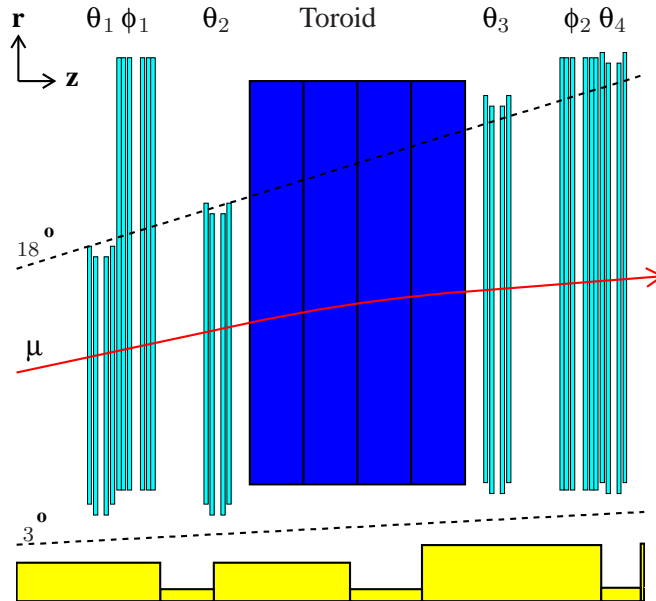


Figure 4.6: The Forward Muon Detector. The first three planes are in front of the toroidal magnet while the the last three planes are behind the magnet. Four out of six planes can determine the polar angle θ while the other two are designed to measure the azimuthal angle ϕ .

During the reconstruction of the FMD, hits of the two drift cell layers are combined to form hit-pairs. These hit pairs are then further combined to track segments and finally linked to track candidates.

FTS

Particles with rapidities large enough to escape the FMD can be detected by the Forward Tagger System (FTS) shown in Fig. 4.7. The FTS includes stations of scintillating counters at a distance of 26 m, 28 m, 53 m and 92 m from the nominal IP. Each station consists of four scintillators mounted symmetrically around the beam pipe. The last two stations at 92 m and 53 m contain two scintillators for each counter while the first two stations have only one scintillator per counter. To protect the counters from synchrotron radiation, each station is shielded by a 1 mm lead plate.

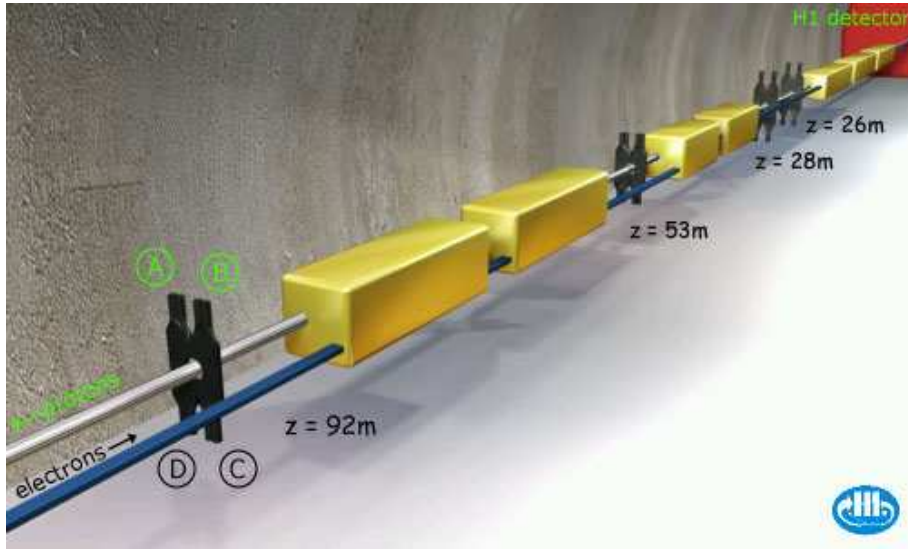


Figure 4.7: The Forward Tagger System.

FNC

The Forward Neutron Counter (FNC) is situated at $z = 107$ m and its purpose is to measure energies and angles from fast neutrons coming from reactions

$$ep \longrightarrow enX \quad (4.6)$$

(V)FPS

To measure protons which are scattered at extremely low polar angles the (Very) Forward Proton Spectrometer ((V)FPS) was installed. Scintillating fiber hodoscopes located in movable vacuum sections, so called roman pots, detect the protons at the FPS stations at 63 m and 80 m horizontally and at 81 m and 90 m vertically. The VFPS station is located at 220 m from the nominal IP.

4.2.4 Superconducting Coil and Iron Yoke

The solenoid provides a magnetic field of 1.2 Tesla parallel to the z-axis and bends the track for the determination of the momentum in the transverse plane.

The iron yoke is instrumented with streamer tubes and measures the leakage of hadronic showers outside the Calorimeter (Tail Catcher). The hit pattern in the muon system (streamer tubes) allows to reconstruct particle tracks penetrating the detector (muons).

4.2.5 Trigger System and Reconstruction

The bunch crossing frequency is 10.4 MHz while the bandwidth for recording events is limited to about 10 Hz. Therefore it is not possible to store all collision events on tape for later analysis, but rather a small sample of selected events. To determine which events are to be kept and which ones can be rejected, the *H1 Trigger System* (CT) was developed. The entire trigger system is set up in 4 levels:

- The first level (L1) has $2.3 \mu\text{s}$ to decide whether the event is passed on to the second level (L2) or already rejected at L1. The decision is based on several signals from the subdetectors, which are combined into 256 trigger elements reducing the event rate to roughly 1 kHz. Trigger elements are mostly formed by thresholds which have to be exceeded to set the corresponding subtrigger. The trigger elements are combined to 128 subtriggers. During the Level 1 latency all readout signals are stored in pipelines while the H1 detector remains active throughout the complete latency time and capable of triggering. This guarantees a dead-time free first trigger level. The OR of all subtriggers is taken as trigger decision.

In order to limit their rate, most subtriggers are to some extent prescaled. The prescale factor is an internal counter set to n , rejecting the first $n - 1$ events with a positive trigger decision from the respective subtrigger, keeping the n^{th} event, rejecting the following $n - 1$ events again and so on. This counter is set for each subtrigger individually.

- After a positive L1 trigger decision (L1 Keep), the second level (L2) is started. The L2 provides another 96 trigger elements which are combined with the full information from L1 to make a trigger decision within $20 \mu\text{s}$ of the preceding L1 Keep signal. In case of a positive decision the data taking halts and the readout of the entire subdetector information is initiated. The event rate is further reduced to 100 - 200 Hz. If the third trigger level is not active, the event rate is even reduced to 50 Hz.
- The third level (L3) was not implemented in the 2005 data taking period. Its purpose is to make another validation after $\sim 100 \mu\text{s}$. This reduces the event rate further to about 50 Hz.
- The fourth level (L45) is purely software based and has access to all subdetector information. This level is not integrated in the detector, but rather hosted by a processor farm performing the full event reconstruction within 100 ms. Its algorithms (finders) are tuned to select well

known physical processes as well as reject background events, mainly from beam-gas or beam-wall interactions. The event rate after L45 is of the order of 5 Hz, corresponding to 1 event for every 2 million bunch crossings.

The L45 raw data is processed by *HIREC*, the reconstruction software used at H1. The final events are classified as candidates for selected physics processes and written to *Production Output Tapes* (POT). A shorter version is written to *Data Summary Tapes* (DST). Since the upgrade project, the full DST information is additionally converted to the *Object Data Storage* (ODS) which is based on object oriented C++.

For the present analysis a dedicated subtrigger was implemented, called s14 (subtrigger 14). The decay of the ρ^0 yields only two low p_T tracks and very little activity in the calorimeters, which lead to a subtrigger definition that is based on information from the tracking system:

```
s14  FTT_mul_Tb>1 && FTT_mul-Ta<4 && FTT_chg_1 && (!LAr_IF) &&
      CIP_sig>2 && CIP_mul<6      v:5 t:0 d:1
```

The subtrigger elements are explained in detail in Sect. 6.1. The average prescale factor for this subtrigger is 24.81 for the considered run range.

4.2.6 Luminosity System

The determination of the *Integrated Luminosity* ($\int \mathcal{L} dt$) is necessary for the calculation of cross sections. For this purpose the Bethe-Heitler-Process $ep \rightarrow ep\gamma$ is used, a precisely calculable QED process. The detection of the scattered electron and the photon takes place in two calorimeters, the *Electron Tagger* (ET6) and the *Photon Detector* (PD) located at 5.4 m and 101.8 m, respectively up the proton beam (negative z-axis).

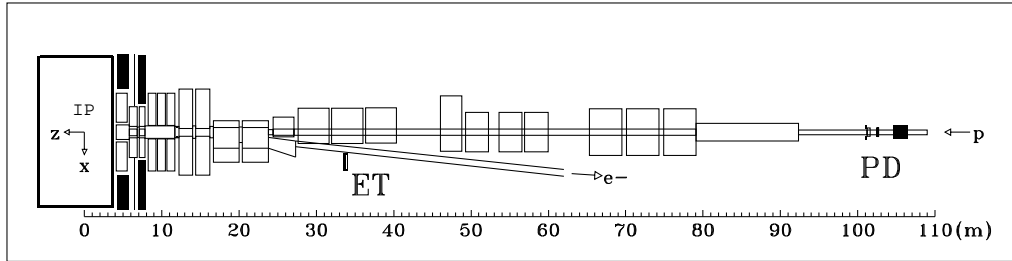


Figure 4.8: The Luminosity system of H1. The H1 detector is on the left. The scale is along the negative z-axis starting at the nominal interaction point ($z = 0$).

The fully corrected integrated luminosity for the presented data sample adds up to

$$\mathcal{L}_{\text{tot}} = \int \mathcal{L}_{\text{run}} dt = 570 \text{ nb}^{-1} \quad (4.7)$$

Chapter 5

The Fast Track Trigger

With the upgrade of the HERA machine, the interaction rate as well as the background rate were significantly increased. To take advantage of the higher interaction rates, it is necessary to provide triggers with a high selectivity to reliably separate the interesting physics from the background. Therefore the H1 trigger system was upgraded to increase the event yield for physics processes while keeping the overall event rate as before and preventing the need to replace the data acquisition. The main components of the trigger upgrade project are the CIP2000 proportional chamber trigger [61, 65–67], the jet trigger based on the LAr Calorimeter and the Fast Track Trigger FTT [68, 69] that uses information from the CJC.

5.1 General Introduction

A big advantage of the FTT over its predecessor, the so called DCR Φ trigger, is its ability to precisely count single tracks with transverse momenta as low as 100 MeV. With this capability, the FTT is particularly suitable for low Q^2 events such as light vector meson photoproduction which are mainly triggered by track based information.

The FTT uses information from 12 out of 56 CJC sense wires in a wire plane. These are combined in four trigger layers of 3 sense wires each. Three trigger layers are located in CJC1 while the fourth is located in CJC2 (Fig. 5.1). The analog signals from both ends of the sense wires are sent to the FTT Front End Modules (FEM), where the digitization and hit finding is performed similarly to the Qt algorithm of the CJC (Sect. 4.2.1).

During the hit finding an internal FTT analog threshold discriminates between electronic noise and real hits. Of course one wants to set the analog threshold as low as possible to detect also small pulse-integrals without being sensitive to electronic noise on the input channel.

The result of the hit finding for each wire is filled into shift registers synchronized at 20 MHz. If all three wires in a trigger layer have a hit and the hit pattern in the shift register is compatible with a track hypothesis originating from the beam line, the hit pattern is associated with a track segment characterized by the track parameters ($\kappa \propto 1/p_T, \varphi$) of the respective track hypothesis (Fig. 5.2).

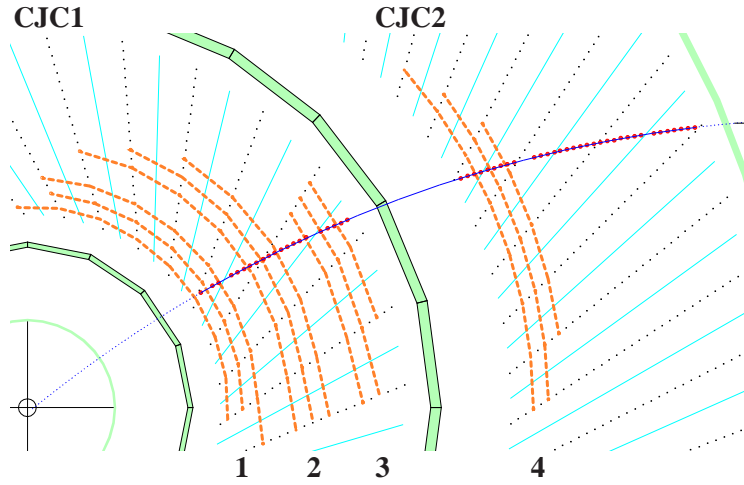


Figure 5.1: A cut through the Central Jet Chambers perpendicular to the beam line (located in the lower left corner), showing the twelve wire layers combining to the four trigger layers used for the FTT.

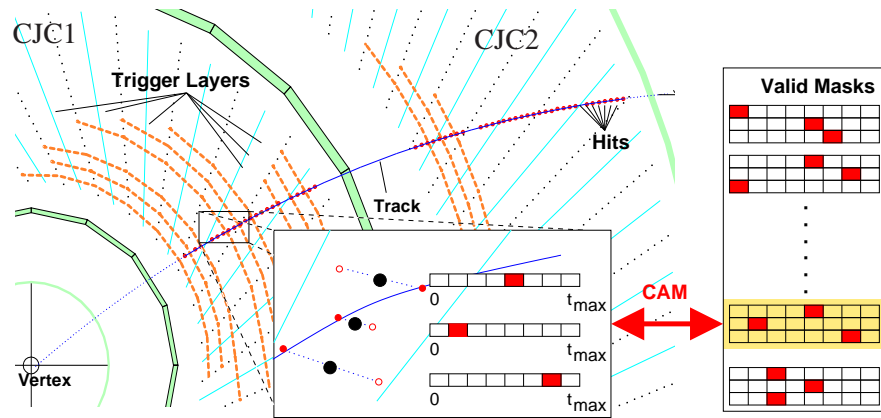


Figure 5.2: The hits from sense wires within a trigger layer are filled to shift registers and compared to pre-calculated hit patterns of track hypotheses originating from the beam line (valid masks) using CAMs (see text).

The track parameters of the identified track segments are entered in $\kappa - \varphi$ histograms. These histograms are passed via merger cards to the L1 linker card where the four histograms from the group layers are overlaid and the track segments are combined to track candidates. In order to form a track candidate, at least two out of the four layers have to have an entry within a sliding window of 3×1 as illustrated in Fig. 5.3. Based on these track candidates, the FTT forms trigger elements and transfers them to the central trigger.

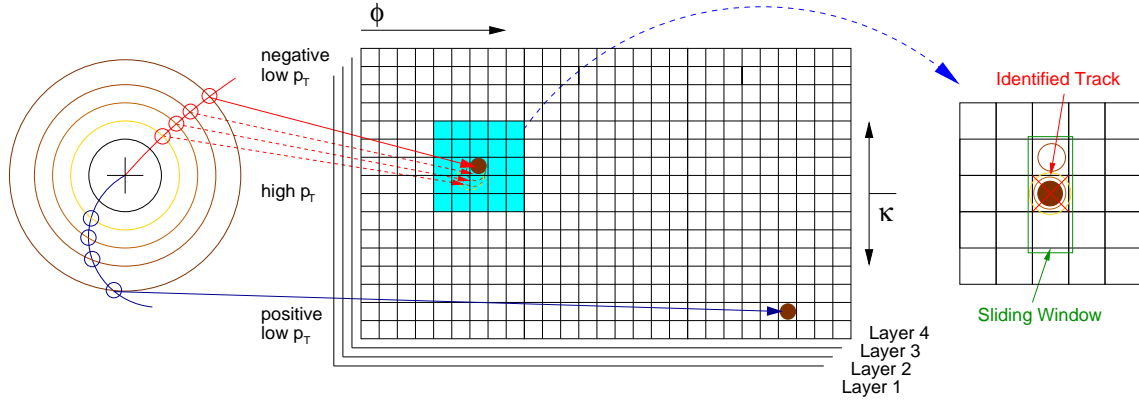


Figure 5.3: The track parameters of the identified track segments (left) are entered into the $\kappa - \varphi$ histogram of the corresponding trigger layer (middle), overlaid and using a sliding window of size 3×1 combined to track candidates (right).

The FTT uses modern technologies based on high speed, highly integrated circuits implemented on printed circuit boards (PCB) such as the FEM or the merger cards. Further key technologies are the field programmable gate arrays (FPGA) providing the high throughput and flexibility of the FTT and the content addressable memories (CAM) used for the fast pattern matching. A detailed description of the FTT and its components can be found in [70].

5.1.1 Level 1

On the first trigger level (L1), the FTT reconstructs and classifies the track candidates in 16×30 bins in $\kappa - \varphi$. The κ segmentation of 16 bins corresponds to 8 different thresholds in p_T , given in Table 5.1, separately for positive and negative charges. The charge of a track can easily be found from the sign of κ (Sect. 4.2.1).

Trigger Elements

The FTT computes internally on the first trigger level up to 32 trigger bits. A total of 16 bits can be transferred to the central trigger. Besides the timing information t_0 also five p_T thresholds are chosen, where the track multiplicity exceeding one of the five thresholds is counted. A so-called segment bit, the summed charge of the tracks and up to 8 topological information conclude the L1 subtrigger elements from the FTT:

Timing The t_0 measured by the FTT (not yet operational).

p_T threshold Counters for the five p_T thresholds 100 MeV, 160 MeV, 400 MeV, 900 MeV and 1800 MeV. For the first threshold (100 MeV) three bits are available, the other thresholds count with two bits. If more than 7 (3) tracks with a p_T above the first (2nd - 5th) threshold are reconstructed, the highest bit state 7 (3) is set, see also Table 5.1.

Segment bit This bit is set, if there is at least one track segment in the third or fourth trigger layer.

Internal p_T thresholds of the FTT on L1			
κ -Bins	p_T [MeV]	trigger element	n_{\max}
1/16	100	FTT mul Ta	7
2/15	125	—	3
3/14	160	FTT mul Tb	3
4/13	250	—	3
5/12	400	FTT mul Tc	3
6/11	600	—	3
7/10	900	FTT mul Td	3
8/9	1800	FTT mul Te	3

Table 5.1: Internal thresholds of the FTT on L1. As trigger elements only the track multiplicities exceeding the five thresholds 100 MeV, 160 MeV, 400 MeV, 900 MeV and 1800 MeV are used. The quantity n_{\max} denotes the highest bit state of the corresponding trigger element. So up to 6 single tracks with p_T above 100 MeV can be counted while '7' corresponds to ≥ 7 tracks.

Total charge The sign of κ also defines the charge for a track. The sum of the charges for all tracks is encoded in three bits and covers a range between $[-3, 3]$.

Topological information On L1, the FTT divides the event in 10 sectors in the transverse plane. A topology is a specific arrangement of these sectors with activity in the FTT, such as back-to-back where two tracks emerge with nearly 180° opening angle in φ and hence only the two sectors diametrically opposed show an activity. The coherent description of different circular topologies is done with the topology description function [71].

5.1.2 Level 2

On the second trigger level, the available decision time is $20 \mu\text{s}$ allowing for a much finer binning of 40×640 bins in $\kappa - \varphi$. Additionally up to 48 tracks can be fitted resulting in a track parameter resolution which is comparable to the offline resolution¹. For a two track combination the invariant mass is calculated.

5.1.3 Level 3

For the third level $100 \mu\text{s}$ are available. Within this time the FTT combines information from several other subdetectors such as i.e. the LAr, with the high resolution tracks of the second trigger level to perform a partial event reconstruction on a farm of commercial Power PCs.

¹The offline resolution is given by the much more refined algorithms used during the offline reconstruction on L45.

5.2 FTT Tracks compared to Offline Reconstructed Tracks

To determine the trigger efficiencies it is essential to match the tracks seen by the FTT with the tracks found by the offline reconstruction. The offline reconstructed tracks (offline tracks) are required to be selected by the standard H1 track selection and further on referred to as selected tracks.

The FTT tracks from L1 are assigned κ and φ values according to the L1 binning. To be comparable with the FTT tracks, all selected tracks are filled into $\kappa - \varphi$ histograms with identical binning. From there it is possible to match the FTT tracks to the selected tracks using a window technique similar to the L1 linker and hence determine the single track efficiency of the FTT which reflects the probability for a selected track with given track parameters to be reconstructed by the FTT.

The main steps of the matching between FTT tracks and selected tracks are the following:

- Assign link candidates
- Determine best possible solution
- Recursive algorithm to find best possible assignment

In the following, the individual steps are explained in more detail:

Assign link candidates

In a first step, all FTT tracks within a 7×7 bin window from the selected track in the $\kappa - \varphi$ histogram are assigned to the selected track as possible link candidates. If more than one possible link candidate is present, the candidates are ordered with increasing distance $d = \Delta\kappa_{\text{bin}} + \Delta\varphi_{\text{bin}}$ from the selected track. The distance d also determines the link quality of each candidate. The relation between the distance and the link quality is summarized in Table 5.2.

Link quality relation for FTT tracks							
Distance d	0	1	2	3	4	5	6
Link quality	100	80	50	20	10	8	5

Table 5.2: Relation between the link quality and the distance $d = \Delta\kappa_{\text{bin}} + \Delta\varphi_{\text{bin}}$ of a FTT link candidate to the selected track in the $\kappa - \varphi$ histogram.

Determine best possible solution

After the first step, a list of possible FTT link candidates belongs to each selected track where the link candidate with the highest link quality is first in the list and decreasing link quality for the following link candidates.

Therefore summing all link qualities of the first link candidate for each selected track yields an

upper bound Λ on the total link quality of the event. This upper bound Λ on the link quality defines the best possible assignment of FTT tracks to selected tracks and corresponds to the maximum number of assigned link candidates, while for each selected track the closest possible link candidate is considered.

If no FTT track is assigned to more than one selected track, the best possible assignment is simply given by the first link candidate for each selected track. But if one or more FTT tracks can be assigned to more than one selected track, a recursive algorithm is used to determine the maximum number of possible assignments.

Recursive algorithm

The algorithm loops over all selected tracks and associates the link candidate with the highest link quality in the list that *hasn't been assigned to a previous selected track*. The resulting assignment is evaluated by summing the link quality of all associated link candidates and stored.

The next assignment is achieved by associating the second best link candidate to the first selected track with multiple link candidates and the best link candidate that hasn't been assigned to a previous selected track for all other selected tracks. Again the resulting assignment is evaluated and compared to the first result. If the new sum of link quality is larger than the stored result, the new assignment is stored, otherwise it is ignored.

The algorithm continues to associate the link candidates to the selected tracks until either all possible combinations have been evaluated and the one with the largest sum of link qualities remains or the sum of link quality equals the upper bound Λ corresponding to the best possible assignment.

The efficiency determination is visualized in Fig. 5.4 using an artificial event for demonstration. Of course the single track efficiency depends on the size of the window. However for this analysis only events with two or three FTT tracks and two offline tracks are considered. Thus a typical event is displayed in Fig. 5.5 showing that the size of the window is not really of importance.

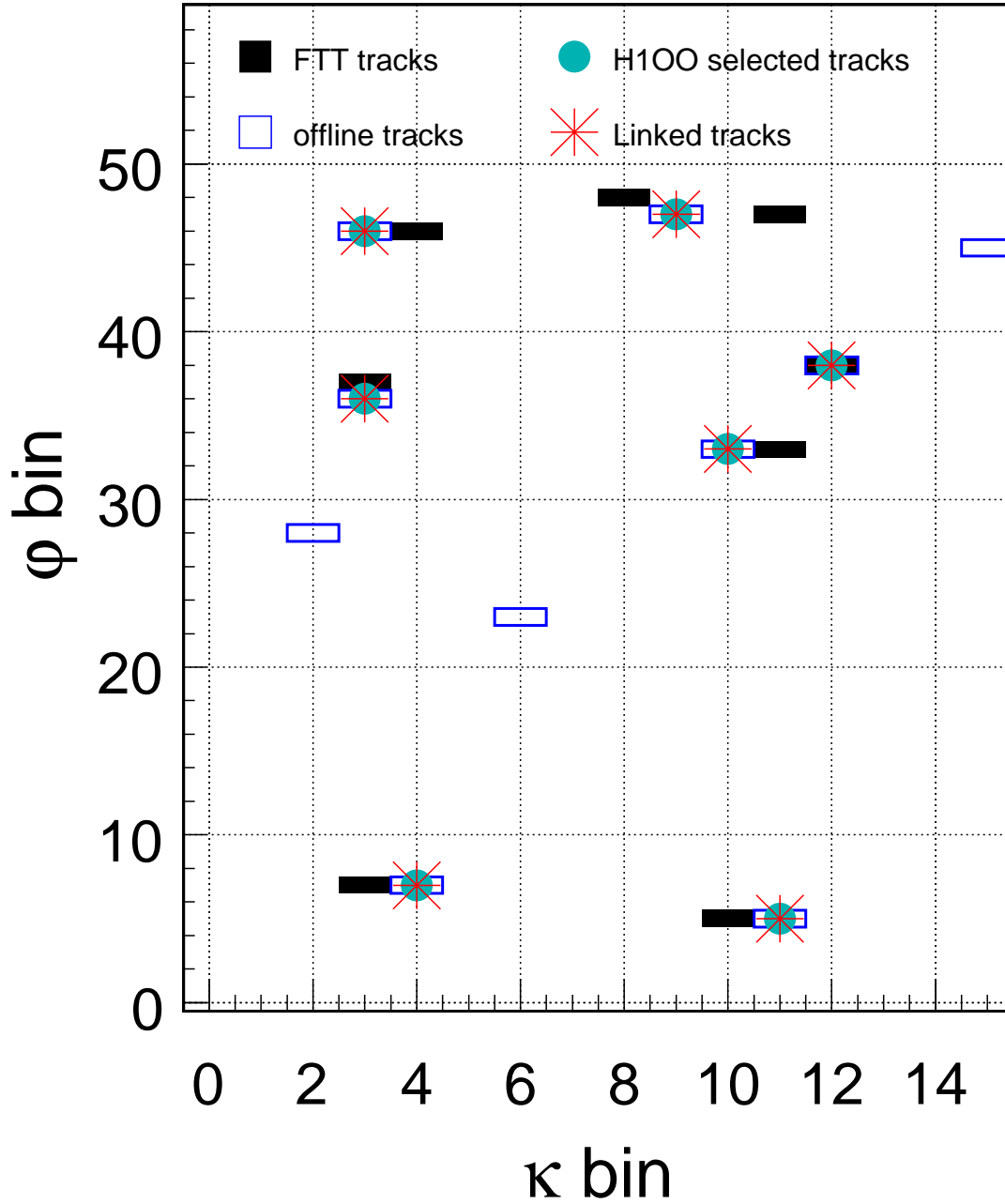


Figure 5.4: The offline matching for the determination of the FTT efficiency. All offline tracks (open squares) as well as the selected tracks (solid circles) are filled to the $\kappa - \phi$ -histogram containing the FTT tracks (solid squares). With a recursive procedure each selected tracks gets an assignment to a FTT track. The selected tracks with a positive assignment are marked with a star (*).

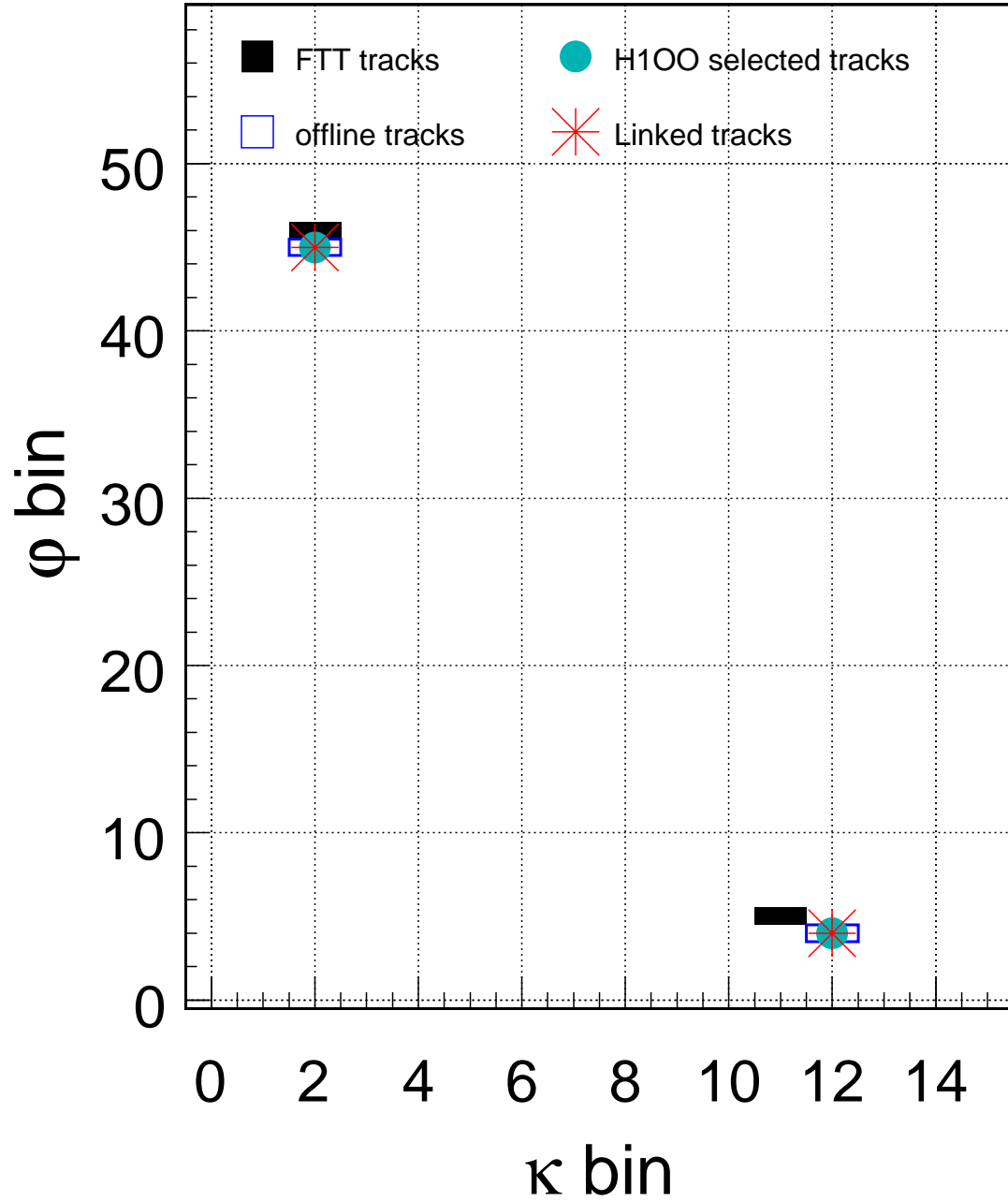


Figure 5.5: The typical ρ^0 event has exactly two selected tracks (solid circles). It is obvious that such a topology is not sensitive to the size of the window used to find possible FTT tracks (solid squares) as link candidates (*).

Chapter 6

Data Selection

The FTT trigger elements became available early 2005. During the 2005 data taking period, there was one change of the FTT analog threshold and two changes in the CJC high voltage parameters. To minimize systematic effects, the data analyzed in this thesis was restricted to a three-month running period from July to September 2005 with a stable set of parameters.

6.1 The ρ^0 Photoproduction Trigger

The Trigger System of the H1 detector consists of 4 levels (Sect. 4.2.5). Based on the FTT, a dedicated ρ^0 photoproduction trigger was introduced (s14) with requirements on trigger level 1 and 4.

```
s14  FTT_mul_Tb > 1 && FTT_mul-Ta < 4 && FTT_chg_1 && !LAr_IF &&
      CIP_sig > 2 && CIP_mul < 6      v:5 t:0 d:1
```

The individual trigger elements of s14 on L1 are explained below.

- $\text{FTT_mul_Tb} > 1$: The FTT reconstructed at least 2 track candidates with a p_T greater than 160 MeV.
- $\text{FTT_mul_Ta} < 4$: Not more than 3 track candidates are reconstructed by the FTT with a p_T larger than 100 MeV.
- FTT_chg_1 : The total charge of all track candidates reconstructed by the FTT is between -1 and +1.
- !LAr_IF : All clusters from the IF section of the LAr with an energy deposition above 0.8 GeV are summed and the total energy deposition in the inner forward region is below 2 GeV.
- $\text{CIP_sig} > 2$: At least 4 times more valid masks of the CIP trigger in the central region than the backward region (see Sect. 4.2.1).

- $\text{CIP_mul} < 6$: The total number of valid masks matched by the CIP trigger is less than 30 (see Sect. 4.2.1).
- $v:5$: Standard vetoes against beam-gas background.
- $t:0$: Timing taken from the CIP.
- $d:1$: No hits in the FTI¹.

On L4 a dedicated algorithm for identifying ρ^0 mesons is applied. It uses the following selection criteria.

- $\text{I_KTNR_ZVER} > 0$: The event has a valid reconstructed vertex,
- $\text{R_KTNR_ZVER} > -50.$: The z-position of the reconstructed vertex is between -50 cm...
- $\text{R_KTNR_ZVER} < 50.$: ... and +50 cm.
- $\text{I_KTNR_VVM_NTRA} = 2$: exactly two reconstructed and vertex fitted tracks.
- $\text{R_KTNR_VVM_MRHO} < 4.0$: the invariant mass of the two tracks under a charged pion mass hypothesis is smaller than 4 GeV.
- $\text{R_KTNR_VVM_EMAX} < 0.6$: maximum energy deposition in LAr not associated to a track is smaller than 0.6 GeV.

6.2 Run Selection

Within the data taking period presented in this analysis, only runs with certain quality criteria were used. Those criteria were

- Run Range
The run range was given by the three-month running period where the parameter set (FTT analog threshold and CJC HV parameters) was stable and includes the runs 421402 - 427934. Explicitly excluded was the run range 421550-421878 which was affected by a faulty RF System of the HERA machine.
- Active detector components
All relevant subdetectors were required to be powered and active. These are: CJC, CIP, LAr, TOF, LUMI, FMD, FTS, SpaCal.
- FTT included in readout
The FTT has to be read out to assure that the FTT is fully operational and the obtained information is available to monitor its performance.

¹A plane of scintillators mounted around the beam pipe between the forward tracker and the LAr calorimeter.

- Vertex constraint
The z-position of the primary interaction (z-vertex) has to be within 35 cm of the nominal IP.
- CJC gain range
The CJC gain is expressed in FADC² counts/MIP³ and normalized to 400 FADC counts/MIP. The gain has to be within the intervals given in Table 6.1 as is explained in Sect. 6.2.1.

CJC Gain Range	
CJC 1	$0.872 < \text{Gain} < 0.950$
CJC 2	$0.948 < \text{Gain} < 0.980$

Table 6.1: The CJC gain restrictions for the run selection. A gain of 1.0 corresponds to 400 FADC counts/MIP (see text).

6.2.1 CJC Gain

A charged particle in a drift chamber ionizes the gas atoms and the primary e^- drift toward the sense wires. As the primary e^- approach the sense wires, the electric field strength increases with roughly $1/r$ and the e^- initiate an avalanche of secondary electrons (gas amplification) which are read out as current on the sense wires.

The avalanche leaves the ionized atoms as positive charge in the close environment of the sense wire. These ions drift rather slowly out of the gas amplification zone and virtually increase the diameter of the sense wire (screening). The result is a reduced gas amplification of the drift chamber and hence a lower gain.

During normal operation, the drift chamber is continuously exposed to a certain level of ionizing particles. Variations of this particle flux lead to a change in the gas amplification and thus in the CJC gain. Particles emerging from beam-gas interactions are a major source of such ionizing particles and their flux is proportional to the electron beam current which decreases significantly during a luminosity fill. The corresponding increase in the CJC gain is shown in Fig. 6.1 for a single luminosity fill.

This gain dependence affects all sense wires in the CJC and since the FTT uses only 12 sense wires per wire plane and asks for 3 out of 3 hits in a trigger layer, the screening effect has a direct influence on the FTT performance. With a lower CJC gain, the trigger efficiency for the FTT is markedly reduced. To ensure stable operation conditions, the CJC gain was restricted to the range given in Table 6.1. Both CJC rings are affected equally as can be seen in Fig. 6.2 while the effect on the FTT is mainly influenced by CJC1.

²Fast Analog-to-Digital Converter, an electronic device used to digitize the analog read out.

³Minimum ionizing particle.

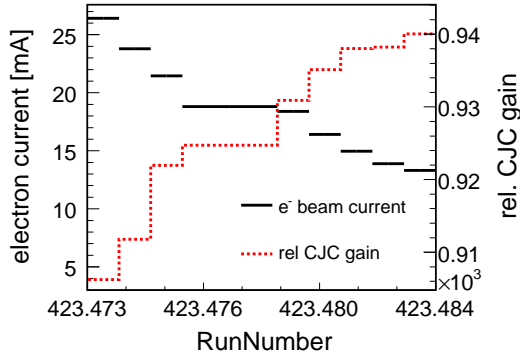
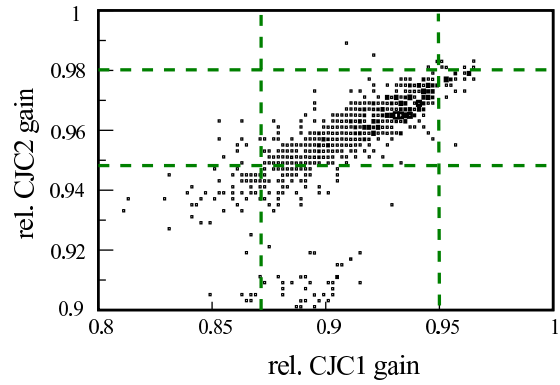


Figure 6.1: The relative CJC gain for a single luminosity fill versus the electron beam current. During the luminosity fill the electron beam current decreases from over 26 mA to roughly 13 mA while the CJC gain continuously increases from 0.906 to 0.944 FADC counts/MIP.

Figure 6.2: The relative CJC gain for both CJC rings are plotted against each other. The dashed lines indicate the cuts from Table 6.1 and enclose over 85 % of the events. The events at a CJC2 gain of less than 0.92 were affected by a gas leakage in the second CJC ring.



6.2.2 Event Yield

By plotting the number of selected events per luminosity, one can monitor the performance of the trigger over the run range. In Fig. 6.3, the number of selected events per nb^{-1} is given as function of the run range (yield plot).

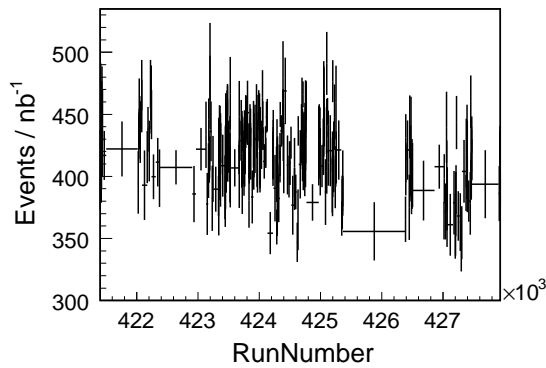


Figure 6.3: The full data range was split in bins of roughly 0.5 nb^{-1} . For these bins the ρ^0 candidates (see Sect. 6.4) are counted and corrected with the respective luminosity (yield plot). For a uniform trigger a flat ratio of events/luminosity is expected.

The variations in the CJC gain directly influence the FTT performance and hence the yield. The correlation between the CJC gain and the relative yield which was normalized w.r.t. the maximum yield, is given in Fig. 6.4(a). The lower plot shows the bin-wise projection w.r.t. to the yield and

was parameterized to a straight line of the form

$$y(x) = 1 + a \cdot (x - m) \quad (6.1)$$

with a being the slope of the dependence and m is fixed to the mean relative CJC gain ($m = 0.918$). The fitted slope is $a = 1.62 \pm 0.125$ and is used to compensate the yield for the gain dependence. The corrected yield is given in Fig. 6.5 and the bin-wise projection (lower plot) w.r.t. to the yield shows almost no gain dependence ($a = 0.27 \pm 0.126$).

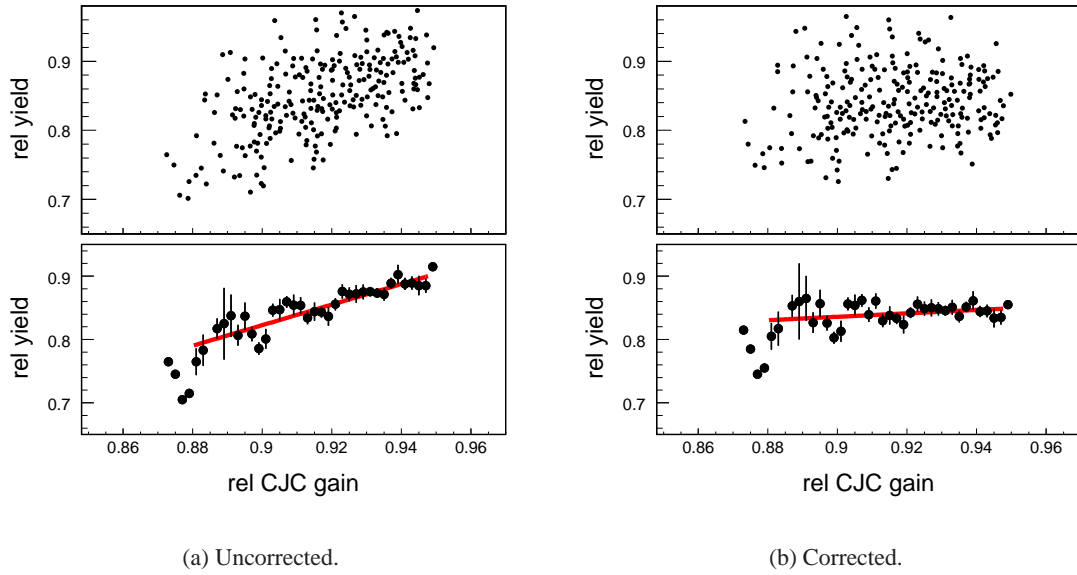


Figure 6.4: The upper plots show the relative yield as function of the CJC gain, the lower plots are the bin-wise projections w.r.t. the yield. In (a) the gain dependence of the yield is obvious and was parameterized by a straight line. Correcting the yield with the parameterization reduces the gain dependence significantly (b).

The yield plot for the corrected yield (Fig. 6.5) is less spiky but still not flat. The very fine binning of 0.5 nb^{-1} introduces sizeable statistical fluctuations. The pull plot in Fig. 6.6 indicates that the remaining variations in the yield plot are dominated by the statistical fluctuations and the performance of the FTT can be taken as uniform for the running period under study.

6.2.3 Final Run Selection

With these selection criteria, a total of 660 runs with 989'741 events are enclosed in the data sample used for this analysis. The corresponding HV and subtrigger corrected luminosity is 570 nb^{-1} .

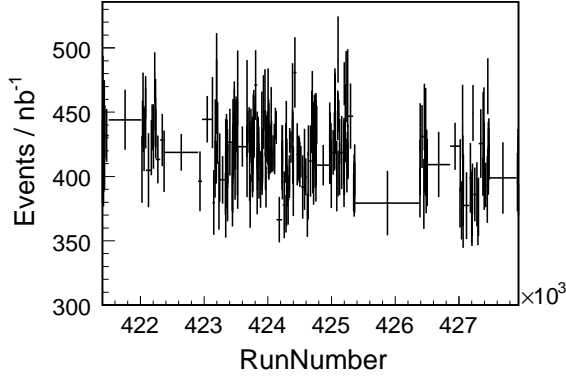
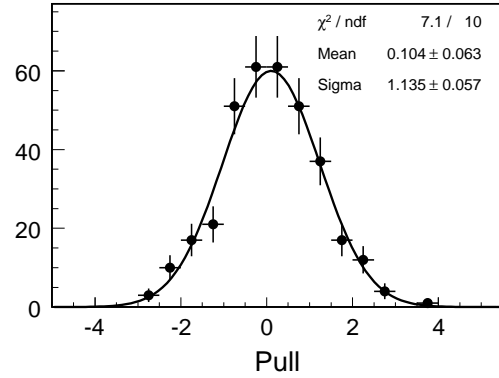


Figure 6.5: The yield plot from Fig. 6.3 corrected for the CJC gain dependence according to Eq. (6.1).

Figure 6.6: The difference of each bin to the mean yield is plotted and fitted with a gaussian. The width of $\sigma \sim 1$ indicates, that the remaining fluctuations in the corrected yield plot (Fig. 6.5) are statistical variations due to the fine binning.



6.3 Reconstruction of Kinematic Quantities

The kinematic variables describing the ρ^0 photoproduction are introduced in Sect. 2.1. For the events studied in this analysis, only the two decay pions were measured and therefore only the pion track parameters are available to reconstruct the kinematic quantities.

Four momentum transfer at the electron vertex Q^2

During the reconstruction of the event dedicated electron finders identify electron candidates in the LAr and the SpaCal calorimeters. The scattered electron is determined from these electron candidates by requiring

- The energy of the scattered electron candidate has to be greater than 8 GeV.
- The fraction of the energy of clusters within an $\eta - \phi$ distance of 0.5 of the scattered electron candidate and the scattered electron candidate's energy has to be less than 1.03, the so called isolation criteria.

If more than one scattered electron candidate is found, only the one with the highest transverse momentum is flagged as scattered electron.

The value of Q^2 can then be reconstructed using the relation

$$Q^2 = 2EE' (1 + \cos \theta) \quad (6.2)$$

with E being the initial electron energy (27.6 GeV) and E' the energy of the scattered electron. The backward calorimeter SpaCal can detect the scattered electron with scattering angles larger than approx. 4.5° ($\theta < 175.5^\circ$). The selection cuts from Sect. 6.4 explicitly reject events containing the scattered electron and limit Q^2 to values below $Q^2 \approx 4 \text{ GeV}^2$. The lower limit is given by [72]:

$$Q_{\min}^2 = \frac{m_e^2 y^2}{(1 - y)} \approx 10^{-12} \text{ GeV}^2 \quad (6.3)$$

The average Q_{gen}^2 value of all events passing the selection cuts (Sect. 6.4) was determined from Monte Carlo studies and amounts to 0.01 GeV^2 . In Fig. 6.7 the average Q_{gen}^2 value as function of t_{rec} is plotted.

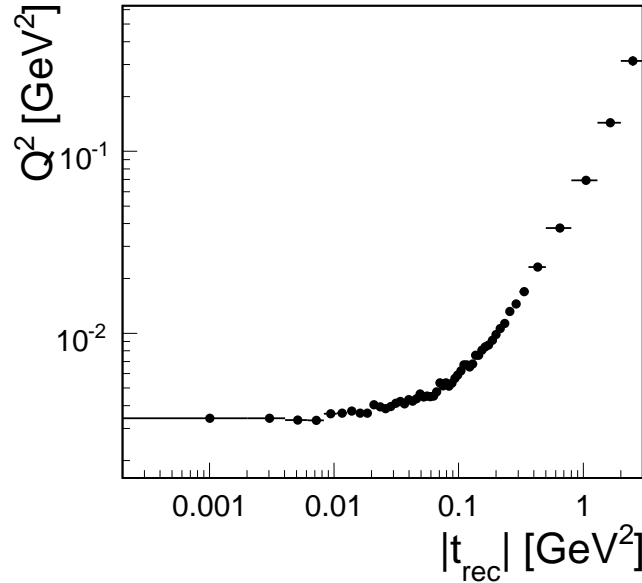


Figure 6.7: The average Q_{gen}^2 value for each reconstructed W/t -bin. It rises from 0.0034 GeV^2 for low $|t|$ to 0.33 GeV^2 for the high $|t|$ values.

The remaining kinematic variables $m_{\pi\pi}$, $W_{\gamma p}$ and t can be calculated from the four-momentum of the ρ^0 . From the measured pion track momentum one can extract the four-momentum of the decay pions using the charged pion mass hypothesis and from that easily reconstruct the four-momentum of the ρ^0 ($p_\rho = (E_\rho, \vec{p}_\rho)$) by addition.

Di-pion mass $m_{\pi\pi}$

The invariant mass $m_{\pi\pi}$ of the two pions is obtained from p_ρ by

$$m_{\pi\pi} = \sqrt{E_\rho^2 - |\vec{p}_\rho|^2} \quad (6.4)$$

In Fig. 6.8 the reconstructed values for $m_{\pi\pi}$ are compared to the generated values for the MC events. On the right side the difference $m_{\pi\pi}^{\text{rec}} - m_{\pi\pi}^{\text{gen}}$ is plotted versus the generated $m_{\pi\pi}^{\text{gen}}$. Apart from single outliers, the quality of the reconstructed $m_{\pi\pi}$ value is good as can be seen from the right plot of Fig. 6.8.

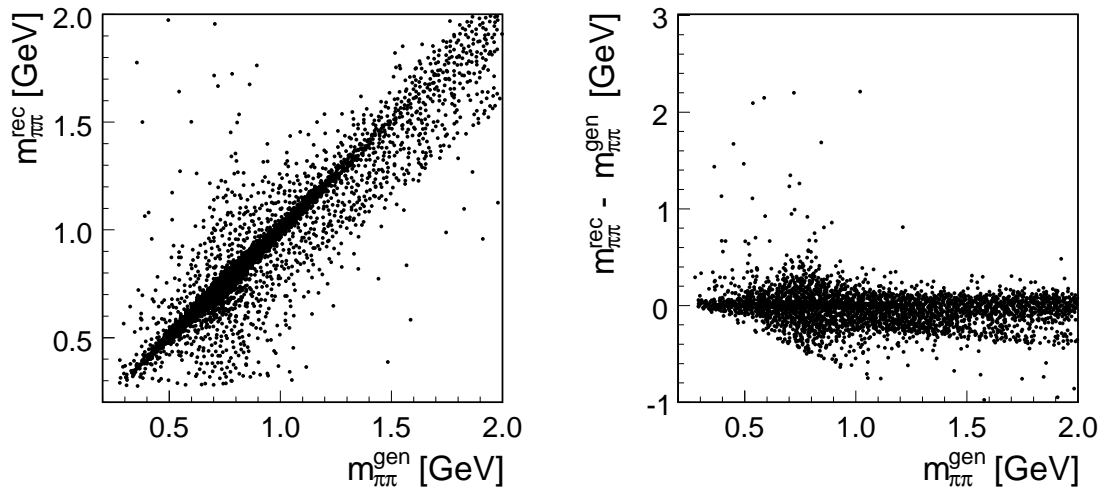


Figure 6.8: The left plot shows MC reconstructed versus generated $m_{\pi\pi}$. On the right side is the difference $m_{\pi\pi}^{\text{rec}} - m_{\pi\pi}^{\text{gen}}$ shown versus $m_{\pi\pi}^{\text{gen}}$. The distributions are shown after all selection cuts were applied.

γp center of mass energy $W_{\gamma p}$

For $Q^2 = Q_{\text{min}}^2$ the transverse momentum of the virtual photon is zero and hence the longitudinal momentum can be expressed by $-E_\gamma$, considering Eq. 6.3 where Q_{min}^2 is ≈ 0 for the kinematic phase space considered in this analysis. Then energy and longitudinal momentum conservation can be written in the form

$$E_\gamma + E_p = E_\rho + E_{p'} \quad (6.5)$$

$$P_{z,\gamma} + P_{z,p} = P_{z,\rho} + P_{z,p'} \quad (6.6)$$

The incoming protons have only longitudinal momentum and therefore $E_p \approx P_{z,p}$, and since the proton is scattered at very low angles, the transverse momentum of the scattered proton is negligible and $E_{p'} \approx P_{z,p'}$. Thus subtracting Eq. 6.6 from Eq. 6.5 results in

$$E_\gamma - P_{z,\gamma} = 2E_\gamma \approx E_\rho - P_{z,\rho} \quad (6.7)$$

With Eq. 2.5 the photon-proton center-of-mass energy can be written as

$$W_{\gamma p}^2 \approx 4E_\gamma E_p \approx 2(E_\rho - P_{z,\rho})E_p \quad (6.8)$$

where the energy and the longitudinal momentum of the ρ^0 can be extracted from p_ρ . The reconstructed values for $W_{\gamma p}$ are compared to the generated values for the MC events and shown in Fig. 6.9 along with the quantity $(W_{\gamma p}^{\text{rec}} - W_{\gamma p}^{\text{gen}})/W_{\gamma p}^{\text{gen}}$ versus $W_{\gamma p}^{\text{gen}}$.

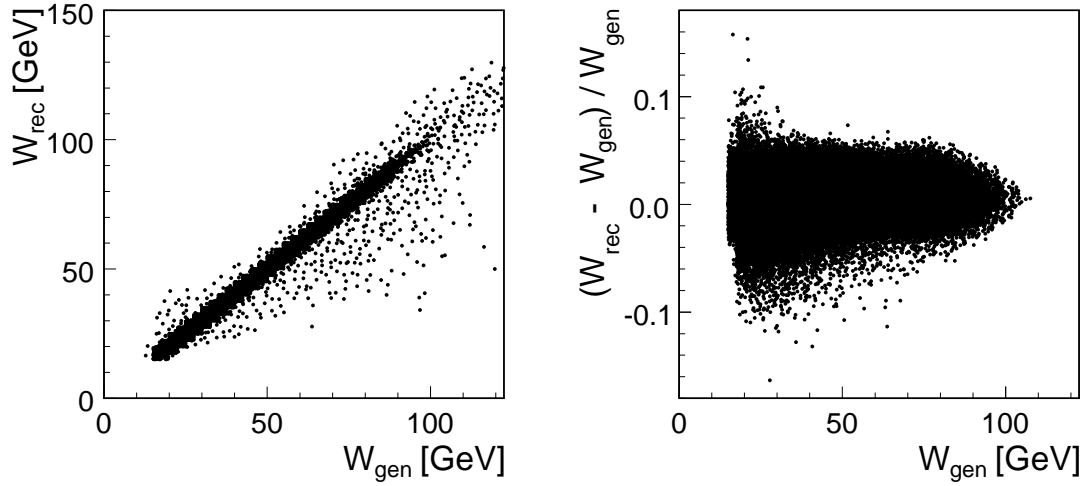


Figure 6.9: The left plot shows MC reconstructed versus generated $W_{\gamma p}$. On the right side is the quantity $(W_{\gamma p}^{\text{rec}} - W_{\gamma p}^{\text{gen}})/W_{\gamma p}^{\text{gen}}$ shown versus $W_{\gamma p}^{\text{gen}}$. The distributions are shown after all selection cuts were applied.

Within the $W_{\gamma p}$ range considered for this analysis ($20 < W_{\gamma p} [\text{GeV}] < 90$) the reconstructed values are well described. A comparison between the reconstructed MC values of $W_{\gamma p}$ and the data is given in Fig. 6.10. For the MC events, the elastic and proton-dissociative production is shown individually as well as as the total γp MC.

Four momentum transfer at the proton vertex t

The four-momentum transfer at the proton vertex t in the approximation $Q^2 \approx 0$ and $E_\gamma \approx -P_{z,\gamma}$ can be expressed as

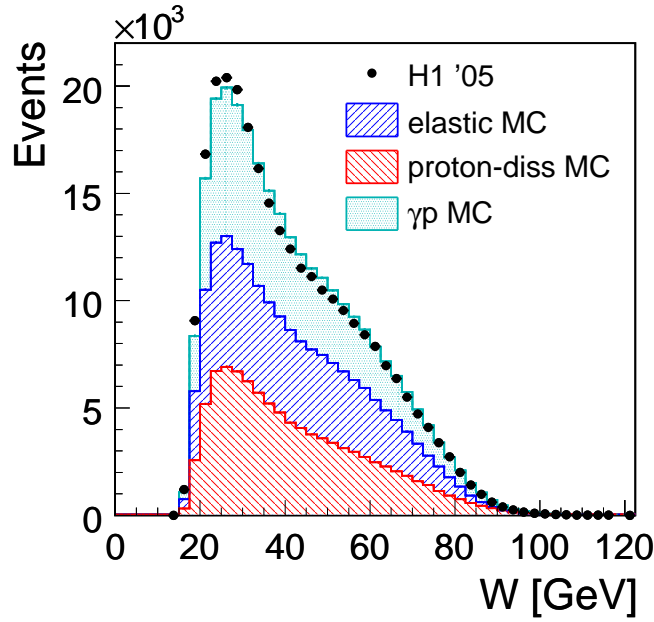


Figure 6.10: The kinematic variable $W_{\gamma p}$ calculated from reconstructed quantities as in Eq. 6.8 for data and Monte Carlo events. The total γp MC corresponds to the sum of elastic and proton-dissociative photoproduction of ρ^0 vector mesons.

$$\begin{aligned}
 t &= -Q^2 - 2qp_\rho + m_\rho^2 \\
 &\approx -2E_\gamma(E_\rho + P_{z,\rho}) + m_\rho^2 \\
 &\stackrel{(6.7)}{\approx} -(E_\rho - P_{z,\rho})(E_\rho + P_{z,\rho}) + m_\rho^2 \\
 &\approx -(E_\rho^2 - P_{z,\rho}^2) + m_\rho^2 \\
 &\approx -P_{T,\rho}^2
 \end{aligned} \tag{6.9}$$

In Fig. 6.11 the comparison between reconstructed and generated values for $|t|$ is shown in the same way as before for $m_{\pi\pi}$, while Fig. 6.12 shows the comparison between the reconstructed MC values and the data for $|t|$.

Of course the approximation $Q^2 \approx 0$ in Eq. (6.9) is not strictly true as can be seen from Fig. 6.7. Especially at higher t values the contribution from non-zero Q^2 values to the transverse momentum of the ρ^0 increases. This is reflected in a larger calculated t value than the actual four-momentum transfer at the proton vertex. However this contribution is small for the t range of this analysis ($t < 3 \text{ GeV}^2$) as is shown in Fig. 6.13, where the relative fraction of the events with a Q_{gen}^2 value larger than a certain threshold is plotted against the reconstructed $|t|$.

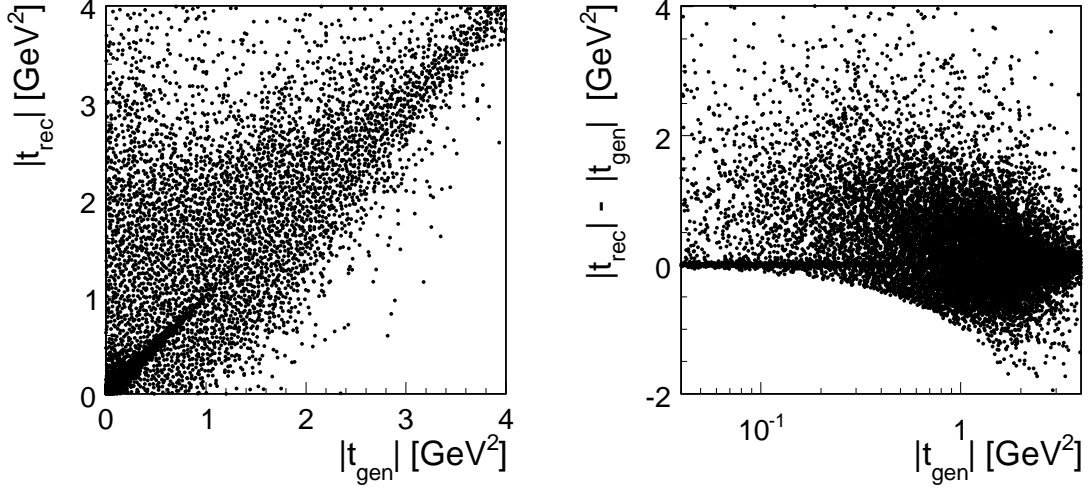


Figure 6.11: The left plot shows MC reconstructed versus generated $|t|$. On the right side is the difference $|t|^{\text{rec}} - |t|^{\text{gen}}$ shown versus $|t|^{\text{gen}}$. The distributions are shown after all selection cuts were applied.

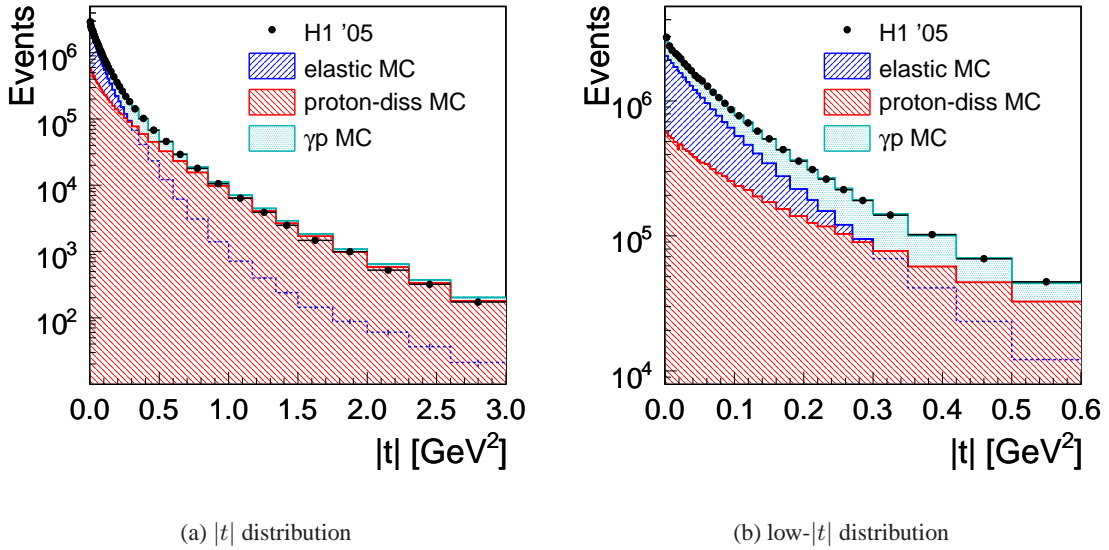


Figure 6.12: The kinematic variable t calculated from reconstructed quantities as in Eq. (6.9) for data and MC events. The total γp MC corresponds to the sum of elastic and proton-dissociative photoproduction of ρ^0 vector mesons.

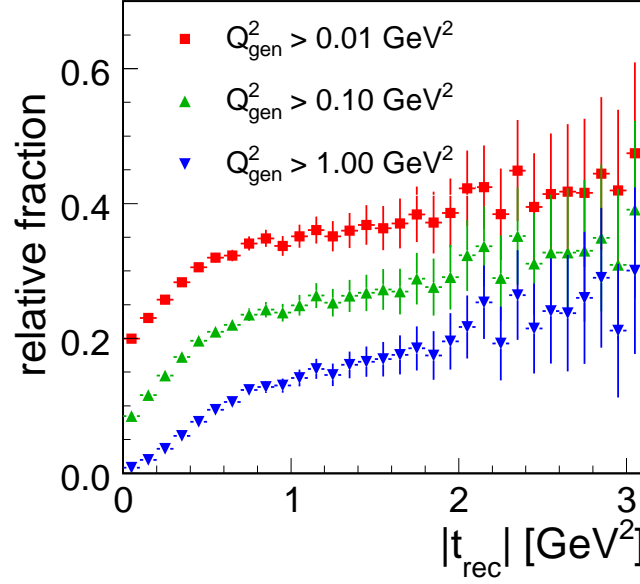


Figure 6.13: The relative fraction of events with non-zero Q_{gen}^2 values as determined from Monte Carlo studies plotted versus the reconstructed t value.

Fraction of the photon momentum carried by the pomeron $x_{\mathbb{P}}$

The last kinematic variable needed for the analysis is $x_{\mathbb{P}}$. It is defined as

$$x_{\mathbb{P}} = \frac{M_Y^2 + Q_{\text{gen}}^2}{W_{\gamma p}^2 + Q_{\text{gen}}^2} \quad (6.10)$$

and can be interpreted as fraction of the photon momentum carried by the pomeron. By requiring $x_{\mathbb{P}} < 0.01$ the mass of the dissociative system M_Y is restricted to values below ~ 20 GeV and thus ensures the diffractive nature of the interaction.

6.4 Event Selection

The diffractive production of ρ^0 mesons is mediated by a colorless exchange particle and yields therefore no further final state particle besides the vector meson's decay pions, the scattered electron and in case of dissociation the proton dissociative system (proton remnant) in forward direction. The charged decay pions from the ρ^0 meson are therefore the only final state particles in the central region of the H1 detector.

This clean signature mainly motivates the selection cuts listed below.

No scattered electron

In the photoproduction regime the electron emits a quasi real photon with very low momentum transfer Q^2 . Hence the electron escapes the detector through the beam pipe. Therefore the presence of a scattered electron after the reconstruction is explicitly excluded.

Z-Vertex

The z-vertex position is required to be within 25 cm of the nominal IP. Events with a z-vertex outside this signal region are treated as background.

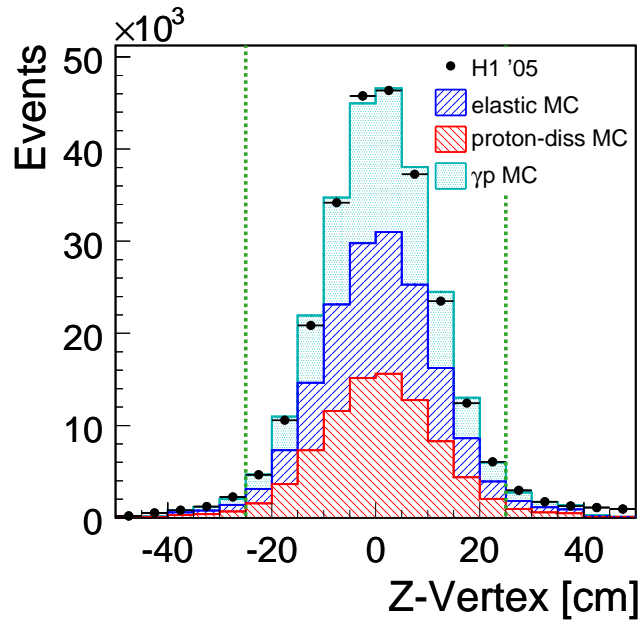


Figure 6.14: The distribution of the reconstructed z-vertex for the selected events. The dashed lines indicate the signal region within 25 cm around the nominal IP.

No unassociated energy cluster above 500 MeV

As the $\pi^+\pi^-$ from the ρ^0 are the only final state particles in the central part of the detector, the calorimeter only contains energy depositions (clusters) associated with the two decay pions. All events with at least one unassociated energy cluster above noise level (500 MeV) are thus rejected.

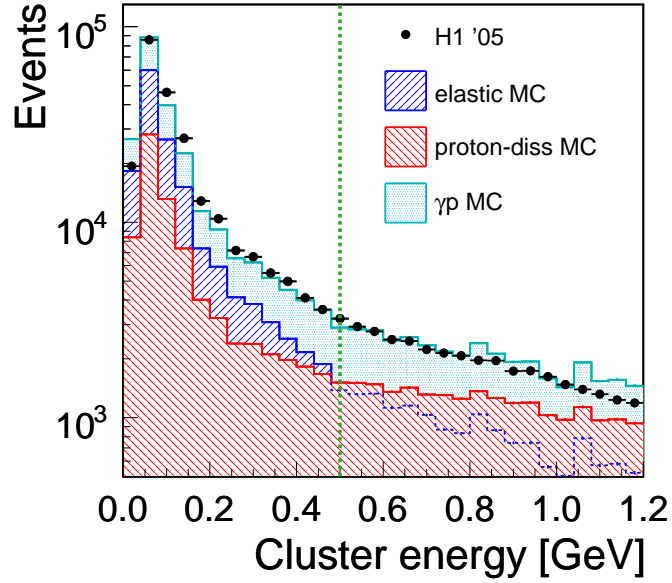


Figure 6.15: The maximum energy cluster in the LAr calorimeter, not associated to a track.

Tracking

During the reconstruction of the event a standard track selection is applied with the track selection criteria listed in Table 6.2. Only tracks passing these selection criteria are considered. The event should contain exactly two such tracks in the central region.

Track selection for central tracks	
Minimal p_T [MeV]	120
Range in θ	$20^\circ - 160^\circ$
Maximal R_{start} [cm]	50
Minimal R_{length} [cm]	10
	(5 if $\theta > 150^\circ$)

Table 6.2: The track selection criteria for reconstructed tracks in the central regions applied during the reconstruction.

Transverse momentum

The transverse momentum of each track has to be larger than 200 MeV while the trigger s14 requires at least two tracks with $p_T > 160$ MeV. This cut precludes possible threshold effects arising from the trigger condition. From the back-to-back decay of a ρ^0 (770 MeV) at rest into two π 's (140 MeV) a mean transverse momentum per π of $(770 - (2 \cdot 140))/2 = 250$ MeV is expected. But the bulk of the ρ^0 are produced with low transverse momentum and not at rest. The transverse momentum for the reconstructed π tracks is therefore slightly larger and is given in Fig. 6.16.

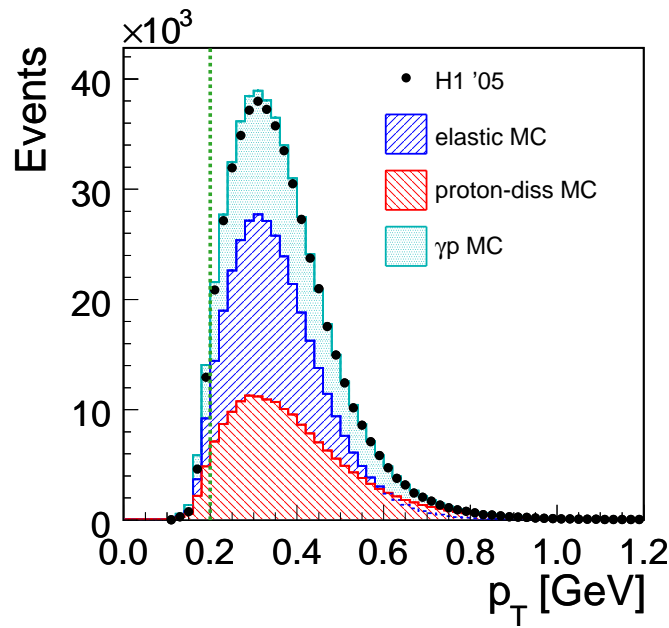


Figure 6.16: The transverse momentum of the reconstructed tracks. The mean transverse momentum is roughly 300 MeV due to the non-zero transverse momentum of the ρ^0 meson.

Central region

The polar angle θ of each pion track has to be in the central region defined as

$$20^\circ < \theta < 160^\circ \quad (6.11)$$

Invariant Mass

The invariant mass of the two tracks $m_{\pi\pi}$ under the charged pion mass hypothesis should be within

$$0.6 < m_{\pi\pi} [\text{GeV}] < 1.1 \quad (6.12)$$

with the nominal mass of the ρ^0 vector meson being 0.768 GeV [51].

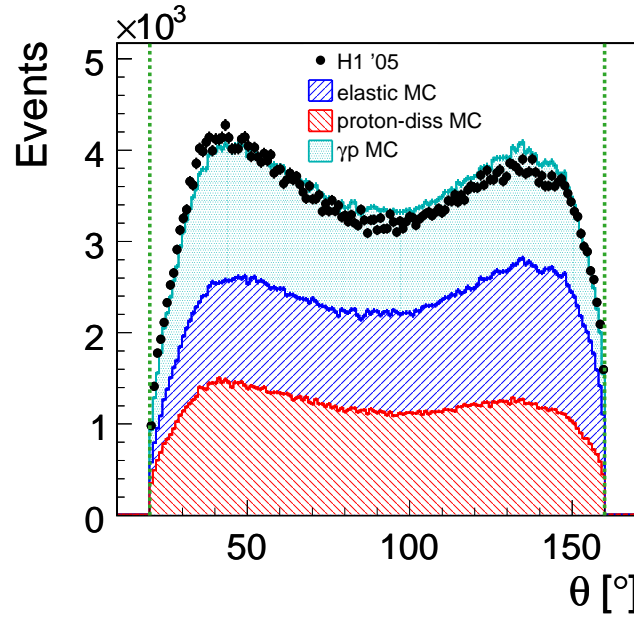


Figure 6.17: The polar angle θ of the reconstructed tracks.

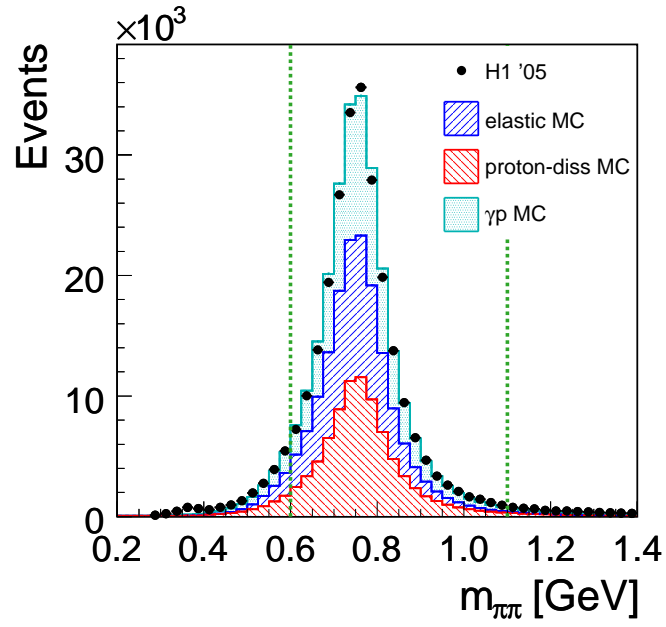


Figure 6.18: The dipion mass under the charged pion mass hypothesis.

Kinematic phase space

The relevant kinematic variables are the momentum transfer at the proton vertex t and the center of mass energy for the proton-photon system $W_{\gamma p}$, both defined in Sect. 2.1 and reconstructed as stated in Sect. 6.3. As the aim of the analysis is to measure the $W_{\gamma p}$ dependence of the ρ^0 photoproduction cross section and study the dependence as function of t , it is natural to split the data sample into 2-dimensional analysis bins $(W_{\gamma p}, t)$. For that purpose, the data sample is divided in 12 t bins between 0 and 3 GeV^2 . Each t bin is further subdivided in either 10 or 5 $W_{\gamma p}$ bins, depending on the t value. In total 80 bins in t and $W_{\gamma p}$ are defined and referred to as W/t -bins. The bin edges are listed in Table 6.3 and illustrated in Fig. 6.20 in the $W_{\gamma p}$ - t plane.

The determination of the W/t -bin edges was based on two criteria:

1. The acceptance dependence within the bins should be small. The acceptance is discussed in more detail in Sect. 7.2.
2. The number of events per bin should be roughly constant to ensure comparable statistical errors for the cross sections, Fig. 6.19. Up to $|t| \sim 0.5 \text{ GeV}^2$ the variation within a t bin as well as between the t bins are rather moderate. The significant drop of number of events per bin for larger $|t|$ values is due to the exponential fall off of the cross section and the bin width of the t bins.

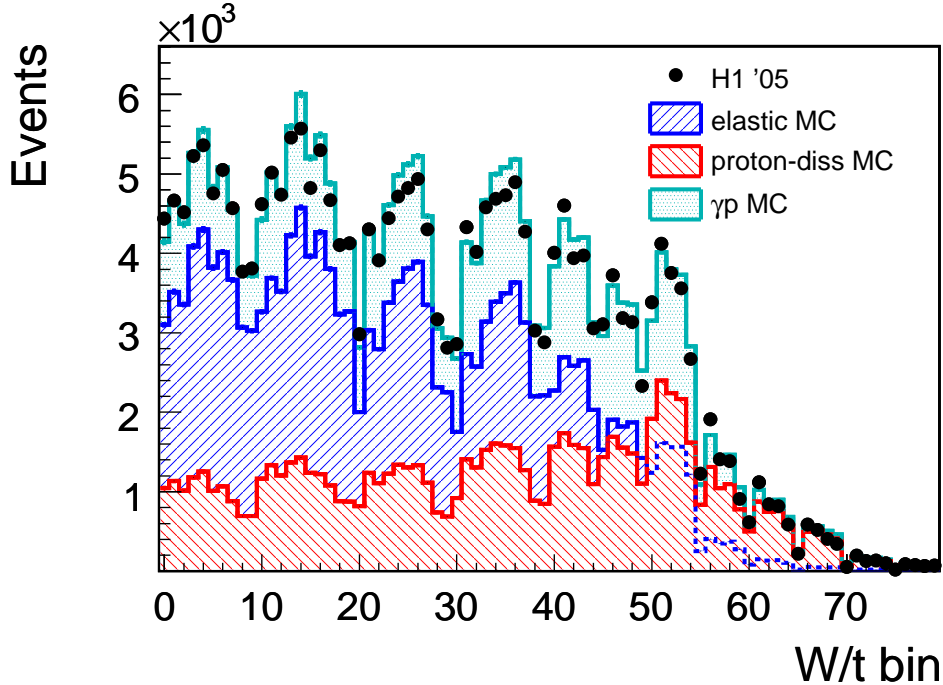


Figure 6.19: Raw event numbers of selected events per W/t -bin.

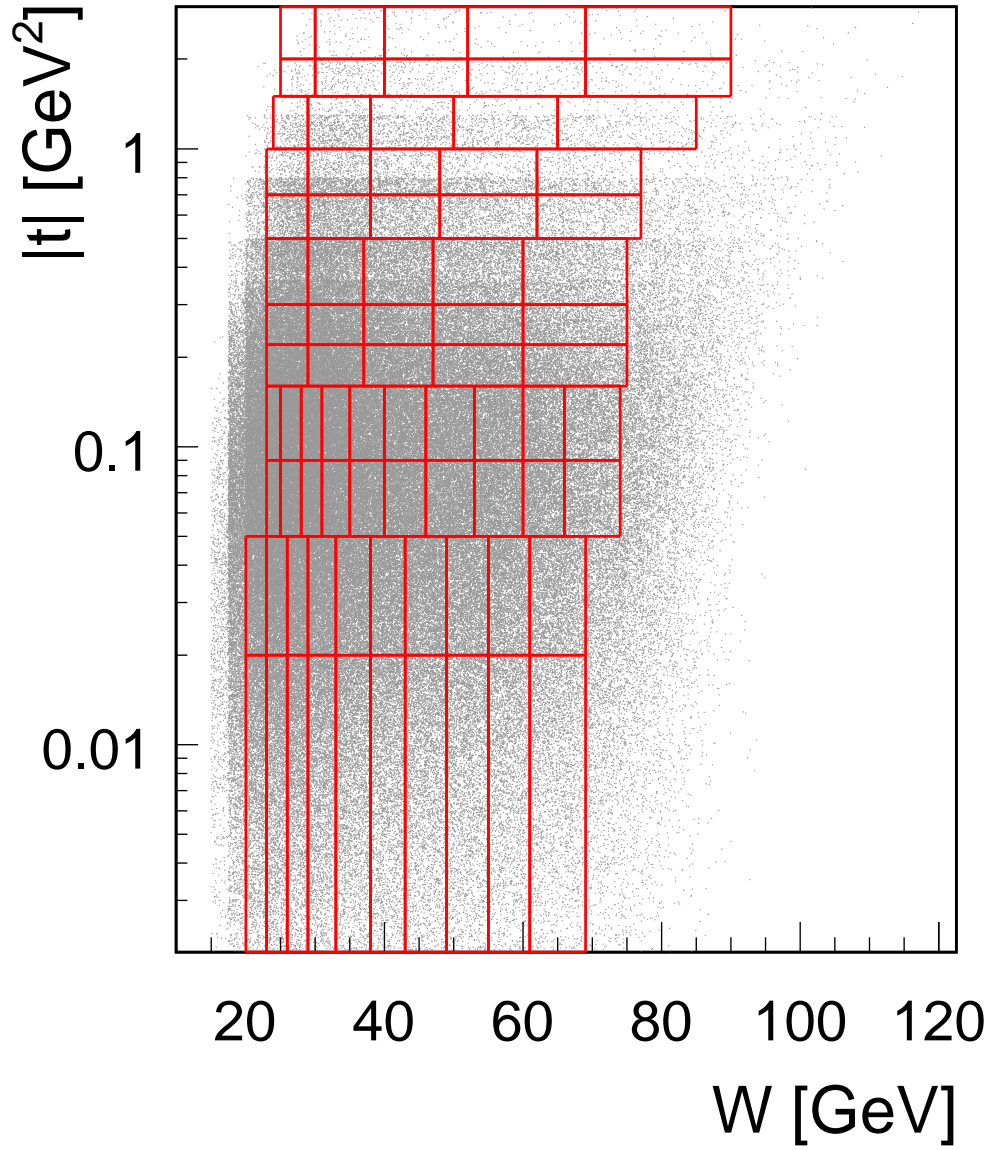


Figure 6.20: The 80 W/t -bins shown 2 dimensionally. The solid lines represent the grid of the bin edges defining the analysis bins.

Analysis Bin in $W_{\gamma p}$ - t Plane		
$ t $ range [GeV ²]	Number of W -Bins	$W_{\gamma p}$ binedges [GeV]
0.00 - 0.02	10	[20, 23, 26, 29, 33, 38, 43, 49, 55, 61, 69]
0.02 - 0.05	10	[20, 23, 26, 29, 33, 38, 43, 49, 55, 61, 69]
0.05 - 0.09	10	[23, 25, 28, 31, 35, 40, 46, 53, 60, 66, 74]
0.09 - 0.16	10	[23, 25, 28, 31, 35, 40, 46, 53, 60, 66, 74]
0.16 - 0.22	5	[23, 29, 37, 47, 60, 75]
0.22 - 0.30	5	[23, 29, 37, 47, 60, 75]
0.30 - 0.50	5	[23, 29, 37, 47, 60, 75]
0.50 - 0.70	5	[23, 29, 38, 48, 62, 77]
0.70 - 1.00	5	[23, 29, 38, 48, 62, 77]
1.00 - 1.50	5	[24, 29, 38, 50, 65, 85]
1.50 - 2.00	5	[25, 30, 40, 52, 69, 90]
2.00 - 3.00	5	[25, 30, 40, 52, 69, 90]

Table 6.3: The selected data events with the 80 analysis bins in $W_{\gamma p}$ - t plane. The four t bins below 0.16 GeV² are subdivided into ten $W_{\gamma p}$ bins, the other eight t bins encompass five $W_{\gamma p}$ bins.

6.5 Invariant Mass Distribution

The invariant mass distribution of the two tracks under a charged pion mass hypothesis is shown in Fig. 6.21. The dipion mass spectrum for the resonant ρ^0 decaying to $\pi^+\pi^-$ is well described by a relativistic Breit-Wigner function. However, due to the large width of the ρ^0 meson there is a sizeable interference between the resonant ρ^0 production and nonresonant dipion production.

This interference results in a distortion of the line shape with respect to a relativistic Breit-Wigner distribution and is referred to as *skewing*. The distortion of the ρ^0 line shape was already seen in fixed-target experiments and first discussed in 1965 [73]. Several parametrizations were proposed in the 60ies and 70ies to extract the resonant ρ^0 mesons from the invariant $\pi^+\pi^-$ mass spectrum.

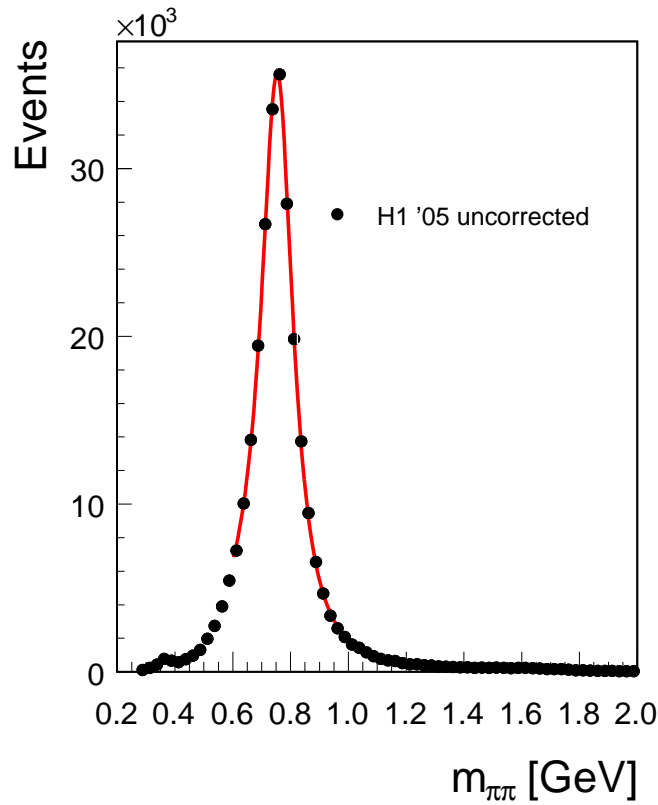


Figure 6.21: The invariant mass distribution of the two tracks under the charged pion mass hypothesis. The line shape is distorted with respect to a relativistic Breit-Wigner distribution which is referred to as *skewing*. The low mass side is enhanced whereas higher masses are suppressed.

For this analysis two different parametrizations were used and the results were compared. Both parametrizations are based on the relativistic Breit-Wigner distribution:

$$BW(m_{\pi\pi}) = \frac{m_\rho m_{\pi\pi} \Gamma_\rho}{(m_\rho^2 - m_{\pi\pi}^2)^2 + (m_\rho \Gamma_\rho)^2} \quad (6.13)$$

with m_ρ the nominal ρ^0 mass and Γ_ρ the momentum dependent width [74] defined as

$$\Gamma_\rho = \Gamma_{\rho,0} \left(\sqrt{\frac{m_{\pi\pi}^2 - 4m_\pi^2}{m_\rho^2 - 4m_\pi^2}} \right)^3 \left(\frac{m_\rho}{m_{\pi\pi}} \right) \quad (6.14)$$

where $\Gamma_{\rho,0}$ is the nominal ρ^0 width. The methods differ in the modelling of the lineshape distortion.

Ross-Stodolsky The ansatz by M. Ross and L. Stodolsky [54] introduces a dipion mass variation $(m_\rho/m_{\pi\pi})^n$ in the production process of the ρ^0 with n being the so-called skewing parameter. This skewing term is multiplied with the relativistic Breit-Wigner:

$$\frac{dN}{dm_{\pi\pi}} = N_{BW} \cdot BW(m_{\pi\pi}) \cdot \left(\frac{m_\rho}{m_{\pi\pi}} \right)^n + B \quad (6.15)$$

with the normalization factor for the Breit-Wigner contribution N_{BW} and the remaining background B . In Fig. 6.23 the dipion mass spectrum is fitted with the Ross-Stodolsky model from Eq. (6.15) and compared to the unskewed relativistic Breit-Wigner.

Söding P. Söding [73] describes the $\pi^+\pi^-$ photoproduction as sum of the resonant $\pi^+\pi^-$ production given by the Breit-Wigner and a non-resonant $\pi^+\pi^-$ background from 'Drell-like' processes [75]. The diagrams for the corresponding processes are given in Fig. 6.22.

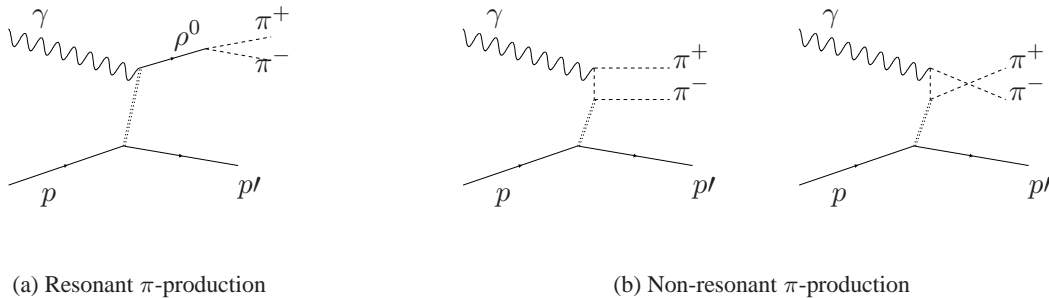


Figure 6.22: Diagrams representing the different $\pi^+\pi^-$ production processes, resonant (a) and non-resonant (b).

The full parametrization can be written in the form

$$\frac{dN}{dm_{\pi\pi}} = \frac{N_{BW} \cdot m_{\rho} m_{\pi\pi} \Gamma_{\rho} + I \cdot (m_{\rho}^2 - m_{\pi\pi}^2)}{(m_{\rho}^2 - m_{\pi\pi}^2)^2 + (m \Gamma_{\rho})^2} + B \quad (6.16)$$

with the normalization factors for the Breit-Wigner contribution N_{BW} , the interference part I and the remaining background B . Fig. 6.24 shows the mass spectrum fitted with the Söding model and its contributions.

The parametrization from Ross-Stodolsky is taken as default model, while the ansatz by P. Söding serves as control model. It will be shown that both models lead to compatible results.

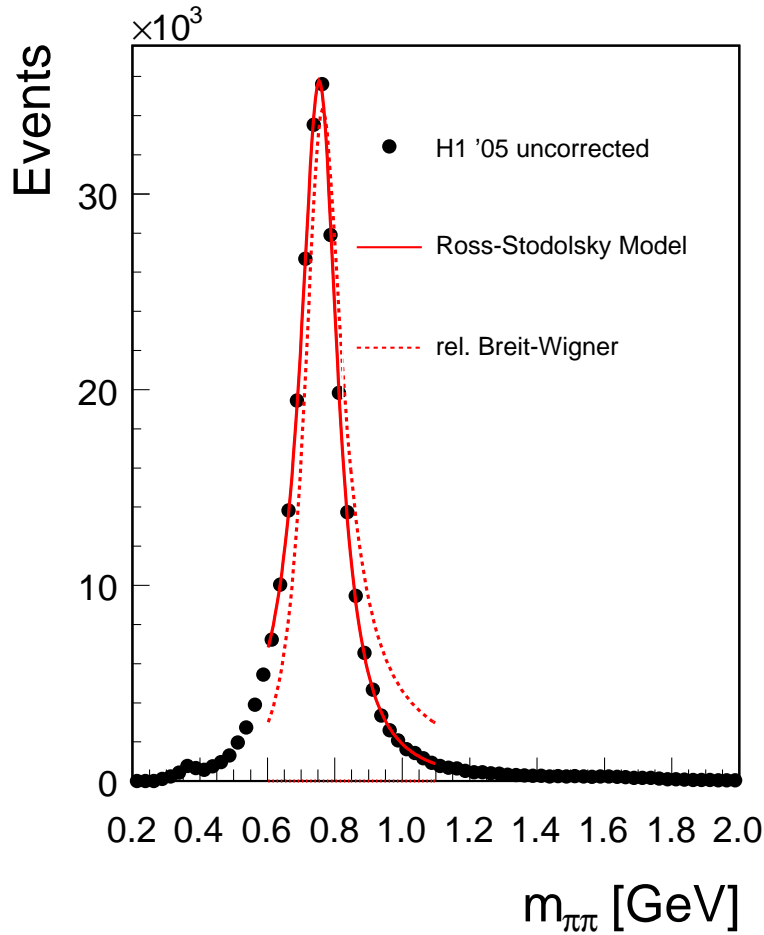


Figure 6.23: The dipion mass distribution fitted with the model by Ross-Stodolsky. The solid line corresponds to the fit with a non-zero skewing parameter n . The dashed line represents the resonant contribution corresponding to an unskewed relativistic Breit-Wigner.

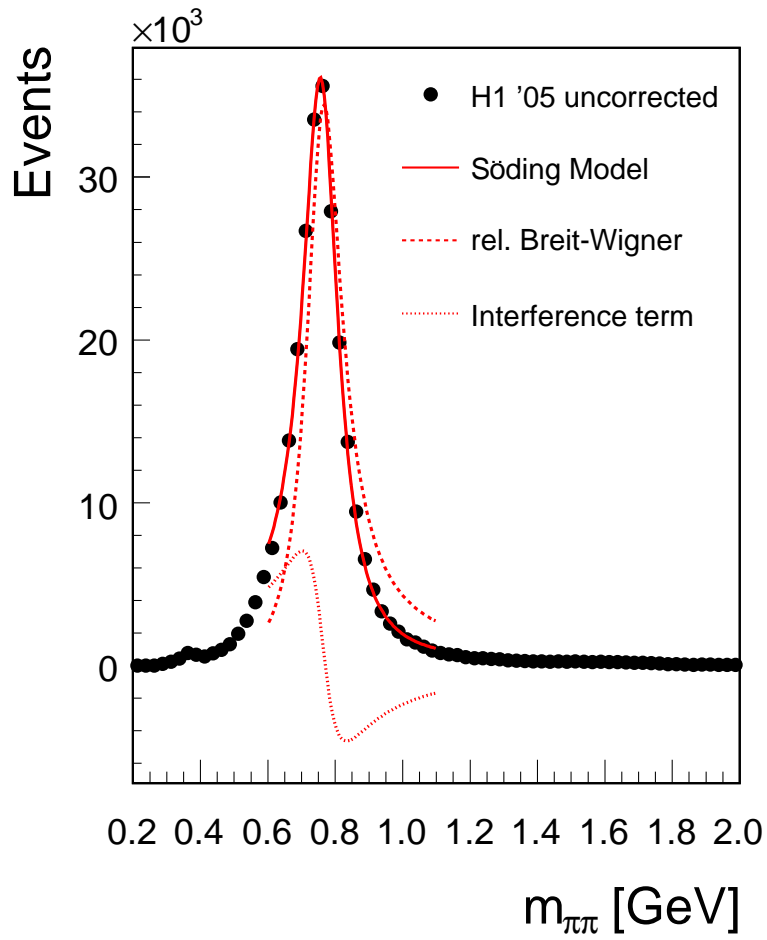


Figure 6.24: The invariant mass distribution fitted with the method by P. Söding. The solid line corresponds to the full fit. The dashed line represents the resonant contribution and the dotted line shows the interference responsible for the lineshape distortion.

6.6 Forward Tagging

To separate the elastic and inelastic events, the forward region of the H1 detector is used. The separation is based on tagging the inelastic events by the detector response in the forward region originating from the proton remnant.

The available subdetectors for the run period under study are the Forward Tagging System (FTS) and the Forward Muon Detector (FMD), both described in Sect. 4.2.3. The detector response for the two subdetectors are given in Fig. 6.25 and Fig. 6.26 respectively.

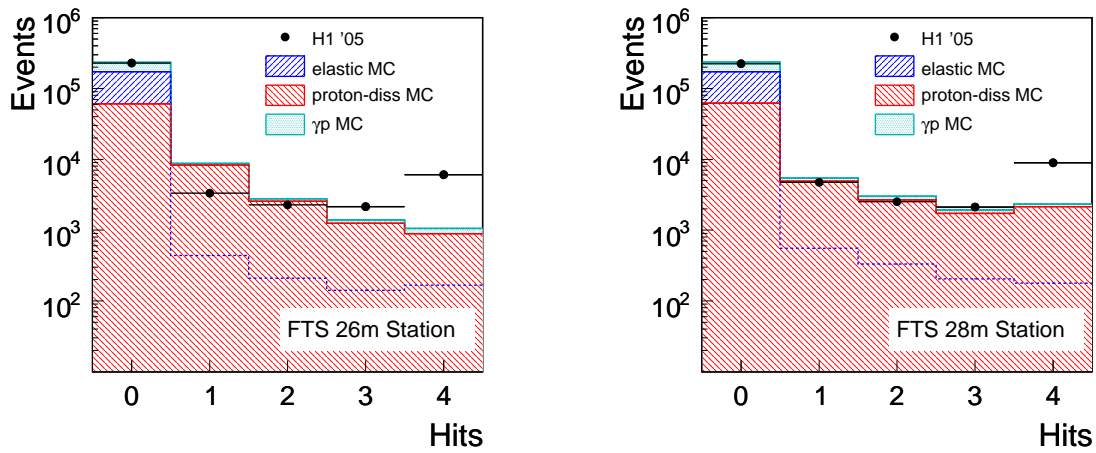


Figure 6.25: Detector response of the Forward Tagging System without corrections. Only the two closer stations at 26 m and 28 m are considered.

All events containing at least one positive response (hit) from any subdetector is considered as inelastic. For the FTS any hit in a scintillator counter is taken as positive signal while for the FMD at least 2 hit pairs were defined as positive response.

$$\text{tag}_{\text{forward}} = (\text{hit}_{\text{FTS26m}} \parallel \text{hit}_{\text{FTS28m}} \parallel \text{hit}_{\text{FMD}}) \quad (6.17)$$

The description of the hit multiplicity in the FTS is rather poor (Fig. 6.25). Particles interacting with the beam pipe produce secondary particles which can be detected in the FTS. In most cases these secondary particles are the product of a hadronization process and are grouped in narrow jets. In the MC simulation the jet shape is responsible for the spread of these particles. An inadequate jet shape in the simulation can cause differences in the hit multiplicity.

Another origin of differing hit multiplicities is the fact, that the H1 simulation program (H1SIM), which is based on GEANT, tracks only particles above a threshold of 1 GeV or 5 GeV, depending on the material. Therefore the number of particles in the MC simulation reaching the FTS is certainly smaller than for real data.

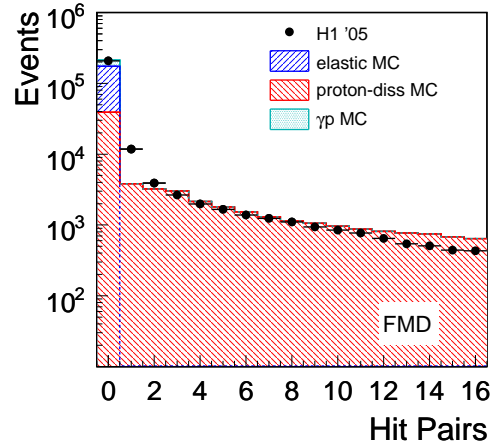


Figure 6.26: Detector response of the Forward Muon Detector without corrections.

A subsample of 100'000 events was reprocessed using H1SIM with a threshold of 10 MeV. The description of the hit multiplicity for the individual FTS scintillators improved while the time needed by the simulation program increased by a factor of 7 (2) for the elastic (proton-dissociative) MC sample.

The purpose of the FTS is to serve as tag for inelastic events, therefore it is not important how many scintillators detect a hit, but rather if any of the scintillators deliver a positive signal. The relevant ratio for this analysis is therefore the description of 'hit' to 'no hit' (Fig. 6.27).

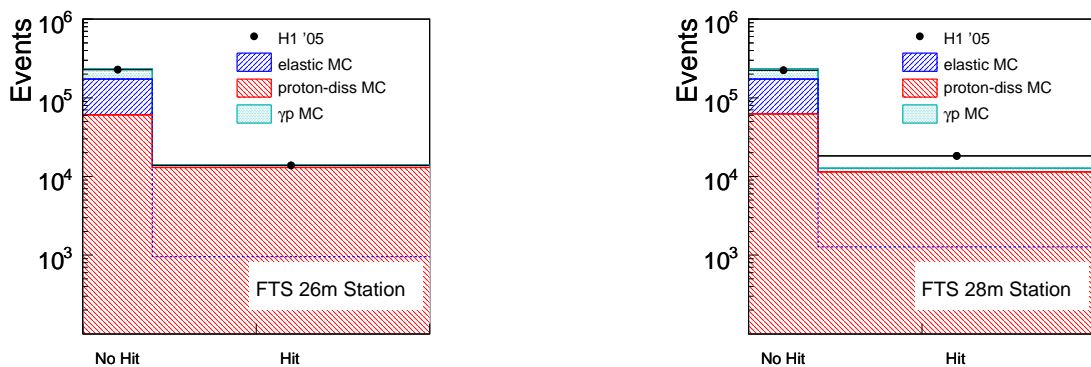


Figure 6.27: The detector response of the two FTS stations where only the station hits are counted and not further segmented to the individuals scintillators.

The overall hit - no hit description improved only little when using the lower threshold for H1SIM and therefore the refined MC simulation was not applied to all events. A reweighting factor for the default MC sample is determined nevertheless and used for the systematic error estimation, described in Sect. 8.4.

The simulation of the detector response in the H1SIM program does not include noise, which can be seen from the FMD response for elastic MC events in Fig. 6.26. Therefore a dedicated study was performed to estimate the noise contribution using random triggered events. During the entire data taking a random trigger is active with a trigger rate of 0.2 Hz.

The aim was to determine the contributions to the forward activity not associated with the proton remnant. Therefore only those events were selected, where an additional ρ^0 from photoproduction would still satisfy the s14 trigger requirement:

- Not more than 1 reconstructed track.
The s14 trigger allows for a third track. A second track in the random event would violate the trigger element $\text{FTT_mul_Ta} < 4$.
- No veto condition is active
If any of the s14 vetoes would be set, the event is rejected already at trigger level.

The detector response from the FTS and the FMD for this selection is interpreted as noise and combines all contributions from electronic noise and overlap events. For the MC simulation, each event is altered by adding hits to the FTS and the FMD response from random distributions equivalent to the obtained noise distributions as pictured in Fig. 6.28.

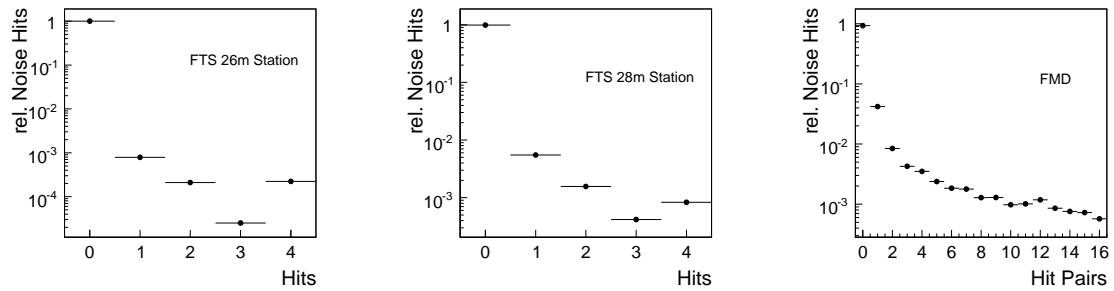


Figure 6.28: Noise contributions for the forward subdetectors taken from random triggered events. In most cases ($> 92\%$) there is no noise contribution (left bin). The remaining percentage of the events has a certain probability of some additional hits due to noise.

The description of the FMD hit pair multiplicity is overestimated in the MC simulation. To compensate for this an additional inefficiency is introduced where in average 40% of all hits in the event are removed.

Finally the description of the FTS and the FMD in the MC simulation is in well agreement with the observed behavior (Fig. 6.29). Even though the FMD hit pair multiplicity is still overestimated for large hit multiplicities (Fig. 6.29(c)), the description for a few hits is fine and sufficient for the purpose of tagging inelastic events with at least 2 hit pairs.

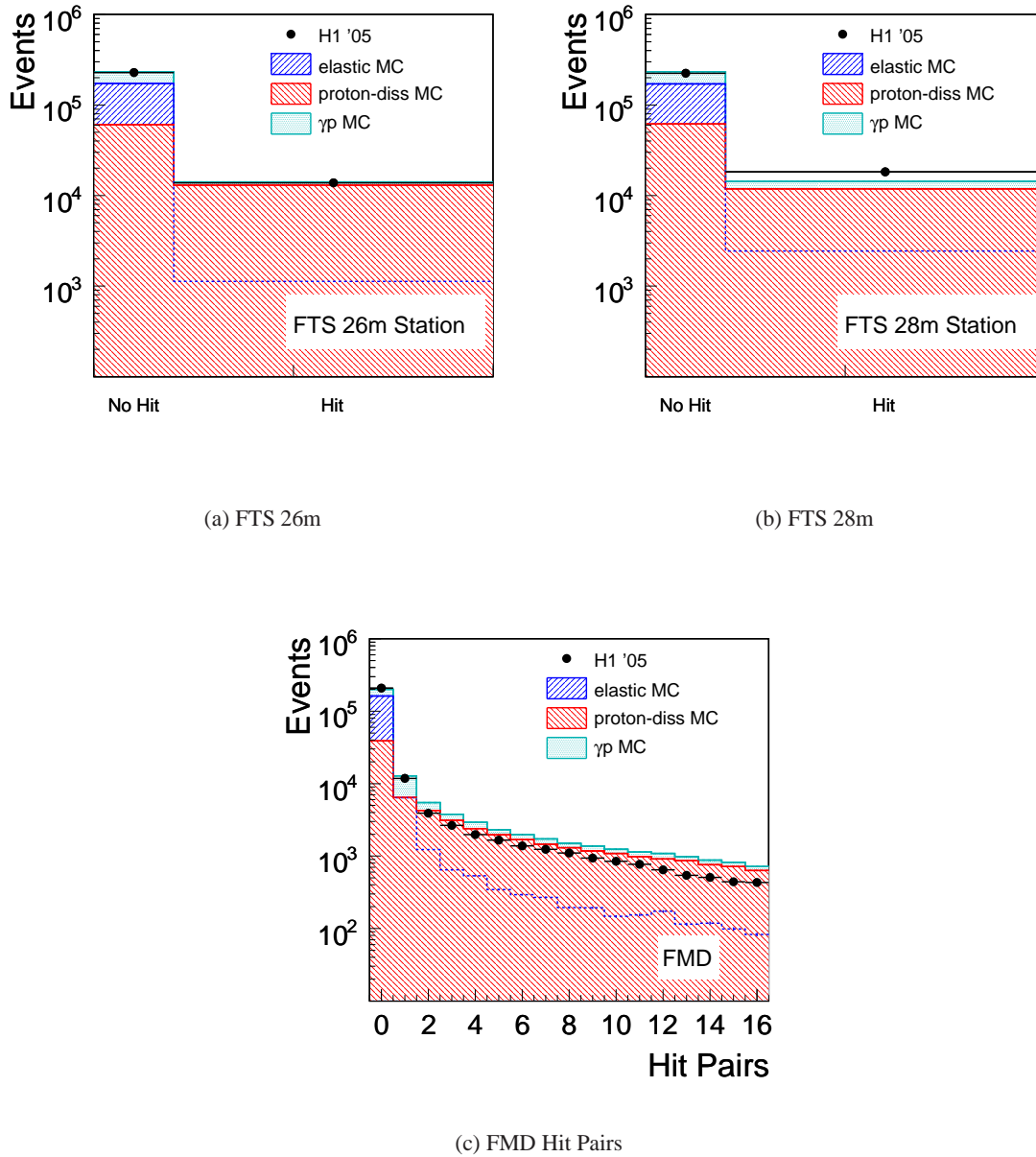


Figure 6.29: Detector response for the forward detectors after the correction for the noise contributions. These distributions are used in this analysis.

6.6.1 Tagging Probability

The tagging probability is determined from MC studies for elastic and proton-dissociative ρ^0 production separately and differentially in t (Fig. 6.30). These probabilities are relevant for the determination of the elastic and proton-dissociative cross section in Sect. 8.2.

For the proton-dissociative ρ^0 production, the mass of the dissociating system M_Y is directly related to the spread of the proton remnant. The dependence of the tagging probability as function of the mass M_Y is given in Fig. 6.31. The FTS is rather flat and therefore independent of the M_Y description in the MC simulation. The FMD on the other hand is sensitive to variations in the M_Y description. To account for the unknown mass spectrum of the dissociative system, the proton-dissociative events are reweighted according to $M_Y^{\pm 0.3}$ in the estimation of the systematic error.

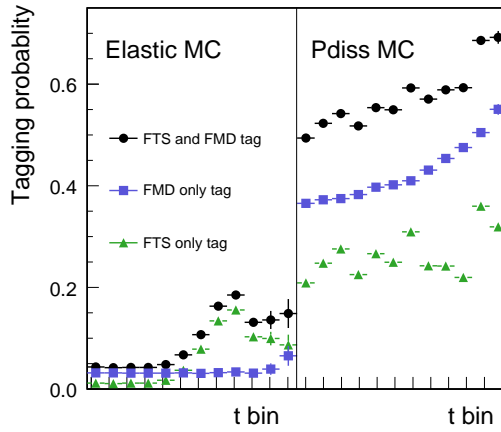
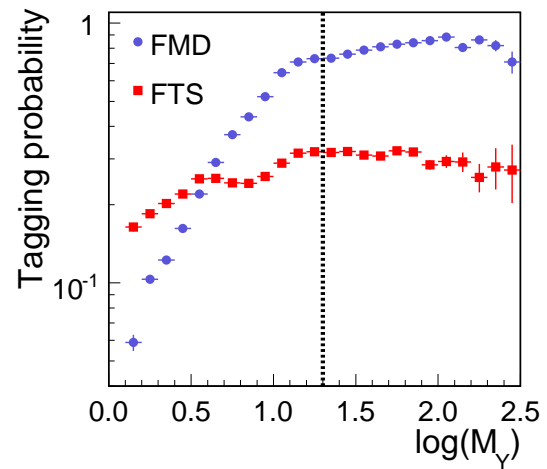


Figure 6.30: The tagging probability of the forward tag (Eq. (6.17)) for elastic and proton-dissociative MC events. The individual tagging probabilities of the two subdetectors are overlaid.

Figure 6.31: The forward tag detects the secondary particles from the proton remnant and hence depends on the mass of the dissociative system M_Y . The tagging probability for the two forward detectors is given as function of M_Y . The dashed line indicates the upper bound on M_Y due to the $x_{\mathbb{P}}$ cut in the visible cross section definition. Within the considered range, the FTS is rather independent on M_Y , whereas the FMD tag heavily depends on the mass. This is taken into account in the systematic error estimation.



6.7 Background

The main background for ρ^0 production is the non-resonant dipion production. Furthermore, the following background sources are studied in more detail:

- ϕ meson production
- ω meson production
- $\rho(1450)$ and $\rho(1700)$ meson production decaying to $\pi^+\pi^-\pi^0\pi^0$
- ρ^0 meson production outside the kinematical signal definition of $Q^2 < 4 \text{ GeV}^2$ and $x_{\mathbb{P}} < 0.01$

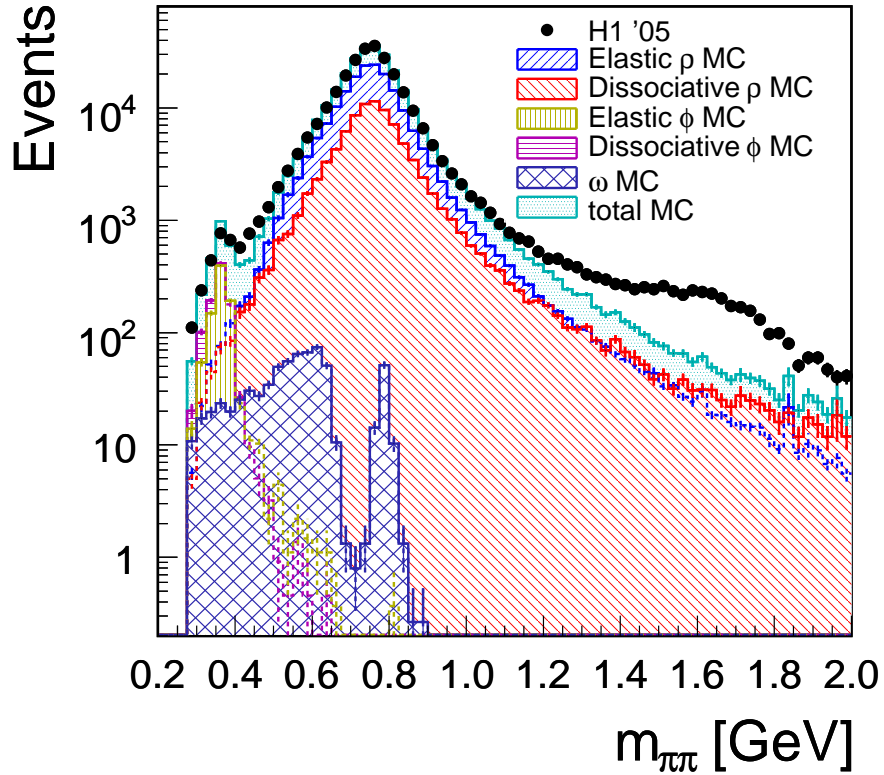


Figure 6.32: The dipion mass spectra from Fig. 6.21 including the contributions from Monte Carlo studies of ϕ and ω mesons. The enhancement of the data around 1.6 GeV is assigned to the $\rho' \rightarrow \pi^+\pi^-$ channel.

The non-resonant dipion production is already taken into account within the Ross-Stodolsky and the Söding model when fitting the invariant mass shape.

The event topology of the decay $\phi \rightarrow K^+ K^-$ is similar to the ρ^0 decay into two charged pions. However, reconstructing the two kaons under the charged pion mass hypothesis yields an invariant mass which is always below 0.6 GeV and thus the background from this channel is completely negligible.

The ω meson can either decay into 2 charged pions and a neutral pion or into two charged pions only. For the first decay mode $\omega \rightarrow \pi^+ \pi^- \pi^0$ the selection cut on the unassociated energy suppresses already a large fraction of the events while the bulk of the remaining events has a reconstructed dipion mass of less than 0.6 GeV. The second mode $\omega \rightarrow \pi^+ \pi^-$ is heavily suppressed w.r.t. to the three pion decay and can be seen in the $\rho - \omega$ interference which can be neglected [17] as well.

The heavy ρ mesons ($\rho(1450), \rho(1700)$) are also referred to as ρ' . The Crystal Barrel collaboration measured the ratio $BR(\rho' \rightarrow 4\pi)/BR(\rho' \rightarrow 2\pi)$ to be 0.37 ± 0.10 and 0.16 ± 0.04 for the $\rho(1450)$ and $\rho(1700)$ respectively [76]. As the channel $\rho' \rightarrow 4\pi$ is dominated by the decay to four charged pions $2\pi^+ 2\pi^-$, which is already rejected at trigger level, the branching ratio for the decay to 2 charged and 2 neutral pions ($\pi^+ \pi^- \pi^0 \pi^0$) is significantly smaller [77]. The contribution of the channel $\rho' \rightarrow \pi^+ \pi^-$ can be estimated from the dipion mass spectra (as in Fig. 6.32), which shows an indication in the expected mass region around $m_{\pi\pi} \approx 1.6$ GeV at a level of 0.5% compared to the ρ^0 signal.

The total background contribution arising from the production of the vector mesons ϕ, ω , and ρ' is estimated to be smaller than 2% and treated as normalization uncertainty on the result.

The background from ρ^0 production outside the visible cross section $Q^2 < 4 \text{ GeV}^2$ and $x_{\mathbb{P}} < 0.01$ (see Sect. 7.1) is included in the Monte Carlo simulation and is taken into account in the reconstruction efficiency.

Chapter 7

Acceptance and Efficiency

The selected events in the data sample represent ρ^0 candidates within a well defined geometrical region and phase space. If the ρ^0 decay pions escape through the beam pipe the H1 detector is obviously not able to detect them (geometrical limitation). The same is true if one of the decay pions has a transverse momentum of less than 100 MeV (kinematical limitation). The overall loss of events due to these limitations is called *acceptance* A . In addition, events can be lost if the H1 reconstruction fails or through trigger inefficiencies which are combined in the *efficiency* ε .

To compensate for all these losses the obtained number of events from the data sample is corrected with an overall efficiency determined from Monte Carlo studies. The generated ρ^0 events from the MC generator are passed through the H1 detector simulation H1SIM and fed to the reconstruction routines of H1REC. To obtain the FTT subtrigger elements in the MC simulation, the FTT emulation program FTTEMU is used. As the overall efficiency strongly depends on the kinematical variables $W_{\gamma p}$ and t , it is determined for each of the 80 W/t -bins (Table 6.3) separately as a function of $m_{\pi\pi}$ in bins of 25 MeV.

The number of events is extracted from the invariant mass distribution in the mass range $0.6 < m_{\pi\pi} [\text{GeV}] < 1.1$, therefore only the correction factors within this mass range are relevant (the unshaded area in the figures).

The figures showing the individual correction factors will only show nine selected W/t -bins instead of all 80 bins. The selected W/t -bins represent the low t ($t = -0.010 \text{ GeV}$, upper row), medium t ($t = -0.069 \text{ GeV}$, middle row) and high t ($t = -0.58 \text{ GeV}$, lower row) domain as well as the low $W_{\gamma p}$ (left column), medium $W_{\gamma p}$ (middle column) and the high $W_{\gamma p}$ (right column) region. The individual $W_{\gamma p}$ range for the various t -regions depend on the t value itself.

7.1 Visible Cross Section Definition

The cross section for a process can only be determined for a well defined phase space and is referred to as visible cross section. As the data events shall be corrected with respect to the visible

cross section, the Monte Carlo sample is restricted to the corresponding phase space defined as

$$Q_{\text{gen}}^2 < 4 \text{ GeV}^2 \quad (7.1)$$

$$x_{\mathbb{P}} < 0.01 \quad (7.2)$$

with $x_{\mathbb{P}}$ defined as in Eq. (6.10).

The upper bound on Q^2 limits the phase space to the γp regime and the $x_{\mathbb{P}}$ cut pins down the diffractive region for the proton dissociation. All correction factors determined by Monte Carlo methods are always with respect to this phase space.

7.2 Acceptance

Since the H1 detector does not have a complete 4π coverage, there are certain geometrical areas where the final state is not or only partially detected. These areas are excluded and according to MC simulation taken into account. As this correction is of a purely geometrical nature it is described very well in the MC simulation.

Also kinematical limits such as the lower bound on the p_T of a charged particle are corrected for by the acceptance in the MC simulation.

For this measurement the acceptance of the detector is defined as follows

$$20^\circ < \theta_{\text{gen}} < 160^\circ \quad (7.3)$$

$$0.2 \text{ GeV} < p_{\text{T}}^{\text{gen}} \quad (7.4)$$

whereas both requirements are applied to the generated quantities of each pion four vector in the event.

The acceptance correction A is then defined as

$$A = \frac{N_{\text{acc}}}{N_{\text{visible}}} \quad (7.5)$$

where N_{acc} denotes the number of events within the detector acceptance and N_{visible} stands for all generated events inside the phase space of the visible cross section.

The acceptance correction A integrated over the mass in the range $0.6 < m_{\pi\pi} [\text{GeV}] < 1.1$ is shown in Fig. 7.1 as determined from MC studies for each W/t -bin.

The decrease of the acceptance at the t bin edges comes from the θ requirement at low (high) $W_{\gamma p}$ and corresponds to a boost in forward (backward) direction where the pions are more and more outside the θ range given in (7.3).

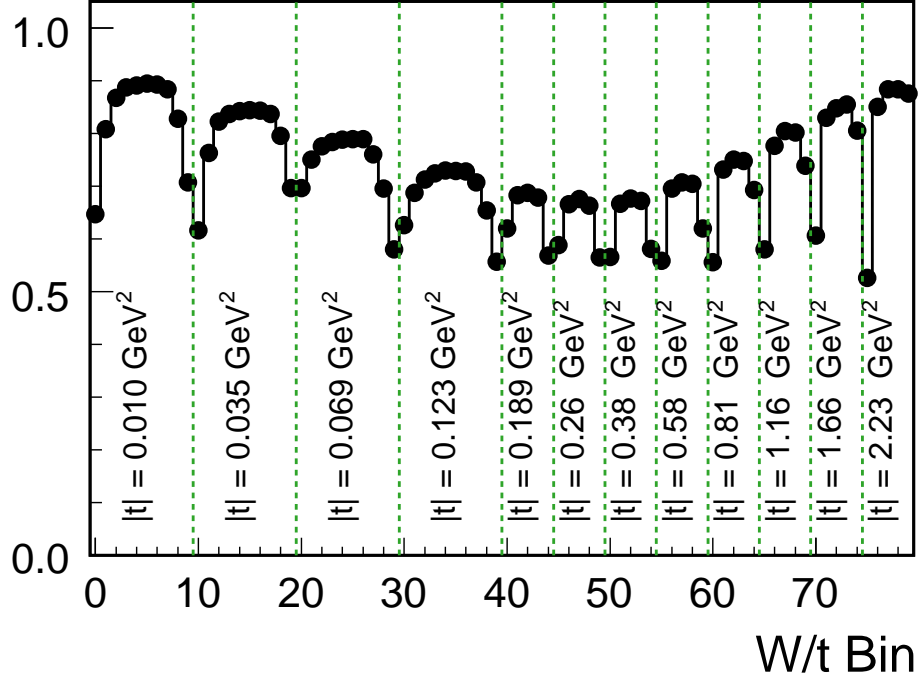


Figure 7.1: The acceptance A for each W/t -bin integrated over $m_{\pi\pi}$ in the range $0.6 < m_{\pi\pi} [\text{GeV}] < 1.1$.

The acceptance variation along the t bins originates from the p_T threshold (Eq. (7.4)). For a ρ^0 produced at rest, the expected transverse momentum of the decay pions is 250 MeV. If the ρ^0 is boosted in the transverse plane, the transverse momentum of the pions as measured in the laboratory frame is boosted as well. If the decay plane of the pions is not perpendicular to the boost direction, one pion will be boosted along the ρ^0 boost and is reconstructed with a larger p_T in the laboratory frame while the other pion is boosted in the opposite direction and will be reconstructed with a lower p_T . With increasing boost t , the opposite pion will eventually drop below the p_T threshold and fail the acceptance requirement.

For $|t| = 0.5 \text{ GeV}^2$ the decay pion emerging exactly opposite to the boost direction remains at rest in the laboratory frame. The acceptance A reaches a minimum over the t bins around $|t| \sim 0.5 \text{ GeV}^2$.

For $|t| > 0.5 \text{ GeV}^2$ both decay pions will be boosted along the ρ^0 boost. For large enough t , both decay pions will be reconstructed with a p_T larger than 200 MeV and the acceptance A rises again.

In Fig. 7.2 the acceptance A is shown for the nine selected W/t -bins differentially in $m_{\pi\pi}$. The mass dependence of the acceptance is dominated by the p_T threshold for the low mass region at low $|t|$. The drop at high masses comes from the fact, that for large $m_{\pi\pi}$ the opening angle of the pions in θ is large and therefore one pion is more likely to escape the θ range.

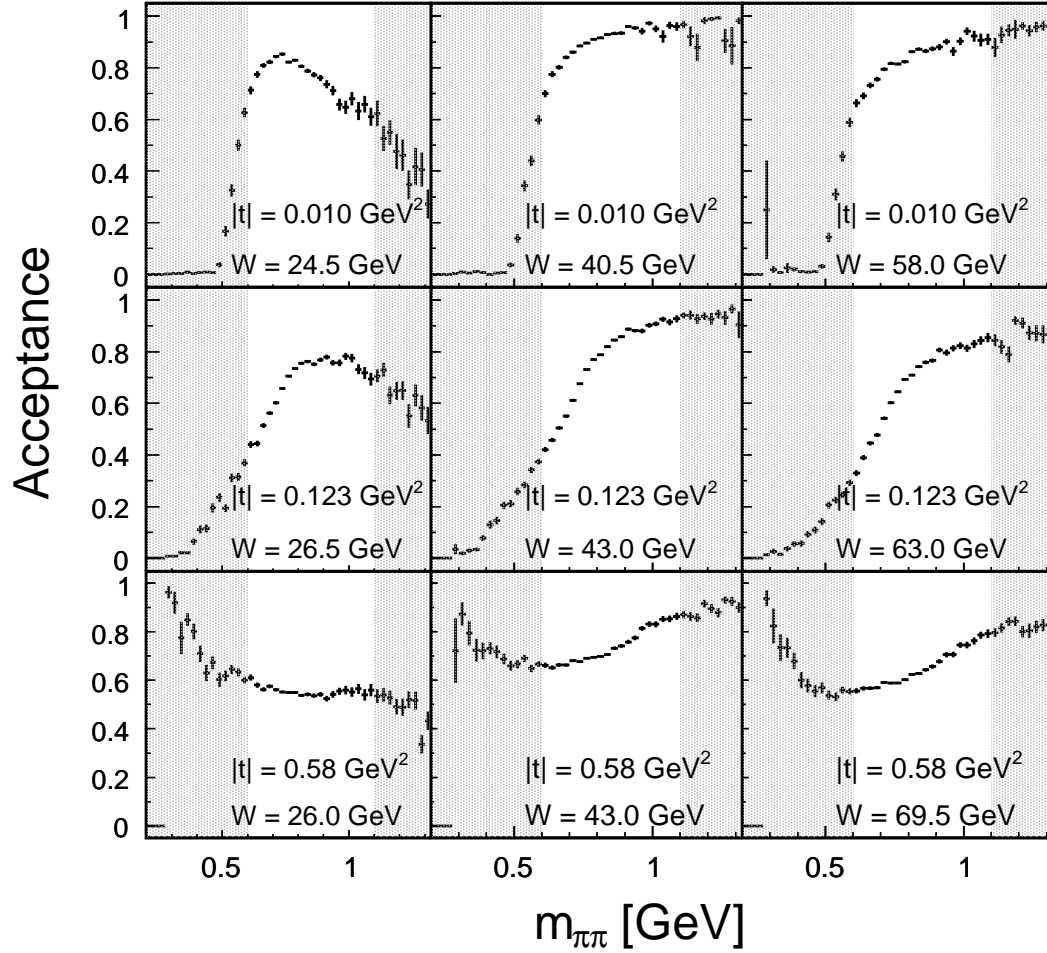


Figure 7.2: The acceptance A as function of $m_{\pi\pi}$ for the nine selected W/t -bins.

7.3 Efficiency

While the acceptance accounts for those events, which cannot be seen by the detector for geometrical and/or kinematical reasons, the efficiency accounts for all events which are lost due to inefficiencies in the data processing and trigger chains. The two main contributions are the reconstruction efficiency and the trigger efficiency.

7.3.1 Reconstruction Efficiency

The reconstruction efficiency compensates for all inefficiencies which arise during the reconstruction of the event as well as the efficiencies of the selection cuts. The reconstruction efficiency is determined from the reconstructed variables of the Monte Carlo simulation and includes therefore

all migrations between the individual W/t -bins due to the smearing of the kinematical variables $W_{\gamma p}$ and t during the reconstruction. The reconstruction efficiency ε_{rec} is defined as

$$\varepsilon_{\text{rec}} = \frac{N_{\text{rec}}}{N_{\text{acc}}}, \quad (7.6)$$

with N_{rec} denoting the number of reconstructed events after the selection cuts.

The reconstruction efficiency ε_{rec} for the selected W/t -bins is shown in Fig. 7.3. In the relevant mass range the efficiency ε_{rec} is rather flat and decreases with larger t from $\sim 60\%$ to $\sim 40\%$.

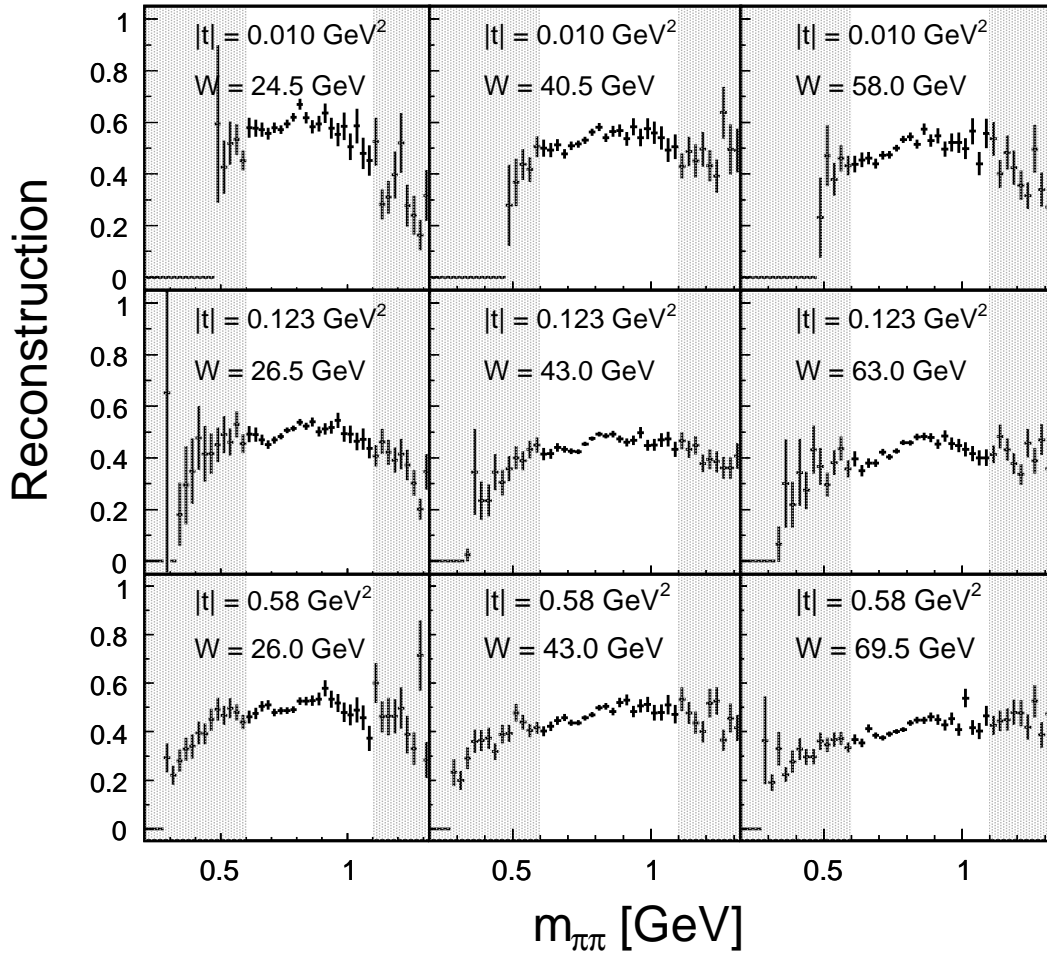


Figure 7.3: The reconstruction efficiency ε_{rec} for the nine selected W/t -bins.

The migration of events between the bins can be monitored using the quantities *Purity* and *Stability* defined as

$$\text{Purity} = \frac{N_{\text{rec}\&\text{gen}}}{N_{\text{rec}}} \quad (7.7)$$

$$\text{Stability} = \frac{N_{\text{rec}\&\text{gen}}}{N_{\text{gen}}} \quad (7.8)$$

$$(7.9)$$

with N_{rec} (N_{gen}) the number of reconstructed (generated) events in the W/t -bin and $N_{\text{rec}\&\text{gen}}$ the number of events which are reconstructed in the same W/t -bin as they are generated. The purity is a measure for events migrating into a W/t -bin during the reconstruction. For a high reconstruction efficiency the stability measures the migration out of a W/t -bin. For this analysis however, the stability is dominated by the (low) reconstruction efficiency. Both quantities are shown in Fig. 7.4.

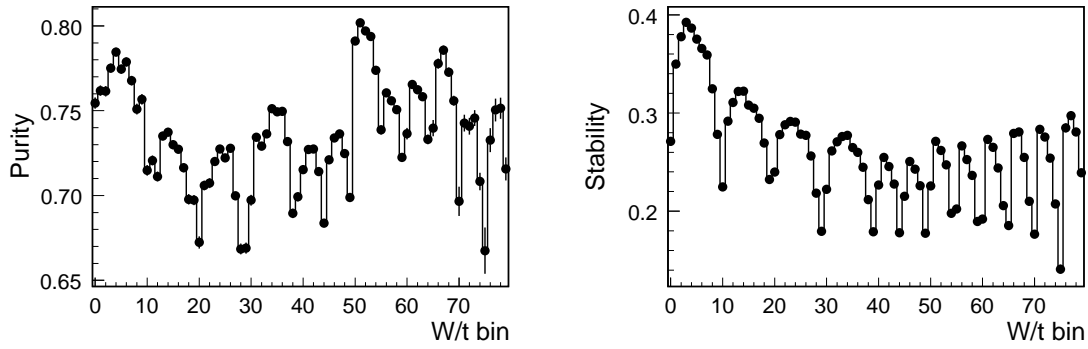


Figure 7.4: Purity and stability can be used to monitor the migrations of events between W/t -bins during the reconstruction. Migrations are due to smearing in the kinematical variables. For this analysis the stability is dominated by the reconstruction efficiency and hence not very useful to monitor the migration out of a W/t -bin.

7.3.2 Trigger Efficiency

To assure that the trigger elements are correctly modelled in the MC simulation, an independent data sample - called monitor sample - is used. It was triggered by inclusive DIS subtriggers depending only on trigger elements based on the backward calorimeter (SpaCal):

```
s0  SPCLe_IET > 1 v:3 f:0
s3  SPCLe_IET > 2 v:5 f:0
```

The monitor sample is compared to MC simulations for elastic and inelastic DIS ρ^0 production generated by the diffVM generator. The simulation of the FTT and the CIP trigger elements for the MC events show deviations w.r.t. the monitor sample. Thus the MC events need to be reweighted

in order to obtain the best possible description in the MC simulation.

To obtain a clean monitor sample with similar event topologies and especially comparable tracker occupancy, the following selection cuts are applied to the monitor events:

- scattered electron
The subtrigger s0 and s3 explicitly trigger on the scattered electron. The presence of the scattered electron is therefore also required. Only events where the scattered electrons has an energy larger than 20 GeV are accepted.
- Z-Vertex
The z-vertex position is required to be within 25 cm of the nominal IP.
- Tracking
Exactly two reconstructed and primary vertex fitted tracks of opposite charge in the central region.
- Transverse momentum
The reconstructed tracks must have at least 200 MeV transverse momentum each
- Invariant mass
The invariant mass of the two tracks under the charged pion mass hypothesis should be within $0.6 < m_{\pi\pi} [\text{GeV}] < 1.1$ with the nominal mass of the ρ^0 vector meson being 0.768 GeV [51].

The selection criteria are as close as possible to the selection cuts for the analysis data sample (Sect. 6.4). This is necessary in order to be able to compare the monitor sample in DIS with the analysis sample in γp and hence to be able to apply the reweighting functions obtained in DIS to the γp regime.

FTT trigger efficiency

As the FTT delivers track wise information, the trigger efficiency for a single track as function of the track parameters p_T , ϕ and θ can be determined. This single track efficiency depends only on the track parameter set (p_T , ϕ and θ) and is independent of the production regime (DIS or γp) for a given tracker occupancy.

In Fig. 7.5 the individual dependencies of the single track trigger efficiency are shown. The efficiency obtained from the MC events overestimates the efficiency in the data by 4% while the shape of the dependencies is well modelled. In general the single track trigger efficiency varies around 90%.

For the θ dependency a significant drop around 90° is observed, called θ dip. Particles penetrating the tracker chamber under $\theta \sim 90^\circ$ deposit less energy in the tracking volume and induce thus lower currents on the sense wire. The single hit efficiency is therefore reduced and observed as dip in the single track efficiency.

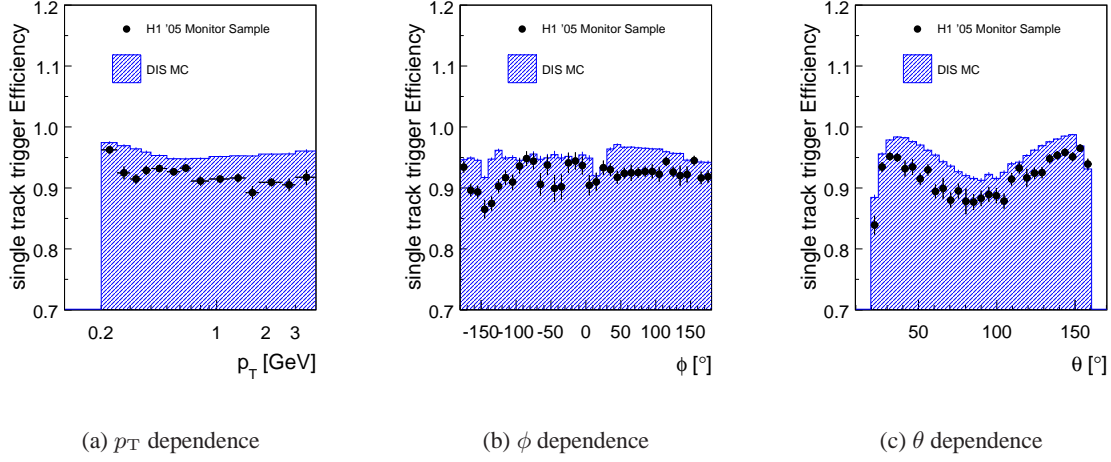


Figure 7.5: Efficiencies of the FTT subtrigger 14 as function of p_T , ϕ and θ for Data and MC. The efficiencies obtained from MC events overestimate the efficiency determined from the data sample by roughly 4%. The dip around $\theta \sim 90^\circ$ (c) is due to a lower energy depositions of particles passing the tracker perpendicular to the beam pipe.

Besides the overall normalization correction of 4%, the single track efficiency is reweighted in the variables p_T and θ . To account for the correlation of the two variables the reweighting is done simultaneously using a 2-dimensional fit of the form:

$$f_{\text{FTT}}(p_T, \theta) = A_0 - A_1 \sqrt{p_T} + (A_2 + A_3 \sqrt{p_T}) \cdot (\theta - A_5)^2 - A_4 \cdot (\theta - A_5)^4 \quad (7.10)$$

The six parameters A_k can be interpreted as follows:

A_0 : The overall normalization of the correction.

A_1 : Coefficient of the pure p_T dependence.

A_2 : Parameter for the depth of the θ dip.

A_3 : Parameter for the depth of the θ dip dependent on $\sqrt{p_T}$.

A_4 : Coefficient of the pure θ dependence.

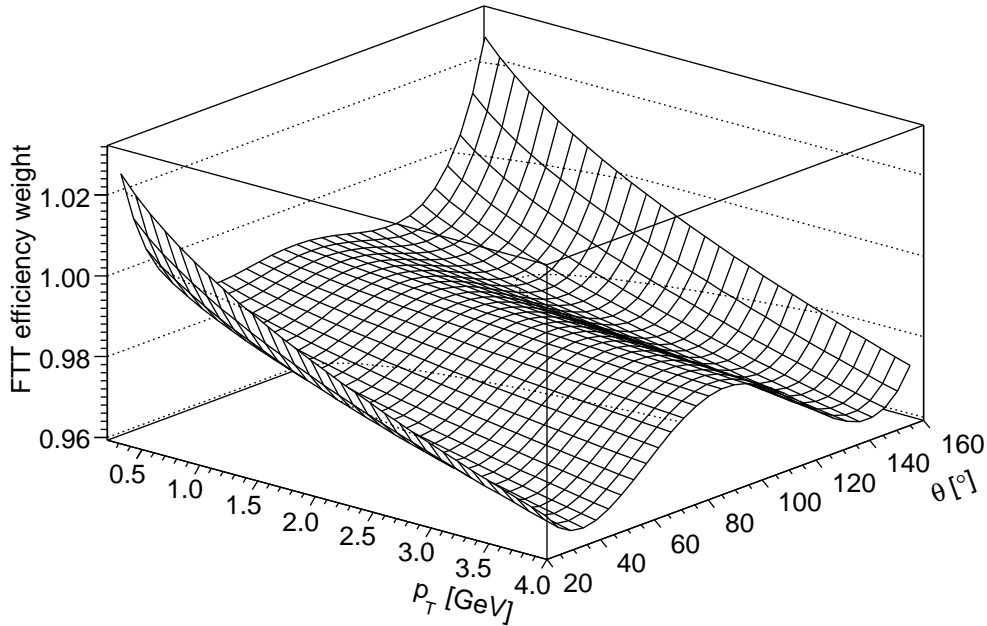
A_5 : Position of the θ dip.

The function parameters obtained by the fits to the data and the MC events are summarized in Table 7.1.

Parameters for the FTT reweight function						
	A_0	A_1	$A_2 [\cdot 10^5]$	$A_3 [\cdot 10^6]$	$A_4 [\cdot 10^9]$	A_5
H1 '05 Data	96.3 ± 2.7	325 ± 164	3.6 ± 2.0	2.6 ± 6.8	8.2 ± 4.3	91.8 ± 4.2
MC events	96.8 ± 1.1	284 ± 64	3.8 ± 0.7	9.2 ± 2.9	11.1 ± 1.4	91.1 ± 1.1

Table 7.1: Parameters used to reweight the FTT efficiency in the MC events using Eq. (7.10).

The ratio $f_{\text{FTT}}^{\text{Data}}(p_T, \theta) / f_{\text{FTT}}^{\text{MC}}(p_T, \theta)$ is plotted in Fig. 7.6 and applied to each reconstructed track in the MC events to obtain a sufficient description of the FTT efficiency in the MC simulation. The corrected single track efficiencies are given in Fig. 7.7. Not only the p_T and θ distributions are much better modelled but also the ϕ distribution is correctly described.

Figure 7.6: The correction function $f(p_T, \theta)$ from Eq. (7.10) that is applied to the MC events.

CIP trigger efficiency

After reweighting the FTT trigger efficiency, the CIP trigger efficiency is studied. The CIP trigger only delivers trigger elements for the whole event, not for individual tracks. Thus it is necessary to define a variable with comparable trigger dependencies between the DIS and the γp regime. Such a variable is the arithmetic mean of the polar angle $\bar{\theta} \equiv \frac{1}{2}(\theta_1 + \theta_2)$ of the two reconstructed pion

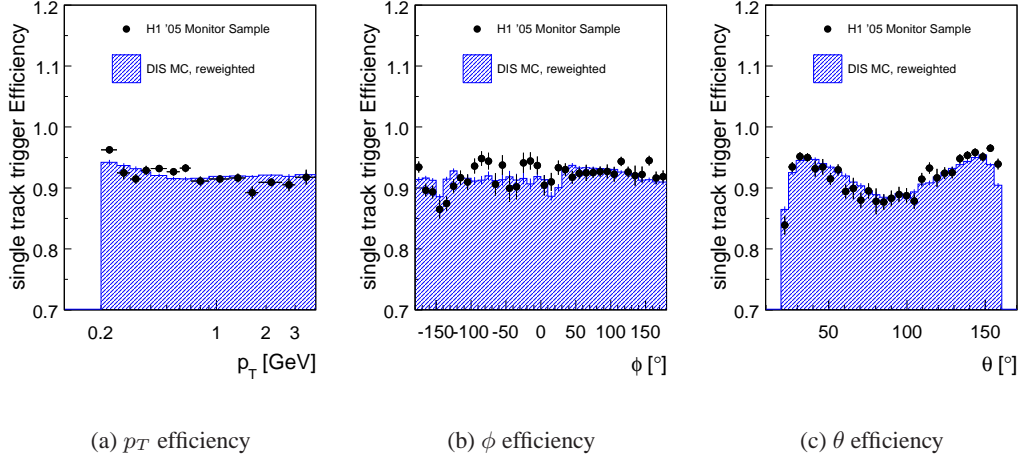


Figure 7.7: Efficiencies of the FTT subtrigger 14 as function of p_T , ϕ and θ corrected with a 2-dimensional function in p_T and θ for Data and MC events.

tracks and has a similar phenomenology as $W_{\gamma p}$:

For small values of $\bar{\theta}$, both pions are reconstructed more towards the forward region as for low $W_{\gamma p}$ while for large values of $\bar{\theta}$ the pions are rather detected in the backward region (large $W_{\gamma p}$). This allows to characterize the CIP trigger efficiency in a production independent manner and to some extent differentially w.r.t. $W_{\gamma p}$.

In Fig. 7.8(a) the efficiency for the CIP trigger elements is plotted versus $\bar{\theta}$. The uncorrected MC distribution was fitted with a quadratic polynomial of the form

$$f_{\text{CIP}}^{\text{MC}}(\bar{\theta}) = C_0 + C_1 \cdot \bar{\theta} + C_2 \cdot \bar{\theta}^2, \quad (7.11)$$

the obtained parameters are listed in Table 7.2.

Parameters for the CIP reweight function			
	C_0	$C_1 [\cdot 10^{-3}]$	$C_2 [\cdot 10^{-5}]$
MC events	1.02 ± 0.03	-5.1 ± 0.7	2.86 ± 0.38

Table 7.2: Parameters used to reweight the CIP efficiency in the MC events using Eq. (7.11).

The efficiency obtained from data events is flat in $\bar{\theta}$ with a mean value of 93.4%. The MC simulation is corrected according to:

$$w_{\text{CIP}}(\bar{\theta}) = \frac{0.934}{f_{\text{CIP}}^{\text{MC}}(\bar{\theta})} \quad (7.12)$$

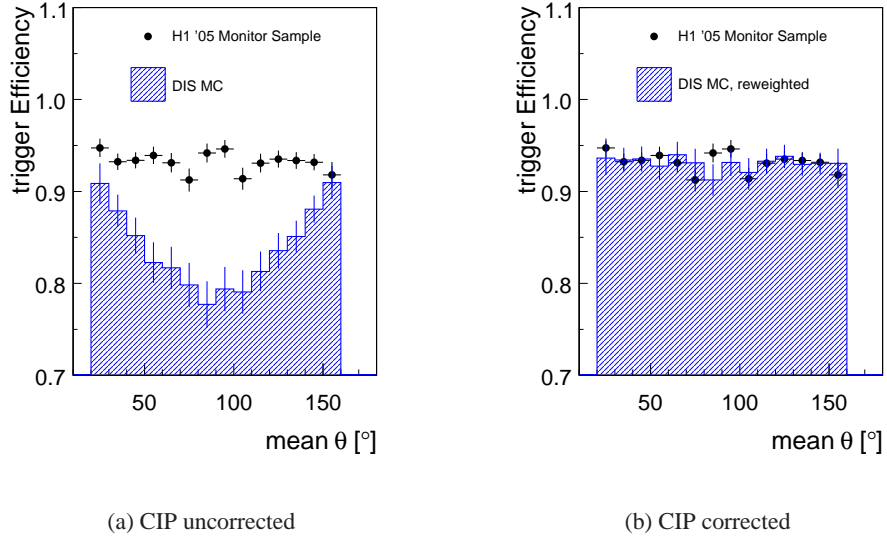


Figure 7.8: Efficiencies of the CIP trigger as function of $\bar{\theta}$. The efficiency of the CIP trigger as determined from the data is flat in $\bar{\theta}$ with a mean value of 0.934 whereas the MC simulation shows a sizeable drop around $\bar{\theta} \approx 90^\circ$ (a). The MC events are fitted with a quadratic polynomial and the result is used to correct for the drop in the MC simulation (b).

The efficiencies of the FTT and the CIP for the nine selected W/t -bins is given in Fig. 7.9.

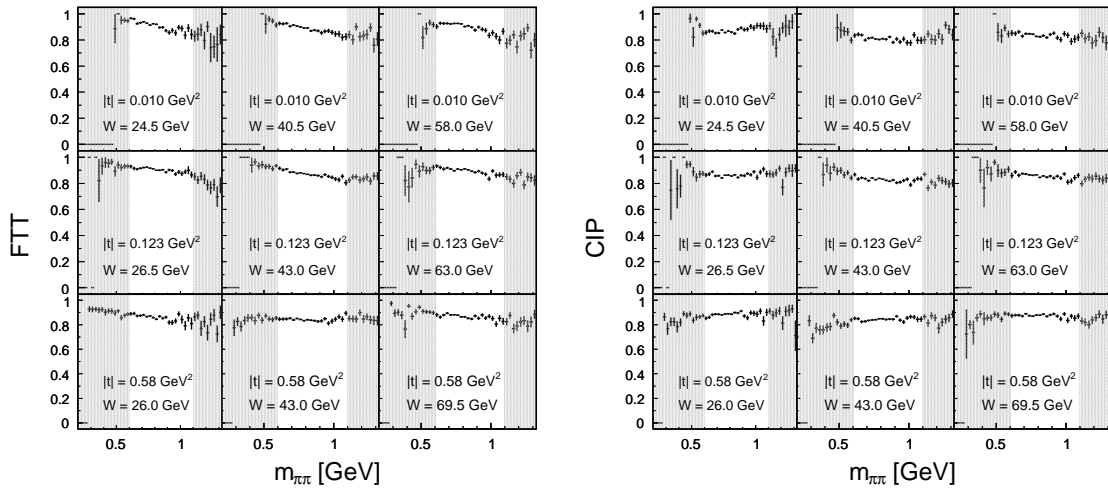


Figure 7.9: The FTT (left) and CIP (right) trigger efficiencies for nine selected W/t -bins.

Veto efficiencies

The remaining contributors to the s14 subtrigger are the vetos from the LAr, the veto wall and the FTI scintillator. The selection cut on the unassociated energy is a much tighter requirement than the LAr inner forward veto as can be seen in Fig. 7.10.

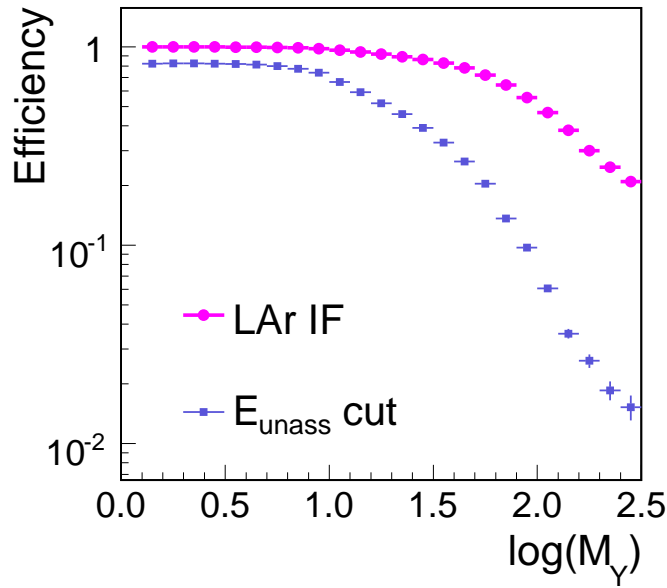


Figure 7.10: LAr IF veto versus unassociated energy cut as function of the mass of the dissociative system M_Y .

In the MC simulation the LAr subtrigger element is described within 2% after the reweighting of the FTT and the CIP which is added to the systematic error while no reweighting is applied.

The other veto conditions are not included in the MC simulation and are estimated from random trigger events. For the FTI no significant contribution was found, the veto wall efficiency is described within 0.5% and also added to the systematic error estimation.

All variation in the veto conditions are applied as constant weights and have therefore no influence on the measurement of the energy dependence or the pomeron trajectory.

Trigger efficiency

For the overall trigger efficiency the trigger elements from the FTT, the CIP and the LAr IF are requested in the MC simulation and the trigger efficiency is defined as

$$\varepsilon_{\text{trig}} = \frac{N_{\text{trig}}}{N_{\text{rec}}} \quad (7.13)$$

with N_{trig} denoting all reconstructed and selected events passing the trigger requirement. The overall trigger efficiency is given in Fig. 7.11 for the nine selected W/t -bins.

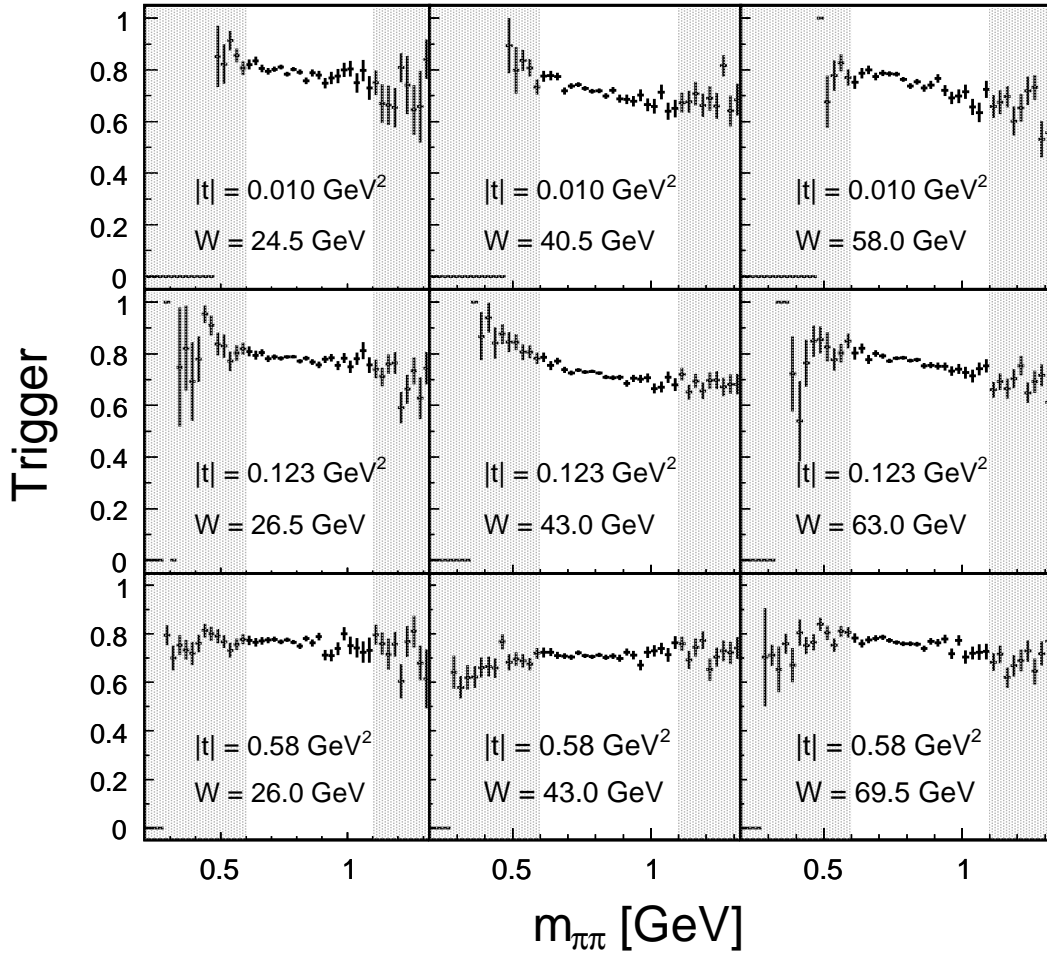


Figure 7.11: The trigger efficiency for the nine selected W/t -bins.

7.4 Overall Correction

The acceptance A and efficiency ε are combined to the overall correction factor, determined triple differentially in $W_{\gamma p}$, t and $m_{\pi\pi}$:

$$\varepsilon_{\text{overall}} = A \cdot \varepsilon_{\text{rec}} \cdot \varepsilon_{\text{trig}} = \frac{N_{\text{trig}}}{N_{\text{visible}}} \quad (7.14)$$

The overall correction factors are shown in Fig. 7.12 for the selected W/t -bins. Each correction

factor is applied to the corresponding W/t -bin with the uncorrected invariant mass spectrum. The obtained fully corrected mass distributions can be fitted to extract the number of resonant ρ^0 photoproduction events.

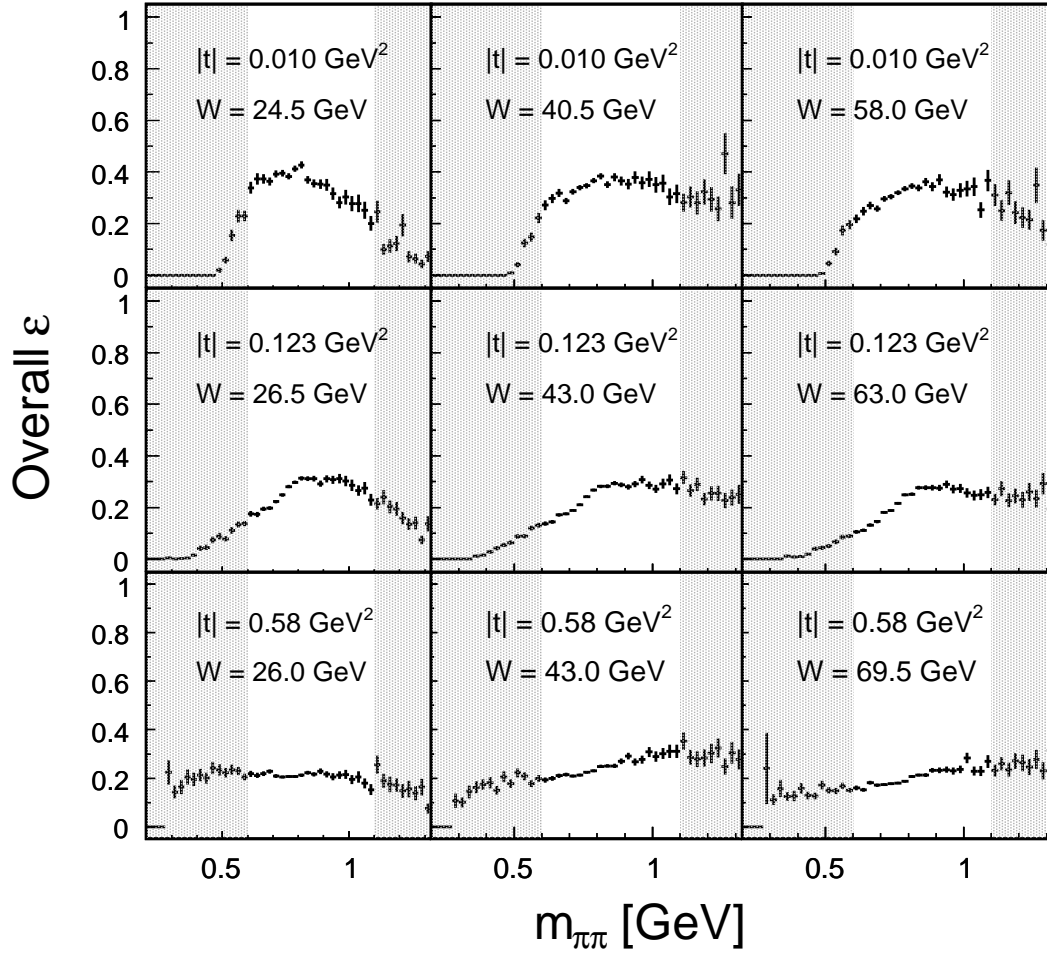


Figure 7.12: The Overall correction factors for the nine selected W/t -bins. The correction is determined triple differentially in $W_{\gamma p}$, t and $m_{\pi\pi}$. The correction factors are roughly flat within the mass range $0.6 < m_{\pi\pi} [\text{GeV}] < 1.1$ and vary between 40% for the low t bins and 20% for the highest t bins.

Chapter 8

Cross Section Determination

8.1 Fitting the Invariant Mass Distribution

The invariant mass distribution of dipion events is distorted with respect to a resonant pion production from the ρ^0 decay. As described in Sect. 6.5, the resonant pion production can be extracted by fitting the invariant mass spectra with modified Breit-Wigner functions.

Fig. 8.1 shows the dipion mass spectra after the overall corrections and integrated over all W/t -bins. In Fig. 8.1(a) the Ross-Stodolsky method was applied to extract the parameters of the ρ^0 while in Fig. 8.1(b) the Söding method was used. Both spectra were fitted within the mass range $0.6 < m_{\pi\pi} [\text{GeV}] < 1.1$. The fit results for the mass and width of the ρ^0 are summarized in Table 8.1.

Fit Results for Integrated Mass Spectrum		
ρ^0 Parameter	Ross-Stodolsky	Söding
Mass [MeV]	766.7 ± 0.5	766.7 ± 0.4
Width [MeV]	144.8 ± 0.8	144.6 ± 0.8

Table 8.1: Integrated Mass Spectra Fit for the models Ross-Stodolsky and Söding.

The dipion mass distributions are also fitted in the individual W/t -bins in the same manner. In Fig. 8.2 the results for the ρ^0 parameters for the Ross-Stodolsky model is compared to the result from the integrated mass fit indicated as horizontal line. Fig. 8.3 gives the result for the ρ^0 parameter extraction using the Söding ansatz.

The variations in the fitted mass and width of the ρ^0 for the individual W/t -bins are purely statistical. For the determination of the cross section, the mass and width of the ρ^0 are fixed to the integrated parameters in the fit methods and the invariant mass spectra is refitted in the individual W/t -bins.

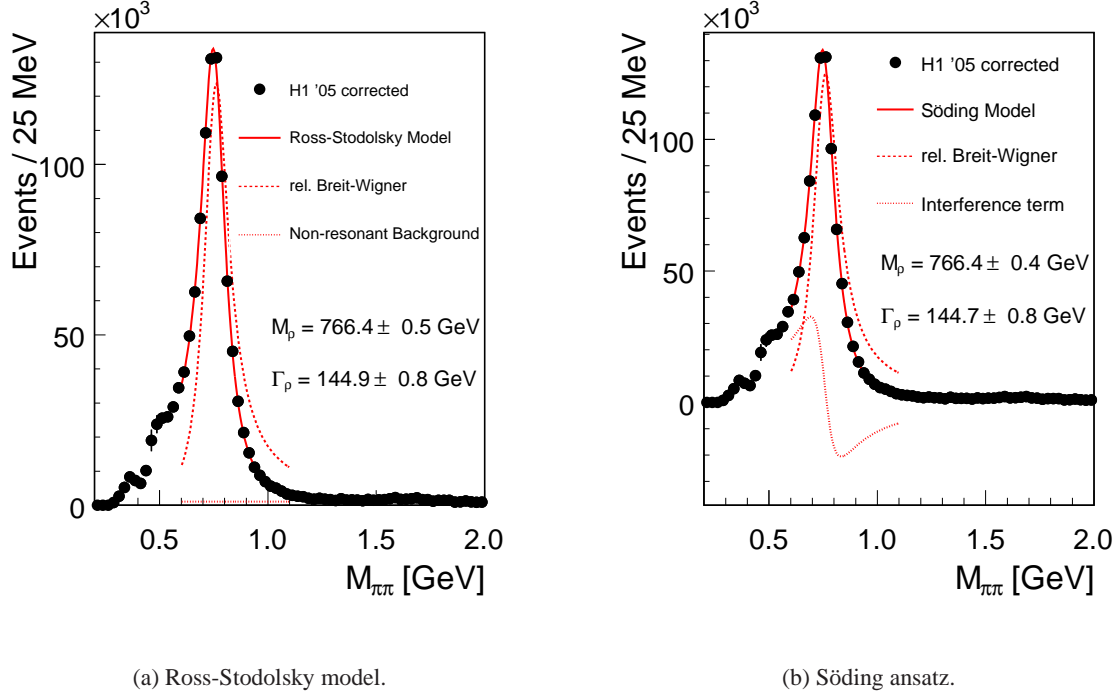


Figure 8.1: Integrated dipion mass spectra with the fit result for the Ross Stodolsky (a) and the Söding (b) parameterization. Only statistical errors are given. The two different models for extracting the resonant ρ^0 are explained in Sect. 6.5.

The number of resonantly produced ρ^0 events is obtained by integrating the relativistic Breit-Wigner of the refitted mass spectra in the mass range $2m_\pi < m_{\pi\pi} < m_\rho + 5\Gamma_{\rho,0} = 1.52 \text{ GeV}$:

$$N_{\text{obs}} = N_0 \int_{m_{\pi\pi}=2m_\pi}^{m_\rho+5\Gamma_{\rho,0}} \frac{m_\rho \Gamma_\rho m_{\pi\pi}}{(m_\rho^2 - m_{\pi\pi}^2)^2 + m_\rho^2 \Gamma_\rho^2} dm_{\pi\pi} \quad (8.1)$$

Spital and Yennie [78] introduced a different convention for the ρ^0 cross section, used e.g. by the Omega collaboration [79], which defines the cross section by

$$\frac{d\sigma}{dt} = \frac{\pi \Gamma_{\rho,0}}{\pi} \left. \frac{d^2\sigma}{dt dm_{\pi\pi}} \right|_{m_{\pi\pi}=m_\rho}. \quad (8.2)$$

For the PDG values of m_ρ and $\Gamma_{\rho,0}$, this definition leads to a cross section which is larger by a factor of 1.050 than the one derived in this analysis.

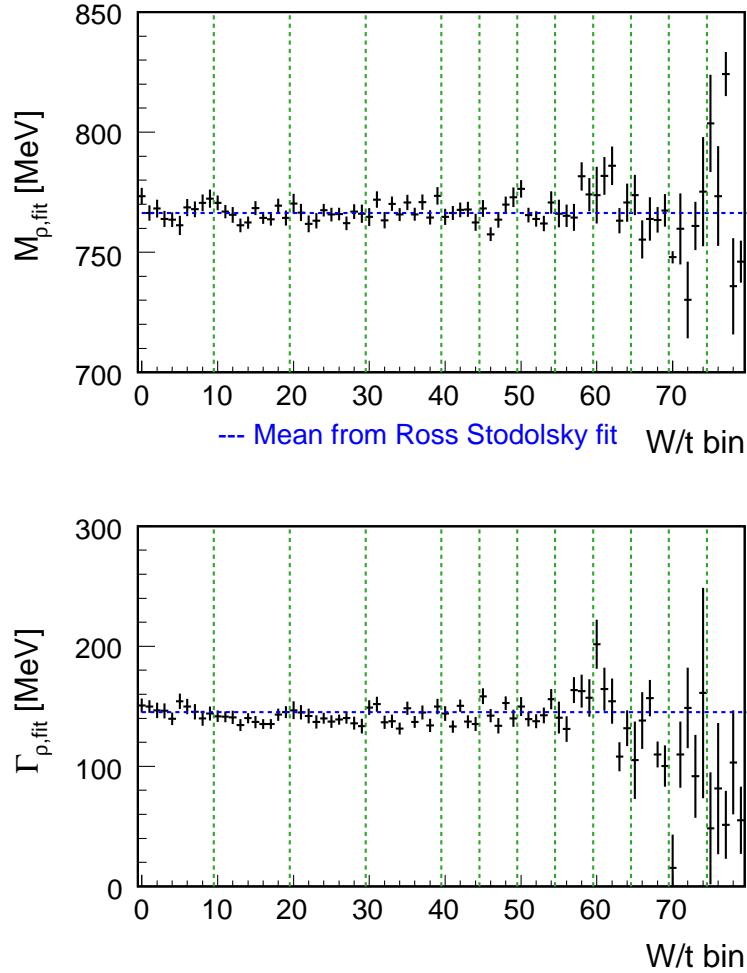


Figure 8.2: The fitted mass and width of the ρ^0 for each W/t -bin within the Ross-Stodolsky model. The horizontal lines represents the ρ^0 parameters from the integrated fit from Fig. 8.1(a).

8.2 Elastic Production vs. Proton-Dissociation

The separation for elastic and proton-dissociative (inelastic) events is needed for the extraction of elastic/inelastic cross sections. Therefore the selected data sample, called *diffractive sample*, was split in two disjoint subsamples: the *tagged sample*, where the forward tag from Eq. (6.17) was required and the *untagged sample* where the forward tag was used as veto. The subsamples are also corrected for acceptance and efficiency effects.

It is obvious, that the sum of tagged (N_{tag}) and untagged (N_{untag}) events has to be equal to the total number of diffractive events (N_{obs}). For the dipion mass spectra this is guaranteed by construction. But the number of resonant ρ^0 ($N_{\text{obs}}^{\text{res}}$) is extracted from a fit result. The sum of

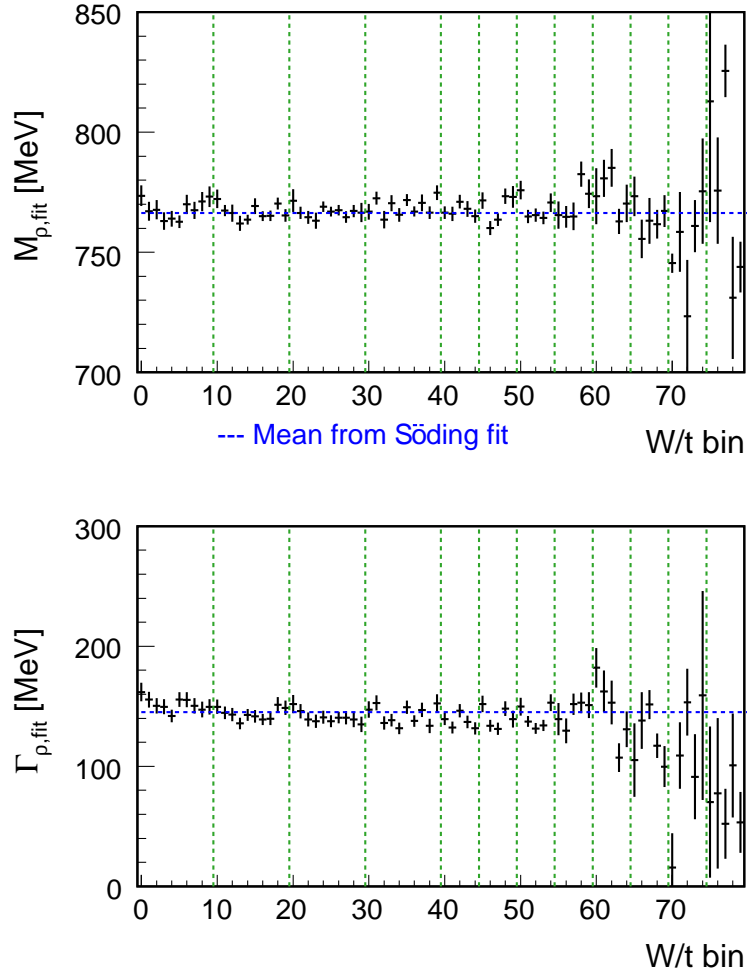


Figure 8.3: The fitted mass and width of the ρ^0 for each W/t -bin within the Söding ansatz. The horizontal lines represents the ρ^0 parameters from the integrated fit from Fig. 8.1(a).

tagged resonant ρ^0 events ($N_{\text{tag}}^{\text{res}}$) and untagged resonant ρ^0 ($N_{\text{untag}}^{\text{res}}$) has to be equal to $N_{\text{obs}}^{\text{res}}$ as well, which is not given if the number of tagged (untagged) resonant ρ^0 is obtained by fitting the tagged (untagged) sample.

$$N_{\text{obs}}^{\text{(res)}} = N_{\text{tag}}^{\text{(res)}} + N_{\text{untag}}^{\text{(res)}} \quad (8.3)$$

To meet this constraint nevertheless, the relative fraction of tagged f_{tag} and untagged f_{untag} events with respect to the diffractive sample is determined from the dipion mass spectra by counting the events in the mass range $0.6 < m_{\pi\pi} [\text{GeV}] < 1.1$. The obtained fractions are shown in Fig. 8.4.

$$f_{\text{tag}} = \frac{N_{\text{tag}}}{N_{\text{tag}} + N_{\text{untag}}} \quad , \quad f_{\text{untag}} = \frac{N_{\text{untag}}}{N_{\text{tag}} + N_{\text{untag}}} \quad (8.4)$$

Under the assumption that the mass shape fit to determine the number of resonant events is independent of the forward tag requirement, the fraction of tagged (untagged) ρ^0 is equal to the fraction of tagged (untagged) resonant ρ^0 . Hence it is sufficient to extract the number of resonant ρ^0 for the diffractive sample by fitting the mass shape and determine $N_{\text{tag}}^{\text{res}}$ and $N_{\text{untag}}^{\text{res}}$ from the fractions f_{tag} and f_{untag} respectively.

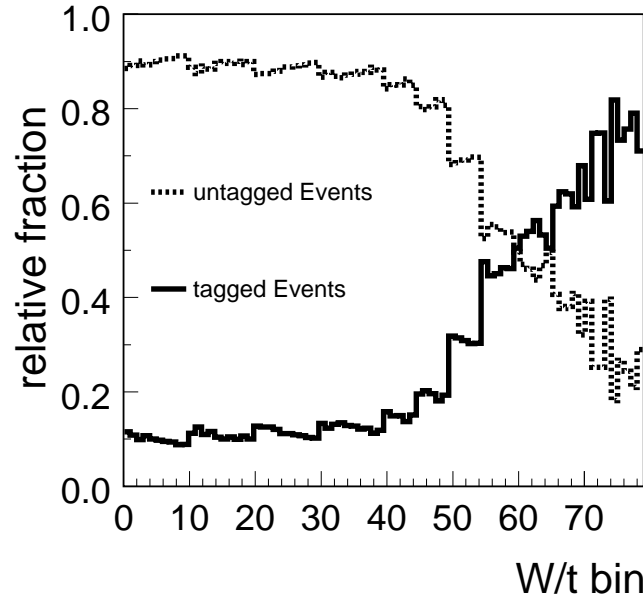


Figure 8.4: The relative fraction of tagged (untagged) events w.r.t. the diffractive sample is shown as solid (dashed) line.

Proton dissociative events where the forward tag is missing due to inefficiencies in the FTS or FMD are considered in the tagging probability ε_{pd} , just as elastic events have a certain probability ε_{el} to be tagged. With these tagging probabilities, the number of tagged and untagged events can be expressed as

$$N_{\text{tag}} = \varepsilon_{\text{el}} \cdot N_{\text{el}} + \varepsilon_{\text{pd}} \cdot N_{\text{pd}} \quad (8.5)$$

$$N_{\text{untag}} = (1 - \varepsilon_{\text{el}}) \cdot N_{\text{el}} + (1 - \varepsilon_{\text{pd}}) \cdot N_{\text{pd}} \quad (8.6)$$

with N_{el} and N_{pd} the true number of elastic and proton-dissociative events. The tagging probabilities are determined for each t -bin from Monte Carlo studies and are given in Fig. 6.30. The tagging probabilities for the two subdetectors as stand-alone tag are also drawn. The tagging probability for the elastic MC arises from the scattered proton hitting the beam pipe which is more likely at higher t values and further away from the primary interaction zone. This is reflected in the larger sensitivity of the FTS and the rise of the tagging probability towards higher t values. The proton dissociative system interacts with the beam pipe and the emerging final state is mainly detected in

the FMD. The FMD becomes more and more efficient as the transverse momentum of the ρ^0 , and thus also of the proton, becomes large.

From Eq. (8.5) and (8.6) N_{el} can be written as

$$N_{\text{el}} = \frac{N_{\text{untag}} + N_{\text{tag}} \cdot \left(1 - \frac{1}{\varepsilon_{\text{pd}}}\right)}{\left(1 - \frac{\varepsilon_{\text{el}}}{\varepsilon_{\text{pd}}}\right)} = N_{\text{obs}} \cdot \frac{\varepsilon_{\text{pd}} - f_{\text{tag}}}{\varepsilon_{\text{pd}} - \varepsilon_{\text{el}}}, \quad (8.7)$$

The statistical error on N_{el} is calculated with error propagation according to

$$(\delta N_{\text{el}})^2 = \left[\frac{(\delta N_{\text{untag}})^2 + \left[\left(\frac{(\delta N_{\text{tag}})}{N_{\text{tag}}} \right)^2 + \frac{\left(\frac{(\delta N_{\text{tag}})}{N_{\text{tag}}} \right)^2}{(1 - 1/\varepsilon_{\text{pd}})^2} \right] \cdot (N_{\text{tag}}(1 - 1/\varepsilon_{\text{pd}}))^2}{N_{\text{untag}} + (N_{\text{tag}}(1 - 1/\varepsilon_{\text{pd}}))^2} + \frac{\left[\left(\frac{\delta \varepsilon_{\text{el}}}{\varepsilon_{\text{el}}} \right)^2 + \left(\frac{\delta \varepsilon_{\text{pd}}}{\varepsilon_{\text{pd}}} \right)^2 \right] \left(\frac{\varepsilon_{\text{el}}}{\varepsilon_{\text{pd}}} \right)}{(1 - \varepsilon_{\text{el}}/\varepsilon_{\text{pd}})^2} \right] \cdot (N_{\text{el}})^2 \quad (8.8)$$

The number of inelastic events N_{pd} is obtained similarly, in Eq. (8.7) the ε_{pd} and ε_{el} have to be exchanged:

$$N_{\text{pd}} = N_{\text{obs}} \cdot \frac{\varepsilon_{\text{el}} - f_{\text{tag}}}{\varepsilon_{\text{el}} - \varepsilon_{\text{pd}}}. \quad (8.9)$$

If the tagging fraction f_{tag} is larger than the proton dissociative tagging probability ε_{pd} , the extracted number of elastic events N_{el} from Eq. (8.7) is negative. In that case the number of elastic events is set to zero ($N_{\text{el}} = 0$) to avoid negative elastic cross sections and all observed events in the W/t -bin are interpreted as proton dissociative ρ^0 events: $N_{\text{pd}} = N_{\text{obs}}$.

A negative proton dissociative cross section is obtained if the tagging fraction becomes smaller than the elastic tagging probability in Eq. (8.9) as long as $\varepsilon_{\text{pd}} > \varepsilon_{\text{el}}$. In Fig. 8.5 the tagging probabilities are given with the tagging fraction. For $t > 1 \text{ GeV}^2$ the tagging fraction can be larger than the proton dissociative tagging probability while the elastic tagging probability is not observed to be lower than f_{tag} .

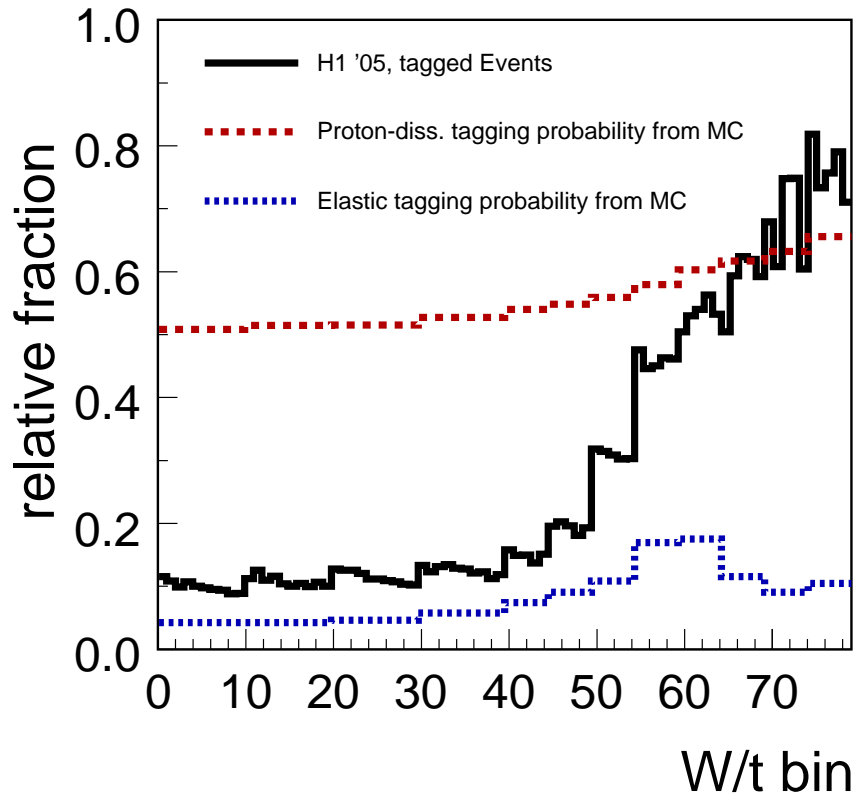


Figure 8.5: The tagging fraction f_{tag} (solid line) together with the tagging probabilities ε_{el} and ε_{pd} . To avoid negative elastic cross section, the tagging fraction has to be larger than the proton dissociative tagging probability. For large $|t|$ values, this is not the case and all observed events in the corresponding bin are treated as proton-dissociative ρ^0 events. Negative proton dissociative cross sections are not encountered.

8.3 Differential Cross Sections

To extract the γp cross section, the ep cross section is divided by the photon flux factor for the corresponding $W_{\gamma p}$ range as introduced in Sect. 2.2. The differential γp cross section is then obtained by

$$\frac{d\sigma_{\gamma p}(\bar{W})}{dt} = \frac{N_{\text{resonant}}^{\text{fit}}}{\int \mathcal{L} \cdot \Delta t \cdot \Delta W \cdot \Phi_{\gamma p}} \quad (8.10)$$

where $N_{\text{resonant}}^{\text{fit}}$ is the number of resonant ρ^0 for the diffractive ($N_{\text{obs}}^{\text{res}}$), elastic (N_{el}) or inelastic (N_{pd}) process, $\int \mathcal{L}$ is the integrated luminosity, Δt and ΔW are the width in t and $W_{\gamma p}$ respectively and $\Phi_{\gamma p}$ is the photon flux factor integrated up to $Q^2 = 4 \text{ GeV}^2$.

The cross sections for all three processes are calculated in each W/t -bin for both mass shape fit methods. In Fig. 8.6 the cross section for the diffractive process for each W/t -bin is shown for the Ross-Stodolsky model and in Fig. 8.7 for the Söding ansatz.

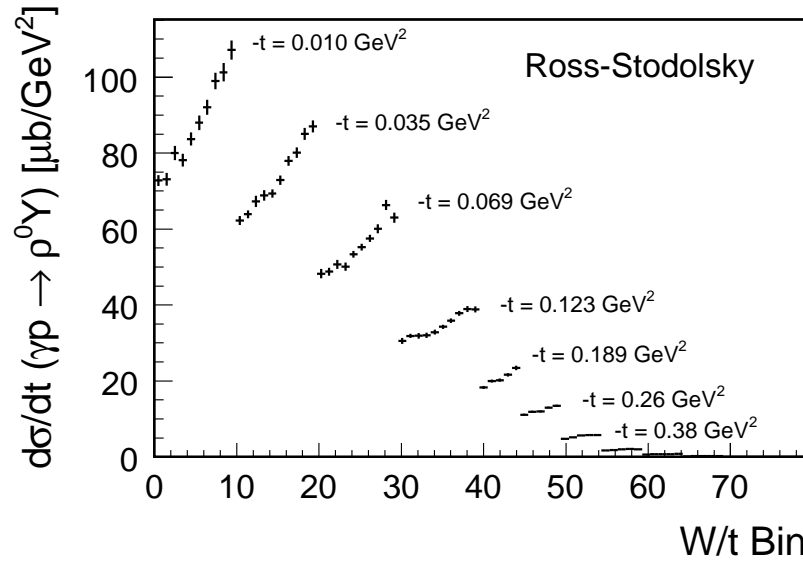


Figure 8.6: Differential cross sections determined in each W/t -bin for the Ross-Stodolsky model.

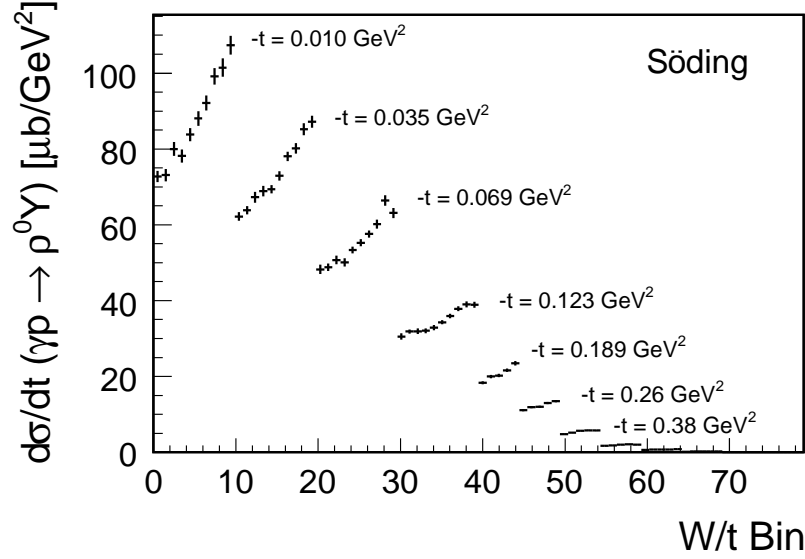


Figure 8.7: Differential cross sections determined in each W/t -bin for the Söding ansatz.

The ratio of the results is given in Fig. 8.8. As can be seen both methods yield compatible results.

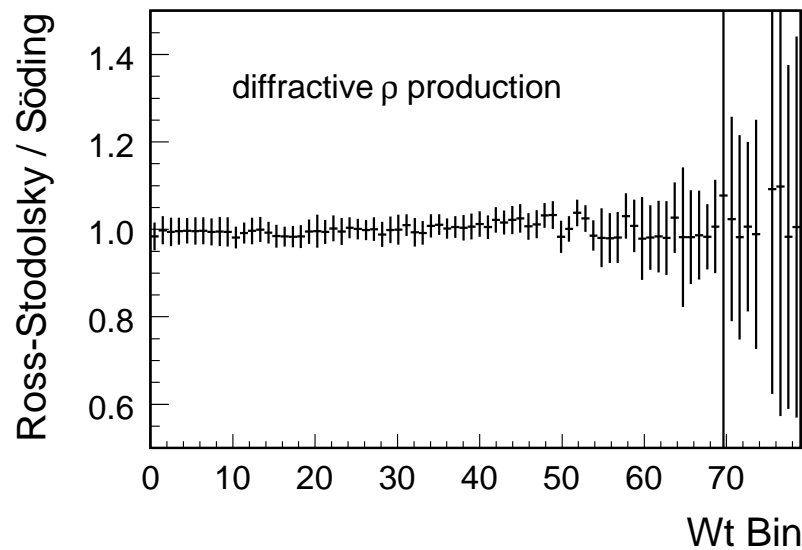


Figure 8.8: The ratio of the cross section determined in each W/t -bin for the Ross-Stodolsky model (Fig. 8.6) and the Söding ansatz (Fig. 8.7).

The 80 W/t -bins yield also 80 double differential cross sections, each of them representing a single point in the $W_{\gamma p}$ - t plane. The mean W and mean t value for each W/t -bin is calculated as follows:

- t bin center

The mean t value for each of the 12 chosen bins is determined by the requirement

$$e^{-b \cdot t_{\text{mean}}} \stackrel{!}{=} \frac{1}{t_{\text{high}} - t_{\text{low}}} \int_{t=t_{\text{low}}}^{t_{\text{high}}} e^{-b \cdot t} dt \quad (8.11)$$

with t_{low} and t_{high} being the lower and upper bin edge respectively and b the slope of the exponential fall-off. The resulting bin center is then

$$t_{\text{mean}} = t_{\text{low}} + \frac{1}{b} \cdot \log(b \cdot \Delta t) - \log(1 - e^{-b \cdot \Delta t}) \quad (8.12)$$

with $b = 10 \text{ GeV}^{-2}$.

- $W_{\gamma p}$ bin center

The bin widths for the $W_{\gamma p}$ bins are small enough to approximate the bin center in $W_{\gamma p}$ by the arithmetic mean of the bin edges to sufficient precision.

All measured differential γp cross sections are plotted in Fig. 9.1 - 9.3, separately for the diffractive, elastic and proton-dissociative process and listed in the appendix A.

8.4 Systematic Uncertainties

Besides the statistical error, the result also has a systematic uncertainty. For this analysis 20 different systematic variations grouped in 4 classes are investigated. The following list summarizes the 4 classes and 20 variations considered.

A: The $W_{\gamma p}$ and t dependence of the simulated ρ^0 photoproduction cross section is varied by altering the parameters of the pomeron trajectory from Table 3.2 in Eq. (3.8).

- (1) Increase the pomeron intercept ε_0 by 0.04
- (2) Decrease the pomeron intercept ε_0 by 0.04
- (3) Increase the pomeron slope $\alpha'_0 =$ by 0.25 GeV^{-2}
- (4) Decrease the pomeron slope $\alpha'_0 =$ by 0.25 GeV^{-2}
- (5) Increase the t -slope parameter b_0 by 10%
- (6) Decrease the t -slope parameter b_0 by 10%

B: The MC parameters for the reweighting function of the FTT efficiency from Table 7.1 are varied according to:

- (7) Increase the p_T dependence $A_1 = 200$
- (8) Decrease the p_T dependence $A_1 = 400$
- (9) Increase the depth at $\theta = 90^\circ$ $A_2 = 2.5 \cdot 10^5$
- (10) Decrease the depth at $\theta = 90^\circ$ $A_2 = 5.0 \cdot 10^5$
- (11) Shift the position of the θ dip towards smaller θ $A_5 = 85$
- (12) Shift the position of the θ dip towards larger θ $A_5 = 95$

The FTT single track efficiency for the varied systematic checks are summarized in Fig. 8.9.

- C: The tagging probabilities for the FTS and FMD are altered. For the FMD the additional inefficiency is varied (default value 40%). For the FTS the overall description of the hit - no hit distribution is reweighted either globally for all events with the same factor or differentially in each t bin. Additionally the reweighting factor for the refined MC simulation is applied or not.

This class only applies to the elastic and proton dissociative results as the diffractive results do not use the forward detector information.

- (13) Decrease the additional inefficiency of the FMD to 30%
- (14) Increase the additional inefficiency of the FMD to 50%
- (15) reweight the FTS response globally
- (16) reweight the FTS response in t bins
- (17) reweight the FTS response globally and correct for the refined MC simulation
- (18) reweight the FTS response in t bins and correct for the refined MC simulation

- D: The diffVM generator describes the M_Y dependence as $1/M_Y^{2(1+\epsilon)}$ behavior (Eq. (3.6)) and is altered according to

$$f_{M_Y}(M_Y) = N_{M_Y} \cdot \left(\frac{M_Y^2}{M_{Y,0}^2} \right)^\delta \quad (8.13)$$

with $N_{M_Y} = 1$ as normalization factor, $M_{Y,0} = 5$ GeV a scaling factor and δ the slope of the alteration. The distribution is reweighted by $(1/M_Y^2)^{\pm 0.15}$ [80].

- (19) Set the slope to $\delta = +0.15$
- (20) Set the slope to $\delta = -0.15$

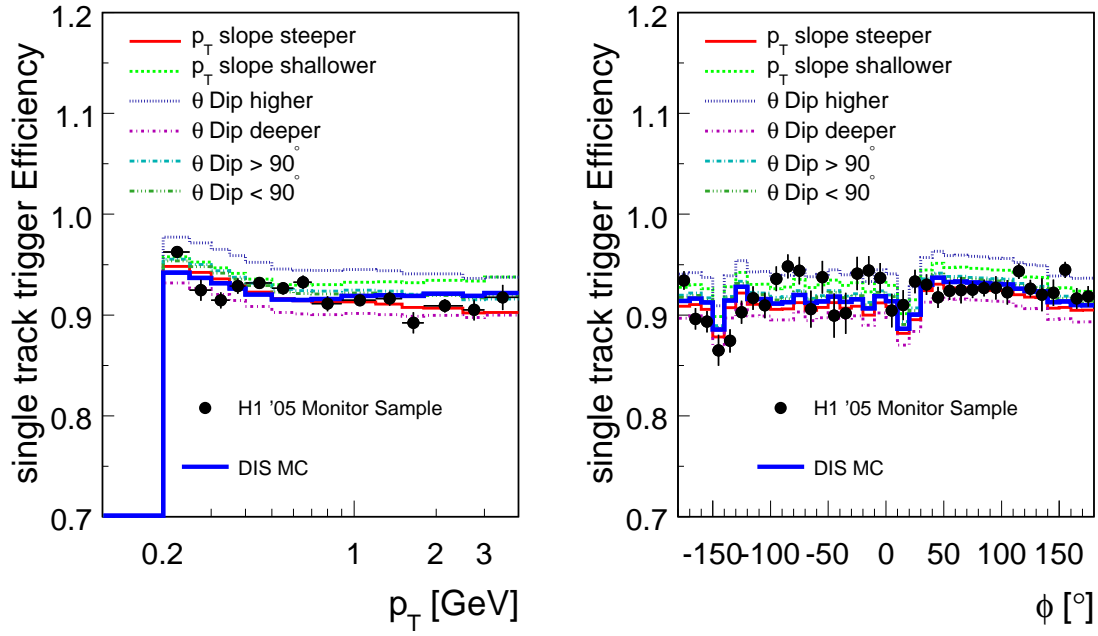
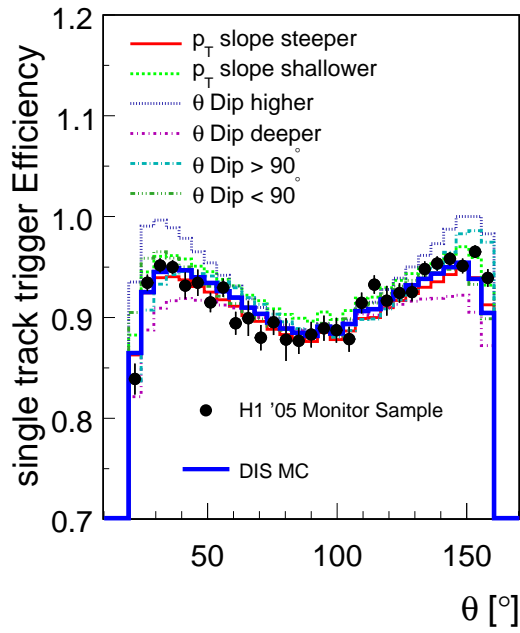
(a) p_T Efficiency(b) ϕ Efficiency(c) θ Efficiency

Figure 8.9: Efficiency of the FTT subtrigger elements as function of p_T , ϕ and θ for the systematic checks (7) - (12). The default value for MC is shown as solid line.

For each systematic check, the corresponding variation is applied and the entire analysis repeated. The results are compared to the default values and the difference is taken as systematic error for the corresponding check. The systematic error for each check is shown in Fig. 8.10 for the elastic cross section $d\sigma^{\gamma p}/dt$ for one W/t -bin.

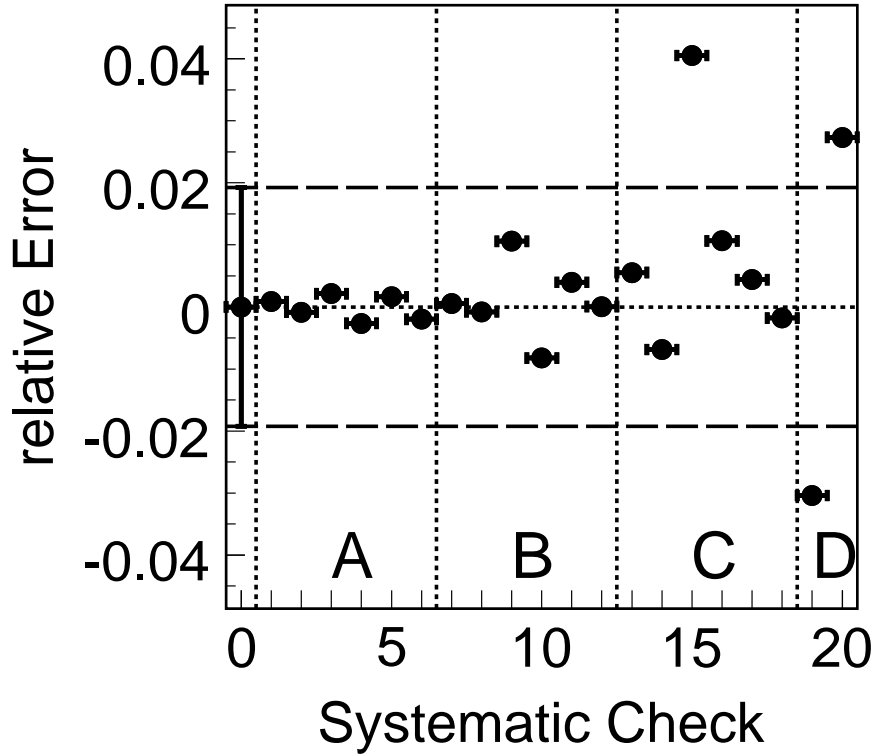


Figure 8.10: Relative difference of $d\sigma^{\gamma p}/dt$ for the elastic process for each systematic check in the W/t -bin ($t = -0.123 \text{ GeV}^2$, $W_{\gamma p} = 43 \text{ GeV}$). The first entry to the left (0) represents the default value with the statistical error (horizontal dashed lines). Most systematic uncertainties yield deviations well below the statistical error. The vertical dashed lines indicate the classes A - D.

The deviations are not necessarily symmetric w.r.t. to the default value. The deviations for the pomeron checks (1-4) and the FTT variations (7-12) are symmetrized, all other deviations are left with the asymmetric structure. The symmetrizing is done by assigning the larger deviation of two corresponding checks¹ with the appropriate sign to both checks.

For each systematic class the total systematic error is computed. The positive and negative contributions are treated separately resulting in asymmetric systematic errors. The individual checks

¹Corresponding checks are the variation of a single parameter, i.e. (1) and (2).

within a class are combined according to the following scheme:

- A: The pomeron checks (1-4) are added in quadrature. The error from the t slope checks (5,6) are added in quadrature to the corresponding positive or negative error-sum from the pomeron checks.
- B: All six checks (7-12) are added in quadrature separately for positive and negative contributions.
- C: The largest and smallest error from the checks on the FTS (15-18) is added in quadrature with the corresponding largest and smallest error from the FMD checks (13-14). If i.e. all systematic checks on the forward region yield positive deviations, only the two largest deviations from the FTS and FMD are added in quadrature for the positive error while the negative error is set to zero.
- D: The two deviations are either added in quadrature or assigned to the corresponding signed error for the class.

The following uncertainties affect only the overall normalization and are therefore only applied to the determination of the differential cross sections:

- The uncertainty on the luminosity measurement is 1.5%;
- The uncertainty on the track reconstruction efficiency is 1.5% per track, 3% in total;
- The uncertainty on the overall normalization of the FTT track triggering efficiency is 1.5% per track, 3% overall;
- The uncertainty on the background contributions is 2%.

All uncertainties are added in quadrature and added symmetrically to the total systematic error of the differential cross sections.

The individual contributions to the systematic uncertainty are shown in Fig. 8.11 for the differential cross section for elastic ρ^0 photoproduction for eight selected W/t -bins. The contributions for the t slope and the pomeron checks are given separately.

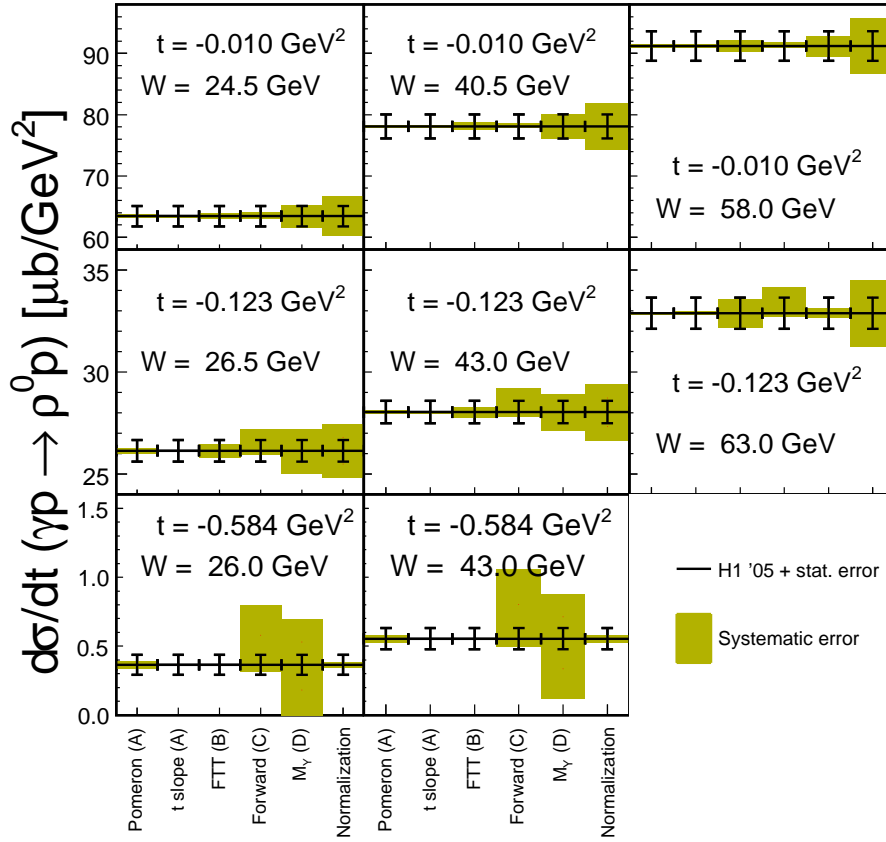


Figure 8.11: The systematic class errors (shaded area) for the elastic cross section of ρ^0 mesons for eight selected W/t -bins. The contributions from the pomeron variation (1-4) and the t slope (5, 6) are shown separately. The error bars give the statistical error on the corresponding W/t -bin and the shaded area is the systematic uncertainty arising from the respective class.

At low $|t|$ values the overall normalization is the dominant contribution while for larger $|t|$ values the uncertainty of the M_Y description is dominating. For large $|t|$ values, the number of elastic events is rather small compared to the proton dissociative events and hence the extraction of the elastic cross section is predominantly given by the tagging probabilities. And these probabilities have a strong dependence on the M_Y description as shown in Sect. 6.6 leading to this behavior of the systematic error.

The systematic errors from the four classes and the normalization uncertainty are added in quadrature to compute the total systematic error. In Fig. 8.12 the elastic cross section from Fig. 8.6 is shown with the systematic error added as shaded area.

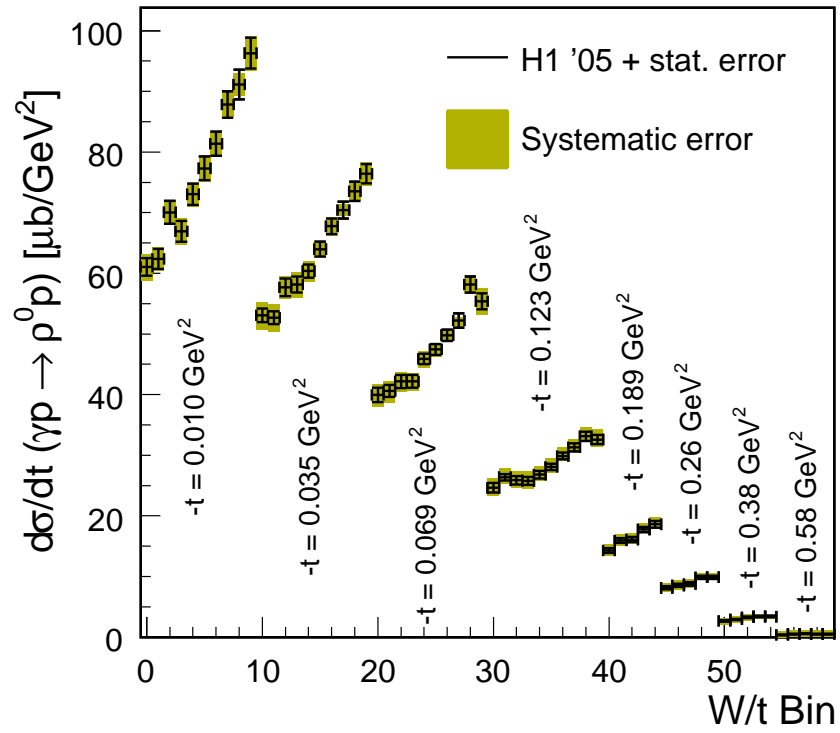


Figure 8.12: The total systematic error (shaded are) for the diffractive cross section of elastic ρ^0 meson photoproduction for all elastic W/t -bins.

Chapter 9

Results

The differential photoproduction cross section for diffractive ρ^0 photoproduction $\gamma p \rightarrow \rho^0 p$ is measured in the kinematic range $x_{\mathbb{P}} < 0.01$ and $Q^2 < 4 \text{ GeV}^2$ from a data sample collected at the H1 experiment using the new Fast Track Trigger.

The diffractive ρ^0 photoproduction shown in Fig. 9.1 is determined for 12 t value between $|t| > 0 \text{ GeV}^2$ and $|t| < 3 \text{ GeV}^2$ over a $W_{\gamma p}$ range of 20 (23) GeV - 69 (90) GeV for the first (last) t value.

Additionally the differential photoproduction cross section for the elastic ρ^0 photoproduction $\gamma p \rightarrow \rho^0 p$ and the proton dissociative ρ^0 photoproduction $\gamma p \rightarrow \rho^0 Y$ are determined using the forward detectors FTS and FMD.

Fig. 9.2 shows the elastic ρ^0 photoproduction cross sections for eight t values between $|t| > 0 \text{ GeV}^2$ and $|t| < 0.7 \text{ GeV}^2$ over a $W_{\gamma p}$ range of 20 (23) GeV - 69 (77) GeV for the first (last) t value. The data is compared to previous measurements of H1 [19], the Omega spectrometer collaboration [79] and the ZEUS collaboration [53, 81]. The measured cross sections from the other experiments were corrected to the closest t value of this measurement using the t dependence as measured by the respective experiment. The cross section from the Omega collaboration were extracted with a different definition of the ρ^0 cross section, they used the convention of Spital and Yennie [78] which yields a 5% larger cross section than the ones derived in this analysis. This correction was also taken in to account for the comparison.

And finally the differential cross section for the proton dissociative photoproduction $\gamma p \rightarrow \rho^0 Y$ is given in Fig. 9.3.

All cross sections belonging to the same t value are furthermore fitted to the form

$$\frac{d\sigma^{\gamma p}(W)}{dt} = \frac{d\sigma^{\gamma p}(W_0)}{dt} \left(\frac{W}{W_0} \right)^{4[\alpha(t)-1]}, \quad (9.1)$$

with $W_0 = 37 \text{ GeV}$ the mean $W_{\gamma p}$ value for this analysis. For the elastic process, the fit parameter $\alpha(t)$ corresponds to the value of the pomeron trajectory for the respective t value $\alpha(t) = \alpha_{\mathbb{P}}(t)$.

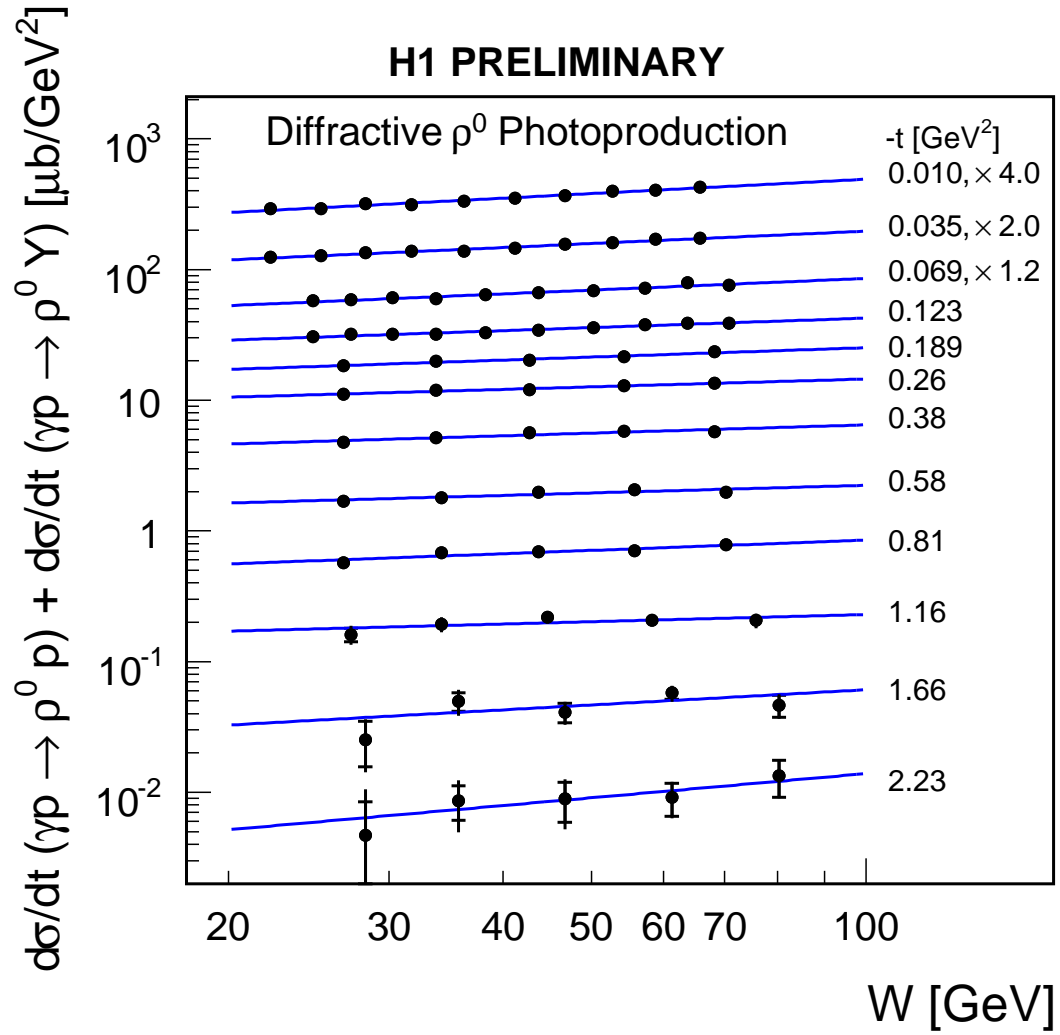


Figure 9.1: The measured differential γp cross section for diffractive ρ^0 photoproduction for 12 $|t|$ values. The inner error bars indicate the statistical error, the outer ones the statistical and systematic uncertainty added in quadrature. The solid lines show the result of a fit $\frac{d\sigma^{\gamma p}}{dt} = a (W/W_0)^{4[\alpha(t)-1]}$ to the data of this analysis.

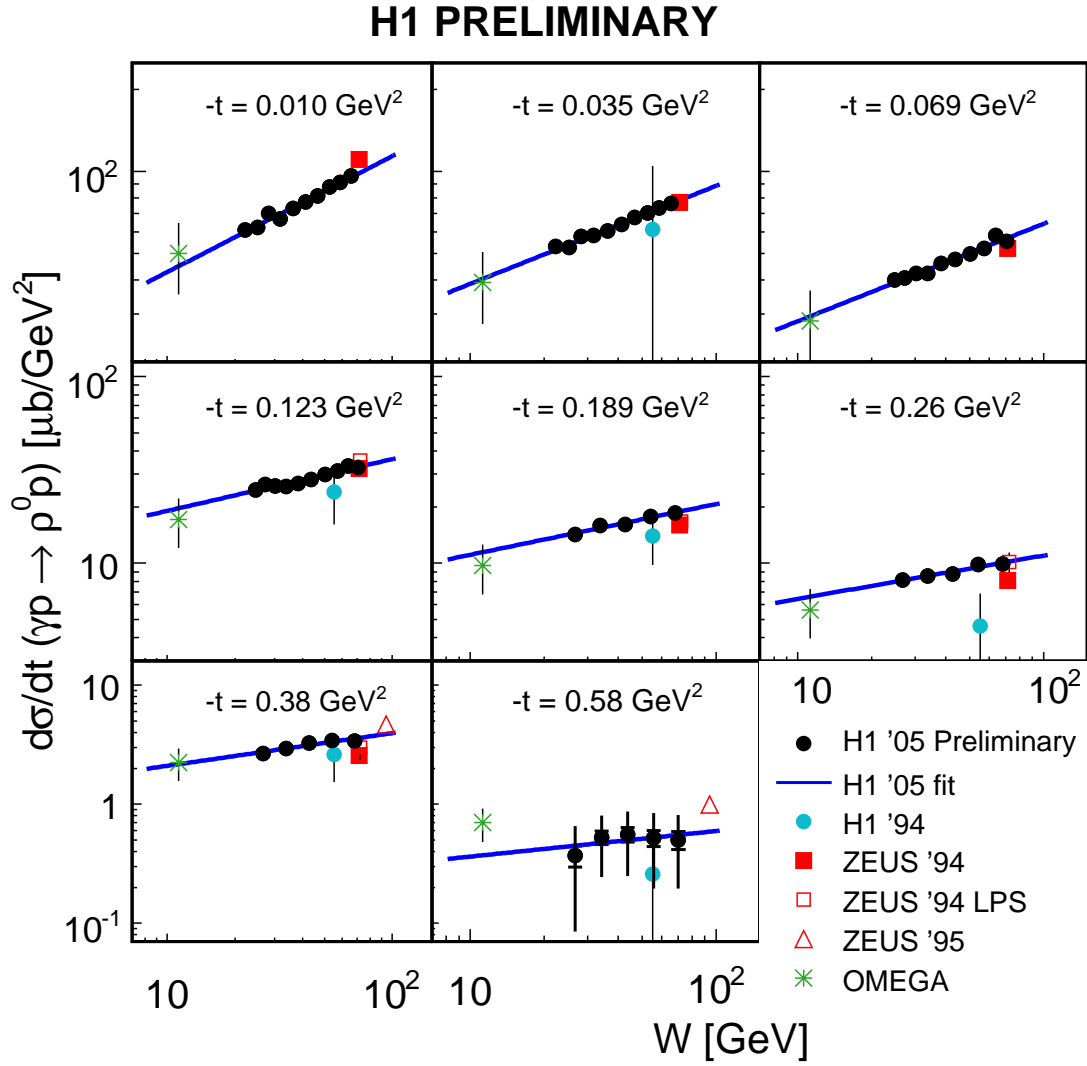


Figure 9.2: The differential γp cross section for elastic ρ^0 photoproduction for the eight $|t|$ values where it was measured. The inner error bars indicate the statistical error, the outer ones the statistical and systematic uncertainty added in quadrature. The measured cross sections are compared to results of previous measurements from the H1 [19], ZEUS [53, 81] and OMEGA collaborations [79]. The solid lines show the result of a fit $d\sigma^{\gamma p}/dt = a (W/W_0)^{4[\alpha(t)-1]}$ to the data of this analysis and is extrapolated for a better comparison.

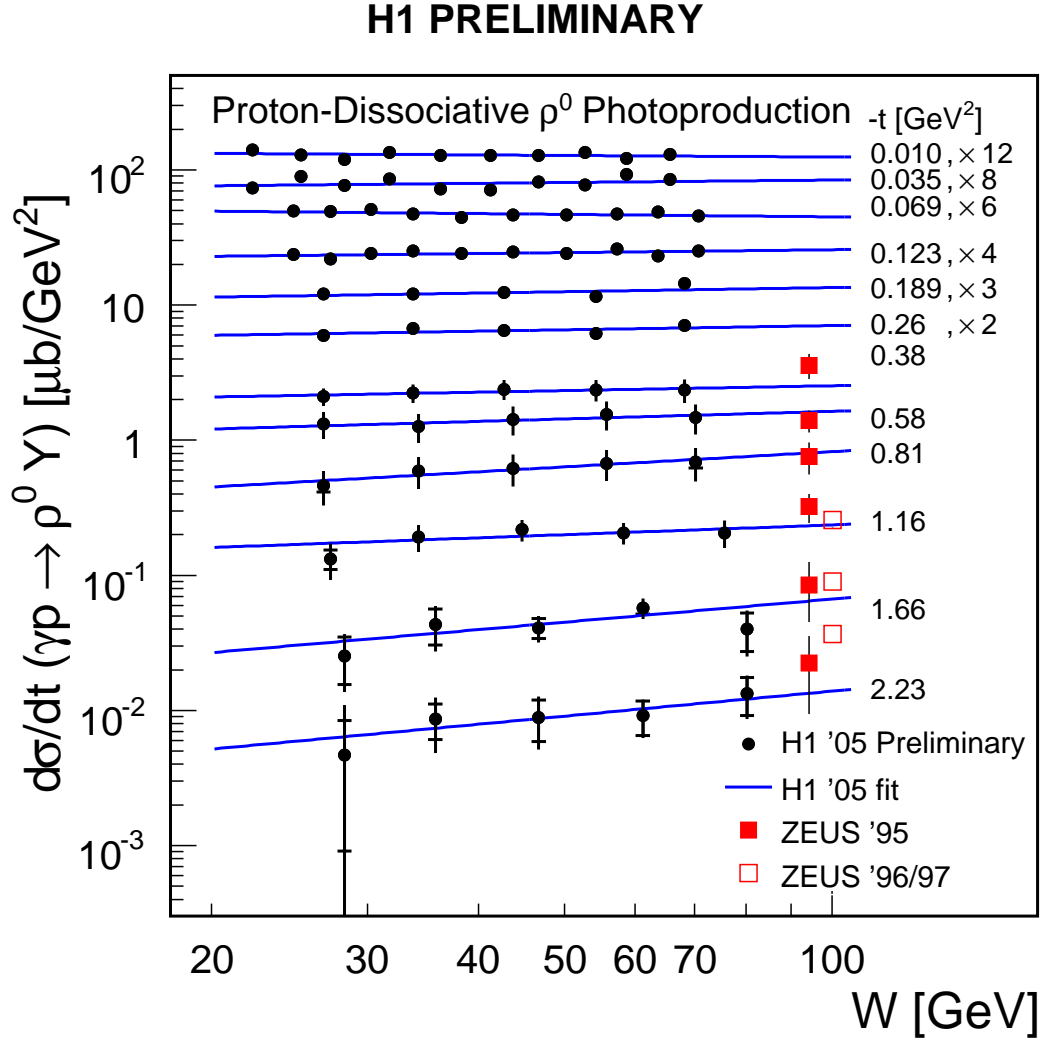


Figure 9.3: The measured differential γp cross section for proton dissociative ρ^0 photoproduction in the range $x_{\mathbb{P}} = (M_Y^2 + Q_{\text{gen}}^2)/(W_{\gamma p}^2 + Q_{\text{gen}}^2) < 0.01$, for 12 $|t|$ values. The inner error bars indicate the statistical error, the outer ones the statistical and systematic uncertainty added in quadrature. The measured cross sections are compared to most recent results from the ZEUS collaboration [81,82]. The inner error bars indicate the statistical error, the outer ones the statistical and systematic uncertainty added in quadrature.

The measured values of the $W_{\gamma p}$ slopes $\alpha(t)$ for the elastic ρ^0 photoproduction are plotted in Fig. 9.4.

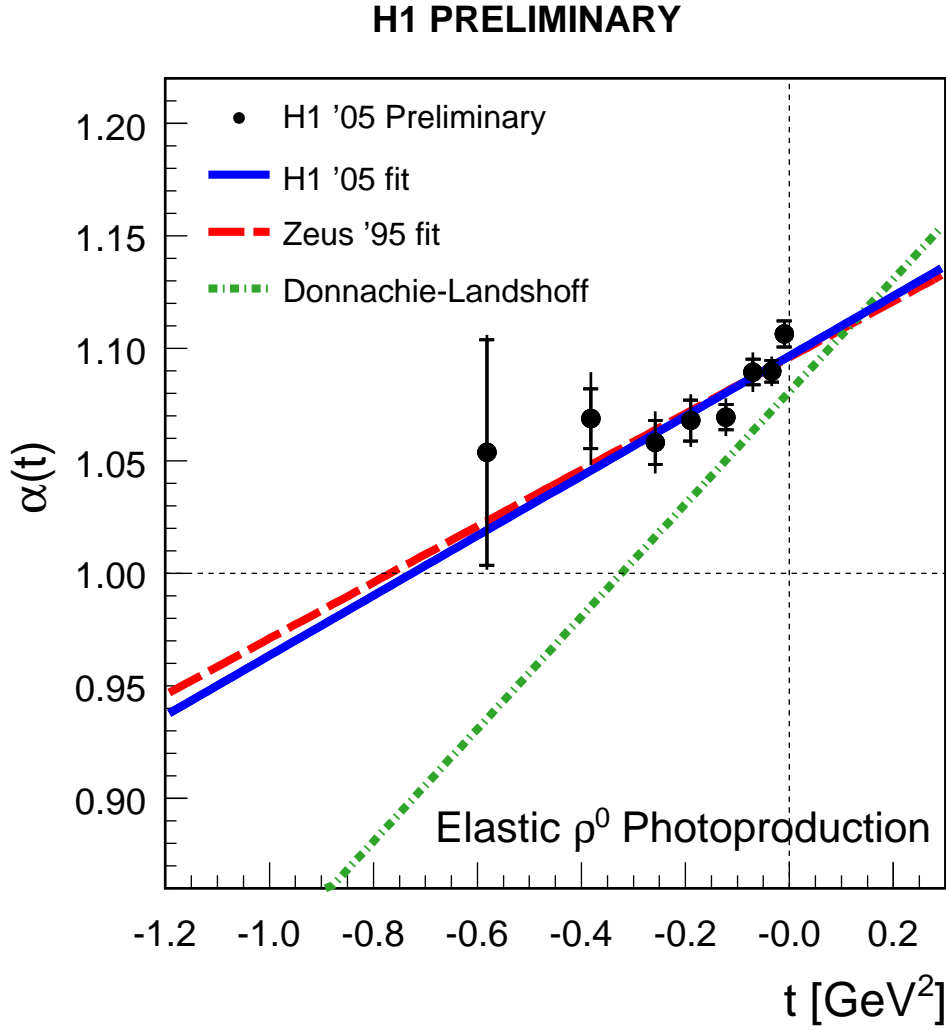


Figure 9.4: Measured $W_{\gamma p}$ slopes for elastic ρ^0 photoproduction (solid dots). The inner error bars indicate the statistical error, the outer ones the statistical and systematic uncertainty added in quadrature. A linear fit to the data yields the pomeron trajectory to be $\alpha_{\mathbb{P}}(t) = 1.097^{+0.009}_{-0.009} + (0.133^{+0.043}_{-0.053}) \text{ GeV}^{-2} \cdot t$. The pomeron trajectory determined by the ZEUS collaboration [81] and the prediction from Donnachie-Landshoff [35] are also shown.

The pomeron trajectory is extracted by fitting the observed $W_{\gamma p}$ slopes to a straight line. The obtained result is

$$\alpha_{\mathbb{P}}(t) = 1.097 \pm 0.004 (stat)_{-0.008}^{+0.008} (sys) + (0.133 \pm 0.027 (stat)_{-0.046}^{+0.033} (sys)) \text{ GeV}^{-2} \cdot t \quad (9.2)$$

The measurement performed by the ZEUS collaboration [81] yielded for the pomeron trajectory

$$\alpha_{\mathbb{P}}(t) = 1.096 \pm 0.021 + (0.125 \pm 0.038) \text{ GeV}^{-2} \cdot t. \quad (9.3)$$

The result presented in this analysis is in excellent agreement to the ZEUS results and supports the observation of a significantly smaller slope $\alpha'_{\mathbb{P}}$ of the pomeron trajectory derived from elastic ρ^0 photoproduction than the value of $\alpha'_{\mathbb{P}} = 0.25 \text{ GeV}^{-2}$ derived from hadron scattering [83, 84].

The energy dependence of the cross section $d\sigma^{\gamma p}/dt$ for the diffractive and proton dissociative ρ^0 photoproduction is extracted as well and the effective $W_{\gamma p}$ slopes are summarized in Fig. 9.5 and Fig. 9.6 respectively.

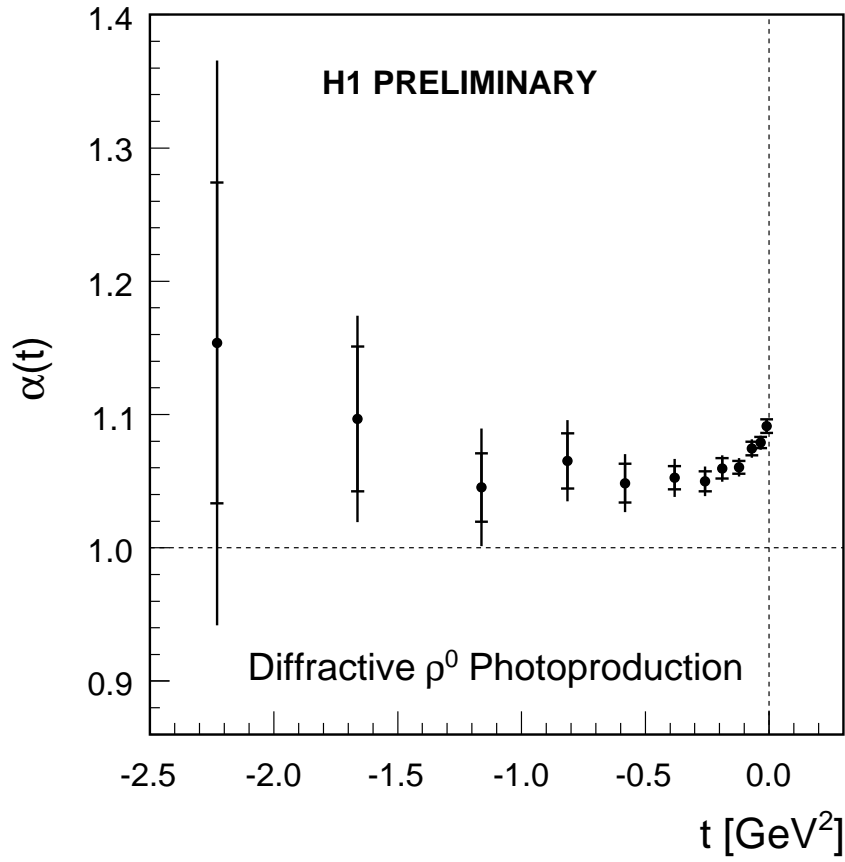


Figure 9.5: The $W_{\gamma p}$ slopes for the diffractive ρ^0 photoproduction as measured from a fit of the form $d\sigma/dt = a(W/W_0)^{4[\alpha(t)-1]}$ to the corresponding cross sections determined in this analysis. The inner error bars indicate the statistical error, the outer ones the statistical and systematic uncertainty added in quadrature.

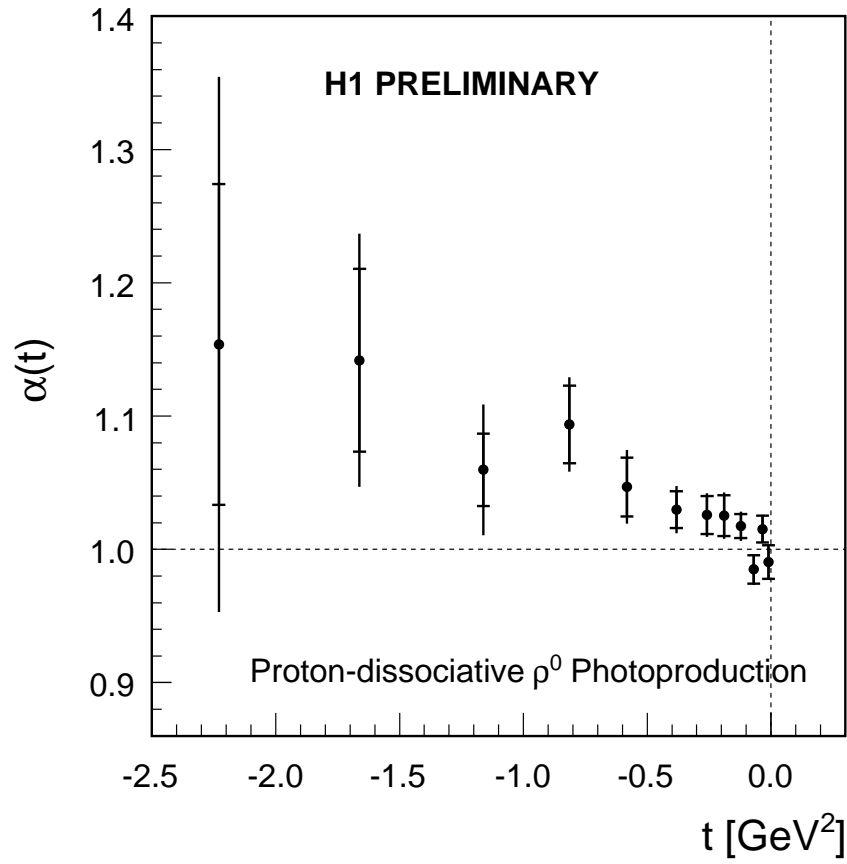


Figure 9.6: The $W_{\gamma p}$ slopes for the proton-dissociative process as measured from a fit of the form $d\sigma/dt = a(W/W_0)^{4[\alpha(t)-1]}$ to the corresponding cross sections determined in this analysis.

9.1 Systematic Uncertainties for the $W_{\gamma p}$ Slopes and the Pomeron Trajectory

The systematic errors were obtained as described in Sect. 8.4 as for each of the 20 systematic checks the full analysis is repeated. The differences of the resulting $W_{\gamma p}$ slopes and parameters of the pomeron trajectories are combined in the same way as for the differential cross sections.

For the energy dependence of the elastic ρ^0 cross section the systematic class errors for all eight $|t|$ values is shown in Fig. 9.7.

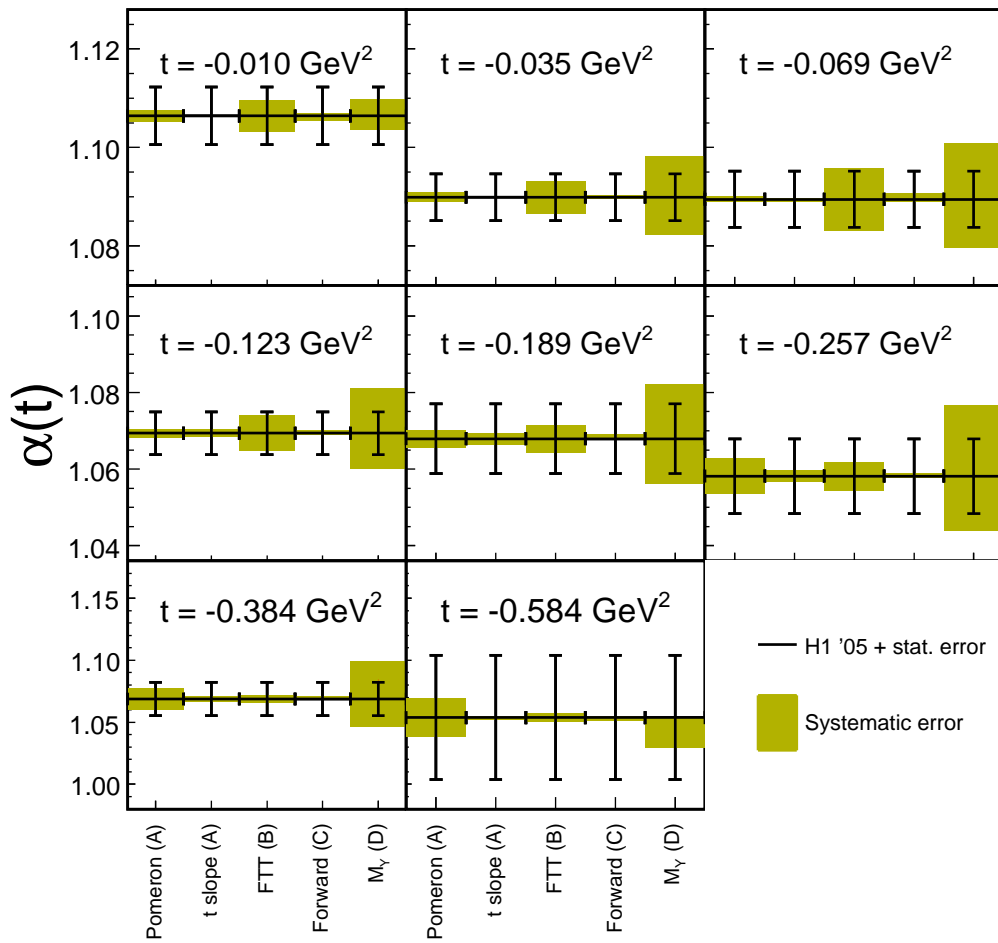


Figure 9.7: The systematic errors for the $W_{\gamma p}$ dependence of the elastic cross section for each systematic class. The statistical error for each $|t|$ value is indicated by the error bar and the systematic error added as shaded area.

The systematic class errors for each $|t|$ values is added in quadrature and yields the total systematic errors for the respective $|t|$ values, Fig. 9.8.

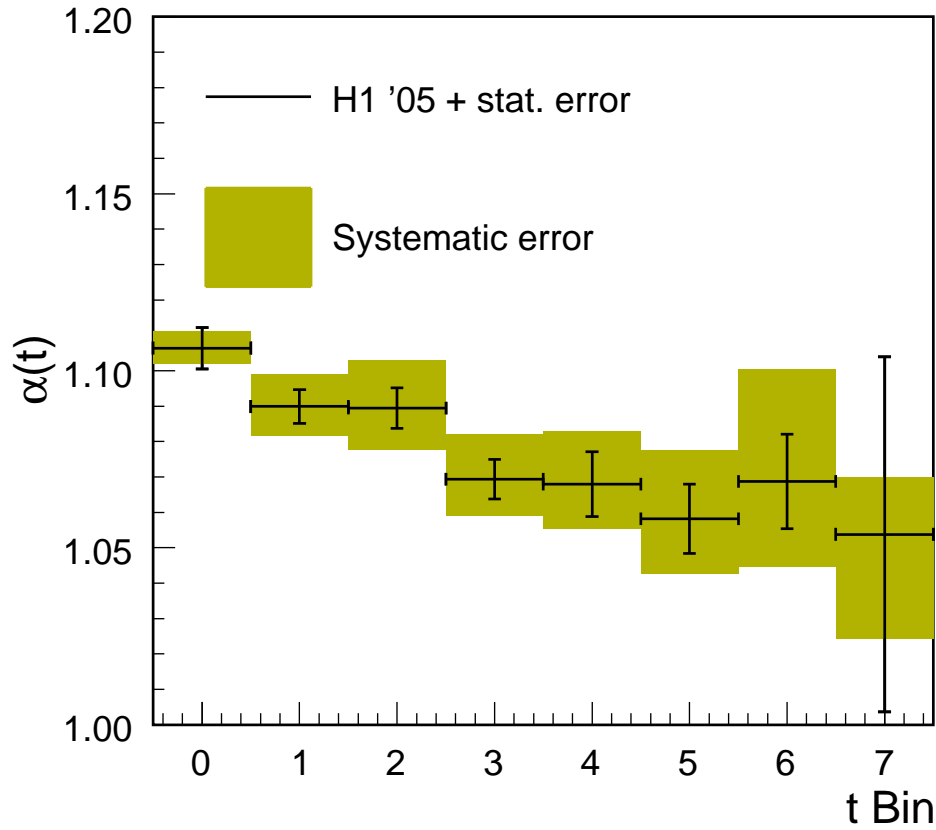


Figure 9.8: The systematic errors for the $W_{\gamma p}$ dependence of the total systematic error. The statistical error for each $|t|$ value is indicated by the error bar and the systematic error added as shaded area.

Using the same procedure, the systematic class errors for the pomeron trajectory parameter α_0 and α' are extracted, Fig. 9.9.

The total systematic uncertainty for the pomeron trajectory is given with the result in Eq. 9.2.

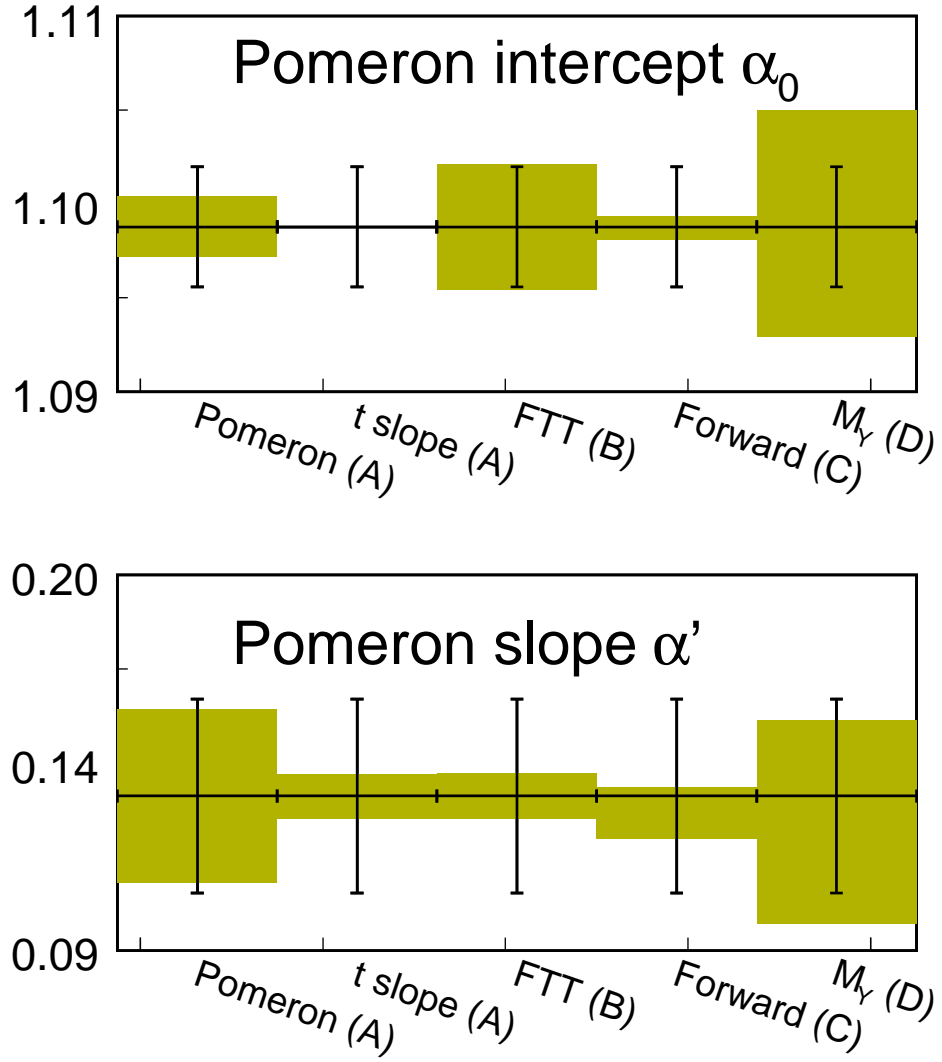


Figure 9.9: The systematic errors for the parameters of the pomeron trajectory as measured in the elastic ρ^0 photoproduction for each systematic class. The statistical error for each $|t|$ value is indicated by the error bar and the systematic error added as shaded area.

Chapter 10

Conclusion

The presented analysis performed measurements on the diffractive photoproduction of ρ^0 vector mesons using the H1 detector at the HERA collider. The data sample was taken in the 2005 HERA II running period and triggered with the new Fast Track Trigger FTT, containing more than 989'000 events in 660 selected luminosity runs with a total integrated luminosity of $\int \mathcal{L} dt = 570 \text{ nb}^{-1}$. The analysis is restricted to γp production with $Q^2 < 4 \text{ GeV}^2$ and the diffractive regime with $x_{\mathbb{P}} = (M_Y^2 + Q_{\text{gen}}^2)/(W_{\gamma p}^2 + Q_{\text{gen}}^2) < 0.01$.

The data sample was split into 12 t bins in the range $0 < |t| < 3 \text{ GeV}^2$ to measure the differential cross section $d\sigma^{\gamma p}/dt$ and each t bin was subdivided in either 10 or 5 $W_{\gamma p}$ bins to extract the energy dependence of the cross section as function of t . A total of 80 analysis bins were defined for which the differential cross sections were extracted.

For each analysis bin the acceptance and efficiencies were determined differentially in $m_{\pi\pi}$ and used to correct the dipion mass spectra for the corresponding W/t -bin. The corrected $m_{\pi\pi}$ distribution is skewed as described by the Ross-Stodolsky model as well as the Söding parametrization. For both models the number of resonant ρ^0 vector mesons were extracted and the differential γp cross sections calculated. The obtained cross sections are in good agreement.

Additionally the number of elastic and proton-dissociative resonant ρ^0 vector mesons were obtained and the respective cross sections determined. For the elastic ρ^0 production the energy dependence of the differential cross sections $d\sigma^{\gamma p}/dt$ in the range $|t| < 0.7 \text{ GeV}^2$ were fitted to the form $W_{\gamma p}^{4(\alpha(t)-1)}$ where $\alpha(t)$ is the value of the pomeron trajectory for the respective t value.

The pomeron trajectory is obtained from a measurement at a single experiment and yields

$$\alpha_{\mathbb{P}}(t) = 1.097_{-0.009}^{+0.009} + (0.133_{-0.053}^{+0.043}) \text{ GeV}^{-2} \cdot t. \quad (10.1)$$

This is in good agreement with the ZEUS result [81], where the measurement at large energies $W_{\gamma p}$ were combined with low energy measurements:

$$\alpha_{\mathbb{P}}(t) = 1.096 \pm 0.021 + (0.125 \pm 0.038) \text{ GeV}^{-2} \cdot t \quad (10.2)$$

The spin density matrix elements r_{00}^{04} , $\text{Re} [r_{00}^{04}]$ and r_{1-1}^{04} were determined as function of t and $W_{\gamma p}$ respectively by studying the decay angular distribution for the ρ^0 meson. These results are presented in the diploma thesis of Magnus Bodin [85].

Part II

Hardware

Chapter 11

Development of the Pixel Barrel Module for the CMS Detector

11.1 Introduction

The Compact Muon Solenoid (CMS) detector [86] is one of two general purpose detectors assembled at the Large Hadron Collider (LHC) at CERN [87]. LHC will be a proton on proton collider with a design center-of-mass energy of 14 TeV and design Luminosity of $\mathcal{L} = 10^{34} \text{cm}^{-2} \text{s}^{-1}$. Proton on proton collisions occur every 25 ns resulting in up to about 1000 tracks at $|\eta| < 3$ per bunch crossing [88]. This level of radiation makes the experimental conditions especially difficult. Not only that all detector components must be radiation proof, but also radiation-induced phenomena such as Single Event Upsets need to be considered.

The central part of CMS contains the tracker. Since 2000 [89] CMS is building an all-silicon version of the tracking system consisting of two independent subdetectors:

- On the outer rim the *silicon strip detector* and
- closest to the beampipe the *pixel detector*.

11.1.1 Secondary Vertex Detection

The main task of CMS is to find the Higgs boson(s) and find evidence for Physics beyond the standard model (BSM). As for $m_H < 140 \text{ GeV}$ the preferred Higgs decay is in two b-quarks and new physics signals show in the heavy-quark sector first, an efficient b-flavor tagging is essential for CMS. Due to the lifetime of b-hadrons ($\beta\gamma c\tau \sim 3 - 5 \text{ mm}$), their decays can be observed as displaced vertices in the detector. To identify a displaced (or secondary) vertex the so-called impact parameter δ is used. For an object in the event, δ is defined as the minimum distance between the track trajectory and the primary vertex in the $r\phi$ -plane. An object coming from a secondary vertex is generally characterized by a large impact parameter as pictured in Fig. 11.1.

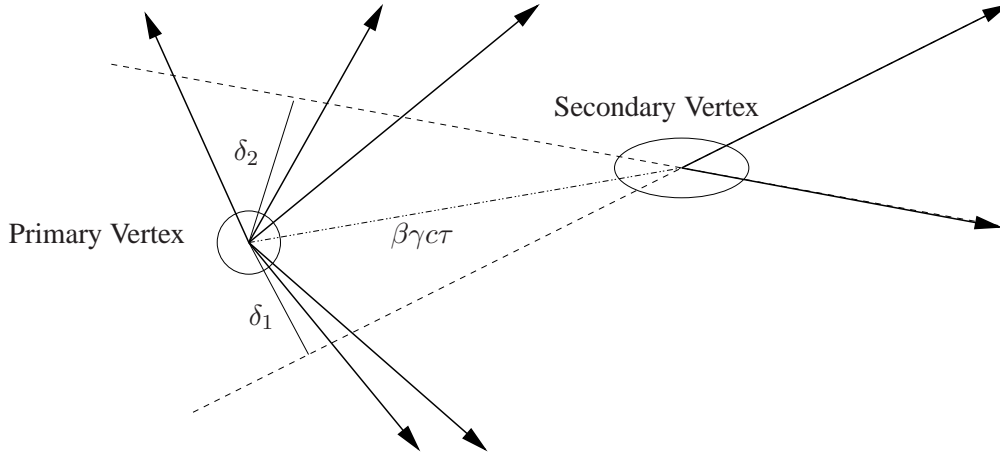


Figure 11.1: The impact parameter δ is the distance of closest approach of a trajectory to the primary interaction vertex. Due to the relative long life time of heavy particles, i.e. B mesons, the decay will on average take place a few mm or even cm from the primary vertex forming a secondary vertex. The decay particles emerging from this secondary vertex are characterized by a large impact parameter δ compared to the impact parameters from the particles emerging from the primary vertex.

Charged particles passing through the tracking detectors lose part of their energy due to interactions with the electric field of the atoms in the matter. The energy deposited in the sensitive silicon area will be detected and read out by specially designed components and is referred to as a "Hit" in the tracker. This information is needed to reconstruct a particle's trajectory through the detector and by extrapolation it is possible to calculate the impact parameter.

The energy loss happens by various interactions and can be described by the radiation length. It is the characteristic amount of matter a particle needs to pass, for the relevant interactions to take place. In case of high-energy electrons it corresponds to the amount of matter traversed over which the electrons lose all but 1/e of their energy by Bremsstrahlung.

The radiation length X_0 is defined as

$$\frac{1}{X_0} = 4\alpha_{\text{em}} r_e^2 \frac{N_A}{A} Z^2 \ln\left(\frac{183}{Z^{-1/3}}\right) \quad (11.1)$$

where α_{em} is the fine structure constant, r_e the electron radius, N_A represents Avogadro's Number and A and Z the atomic weight and number of the material respectively. The unit for the radiation length is $[\text{g cm}^{-2}]$. This definition is independent of the materials density and is convenient for material comparisons. The absolute distance in cm is obtained by dividing the radiation length X_0 by the density $\rho[\text{g cm}^{-3}]$.

The radiation length for compounds and mixtures is calculated as

$$\frac{1}{X_0} = \sum_j \frac{w_j}{X_j} \quad (11.2)$$

where w_j is the fraction by weight and X_j the radiation length for each component in $[g\text{ cm}^{-2}]$.

A common interaction for all charged particles is the multiple scattering. It sums up all deflections by many small-angle scatters within matter. Most deflections are due to coulomb scattering from nuclei and, in case of hadrons, strong interactions (Fig. 11.2).

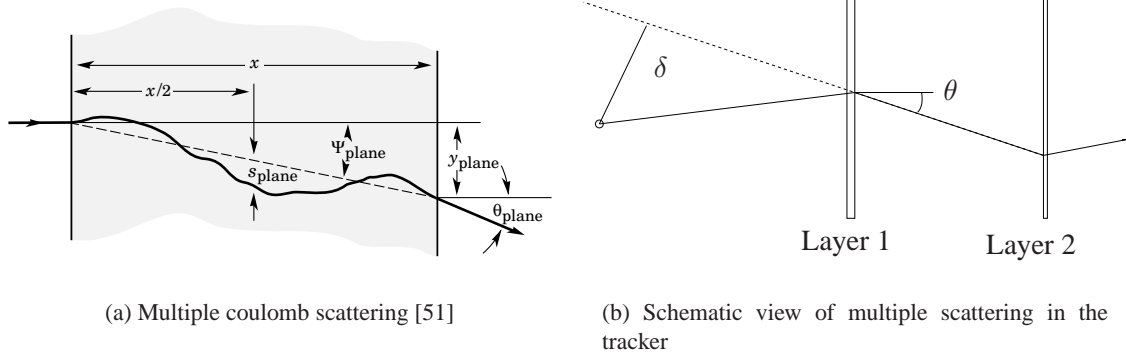


Figure 11.2: Multiple coulomb scattering of charged particles in matter. in (b) the multiple coulomb scattering is shown schematically for two layers and the deflection angle θ defined in Eq. (11.3).

For small deflection angles, the coulomb scattering distribution behaves roughly gaussian, and it is sufficient to use the approximation given by

$$\theta = \frac{13.6 \text{ MeV}}{\beta c p} z \sqrt{x/X_0} [1 + 0.038 \ln(x/X_0)] \quad (11.3)$$

where x/X_0 is the thickness of the material in units of the radiation length X_0 in $[\text{cm}]$.

Within the CMS tracker these deviations occur on each layer randomly. And since the impact parameter is determined by extrapolation, these random deflections introduce an additional error.

The relevant quantity for the error is x/X_0 , where X_0 is the total radiation length of the tracker layers. To minimize the influence of the layers, it is vital to keep the radiation length as large as possible. This can be done by minimizing the amount of material and using materials with large X_0 (see Eq. (11.2)). These information are summarized by the material budget. A large overall X_0 is not only desirable for more accurate tracking information, but also to minimize the energy loss while traversing the tracker and hence to improve the energy resolution of the calorimeters located outside the tracker.

11.2 The Pixel Detector

The main contribution of the CMS pixel detector [90] is to provide high resolution three-dimensional tracking points essential for pattern recognition and b-tagging. The pixel detector consists of up to three barrel layers at radii of $r = 4 \text{ cm}$, 7 cm and 10 cm from the beampipe and two sets of up

to three endcap disks at distances of $z = \pm 33$ cm, ± 46 cm and ± 60 cm from the interaction region ($z=0$). The pixel detector has a modular architecture shown in Fig. 11.3 and the parameters are summarized in Table 11.1.

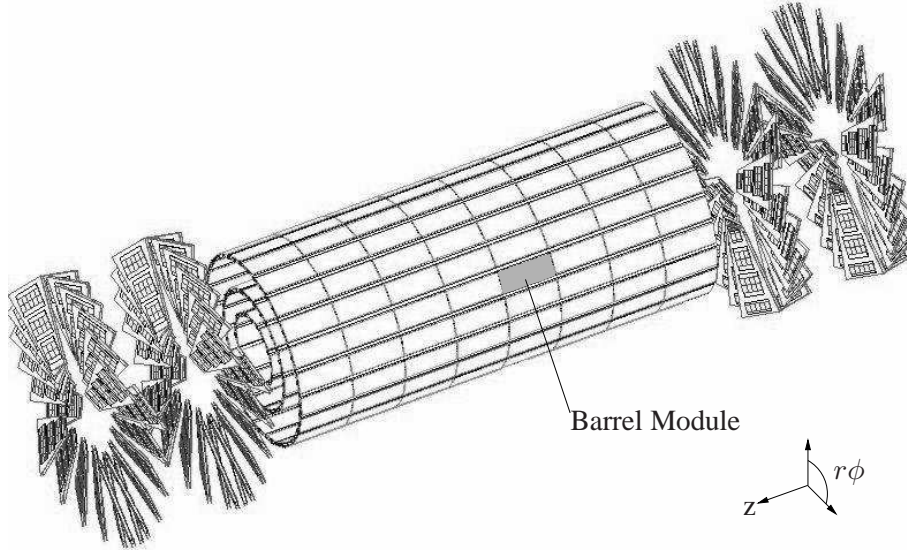


Figure 11.3: CMS pixel barrel with endcaps. The barrel consists of three layers of barrel modules at radii of $r = 4, 7$ and 10 cm. The endcaps encompass three disks each and are located at $z = \pm 33, \pm 46$ and ± 60 cm respectively.

All modules consist of thin, segmented silicon sensors with several equally segmented readout chips connected to them via the bump-bonding technique. Even though the readout chips are the same for the full pixel detector, the modules are different for the barrel and the endcaps. This thesis is focussed on the pixel barrel module.

11.2.1 Pixel Barrel Module

The pixel barrel module consists of a sensor element with the PSI 43 readout chip bump-bonded to it and a hybrid circuit (High Density Interconnect, HDI) mounted on top of it. The readout chips are glued to a thin silicon plate which serves as module base and will be mounted to the cooling frame by six fine swiss watch-maker screws. Electrically, the readout chips are wire-bonded to the hybrid circuit, where all signals are distributed differentially involving the Token Bit Manager Chip. All control signals and commands arrive via a copper-on-kapton cable on the HDI. The kapton cable is also used to send the analog readout from triggered events to the barrel periphery and from there to the Data Acquisition (DAQ) by optical fibres as well as carrying the bias voltage for depleting the sensor. All other supply voltages are brought to the hybrid using a coated Al-cable. A schematic view is given in Fig. 11.4.

CMS Pixel Parameters					
Pixel Barrel	Radius [mm]	Ladders	Modules	ROCs	Pixels [$\times 10^6$]
Layer 1	41-45	18	144	2304	6.35
Layer 2	70-75	30	240	3840	10.6
Layer 3	99-104	42	336	5376	14.8
Total		90	720	11520	31.75
Pixel Endcaps	z-position [cm]	Blades		ROCs	Pixels [$\times 10^6$]
Disk 1	± 33	24		1080	2.97
Disk 2	± 46	24		1080	2.97
Disk 3	± 60	24		1080	2.97
Total		164		6480	17.82
Overall				18'000	49.6

Table 11.1: CMS pixel parameters for the barrel and the endcaps.

11.2.2 Description of all Components

PSI 43 Readout Chip: The readout chip (ROC) of the pixel detector is probably the most crucial part of the module. The ROC reads out the collected charge of the sensor pixels and stores time and location of the Hit as well as the analog pulse height until it is read out by CMS. The PSI 43 ROC has 2'756 pixels organized in a pixel unit cell (PUC) array with 52 columns and 53 rows as shown in Fig. 11.5. A pixel is $150 \times 150 \mu\text{m}^2$ giving a total sensitive area of 62 mm^2 . Two neighbouring columns are grouped to a double column with a common bus line in between and common control blocks in the periphery. The 26 double columns operate independently of each other.

Each PUC is connected to a sensor pixel via an indium bump-bond. The signal from the sensor is first processed by a charge-sensitive preamplifier followed by a shaper configuration and forwarded to the comparator. The preamplifier is capable to deal with some leakage current from the sensor resulting from radiation damages. The comparator decides whether the signal exceeds the threshold and declares a hit. The threshold settings for the comparator consist of a global voltage for the entire ROC and three 'trim bits' per PUC for local fine-tuning.

Once the comparator declares a hit, the pulse height is stored by the sample&hold-mechanism. The double column periphery is notified simultaneously by a wired column OR¹, where the

¹Each column has a dedicated bus line, where all corresponding PUC's are connected. Any PUC storing a hit, sends a signal via this bus to the periphery.

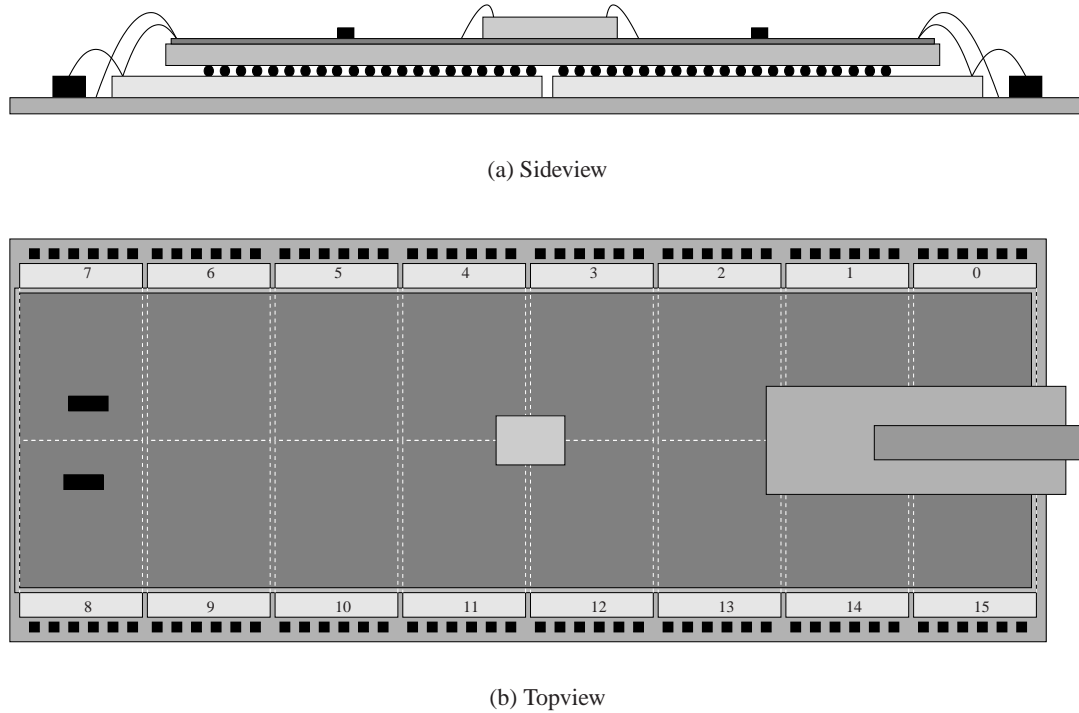


Figure 11.4: A schematic view of the pixel barrel module from the side (a) and the top (b). The main components of the module are the 16 readout chips with the sensor element and a control unit called token bit manager. The other parts serve as support structures and handle the electric feed and the distribution of the control signals.

current bunch crossing number is stored (time-stamp) and the transfer (column drain) is prepared (Fig. 11.6). The periphery sends a fast token through the double column, stopping only at those PUCs which have a stored hit in the corresponding bunch crossing, for which the full hit information (pulse height and pixel address) is transferred to the periphery and stored in data buffers. The remaining PUCs remain active during this process and can record one more hit during the column drain, which will be read out in a subsequent column drain.

The data buffer has four capacitors per entry to store the analog pulse height and the three address bits (A_1 , A_5 and A_{25}) and can hold up to 24 hits. Each address bit has 5 discrete analog levels, giving a total of $5^3 = 125$ possible addresses, where only 106 are used. The time-stamp buffer is digitally encoded with 8 bits allowing trigger latencies of up to 255 bunch crossings and holds up to 8 time-stamps. Both buffers have a circular architecture and if no trigger is present after the trigger latency, the time-stamp and its corresponding data are discarded. The trigger latency is defined by the difference in the SBC (Search Bunch Counter) and the WBC (Write Bunch Counter). Both counters are 8 bits deep and are connected to the time-stamp buffers in all double columns. The WBC is the counter

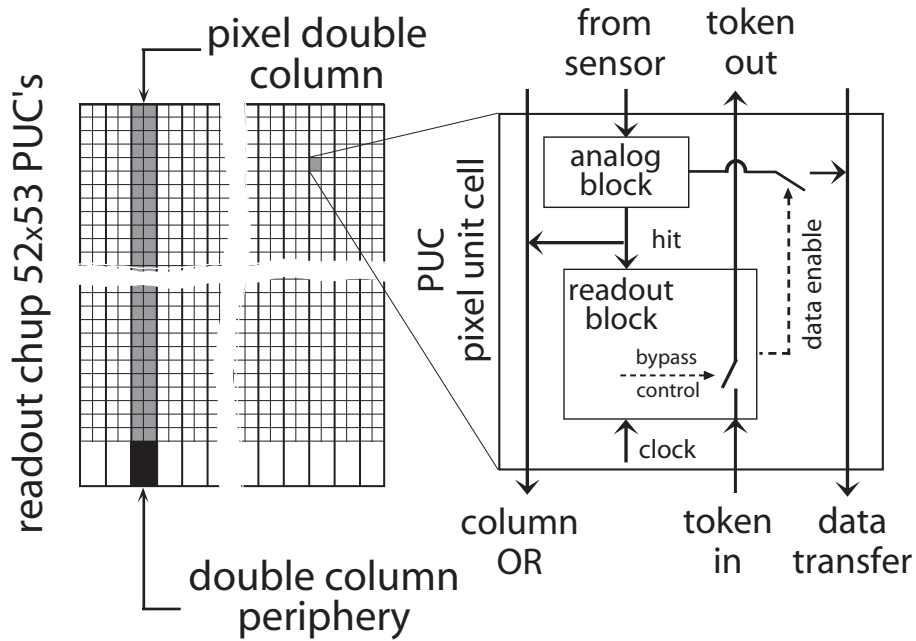


Figure 11.5: Schematic view of a pixel unit cell (PUC) with the double column. Each PUC has an analog block where the signals from the sensors are collected and a hit finding is performed. If a hit is found, the readout block becomes active and the PUC notifies the double column periphery via the column OR. The periphery sends a token through the double column (column drain) which causes the PUC to send its information to the periphery.

which is stored in the time-stamp buffer, whereas the SBC is used to validate the data. The SBC is delayed relatively to the WBC by the trigger latency.

If a trigger is sent to the ROC, it will validate all data whose time-stamp buffer entries match the SBC of the trigger which are then prepared for readout.

Once a set of data is validated it is crucial not to overwrite it. Therefore the double column stops all data acquisition after a trigger validation and awaits the Readout Token Bit (RTB) initiating the readout of the validated data. The pixel address and the analog pulse height are copied to a register containing 6 entries: two for the double column address, three for the pixel address and one for the analog pulse height.

The RTB arriving at the ROC initiates the sending of the chip header, independently of the number of hits in the ROC and is then passed from double column to double column. The chip header is a set of three cycles (Fig. 11.7(a)) and identifies the ROC on the analog readout line. Every double column which is prepared for readout, passes the entries in the register to the analog event multiplexer and eventually to the analog output driver. Fig. 11.7(b) shows the full analog readout sequence for a single pixel hit in a ROC. If more than one hit has to be read out, the data for the second hit is copied to the register while the first hit is transmitted and so on until all hits for the corresponding trigger are read out.

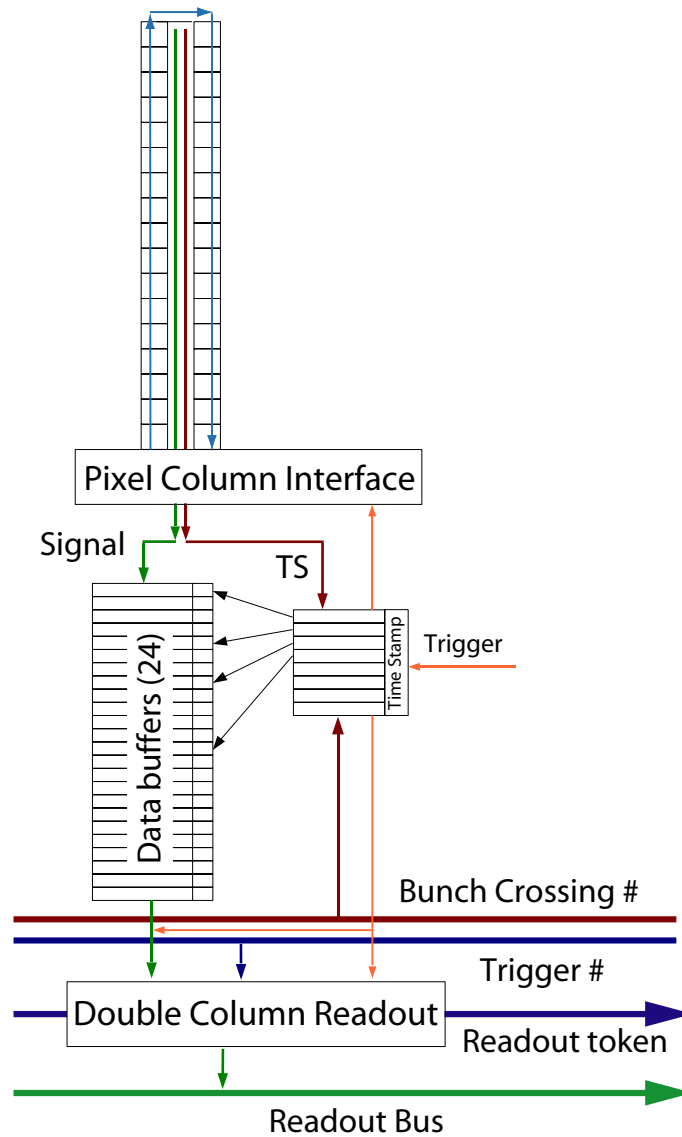


Figure 11.6: The column drain is started if any PUC in the double column declares a hit and sends the 'alert' via the column OR. The column drain passes through the double column and all PUCs with a stored hit send the data and their address to the column periphery where it is stored in data buffers; simultaneously an entry in the time buffer (time stamp) is stored. If after the trigger latency a positive trigger signal is received, the double column will stop the data taking and prepare for the read out which is initiated by the readout token (RTB) from the TBM.

While the last hit is being read out, the RTB is passed to the next double column to guarantee a continuous readout. After the last double column was readout, the RTB is sent to the next ROC. This RTB passing allows serial readout of an arbitrary number of hits and chips.

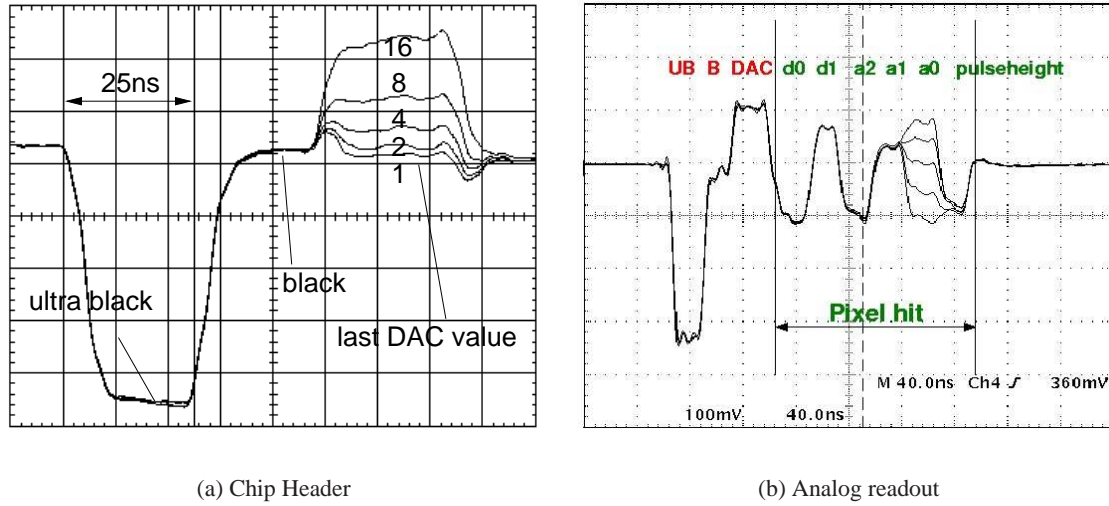


Figure 11.7: The analog readout of a PSI 43 ROC. In (a) the header is shown which is sent once per ROC ahead of the pixel hits. The chip header is used to separate the readout from different ROCs and thus match the pixel hits with the ROCs. The analog readout of a single pixel hit is shown in (b) for five different pixel addresses (a0) overlaid in one plot. The readout sequence is given by eight cycles where the first three cycles belong to the chip header, followed by two cycles with the encoded double column number, three cycles for the pixel address within the double column and in the last cycle the analog pulse height from the PUC.

The PSI 43 ROC needs four negative supply voltages. Each supply voltage is regulated inside the ROC to compensate fluctuations in the external power system. The regulated voltages are to some extent adjustable by Digital-to-Analog-Converters (DACs). The full DAC range for each supply voltage is given in Table 11.2.

Supply Voltages for the ROC				
Voltage	function	DAC	min [V]	max [V]
V_{a-}	preamplifier and shaper	8-bit	-1.6	-2.6
V_{h-}	sample&hold-mechanism	4-bit	-2.6	-3.6
V_{c-}	global comparator threshold	8-bit	-1.8	-2.8
V_{d-}	digital sections in the periphery	4-bit	-4.1	-5.2

Table 11.2: The four supply voltages V_{a-} , V_{h-} , V_{c-} and V_{d-} for the ROC with their DAC range.

The complete PSI 43 ROC configuration involves a total of 21 DACs and a control register holding the trigger latency. For the programming of the ROC, a fast I²C protocol is used. Besides the 21 DAC settings and the trigger latency, the protocol also carries an enable/disable bit for the double columns, the three trimbits and a masking bit for the PUCs.

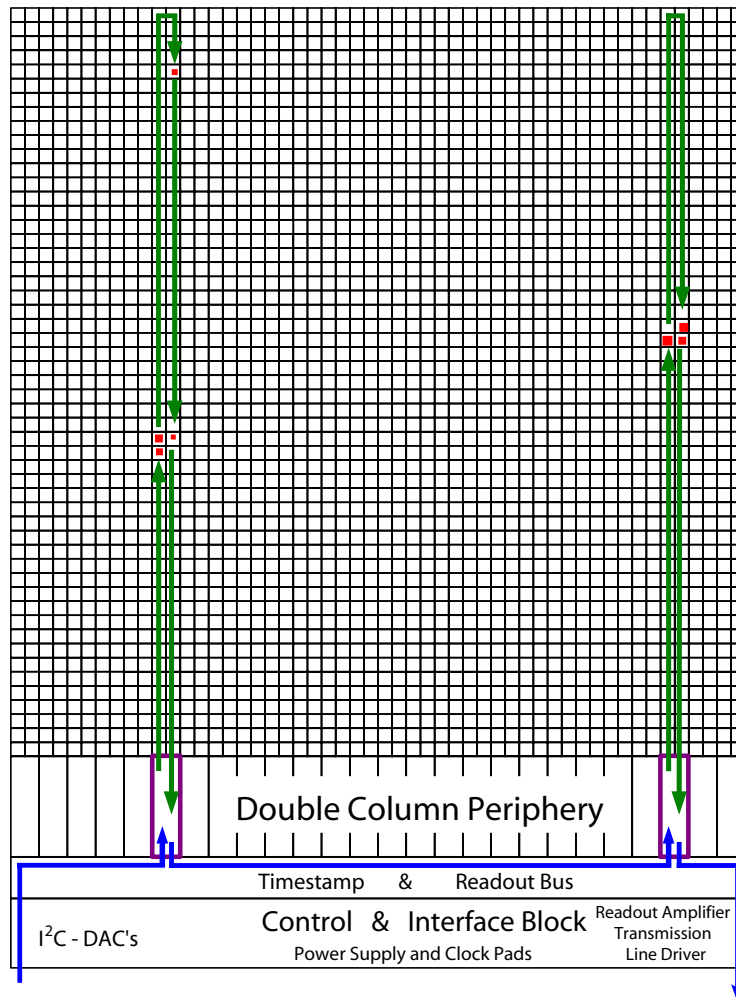


Figure 11.8: The PSI 43 ROC collects all hits from the PUC immediately in the periphery via column drain, where the data is stored until the data is either validated after the trigger latency or ignored. If the data is validated, the RTB is passed from ROC to ROC and initiates the read out of the corresponding data from the double column.

The protocol is sent using a set of low-voltage differential signals (LVDS) and is designed to run at 40 MHz. The address of the ROC is set by wirebonds and identifies the ROC on the serial bus.

The ROC is delivered with a thickness of roughly 540 μm . To improve the material budget, the ROC can be thinned to 160 μm without loss of performance.

The Silicon sensor element: Charged particles passing the sensor element produce electron-hole pairs, which are separated in an electric field. For CMS, the electrons are collected at the anode and passed to the ROC. During the lifetime of a sensor, several radiation induced effects occur and influence the electrical behaviour. The two most obvious ones are *type inversion* and *leakage current*.

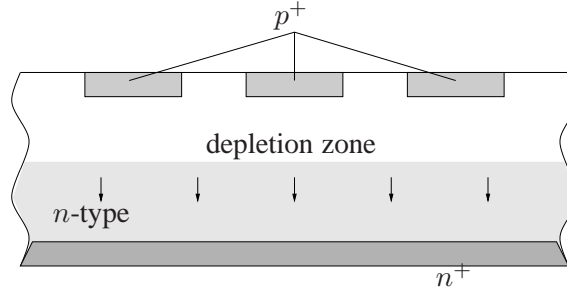


Figure 11.9: p-in-n sensors have to operate fully depleted after type inversion. Therefore the sensor has to have a sufficient high-voltage capability, in the CMS pixel case, this would correspond to more than 1000 V.

Previous pixel detectors (e.g. WA97 [91] or DELPHI [92]) used single-sided “p-in-n” sensors (Fig. 11.9). When a positive voltage is applied to the sensor’s backside, it depletes from the p^+ -side. After a radiation fluence of several 10^{12} cm^{-2} the creation of radiation induced defects with negative space charge becomes dominant and causes a space-charge sign inversion. The highly doped p^+ and n^+ regions are not affected, but the bulk switches from n-type to p-type material (type inversion). Now the depletion zone grows from the n^+ -side. Therefore “p-in-n” sensors need to be operated fully depleted after type inversion which then corresponds to high-voltage capability.

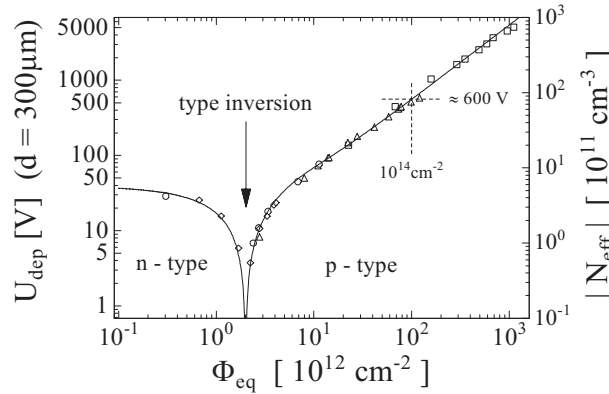


Figure 11.10: Type inversion denotes the switch from n-type to p-type material. This phenomenon is observed in the bulk of the sensor if the radiation fluence exceeds a certain threshold. Highly doped regions (p^+ , n^+) are not affected.

Fig. 11.10 shows an increase in the depletion voltage with increasing fluences. Estimations

for CMS predict a full-depletion voltage at the end of the targeted lifetime of over 1000 V. Since the designed maximum bias voltage is of the order of 600 - 700 V, the sensor needs to be operated partially depleted for a significant period of time. Therefore the double-sided “n-in-n” design was chosen (Fig. 11.11). Before type inversion the full depletion voltage is around 70 V. The detector is operated in fully depleted mode with approximately 100 - 150 V bias voltage. Type inversion is expected after a few weeks of LHC operation and after type inversion the sensor depletes from the pixel side, allowing under-depleted operation.

Since partially depleted operation leads to less spatial resolution, one is concerned to run as long as possible fully depleted. One way to slow down the increase in depletion voltage is to cool the sensor, also outside running periods.

The double-sided processing was necessary to implement the guard-rings on the backside of the sensor to avoid air-breakthroughs between the sensor and the ROC (gap $\sim 20 \mu\text{m}$).

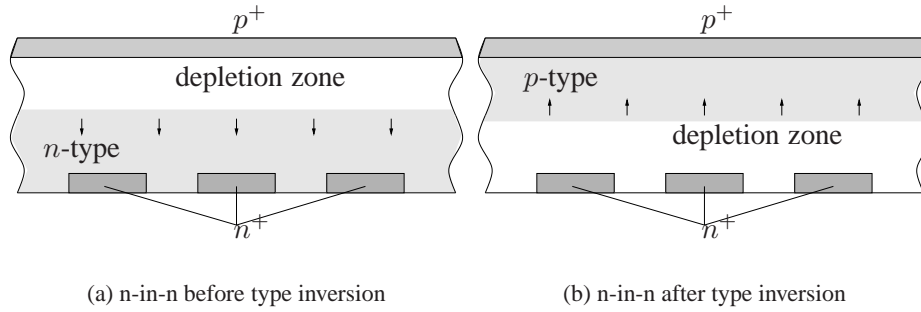


Figure 11.11: n-in-n sensors have to be operated fully depleted before type inversion, where the corresponding depletion voltage is only around 70 V and can be operated partially depleted after type inversion.

A Si crystal always contains some traps and impurities. These defects enhance the creation of electron-hole pairs independently of particles passing through the sensor. If a positive bias voltage is applied, the creation can be measured as a leakage current or dark current. The leakage current also increases with increasing fluence (more traps and defects) and is also temperature dependent. Therefore an effective cooling system is highly desirable for the sensor.

The sensor pixel size is also $150 \times 150 \mu\text{m}^2$ with 2'756 pixels per ROC summing up to 44'096 pixels per sensor element. The dimensions for this element are $66.3 \times 18.5 \text{ mm}^2$ and $280 \mu\text{m}$ thick. In order to keep the costs as low as possible, it is necessary to test the sensors before they are bump-bonded to the ROCs. A good measure for the quality of a sensor is its leakage current, measured with an IV-curve². If mechanical or other major defects are present, the leakage current increases dramatically. Since there is no reasonable way to contact the 44'096 pixels individually another approach was necessary. To measure the leakage current for all pixels, it is necessary to have an electrical connection between

²The measured leakage current (I) is plotted versus the applied high voltage (V).

the single pixels. This connection needs to be good enough to allow testing as well as bad enough to separate the pixels for data taking. The acceptable resistance range was estimated to be roughly between $1\text{ M}\Omega$ and $1\text{ G}\Omega$ [93]. Several resistance concepts are still being pursued. For the PSI 43 module a p-stop solution was chosen. The p-stops are p^+ implants between the n^+ pixels, isolating the pixels perfectly. To allow testing and grounding of unconnected pixels, a gap in the p-stop ring was introduced to allow some current to flow. The layout for the PSI 43 sensor is shown in Fig. 11.12.

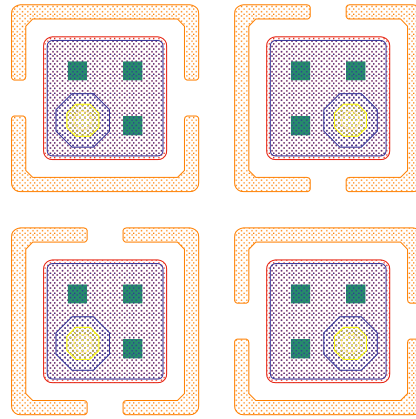


Figure 11.12: p-stop design for the PSI 43 module.

The Baseplate: An efficient cooling is essential for module operation and the cooling of the module happens through the baseplate. Therefore a good thermal conductivity along with a thermal expansion behaviour as close to the ROC's behaviour as possible are required. Poly-crystalline Si is such a material and was used for the prototype modules. Besides the mechanical functionality of mounting the module to the cooling frame, the baseplate is also used for grounding. For this purpose a $2\text{ }\mu\text{m}$ thick copper grid was applied on top. This grid also includes the soldering pads for the decoupling capacitors.

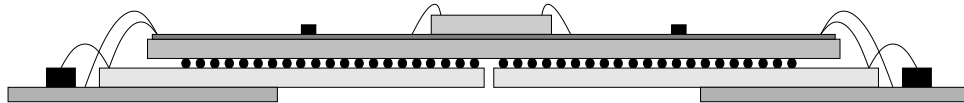


Figure 11.13: Sideview of the barrel module with narrow baseplates.

With $65 \times 25.5\text{ mm}^2$, the baseplate has the largest area of all components and is therefore a strong contributor to the material budget. In an effort to reduce the contribution, we considered reducing the full baseplate to two narrow stripes of 7 mm width each (Fig. 11.13). Possible problems could arise in the mechanical stability of the module as well as in the separation of the ground level for the two ROC sides. During the prototype assembly both types of baseplates were considered. Concerning the assembly, no negative surprises were encountered with the two stripes.

The High Density Interconnect (HDI): The hybrid circuit is routing all signals and supply voltages to their dedicated places. It's made of 55 μm polyimide layers with three intermediate metalization layers (7 μm Copper). The lower level is exclusively for the distribution of the supply voltages (see Fig. 11.15). The upper two layers are used for the routing of the control signals and the readout channels. The dimensions are $63.6 \times 21.4 \text{ mm}^2$. Compared with the sensor, the HDI sticks out by 1.5 mm on each side (flaps). These flaps are bent down to the ROC for wire-bonding. To minimize the bending force needed, the flaps match the width of the wire-bond pads on the ROC. The outline of the HDI is illustrated in Fig. 11.14.

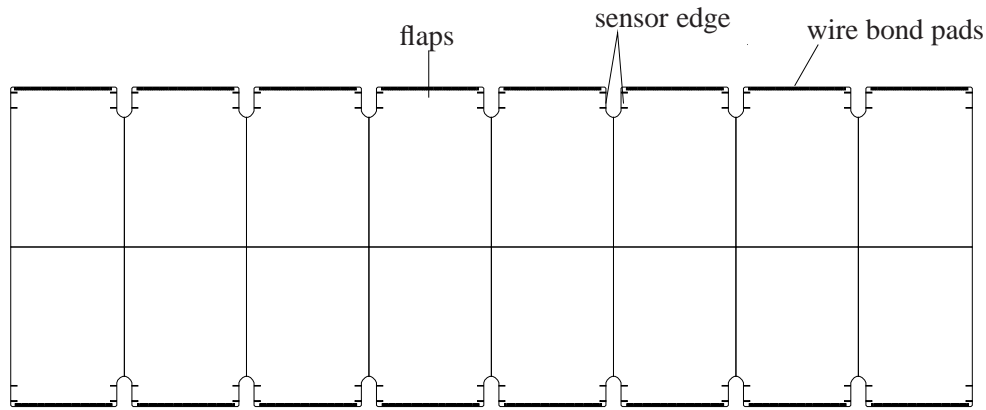


Figure 11.14: The outline of the HDI with a total area of $1'321.2 \text{ mm}^2$. The wire bond pads are used to connect the HDI to the ROC and are located at the very end of the flaps. These flaps are glued to the ROC during the module assembly. A rather complicated and time consuming procedure. For the next generation of modules, the HDI flaps are removed (see also Fig. 11.40).

The total area of the HDI is $1'321.2 \text{ mm}^2$. The area and the fill factor for the intermediate copper layers are given in Table 11.3.

Fill factors for the HDI layers		
Layer	Area [mm^2]	fill factor
1	839.4	63.5
2	313.1	23.7
3	202.2	15.3

Table 11.3: Fill factors for the intermediate copper layers of the HDI.

The total volume of copper is roughly 9.5 mm^3 or 57% of the HDI's weight. Instead of copper, one could also consider aluminium as conductor. The advantages for the material budget are larger radiation length and lower density, whereas the worse electric conductivity is disadvantageous. A comparison for the radiation length of the HDI is given in Table 11.4. The comparison is based on equal resistance for both metal layers.

Aluminium would improve the material budget for the HDI by a factor of 2-3. However, the thermal conductivity is worse by a factor of 1.7. Considering that the HDI is roughly

Radiation length of HDI			
Layer material	Cu	Al	kapton polyimide
Radiation length material [g/cm^2]	12.86	24.01	36.11
Density [g/cm^3]	8.69	2.7	1.42
Volumina for equal R [10^{-3} cm^3]	9.5	15.1	44.9
Total weight HDI [mg]	148.9	104.6	
Fraction of weight	0.57	0.39	0.43 / 0.61
Radiation length HDI [g/cm^2]	17.8	30.2	
Density HDI [g/cm^3]	2.74	1.74	
Radiation length HDI [cm]	6.5	17.3	

Table 11.4: Total radiation length for the HDI.

5% of the weight of the module, the gain in the material budget is not significant. Last but not least, the conventional manufacturers are all working with copper and it would require additional costs and research to introduce aluminium as conductor.

Onto the HDI, the Token Bit Manager (TBM), Termination Chips and two cables are mounted. All components are glued to the HDI and wire-bonded to dedicated bond-pads.

Currents on the HDI		
	digital current	analog current
single ROC	130 mA	40 mA
module	2080 mA	640 mA
Voltage drop on the HDI		
ROC side	digital drop [mV]	analog drop [mV]
0 - 7	75	15
8 - 15	68	15

Table 11.5: Measured currents and voltage drops for the voltage distribution on the HDI.

The power cable carries the four necessary supply voltages for the ROCs (V_{a-} , V_{h-} , V_{c-} and V_{d-}) and their grounds (V_{a+} , V_{h+} , V_{c+} and V_{d+}) to the HDI. On the HDI the three grounds V_{a+} , V_{h+} and V_{c+} are connected and labeled V_{a+} . The remaining 6 potentials are

distributed in 2 parallel identical structures along the module (Fig. 11.15). Each ROC has its own connection to the voltage system. The remaining two ground lines V_{a+} and V_{d+} are connected at each ROC. The average voltage drop along the HDI for the analog and digital voltage is given in Table 11.5.

The kapton cable carries the bias voltage for the sensor as well as the control signals, which are routed to the TBM and from there distributed to the ROCs. The module is segmented in 4 groups of four ROCs each. Every group gets a complete set of control signals from the TBM, whereas the analog readout from the ROCs is combined for two neighbouring groups and routed to the TBM.

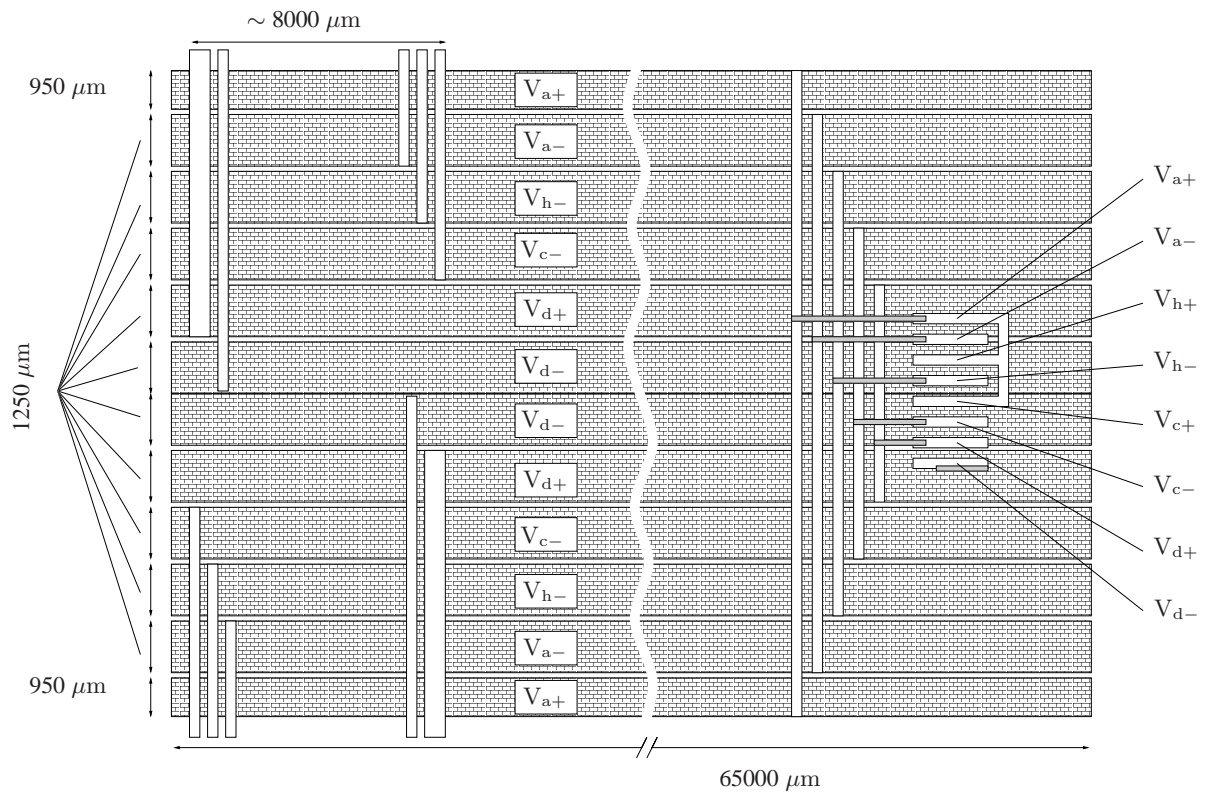


Figure 11.15: Schematic layout of the voltage distribution of the HDI. The three ground potentials V_{a+} , V_{h+} and V_{c+} are connected and labelled V_{a+} . The potentials are spread across the HDI by broad conductor paths on the first metal layer of the HDI. Smaller paths on the second layer distribute the potentials to wire bond pads and eventually to the ROC.

The Token Bit Manager: The Token Bit Manager (TBM) controls the flow of the Readout Token Bit (RTB) and serves as interface between the FrontEnd in the control room and the ROCs. The control signals (Calibrate (CAL), Trigger (TRIG), Reset (RES) and Clock (CLK)) are sent from the FrontEnd Controller (FEC) via optical link, kapton cable and HDI to the TBM. Each TBM controls 2 or 4 groups of 4 ROCs each and distributes all control signals to the groups in parallel. The TBM also refreshes the signals on the HDI after travelling through

the kapton cable.

In parallel, control commands are needed to program the ROCs and the TBM. These commands are sent using the fast I²C protocol. Again, these commands are sent from the FEC via optical link and kapton cable to the TBM. Inside the TBM the hub decodes the module address and sends the remaining commands to the designated device. The module address is stored in the hub and is needed, since one optical link is used to program up to 12 modules in parallel.

Whenever a Level 1 Trigger is received by the TBM, it forwards it immediately to the ROCs, where the corresponding hits are prepared for readout. The TBM then starts the readout chain by sending the RTB to the first chip where the hits (if present) are sent to the analog output driver. After all hits of the ROC are read out, the RTB is passed on to the next ROC and so on. The last ROC returns the RTB to the TBM. If another trigger arrives at the TBM before the RTB has returned, the TBM will pass the trigger to the ROCs as before, but delays the RTB by stacking it. Only after the previous RTB has returned, the new RTB is sent and the entry in the stack is removed. The stack is capable of delaying up to 32 RTB (triggers). The complete readout chain is illustrated in Fig. 11.16.

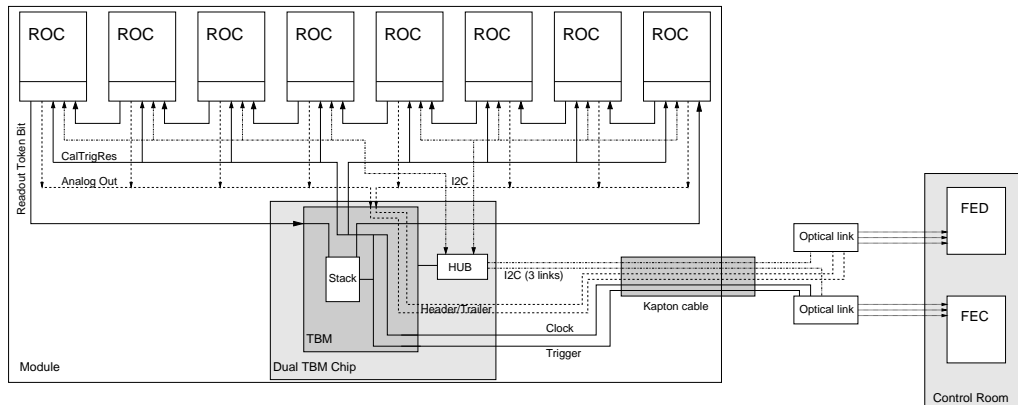


Figure 11.16: Schematic overview of the module readout from the ROC via TBM and kapton cable to the control room.

The number of RTBs waiting in the stack of the TBM is proportional to the number of ROCs a single RTB passes before returning to the TBM. Due to the high trigger rate for the inner two layers, this number is limited to eight ROCs per module. Therefore the TBM is designed as pair in a dual TBM chip (Fig. 11.17) containing two individual TBMs and a common hub. Each TBM is connected to one optical data link to send the analog readout of the ROCs directly to the FrontEnd Driver (FED). The inner most layer will have two optical data links with eight ROCs each, whereas for the second and third layer only one optical data link is needed to read out all 16 ROCs. The second TBM is deactivated and the RTB is sent from ROC#7 to ROC#8 by special wirebonds.

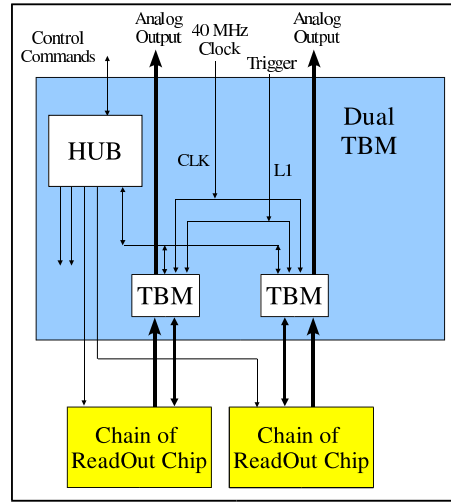


Figure 11.17: The Dual TBM Chip layout with two token bit manager blocks and one HUB. On the first layer of the barrel at a radius of 4 cm, both TBM blocks are used to control eight ROCs each. For the other two layers it is sufficient to use only one TBM block controlling all 16 ROCs.

LVDS Repeater Chips: The prototype generation of modules was operated without TBM. The control commands were distributed directly to the ROC (with only one module, there was no need to identify the module) and the RTB was sent explicitly through the kapton cable. To refresh the control signals we used LVDS Repeater Chips. The routing of all the signals and commands was achieved by special wire-bonds on the HDI.

Termination Chip: The signal lines on the HDI need proper termination, for which a special Termination Chip was designed. It contained four terminations, each one looking like Fig. 11.18.

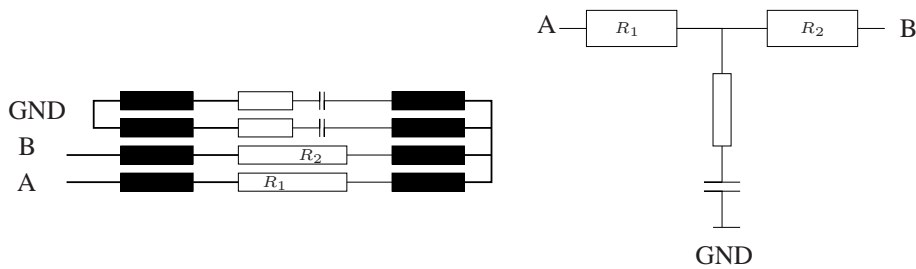


Figure 11.18: The termination layout as implemented in the termination chips (left) and schematically (right).

The differential signal is connected to the two lines A and B. Two ground pads allow AC termination with $25 \Omega/10 \text{ nF}$ or $50 \Omega/20 \text{ nF}$. The signal lines which were terminated are CLK, CAL, TRIG and RES. Each quadrant of the module has its own Termination Chip wire-bonded to the corresponding signal lines. Fig. 11.19 shows simulation and measurements of a prototype module with and without terminating the control signals.

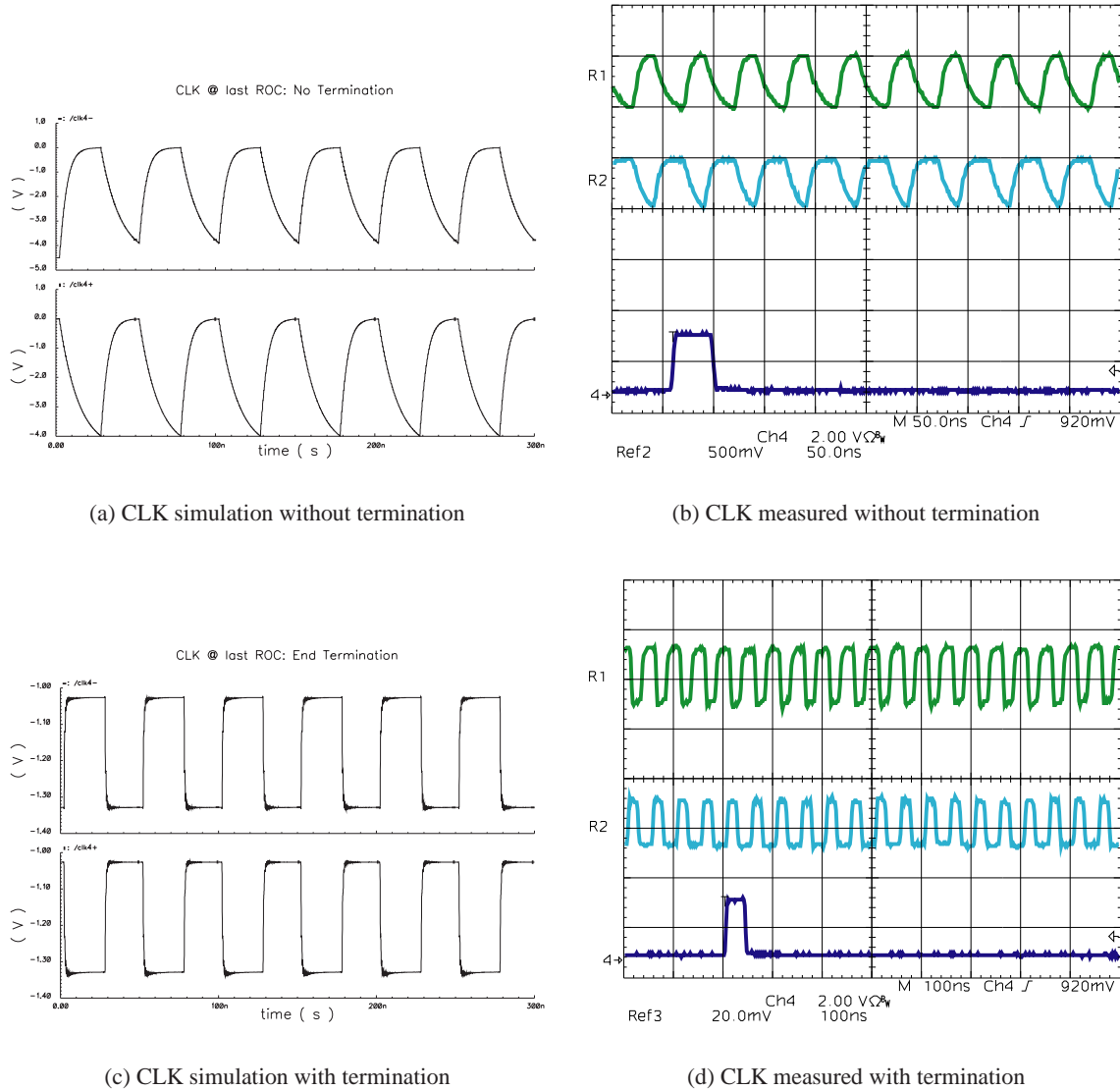


Figure 11.19: The differential control signal for the clock (CLK) in the simulation (left) and measured (right). The upper row is not terminated while the lower row is properly terminated with the termination chips.

The Power cable: Each supply voltage is brought separately to the HDI resulting in eight single cables. We used specially coated Aluminium cables with a core diameter of $250\ \mu\text{m}$ Aluminium coated with Copper and 2 layers of polyamide lacquer.

The eight cables are crimped and mounted to a plug, used for the interface end of the cables. The loose wires are then locally heated to about 220°C causing the outer lacquer (bondcoat) to seal the eight cables to a ribbon. The voltage drop for the ribbon is $10\ \text{mV/cm}$. The

maximum length of the power cable is roughly 40 cm, giving a maximum voltage drop of 400 mV for the ribbon.

The Kapton Cable: The Kapton Cable consists of a $50\ \mu\text{m}$ kapton print with $15\ \mu\text{m}$ copper lines on top and a $15\ \mu\text{m}$ copper plane on the back for grounding, Fig. 11.20. It has 21 lines with a pitch of $300\ \mu\text{m}$. Due to various modifications we used only 15 channels for the prototype modules.

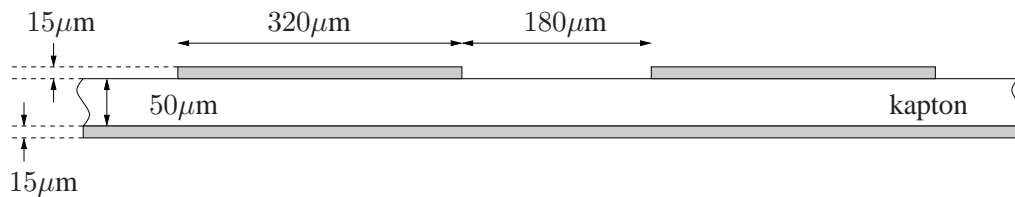


Figure 11.20: Layout of the kapton cable with copper lines on top for the conductor paths and the copper plane for grounding on the reverse.

The Decoupling capacitors: Each ROC needs 6 external capacitors for stabilization and decoupling purposes. The capacitors are wire-bonded to the corresponding pads on the ROC. We used 10 - 100 nF capacitors from Murata Electronics. They are gold plated and therefore wire-bondable as well as solderable.

11.3 ROC Testing

Before the module assembly, the ROCs need to be tested. In summer 2002 we received several wafers from DMILL³ with 74 ROCs per wafer. Two of these wafers (#8 and #10, 148 ROCs) were tested for module production. This was done in a manual probe station where each ROC was tested individually. The test setup is shown in Fig. 11.21.

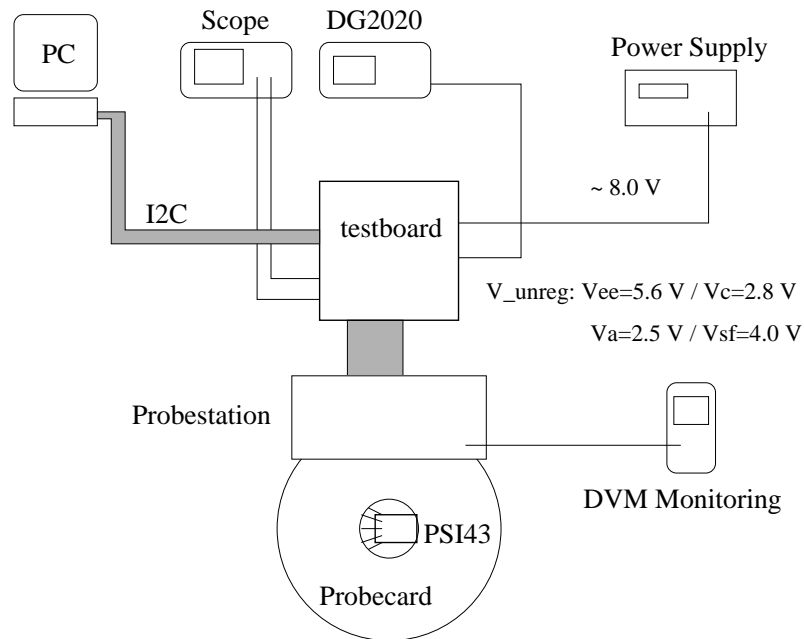


Figure 11.21: The setup for ROC testing. The PSI 43 ROC is placed underneath the probecard which connects electrically to all wire bond pads of the ROC. The testboard acts as front end and sends the control signals and supply voltages to the ROC and gathers the readout from the chip. The control sequences for CLK, CAL, TRIG and RES are generated with a pattern generator (DG2020) while the I2C signals (e.g. trim bits and pixel masking) are provided by a PC.

The probecard contacted each bond pad of the ROC. If no major defect was present, the DAC range of the four regulated supply voltages was tested and set to an acceptable value. The main part of the test sequence was the testing of all 2'756 pixels resulting in a pixel map of the ROC with dead pixels marked. They were categorized according to the pixel map in four groups:

- Good: at most 3 dead pixels, all voltages showed acceptable ranges
- Fair: between 3 dead pixels and two dead double columns, no major problems encountered
- Bad : more than 2 dead double columns or heavy problems with at least one internal voltage
- Dead: not working at all or drawing too much current

The test result and the yield is given in Table 11.6.

³Company in France which manufactures semi-conductors using the DMILL process.

ROC Test Result				
	# of ROCs		Yield	
Category	wafer #8	wafer #10	wafer #8	wafer #10
Good	12	18	0.16	0.24
Fair	13	25	0.18	0.34
Bad	23	18	0.31	0.24
Dead	26	13	0.35	0.18

Table 11.6: Results of the ROC testing for two wafers.

A weak point of the PSI 43 ROC is the rather moderate reference voltage. For stable ROC operation it is essential to have equal and stable internal voltages for every ROC. Since the external voltage varies due to cable resistances and ROC operation, internal voltage regulators were implemented. In order to work properly, these regulators need an independent reference voltage. To achieve homogenous voltage settings for the pixel detector, the reference voltage needs to be stable in time as well as identical in each ROC. In the PSI 43 ROC this reference voltage is off its design value and differs from ROC to ROC. For single ROC operation the moderate reference voltage was no major problem since little modifications on the single ROC setup compensate for the wrong reference voltage. These small modifications were not possible in the module setup and therefore another solution had to be found.

A closer look at the problem

Fig. 11.22 displays schematically the PSI 43 ROC's internal reference voltage generation. The external supply voltages are the unregulated voltages. The internal block ' $V_{\text{ref_source}}$ ' generates the primary reference voltage. This reference voltage is fed into a DAC, generating several secondary reference voltages, one of them is used by the voltage regulators. Another one is responsible for the DAC ranges and various other vital parts of the ROC. If the primary reference voltage already has a wrong value, all other voltages are off their design values as well and the DAC is working only in a limited range or not at all. In both cases the operation of the ROC is extremely limited. For monitoring reasons the V_{vref} voltage was routed to an external bond pad. If one adds a resistor R_X between this pad and ground, one is able to adjust the reference value slightly. For decoupling reasons a capacitor ($C = 1\mu\text{F}$) is added in parallel. This so-called RC-Tower can be adjusted to correct the reference voltage.

During the ROC testing four different values for R_X were used:

$$R_X = 1.5\text{ M}\Omega, \quad 2\text{ M}\Omega, \quad 2.4\text{ M}\Omega \quad \text{and} \quad 2.7\text{ M}\Omega$$

For each ROC it was determined, which value of R_X (if any) was needed, in order to be able to

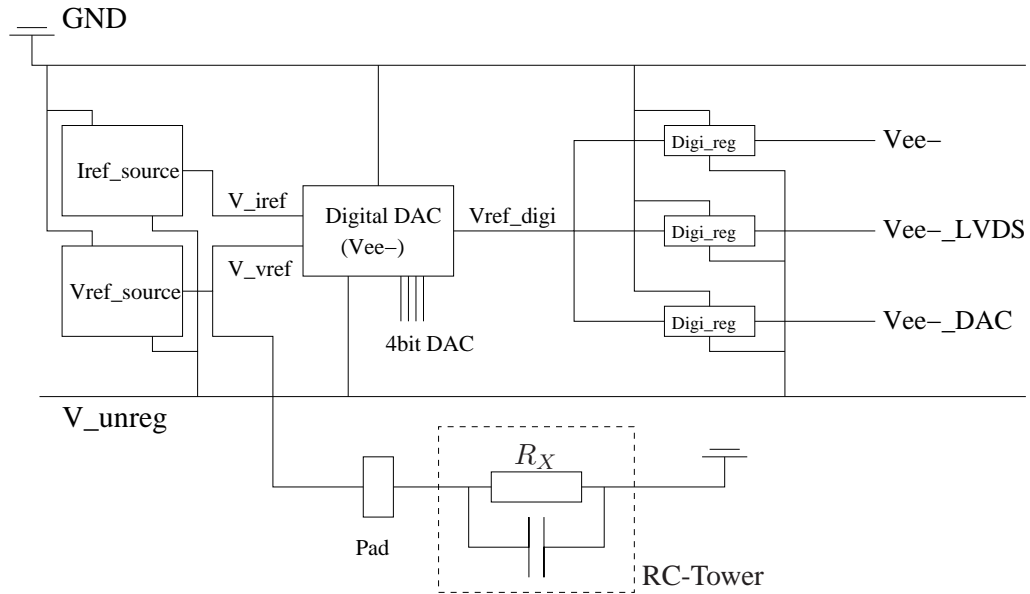


Figure 11.22: Overview of the generation of the internal reference voltage of the ROC. The $V_{\text{ref_source}}$ block generates a primary reference voltage which is used by a digital DAC to derive the internal supply voltages $V_{\text{ee-}}$, $V_{\text{ee-LVDS}}$ and $V_{\text{ee-DAC}}$. For the digital DAC to work properly it is crucial, that the primary reference voltage is in the optimal working range of the DAC. Via the monitoring pad an external RC-Tower can be added to correct for an offset of the primary voltage.

use the full DAC range. Fig. 11.23 shows the four regulated supply voltages for two different R_X of one ROC. Two boundary conditions need to be considered when choosing the correcting R_X :

- The digital voltage $V_{\text{ee-}}$ should be $> 4800 \text{ mV}$
- The analog voltage $V_{\text{a-}}$ should be $< 2000 \text{ mV}$

During the test sequence, we needed to choose the best R_X for each ROC. The distribution of R_X are summarized in Table 11.7.

Determination of R_X					
$R_X [\text{M}\Omega]$	none	1.5	2	2.4	2.7
working ROCs (96 total)	4	6	82	1	3

Table 11.7: Operational ROCs for different values of R_X .

For simplicity reasons only the values $R_X = 1.5 \text{ M}\Omega$ and $R_X = 2 \text{ M}\Omega$ were considered for the assembly. Due to the actual position of the V_{vref} bond pad we had to remove one decoupling capacitor and replace it by the RC Tower.

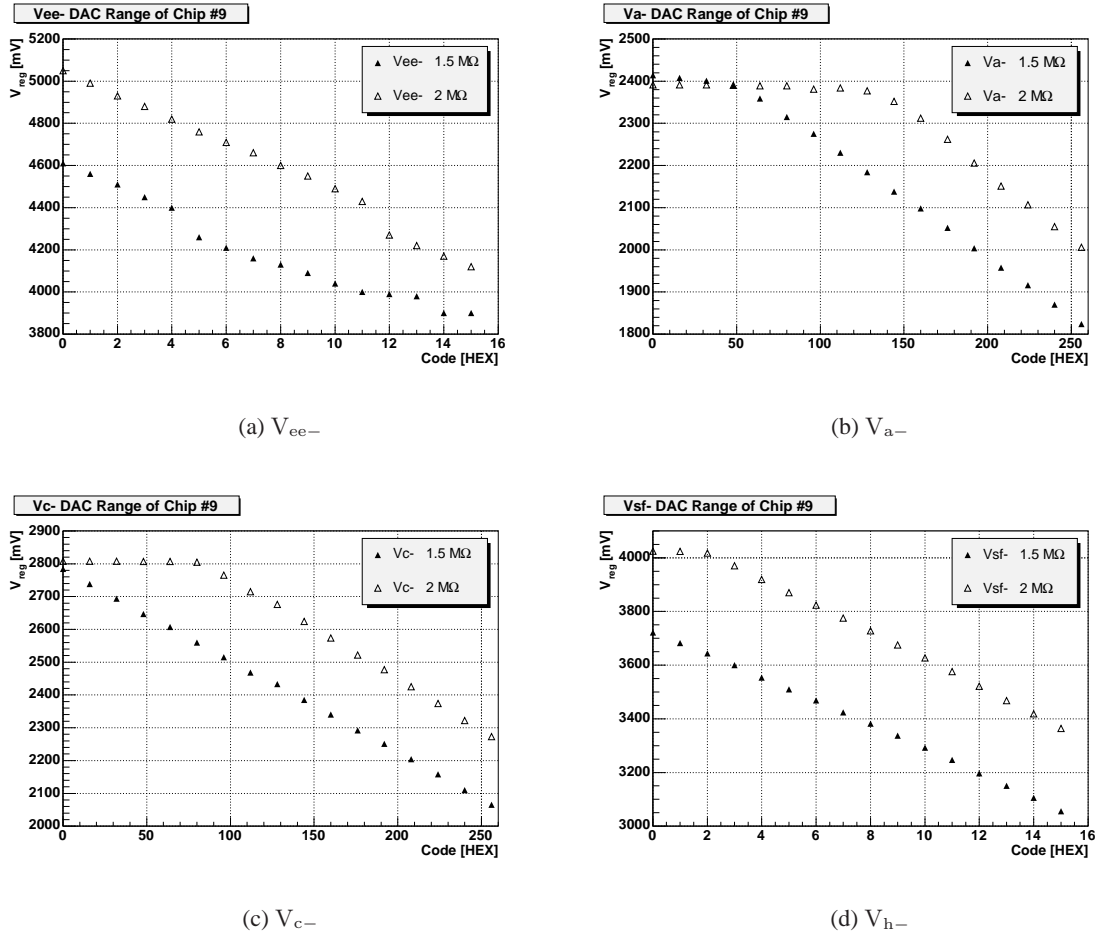


Figure 11.23: DAC ranges for PSI 43 ROC.

11.4 Module Assembly

The actual assembly begins after the ROC testing. Fig. 11.24 gives an overview of the assembly steps. In the beginning the three major components (Baseplate, ROC/sensor and HDI) are processed in parallel. Each one needs an individual processing before they are assembled together.

1. Equipping the Baseplate

The decoupling capacitors are soldered to the baseplate. There are five capacitors and one RC-Tower per chip, giving a total of 80 single soldering steps. For convenience the soldering was done on a heating plate. In future the baseplate will be equipped automatically using standard SMD⁴ capacitors.

⁴SMD (surface mounted device) are commercial electronic devices such as resistors and capacitors of extremely small size. They are generally soldered directly to the electronic board.

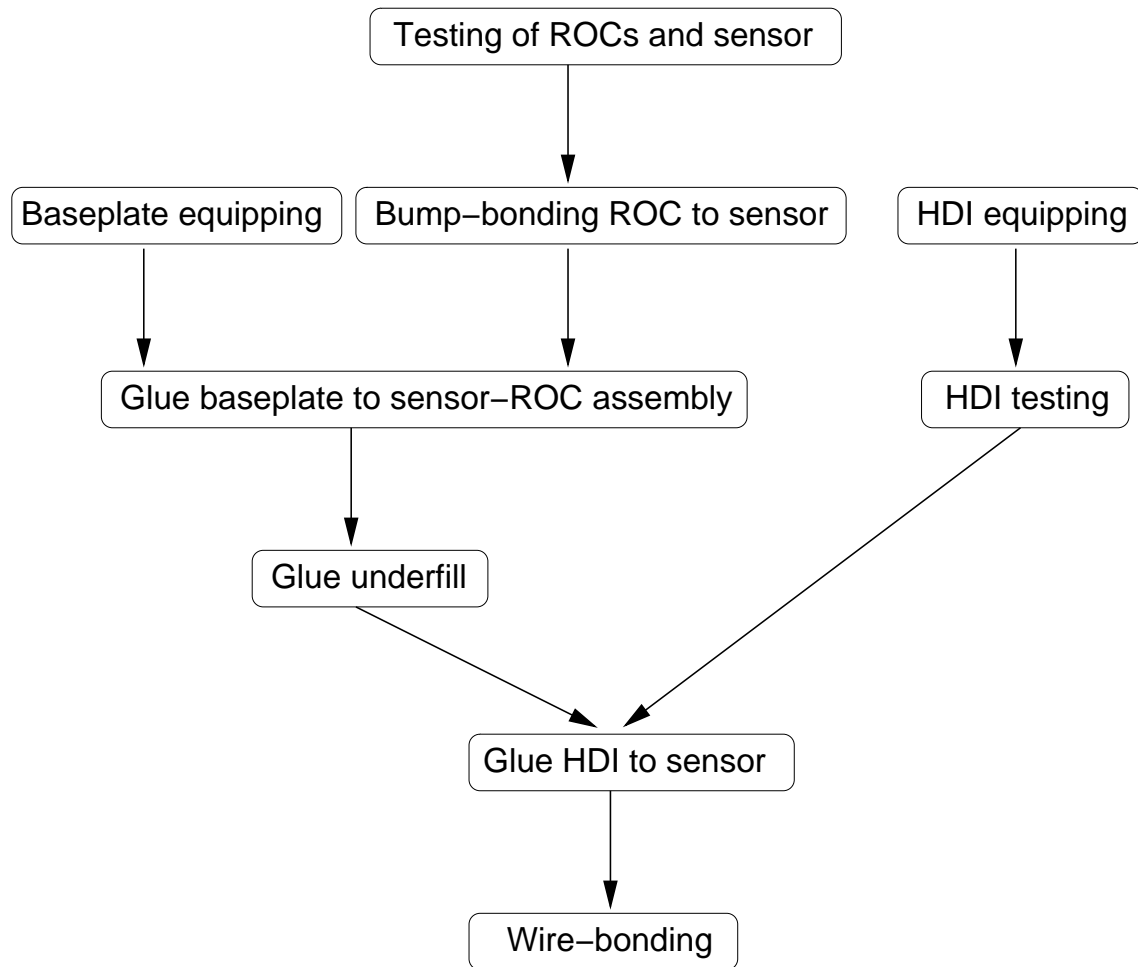


Figure 11.24: Overview of the different steps for the assembly.

2. The Sensor - ROC sandwich

Both components are manufactured and delivered in wafers. For the next generation of ROC wafers, an automatic test station is developed, testing the complete wafer in roughly 1 minute per ROC. For the PSI 43 ROCs this test station was not ready, and the reference voltage required an individual adjustment of the test setup. Therefore the ROCs needed to be diced before the testing. From now on, the ROCs are tested on the wafer, and then processed as described below.

The bump-bonding technique was optimized for our purposes at PSI. The full procedure involves various steps and processings of the wafers. The sensor and ROC wafers are handled almost identical.

Figure 11.25: The bare Si wafer with Al bump-bond pads. Both components are tested.



Figure 11.26: Photoresist ma-N 440 is applied, roughly $6\text{ }\mu\text{m}$ thick.

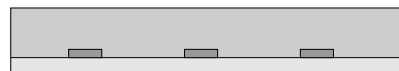


Figure 11.27: With a special mask, the bump-bond openings ($\sim 20\text{ }\mu\text{m}$) are exposed and developed.



Figure 11.28: The Under Bump Metal (UBM) is sputtered using the same mask layout. First a thin layer of Titanium for adhesion and protection of diffusion, followed by the main layer of Nickel for adhesion to the Indium bumps. Finally a thin layer of Gold to prevent the Nickel from oxidation.

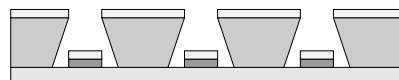


Figure 11.29: ROC wafer only: A total of 2 g Indium is vapor deposited, resulting in a $\sim 1.7\text{ }\mu\text{m}$ thick layer of Indium on the pads.

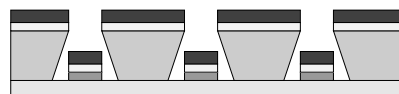


Figure 11.30: ROC wafer only: The photoresist is lifted off. The wafer is now ready for dicing.



Figure 11.31: Sensor wafer: The lift-off for the sensor wafer is done after the UBM is sputtered.



Figure 11.32: A second layer of photoresist is applied to the sensor wafer ($8\text{ }\mu\text{m}$).

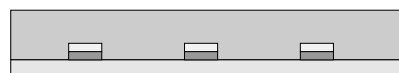


Figure 11.33: A second mask is used for exposure of the photoresist with larger openings ($\sim 40\text{ }\mu\text{m}$) to apply more Indium.



Figure 11.34: A total of 4 g corresponding to $\sim 3.4\text{ }\mu\text{m}$ thick layer of Indium is vapor deposited onto the sensor wafer.

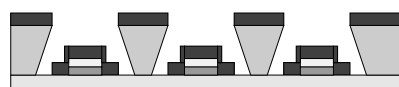


Figure 11.35: The remaining photoresist is removed. The sensor wafer is now ready for dicing.



Figure 11.36: The sensor element is reflowed. This happens in a Nitrogen-HCOOH atmosphere and the sensor is heated to about 150° for 45 seconds. The Indium forms a bump of roughly $20\text{ }\mu\text{m}$ diameter.



Figure 11.37: The next step is the actual bump-bonding of the ROC and the sensor. Therefore the sensor is placed into the bonding machine, and the ROC is aligned in a careful procedure over the sensor. After the ROC was placed in position, a pressure of 4 kg is applied for 1 - 2 minutes. The Indium bumps are pressed together for a first mechanical connection. This procedure is repeated for all 16 ROCs.

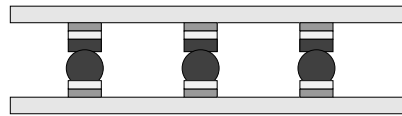
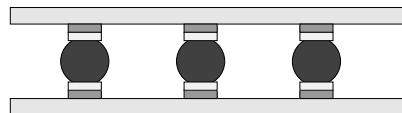


Figure 11.38: Finally, the complete sensor-ROC sandwich is reflowed again. This causes the Indium to melt and combine the two layers strengthening the mechanical connection. There is also some self-alignment taking place: the Indium bumps align themselves to the bump-bond pads on the sensor and the ROCs, aligning the ROC's relative to each other to an accuracy of $2\text{ }\mu\text{m}$.



After reflowing the sensor-ROC sandwich, the mechanical strength of the bump-bonds is tested in a 'Pull-Up test'. Therefore we pull with 200 g at each ROC from the backside as illustrated in Fig. 11.39. If the bump-bonding or the reflow didn't work due to misalignment, contaminations etc., the ROC will detach from the sensor. Otherwise the module can cope with more than 3 kg only with the bump-bonds!

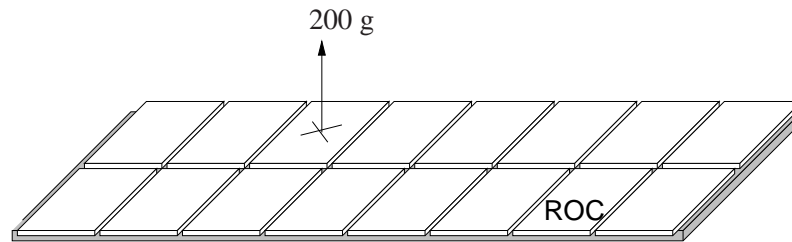


Figure 11.39: The Pull-Up test is used to monitor the quality of the bump bonds.

3. Equipping the HDI

In several steps, the two cables and the various chips (LVDS Repeater and Termination Chips) are glued to the HDI and wire-bonded. The time consuming part is the fact, that after each part was glued to the HDI, the glue needs roughly 12 hours to harden and only afterwards the wire-bonding can take place to connect the cables and the chips electrically to the HDI.

After wire-bonding, the HDI is tested in a laboratory setup. Criterias are the individual currents that the module draws as well as the distribution of power and control signals to all corresponding ROC pads. The LVDS Repeater and Termination Chips are tested as well. The main problems encountered were shortcuts in the power distribution, disconnected signal lines (Fig. 11.40) or defect Repeater Chips. If shortcuts are present, the HDI will not be considered any longer for the assembly. Except for the 2 cables, nothing can be recycled for further use. Disconnected lines are sometimes repairable with soldering paste. Defect Repeater Chips or Termination Chips are replaced. Due to very narrow wire-bond pads on the HDI, a chip shouldn't be replaced more than once.

4. Combine Sensor-ROC and Baseplate

The next step is to glue the sensor-ROC sandwich onto the baseplate. The glue was applied drop by drop to the baseplate. After the sensor was placed on the baseplate, an additional weight of 230 g was applied, to keep the sensor in position during the hardening of the glue.

5. The HDI is added

Now the HDI is glued to the sensor. Since the HDI is already fully equipped and wire-bonded, a special vacuum tool was designed, to hold the HDI while aligning it to the sensor. Again the glue is applied drop by drop and the HDI is kept in place by additional weights during the hardening. The difficulty is to control the two cables, which dominate the mechanical behaviour of the HDI. Therefore we tied them to a small metal extension to the vacuum block holding the HDI.

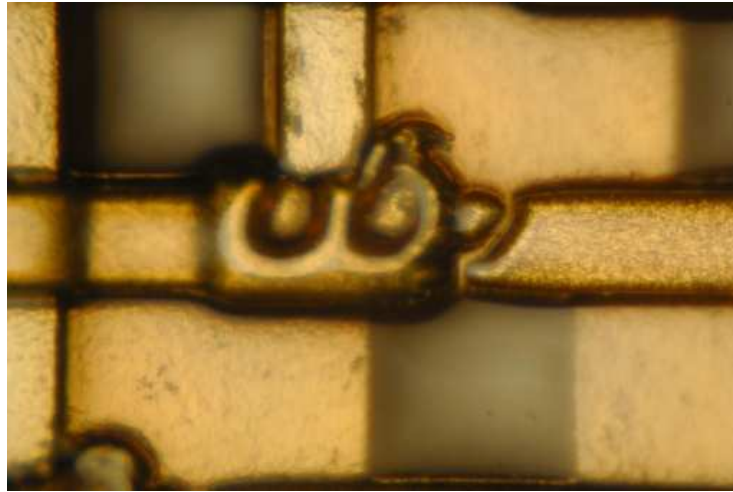


Figure 11.40: An HDI defect observed on a module.

6. Bending of the flaps

As a final glueing process we had to bend down the flaps of the HDI to the ROC. This involves two 12-hour-periods for hardening of the glue. Since the procedure was rather complicated and time-consuming, we decided to skip this step for further modules, and cut off the flaps. This was also motivated, due to the fact, that the next generation modules will not have these flaps.

Nevertheless, removing the flaps brings an important change to the assembly: The wire-bonds connecting the ROC to the HDI will now run from the ROC up to the sensor. To minimize the bondlength and for practical reasons, the new bond pads on the HDI are as close to the edge of the sensor as possible. Since there are no bump-bonds underneath the sensor edges, there is a reasonable risk of breaking the bumps by leverage. To avoid damage we had to ensure the mechanical stability under the sensor's edge. This was achieved by adding some glue underneath the sensor after bump-bonding and glueing the sensor-ROC sandwich to the baseplate (Fig. 11.41).

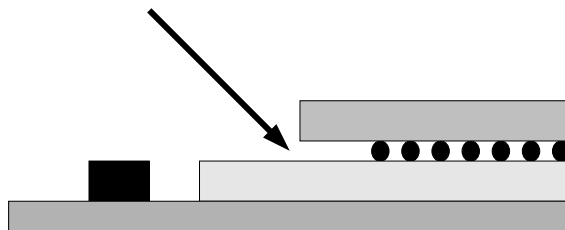


Figure 11.41: After the removal of the HDI flaps, the wire bonds have to be made on the sensor. For mechanical stability it was necessary to fill the gap between the sensor and the ROC (arrow) underneath the new bond pads with glue. This is done between step 4 and 5

Finally the ROCs are wire-bonded to the HDI pads. Fig. 11.42 shows the first Pixel Barrel Module using the PSI 43 DMILL Readout Chips assembled at PSI.

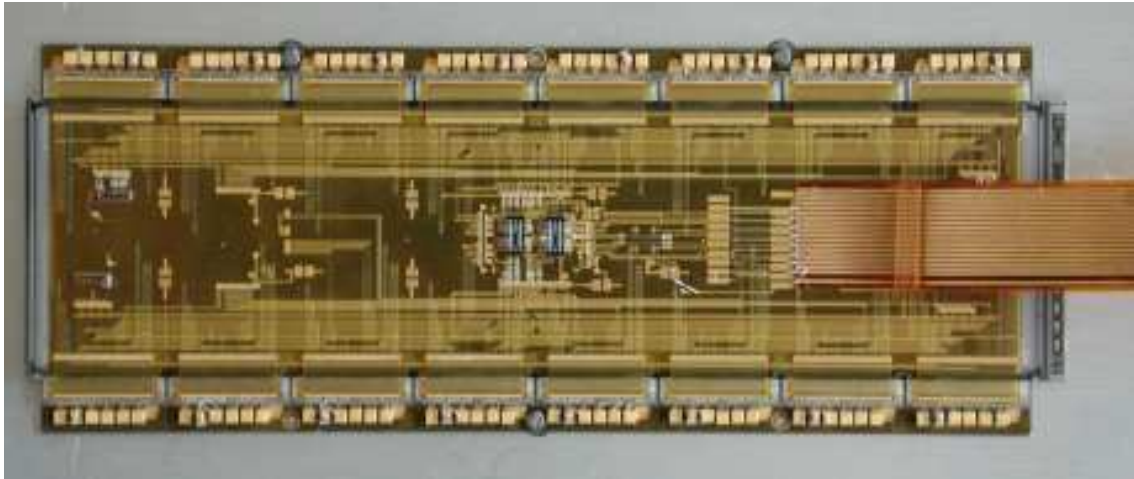


Figure 11.42: Prototype Module of the CMS Pixel Barrel Detector using the PSI 43 readout chip.

11.5 Module Test Setup

The module test setup is shown schematically in Fig 11.43. The same setup is also used to test the fully equipped HDI during the assembly. The pattern generator provides the essential differential control signals (Clock (CLK), Calibrate (CAL), Trigger (TRIG), Reset (RES) and the Readout Token Bit (RTB)) in a well defined sequence while the PC is used to program the ROCs by I²C. The supply voltage is set at -8 V which is regulated on the testboard to the required supply voltages for the ROCs. The module is mounted on a large aluminum block for basic cooling.

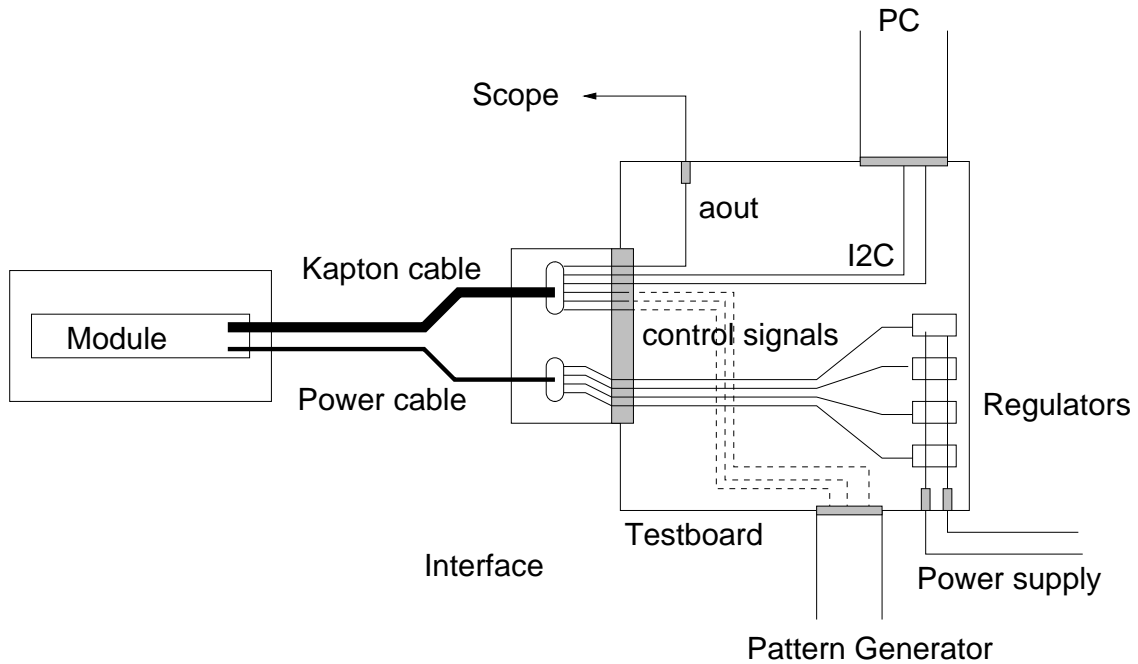


Figure 11.43: Test setup for modules. The components for the control signals (pattern generator and PC), power supply and the analog readout (aout) are identical as for the ROC test setup from Fig. 11.21. The testboard was also taken from the ROC setup but the interface had to be changed. Instead of the probecard, the capton cable and the power cable were used to broadcast the signals and supply voltages. The module itself is mounted on a large aluminum block for cooling purpose.

11.5.1 Impedance Matching

The control signals are sent through various different transmission lines from the generator to the module. Every time the state on the transmission line changes, there is an electric reflection due to an impedance mismatch. These reflections disturb the signal significantly (see Fig. 11.48). To reduce these disturbances, we had to adjust the impedance. The important transmission lines are the testboard (incl. the interface) and the kapton cable.

How to match impedance jumps?

For our purpose, it is sufficient to reduce the disturbances at the end of the transmission line, so-called back termination. This approach does have reflections coming from the module, but at every new transmission line, the reflections are properly terminated (on the way back). We don't care about reflections travelling backwards, as long as the forward signal is not disturbed.

The easiest termination is achieved by resistors. Assuming two transmission lines, with $Z_1 > Z_2$, the impedance is matched by adding a resistor in parallel R_P (Fig. 11.44(a)). Proper back termination requires

$$\frac{1}{Z_2} = \frac{1}{Z_1} + \frac{1}{R_P} \quad (11.4)$$

Back termination means, that the reflection coming from the test point (TP) is properly terminated. The signal coming from the Generator may be reflected, its reflection will be terminated at the other end.

If $Z_1 < Z_2$ a resistor is placed serial (Fig. 11.44(b)) and requires

$$Z_2 = Z_1 + R_S \quad (11.5)$$

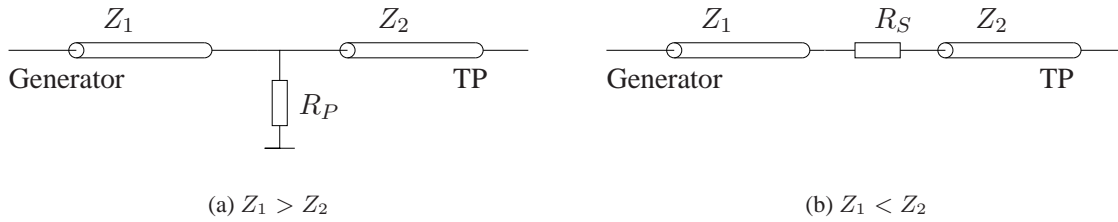


Figure 11.44: A simple impedance matching with parallel (left) and serial (right) resistor.

The most general resistive impedance match is shown in Fig. 11.45. This configuration allows not only to adjust the impedance, but also to regulate the voltage levels for digital signals. The boundary conditions are given by

$$Z_1 = R_1 + (R_3 || (R_2 + Z_2) || R_4) \quad (11.6)$$

$$Z_2 = R_2 + (R_3 || (R_1 + Z_1) || R_4) \quad (11.7)$$

Since we need only back termination, we don't need the resistor R_2 . The last boundary conditions are the voltage levels for the signals. The components on the HDI require roughly 200 mV between logic high and logic low for proper operation. The easiest approach is to interpret the termination resistors as voltage divider. For the two states (logic high and logic low from the generator) we get the two states shown in Fig. 11.46.

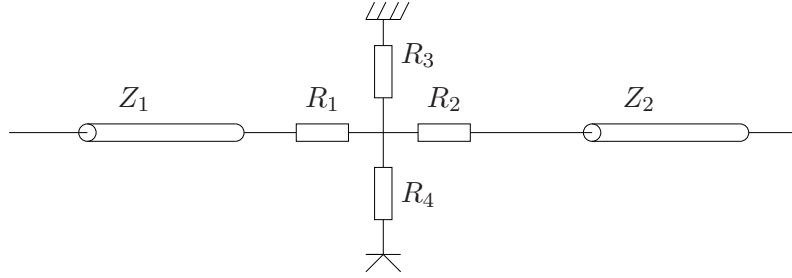


Figure 11.45: The most general impedance match using resistors.

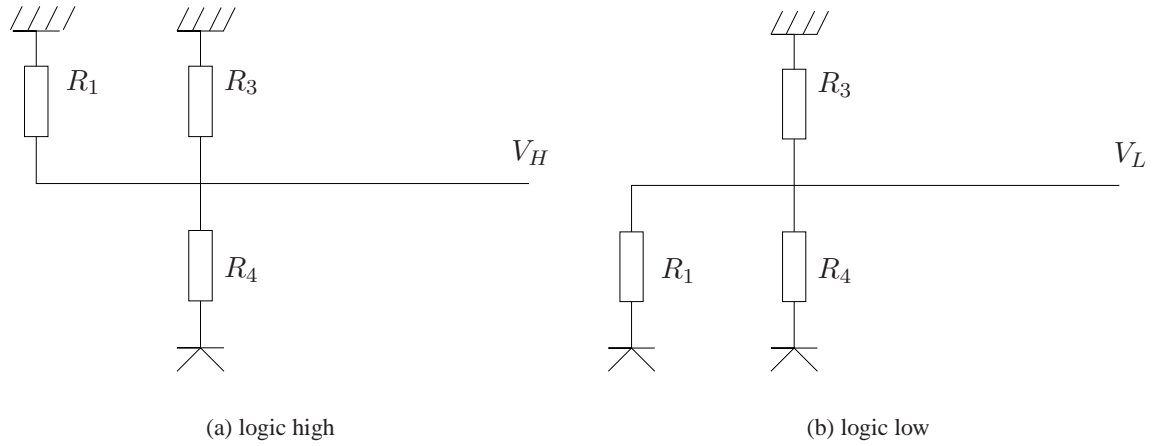


Figure 11.46: Voltage divider

Assuming no current is lost towards the module, the boundary conditions are given by

$$\frac{V_D}{V_H} = \frac{R_3 + (R_1 || R_4)}{R_3} \quad (11.8)$$

$$\frac{V_D}{V_L} = \frac{R_4 + (R_1 || R_3)}{R_1 || R_3} \quad (11.9)$$

In our case, we have the first impedance jump at the entrance to the testboard ($Z_1 = 50 \Omega \rightarrow Z_2 = 73 \Omega$) and the second impedance jump between the testboard and the kapton cable ($Z_1 = 73 \Omega \rightarrow Z_2 = 22 \Omega$). Eventually we ended up with the configuration shown in Fig. 11.47. The voltage levels are $V_H = -1.38 \text{ V}$ and $V_L = -1.58 \text{ V}$ with $\Delta V = 200 \text{ mV}$ as required.

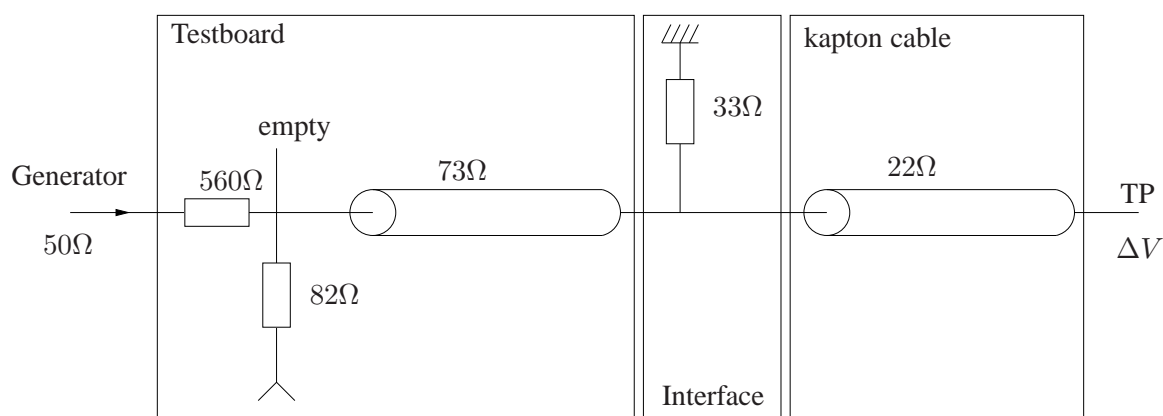


Figure 11.47: The configuration of the impedance matching as it is done for the test setup of the prototype PSI 43 module.

Fig. 11.48 shows a CLK line on the HDI before the impedance match and after. The improvement is clearly visible.

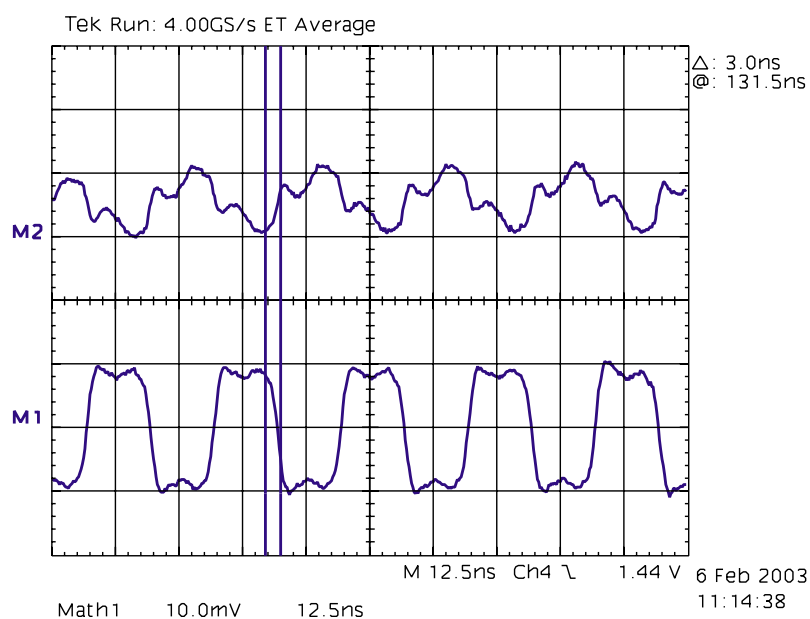


Figure 11.48: The clock line before (upper curve) and after (lower curve) the impedance matching. The voltage difference for the lower curve corresponds to the required 200 mV.

11.6 Results

A total of 6 modules were assembled. First a dummy prototype, followed by three first generation modules and finally two mechanical studies with thinned ROC's. Among the three first generation modules one caused major troubles while wire-bonding and was therefore never operational. The remaining two modules were tested electrically. Both modules were basically working and passed the RTB through the ROC and returned it properly. The analog readout signal showed for the first time all expected Ultrablacks (Chip headers) (Fig. 11.49).

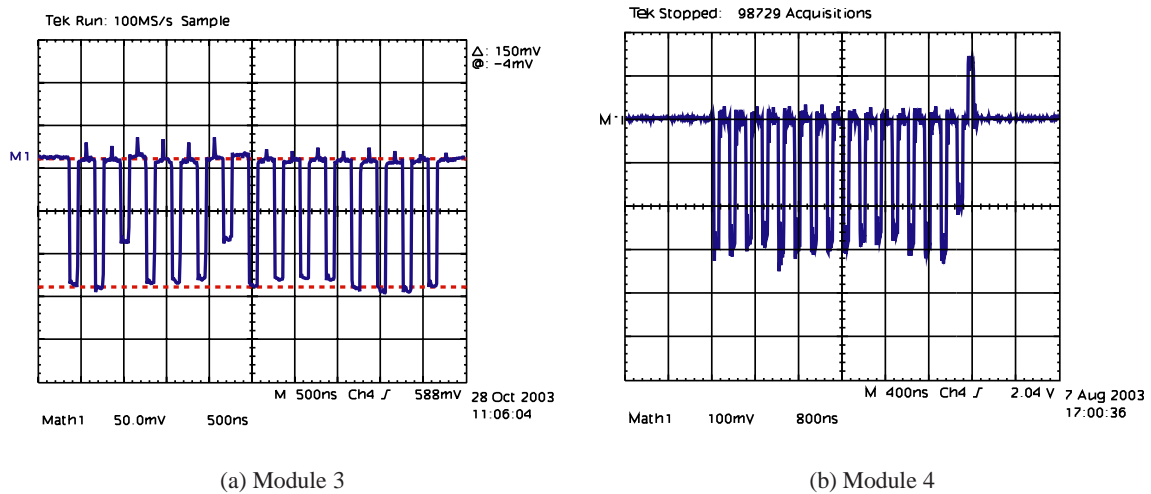


Figure 11.49: All Ultrablacks for the two operational first generation modules. The last ROC on Module 3 was defect and therefore unable to send its header while Module 4 sends all 16 chip headers!

11.6.1 Assembly Line

During the assembly of the first generation modules, many improvements were extracted for future designs and components. But we also learned what mechanical tools are necessary for mass production of the 800 modules needed for the full Barrel. This know-how leads to the development of an assembly line, consisting of 6 tools and various smaller aids for efficient module production. Together with the improvements in design and material, the future capacity of module production is expected to be four modules per day.

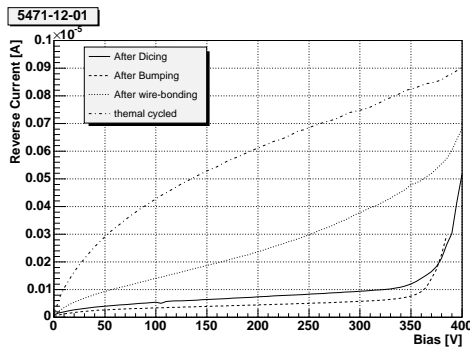
11.6.2 Sensor Leakage Current

Mechanical stress and deformations have an impact on the leakage currents of the Silicon sensor. Both happen during the assembly as well as during installation and operation of the modules. To measure the influence of the assembly on the leakage current, two modules with thinned ROC's were assembled, using the new assembly line at PSI. The major assembly steps for the sensor are:

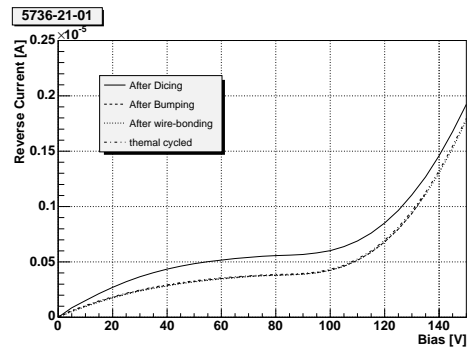
1. Dicing
2. Bump-bonding of the ROC, including reflow and pull-up test
3. Wire-bonding the ROC to the HDI
4. Thermal cycling

At CMS, the pixel detector is supposed to be operated at -10°C . As a first prototype experiment, the modules were heated to 30°C and cooled to -20°C in a thermal cycle, repeated 10 times for about 24 hours.

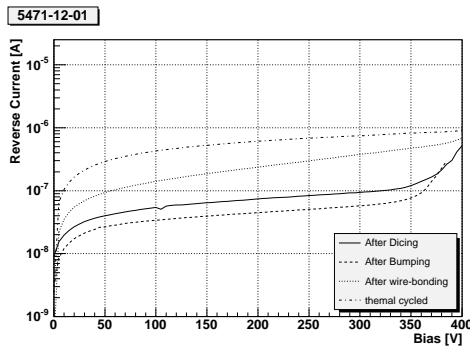
The leakage current was measured after each major assembly step and is shown in Fig. 11.50.



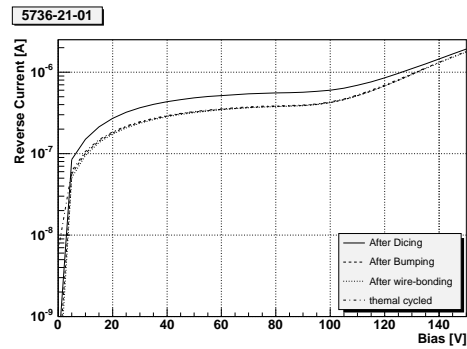
(a) Module 5 with linear scale



(b) Module 6 with linear scale



(c) Module 5 with logarithmic scale



(d) Module 6 with logarithmic scale

Figure 11.50: Leakage current of two modules with thinned ROCs after the major assembly steps and the thermal cycling. The bump-bonding induces a healing which reduced the leakage current w.r.t. to the diced sensors. The further assembly steps and the thermal cycling lead to an increased leakage current but still within a tolerable range.

As a very obvious result, the leakage current does not increase dramatically. The assembly line being at room temperature followed by cooling to -10°C seems to be safe.

As one would expect every step to stress the sensor, it is quite interesting to see a decrease after bump-bonding. It can be explained by the reflow procedure. Heating the sensor to 150°C has some healing effects and causes a decrease in the leakage current.

Appendix A

Cross Section Tables

Cross Section for $\langle t \rangle = -0.01 \text{ GeV}^2$									
	Diffractive $\gamma p \rightarrow \rho^0 Y$			Elastic $\gamma p \rightarrow \rho^0 p$			Proton-dissociative $\gamma p \rightarrow \rho^0 Y$		
$\langle W_{\gamma p} \rangle$ [GeV]	$d\sigma^{\gamma p}/dt$ [$\mu\text{b}/\text{GeV}^2$]	σ_{stat}	σ_{sys}	$d\sigma^{\gamma p}/dt$ [$\mu\text{b}/\text{GeV}^2$]	σ_{stat}	σ_{sys}	$d\sigma^{\gamma p}/dt$ [$\mu\text{b}/\text{GeV}^2$]	σ_{stat}	σ_{sys}
21.5	74.2262	± 1.5	$^{+1.7}_{-1.7}$	62.2399	± 1.5	$^{+2.3}_{-2.4}$	11.9863	± 0.56	$^{+2.7}_{-2.6}$
24.5	74.2767	± 1.7	$^{+0.75}_{-0.81}$	63.3733	± 1.7	$^{+1.9}_{-2.0}$	10.9034	± 0.56	$^{+2.4}_{-2.4}$
27.5	81.1206	± 1.9	$^{+0.94}_{-0.98}$	71.0218	± 1.9	$^{+1.9}_{-2.0}$	10.0988	± 0.56	$^{+2.2}_{-2.2}$
31.0	79.0379	± 1.7	$^{+1.0}_{-1.0}$	67.6983	± 1.7	$^{+2.4}_{-2.4}$	11.3395	± 0.58	$^{+2.4}_{-2.4}$
35.5	84.7713	± 1.7	$^{+1.1}_{-1.1}$	73.9449	± 1.8	$^{+2.1}_{-2.2}$	10.8264	± 0.56	$^{+2.4}_{-2.3}$
40.5	88.8994	± 2.0	$^{+0.86}_{-0.89}$	78.1092	± 2.0	$^{+2.1}_{-2.2}$	10.7902	± 0.59	$^{+2.3}_{-2.3}$
46.0	92.7448	± 2.0	$^{+0.71}_{-0.75}$	82.0087	± 2.0	$^{+2.0}_{-2.1}$	10.7361	± 0.59	$^{+2.3}_{-2.3}$
52.0	99.5798	± 2.2	$^{+0.82}_{-0.89}$	88.3209	± 2.2	$^{+2.0}_{-2.1}$	11.2588	± 0.64	$^{+2.5}_{-2.4}$
58.0	101.5258	± 2.4	$^{+1.2}_{-1.2}$	91.3239	± 2.4	$^{+2.0}_{-2.0}$	10.2020	± 0.64	$^{+2.2}_{-2.2}$
65.0	106.8372	± 2.5	$^{+3.0}_{-3.0}$	96.0139	± 2.5	$^{+3.0}_{-3.1}$	10.8233	± 0.67	$^{+2.4}_{-2.4}$

Table A.1: Cross sections for $0.00 < |t| < 0.02 \text{ GeV}^2$

Cross Section for $\langle t \rangle = -0.03 \text{ GeV}^2$									
	Diffractive $\gamma p \rightarrow \rho^0 Y$			Elastic $\gamma p \rightarrow \rho^0 p$			Proton-dissociative $\gamma p \rightarrow \rho^0 Y$		
$\langle W_{\gamma p} \rangle$ [GeV]	$d\sigma^{\gamma p}/dt$ [$\mu\text{b}/\text{GeV}^2$]	σ_{stat}	σ_{sys}	$d\sigma^{\gamma p}/dt$ [$\mu\text{b}/\text{GeV}^2$]	σ_{stat}	σ_{sys}	$d\sigma^{\gamma p}/dt$ [$\mu\text{b}/\text{GeV}^2$]	σ_{stat}	σ_{sys}
21.5	62.0832	± 1.1	$+1.4$ -1.4	52.9255	± 1.1	$+2.3$ -2.4	9.1577	± 0.39	$+2.0$ -1.9
24.5	63.8621	± 1.1	$+0.53$ -0.56	52.6543	± 1.1	$+2.3$ -2.4	11.2078	± 0.43	$+2.5$ -2.4
27.5	67.1516	± 1.4	$+0.95$ -0.98	57.6020	± 1.4	$+2.0$ -2.1	9.5496	± 0.44	$+2.1$ -2.1
31.0	68.7926	± 1.4	$+1.1$ -1.1	58.1040	± 1.3	$+2.2$ -2.4	10.6886	± 0.46	$+2.4$ -2.3
35.5	69.5310	± 1.1	$+1.0$ -1.0	60.5013	± 1.1	$+1.7$ -1.9	9.0298	± 0.37	$+2.1$ -2.0
40.5	73.1663	± 1.2	$+1.0$ -1.1	64.2424	± 1.2	$+1.3$ -1.5	8.9239	± 0.39	$+2.1$ -2.0
46.0	78.1203	± 1.3	$+1.0$ -1.0	67.8952	± 1.3	$+1.5$ -1.6	10.2251	± 0.42	$+2.4$ -2.3
52.0	80.0969	± 1.4	$+1.4$ -1.3	70.4209	± 1.4	$+1.0$ -1.1	9.6760	± 0.43	$+2.3$ -2.2
58.0	84.9680	± 1.6	$+1.8$ -1.7	73.4172	± 1.6	$+1.5$ -1.5	11.5508	± 0.51	$+2.8$ -2.6
65.0	86.6060	± 1.6	$+3.1$ -2.9	76.0517	± 1.6	$+2.2$ -2.2	10.5543	± 0.48	$+2.6$ -2.4

Table A.2: Cross sections for $0.02 < |t| < 0.05 \text{ GeV}^2$

Cross Section for $\langle t \rangle = -0.07 \text{ GeV}^2$									
	Diffractive $\gamma p \rightarrow \rho^0 Y$			Elastic $\gamma p \rightarrow \rho^0 p$			Proton-dissociative $\gamma p \rightarrow \rho^0 Y$		
$\langle W_{\gamma p} \rangle$ [GeV]	$d\sigma^{\gamma p}/dt$ [$\mu\text{b}/\text{GeV}^2$]	σ_{stat}	σ_{sys}	$d\sigma^{\gamma p}/dt$ [$\mu\text{b}/\text{GeV}^2$]	σ_{stat}	σ_{sys}	$d\sigma^{\gamma p}/dt$ [$\mu\text{b}/\text{GeV}^2$]	σ_{stat}	σ_{sys}
24.0	47.9534	± 1.3	$+0.35$ -0.36	39.7027	± 1.2	$+1.7$ -1.9	8.2507	± 0.40	$+1.9$ -1.8
26.5	48.5480	± 1.0	$+0.61$ -0.62	40.3899	± 1.00	$+1.7$ -1.9	8.1581	± 0.35	$+1.9$ -1.8
29.5	50.5837	± 1.1	$+0.87$ -0.90	42.0752	± 1.1	$+1.7$ -1.9	8.5086	± 0.37	$+2.0$ -1.9
33.0	49.9999	± 1.1	$+0.90$ -0.92	42.1183	± 1.0	$+1.5$ -1.7	7.8816	± 0.35	$+1.9$ -1.7
37.5	53.4148	± 0.89	$+0.80$ -0.81	45.9532	± 0.88	$+1.3$ -1.5	7.4616	± 0.30	$+1.8$ -1.6
43.0	55.2898	± 0.91	$+0.86$ -0.87	47.5208	± 0.90	$+1.1$ -1.3	7.7690	± 0.31	$+1.9$ -1.7
49.5	57.5152	± 0.93	$+1.1$ -1.0	49.7845	± 0.92	$+0.84$ -1.1	7.7306	± 0.31	$+2.0$ -1.8
56.5	59.9429	± 1.2	$+1.4$ -1.3	52.1014	± 1.2	$+0.75$ -0.96	7.8416	± 0.36	$+2.0$ -1.8
63.0	65.9733	± 1.3	$+2.3$ -2.2	57.8331	± 1.3	$+1.3$ -1.5	8.1402	± 0.38	$+2.2$ -1.9
70.0	62.5116	± 1.3	$+3.3$ -3.2	54.9676	± 1.3	$+2.4$ -2.5	7.5439	± 0.36	$+2.1$ -1.8

Table A.3: Cross sections for $0.05 < |t| < 0.09 \text{ GeV}^2$

Cross Section for $\langle t \rangle = -0.12 \text{ GeV}^2$									
	Diffractive $\gamma p \rightarrow \rho^0 Y$			Elastic $\gamma p \rightarrow \rho^0 p$			Proton-dissociative $\gamma p \rightarrow \rho^0 Y$		
$\langle W_{\gamma p} \rangle$ [GeV]	$d\sigma^{\gamma p}/dt$ [$\mu\text{b}/\text{GeV}^2$]	σ_{stat}	σ_{sys}	$d\sigma^{\gamma p}/dt$ [$\mu\text{b}/\text{GeV}^2$]	σ_{stat}	σ_{sys}	$d\sigma^{\gamma p}/dt$ [$\mu\text{b}/\text{GeV}^2$]	σ_{stat}	σ_{sys}
24.0	30.2775	± 0.81	$+0.29$ -0.30	24.4110	± 0.77	$+1.6$ -1.3	5.8666	± 0.27	$+1.3$ -1.6
26.5	31.6162	± 0.54	$+0.42$ -0.43	26.1667	± 0.53	$+1.5$ -1.2	5.4494	± 0.20	$+1.2$ -1.6
29.5	31.7501	± 0.72	$+0.59$ -0.61	25.7470	± 0.70	$+1.6$ -1.3	6.0031	± 0.25	$+1.4$ -1.7
33.0	31.9064	± 0.68	$+0.60$ -0.61	25.6446	± 0.65	$+1.6$ -1.3	6.2618	± 0.24	$+1.4$ -1.7
37.5	32.8234	± 0.66	$+0.60$ -0.62	26.7759	± 0.64	$+1.5$ -1.1	6.0474	± 0.23	$+1.4$ -1.7
43.0	34.2480	± 0.55	$+0.63$ -0.62	28.0624	± 0.53	$+1.4$ -0.98	6.1855	± 0.21	$+1.5$ -1.8
49.5	35.7938	± 0.57	$+0.78$ -0.74	29.7828	± 0.56	$+1.4$ -0.75	6.0110	± 0.21	$+1.5$ -1.8
56.5	37.6564	± 0.65	$+1.1$ -1.0	31.1841	± 0.63	$+1.4$ -0.67	6.4723	± 0.23	$+1.6$ -1.9
63.0	38.6866	± 0.78	$+1.5$ -1.4	32.9264	± 0.76	$+1.5$ -0.77	5.7601	± 0.24	$+1.5$ -1.9
70.0	38.5089	± 0.79	$+2.2$ -2.0	32.2859	± 0.77	$+1.9$ -1.3	6.2230	± 0.25	$+1.7$ -2.0

Table A.4: Cross sections for $0.09 < |t| < 0.16 \text{ GeV}^2$

Cross Section for $\langle t \rangle = -0.19 \text{ GeV}^2$									
	Diffractive $\gamma p \rightarrow \rho^0 Y$			Elastic $\gamma p \rightarrow \rho^0 p$			Proton-dissociative $\gamma p \rightarrow \rho^0 Y$		
$\langle W_{\gamma p} \rangle$ [GeV]	$d\sigma^{\gamma p}/dt$ [$\mu\text{b}/\text{GeV}^2$]	σ_{stat}	σ_{sys}	$d\sigma^{\gamma p}/dt$ [$\mu\text{b}/\text{GeV}^2$]	σ_{stat}	σ_{sys}	$d\sigma^{\gamma p}/dt$ [$\mu\text{b}/\text{GeV}^2$]	σ_{stat}	σ_{sys}
26.0	18.1357	± 0.40	$+0.26$ -0.27	14.1460	± 0.38	$+1.1$ -0.98	3.9897	± 0.17	$+0.99$ -1.1
33.0	19.8102	± 0.42	$+0.39$ -0.40	15.8119	± 0.40	$+1.1$ -0.91	3.9983	± 0.17	$+1.0$ -1.2
42.0	20.1126	± 0.44	$+0.44$ -0.43	16.0143	± 0.42	$+1.0$ -0.78	4.0983	± 0.17	$+1.1$ -1.3
53.5	21.4902	± 0.46	$+0.72$ -0.66	17.6643	± 0.45	$+0.99$ -0.52	3.8259	± 0.17	$+1.1$ -1.3
67.5	23.2163	± 0.55	$+1.3$ -1.1	18.4529	± 0.52	$+1.1$ -0.75	4.7634	± 0.21	$+1.4$ -1.5

Table A.5: Cross sections for $0.16 < |t| < 0.22 \text{ GeV}^2$

Cross Section for $\langle t \rangle = -0.26 \text{ GeV}^2$									
	Diffractive $\gamma p \rightarrow \rho^0 Y$			Elastic $\gamma p \rightarrow \rho^0 p$			Proton-dissociative $\gamma p \rightarrow \rho^0 Y$		
$\langle W_{\gamma p} \rangle$ [GeV]	$d\sigma^{\gamma p}/dt$ [$\mu\text{b}/\text{GeV}^2$]	σ_{stat}	σ_{sys}	$d\sigma^{\gamma p}/dt$ [$\mu\text{b}/\text{GeV}^2$]	σ_{stat}	σ_{sys}	$d\sigma^{\gamma p}/dt$ [$\mu\text{b}/\text{GeV}^2$]	σ_{stat}	σ_{sys}
26.0	10.9512	± 0.27	$+0.26$ -0.26	8.0059	± 0.26	$+0.80$ -0.71	2.9453	± 0.13	$+0.71$ -0.81
33.0	11.7449	± 0.28	$+0.28$ -0.28	8.4173	± 0.27	$+0.82$ -0.73	3.3276	± 0.14	$+0.84$ -0.91
42.0	11.9044	± 0.30	$+0.35$ -0.33	8.6763	± 0.29	$+0.72$ -0.59	3.2281	± 0.15	$+0.87$ -0.92
53.5	12.8561	± 0.25	$+0.54$ -0.47	9.7922	± 0.24	$+0.65$ -0.40	3.0639	± 0.12	$+0.88$ -0.94
67.5	13.3057	± 0.28	$+0.88$ -0.76	9.7966	± 0.26	$+0.68$ -0.42	3.5091	± 0.14	$+1.1$ -1.1

Table A.6: Cross sections for $0.22 < |t| < 0.30 \text{ GeV}^2$

Cross Section for $\langle t \rangle = -0.38 \text{ GeV}^2$									
	Diffractive $\gamma p \rightarrow \rho^0 Y$			Elastic $\gamma p \rightarrow \rho^0 p$			Proton-dissociative $\gamma p \rightarrow \rho^0 Y$		
$\langle W_{\gamma p} \rangle$ [GeV]	$d\sigma^{\gamma p}/dt$ [$\mu\text{b}/\text{GeV}^2$]	σ_{stat}	σ_{sys}	$d\sigma^{\gamma p}/dt$ [$\mu\text{b}/\text{GeV}^2$]	σ_{stat}	σ_{sys}	$d\sigma^{\gamma p}/dt$ [$\mu\text{b}/\text{GeV}^2$]	σ_{stat}	σ_{sys}
26.0	4.6749	± 0.12	$+0.20$ -0.20	2.6125	± 0.11	$+0.51$ -0.57	2.0624	± 0.085	$+0.58$ -0.53
33.0	5.0653	± 0.12	$+0.20$ -0.20	2.8725	± 0.11	$+0.50$ -0.57	2.1928	± 0.084	$+0.66$ -0.58
42.0	5.5820	± 0.13	$+0.27$ -0.25	3.2306	± 0.12	$+0.48$ -0.56	2.3514	± 0.090	$+0.76$ -0.65
53.5	5.7200	± 0.13	$+0.36$ -0.31	3.3889	± 0.12	$+0.41$ -0.49	2.3311	± 0.088	$+0.82$ -0.67
67.5	5.6643	± 0.16	$+0.50$ -0.41	3.3457	± 0.14	$+0.36$ -0.43	2.3186	± 0.10	$+0.89$ -0.70

Table A.7: Cross sections for $0.30 < |t| < 0.50 \text{ GeV}^2$

Cross Section for $\langle t \rangle = -0.58 \text{ GeV}^2$									
	Diffractive $\gamma p \rightarrow \rho^0 Y$			Elastic $\gamma p \rightarrow \rho^0 p$			Proton-dissociative $\gamma p \rightarrow \rho^0 Y$		
$\langle W_{\gamma p} \rangle$ [GeV]	$d\sigma^{\gamma p}/dt$ [$\mu\text{b}/\text{GeV}^2$]	σ_{stat}	σ_{sys}	$d\sigma^{\gamma p}/dt$ [$\mu\text{b}/\text{GeV}^2$]	σ_{stat}	σ_{sys}	$d\sigma^{\gamma p}/dt$ [$\mu\text{b}/\text{GeV}^2$]	σ_{stat}	σ_{sys}
26.0	1.6553	± 0.079	$+0.13$ -0.13	0.3628	± 0.073	$+0.54$ -0.37	1.2925	± 0.088	$+0.39$ -0.56
33.5	1.7522	± 0.072	$+0.13$ -0.13	0.5149	± 0.067	$+0.54$ -0.39	1.2372	± 0.077	$+0.45$ -0.57
43.0	1.9533	± 0.082	$+0.15$ -0.14	0.5493	± 0.077	$+0.59$ -0.44	1.4039	± 0.089	$+0.56$ -0.66
55.0	2.0462	± 0.084	$+0.20$ -0.17	0.5137	± 0.078	$+0.62$ -0.48	1.5325	± 0.094	$+0.67$ -0.72
69.5	1.9534	± 0.094	$+0.25$ -0.19	0.4968	± 0.087	$+0.58$ -0.46	1.4566	± 0.10	$+0.70$ -0.70

Table A.8: Cross sections for $0.50 < |t| < 0.70 \text{ GeV}^2$

Cross Section for $\langle t \rangle = -0.81 \text{ GeV}^2$									
	Diffractive $\gamma p \rightarrow \rho^0 Y$			Elastic $\gamma p \rightarrow \rho^0 p$			Proton-dissociative $\gamma p \rightarrow \rho^0 Y$		
$\langle W_{\gamma p} \rangle$ [GeV]	$d\sigma^{\gamma p}/dt$ [$\mu\text{b}/\text{GeV}^2$]	σ_{stat}	σ_{sys}	$d\sigma^{\gamma p}/dt$ [$\mu\text{b}/\text{GeV}^2$]	σ_{stat}	σ_{sys}	$d\sigma^{\gamma p}/dt$ [$\mu\text{b}/\text{GeV}^2$]	σ_{stat}	σ_{sys}
26.0	0.5562	± 0.038	$+0.083$ -0.083	-	-	-	0.4487	± 0.045	$+0.13$ -0.24
33.5	0.6645	± 0.036	$+0.086$ -0.086	-	-	-	0.5796	± 0.047	$+0.13$ -0.30
43.0	0.6789	± 0.040	$+0.081$ -0.075	-	-	-	0.6093	± 0.053	$+0.14$ -0.31
55.0	0.6960	± 0.043	$+0.087$ -0.072	-	-	-	0.6647	± 0.058	$+0.12$ -0.33
69.5	0.7740	± 0.051	$+0.11$ -0.085	-	-	-	0.6798	± 0.064	$+0.21$ -0.36

Table A.9: Cross sections for $0.70 < |t| < 1.00 \text{ GeV}^2$

Cross Section for $\langle t \rangle = -1.16 \text{ GeV}^2$									
	Diffractive $\gamma p \rightarrow \rho^0 Y$			Elastic $\gamma p \rightarrow \rho^0 p$			Proton-dissociative $\gamma p \rightarrow \rho^0 Y$		
$\langle W_{\gamma p} \rangle$ [GeV]	$d\sigma^{\gamma p}/dt$ [$\mu\text{b}/\text{GeV}^2$]	σ_{stat}	σ_{sys}	$d\sigma^{\gamma p}/dt$ [$\mu\text{b}/\text{GeV}^2$]	σ_{stat}	σ_{sys}	$d\sigma^{\gamma p}/dt$ [$\mu\text{b}/\text{GeV}^2$]	σ_{stat}	σ_{sys}
26.5	0.5562	± 0.038	$+0.083$ -0.083	-	-	-	0.4487	± 0.045	$+0.13$ -0.24
33.5	0.6645	± 0.036	$+0.086$ -0.086	-	-	-	0.5796	± 0.047	$+0.13$ -0.30
44.0	0.6789	± 0.040	$+0.081$ -0.075	-	-	-	0.6093	± 0.053	$+0.14$ -0.31
57.5	0.6960	± 0.043	$+0.087$ -0.072	-	-	-	0.6647	± 0.058	$+0.12$ -0.33
75.0	0.7740	± 0.051	$+0.11$ -0.085	-	-	-	0.6798	± 0.064	$+0.21$ -0.36

Table A.10: Cross sections for $1.00 < |t| < 1.50 \text{ GeV}^2$

Cross Section for $\langle t \rangle = -1.66 \text{ GeV}^2$									
	Diffractive $\gamma p \rightarrow \rho^0 Y$			Elastic $\gamma p \rightarrow \rho^0 p$			Proton-dissociative $\gamma p \rightarrow \rho^0 Y$		
$\langle W_{\gamma p} \rangle$ [GeV]	$d\sigma^{\gamma p}/dt$ [$\mu\text{b}/\text{GeV}^2$]	σ_{stat}	σ_{sys}	$d\sigma^{\gamma p}/dt$ [$\mu\text{b}/\text{GeV}^2$]	σ_{stat}	σ_{sys}	$d\sigma^{\gamma p}/dt$ [$\mu\text{b}/\text{GeV}^2$]	σ_{stat}	σ_{sys}
27.5	0.5562	± 0.038	$+0.083$ -0.083	-	-	-	0.4487	± 0.045	$+0.13$ -0.24
35.0	0.6645	± 0.036	$+0.086$ -0.086	-	-	-	0.5796	± 0.047	$+0.13$ -0.30
46.0	0.6789	± 0.040	$+0.081$ -0.075	-	-	-	0.6093	± 0.053	$+0.14$ -0.31
60.5	0.6960	± 0.043	$+0.087$ -0.072	-	-	-	0.6647	± 0.058	$+0.12$ -0.33
79.5	0.7740	± 0.051	$+0.11$ -0.085	-	-	-	0.6798	± 0.064	$+0.21$ -0.36

Table A.11: Cross sections for $1.50 < |t| < 2.00 \text{ GeV}^2$

Cross Section for $\langle t \rangle = -2.23 \text{ GeV}^2$									
	Diffractive $\gamma p \rightarrow \rho^0 Y$			Elastic $\gamma p \rightarrow \rho^0 p$			Proton-dissociative $\gamma p \rightarrow \rho^0 Y$		
$\langle W_{\gamma p} \rangle$ [GeV]	$d\sigma^{\gamma p}/dt$ [$\mu\text{b}/\text{GeV}^2$]	σ_{stat}	σ_{sys}	$d\sigma^{\gamma p}/dt$ [$\mu\text{b}/\text{GeV}^2$]	σ_{stat}	σ_{sys}	$d\sigma^{\gamma p}/dt$ [$\mu\text{b}/\text{GeV}^2$]	σ_{stat}	σ_{sys}
27.5	0.5562	± 0.038	$^{+0.083}_{-0.083}$	-	-	-	0.4487	± 0.045	$^{+0.13}_{-0.24}$
35.0	0.6645	± 0.036	$^{+0.086}_{-0.086}$	-	-	-	0.5796	± 0.047	$^{+0.13}_{-0.30}$
46.0	0.6789	± 0.040	$^{+0.081}_{-0.075}$	-	-	-	0.6093	± 0.053	$^{+0.14}_{-0.31}$
60.5	0.6960	± 0.043	$^{+0.087}_{-0.072}$	-	-	-	0.6647	± 0.058	$^{+0.12}_{-0.33}$
79.5	0.7740	± 0.051	$^{+0.11}_{-0.085}$	-	-	-	0.6798	± 0.064	$^{+0.21}_{-0.36}$

Table A.12: Cross sections for $2.00 < |t| < 3.00 \text{ GeV}^2$

List of Figures

1.1	Total Cross Section	3
2.1	Two body reactions	5
2.2	Generic ep scattering	6
2.3	ρ^0 production process	8
2.4	Vector meson production in VDM	9
2.5	Diffraction processes	10
2.6	REGGE trajectories	13
2.7	Reggeon exchange	14
2.8	Pomeron trajectory with glueball candidate	16
2.9	BFKL production process	16
3.1	$W_{\gamma p}$ and t Reweighting	22
3.2	$m_{\pi\pi}$ and Z-Vertex Reweighting	24
4.1	The HERA collider	25
4.2	Side view of H1	29
4.3	The H1 tracking system	30
4.4	The central tracking chambers	32
4.5	The LAr calorimeter	34
4.6	The Forward Muon Detector	35
4.7	The FTS	36
4.8	The Luminosity system	38
5.1	Location of trigger layers in the CJC	40
5.2	Track segment finding	40
5.3	From track segments to track candidates.	41
5.4	FTT offline matching with an artificial event.	45
5.5	FTT offline matching with a typical ρ^0 event.	46
6.1	CJC Gain versus electron beam current	50
6.2	CJC gain for both rings	50
6.3	Uncorrected Yield Plot	50
6.4	Yield versus Gain	51
6.5	Corrected Yield Plot	52
6.6	Pull Plot	52

6.7	Mean Q_{gen}^2 in W/t -bins	53
6.8	$m_{\pi\pi}$ comparison of reconstructed versus generated values.	54
6.9	$W_{\gamma p}$ comparison of reconstructed versus generated values.	55
6.10	Kinematic Variable $W_{\gamma p}$	56
6.11	t comparison of reconstructed versus generated values.	57
6.12	Kinematic Variable t	57
6.13	Q^2 contribution versus t	58
6.14	Z-Vertex Distribution	59
6.15	Unassociated Energy	60
6.16	Transverse Momentum of Tracks	61
6.17	Theta of Tracks	62
6.18	Invariant Mass	62
6.19	The W/t -bin edges	63
6.20	The W/t -bins in $W_{\gamma p}$ - t plane	64
6.21	Invariant Mass Distribution	66
6.22	π production processes	67
6.23	Ross-Stodolsky Fit Method	68
6.24	Söding Fit Method	69
6.25	FTS subdetector response	70
6.26	FMD subdetector response	71
6.27	FTS station response	71
6.28	Forward detector noise contributions	72
6.29	Forward detector responses with noise	73
6.30	Tagging probability	74
6.31	Forward tag dependence on M_Y	74
6.32	Background processes	75
7.1	Acceptance for each W/t -bin	79
7.2	Acceptance for selected W/t -bins	80
7.3	Reconstruction efficiency	81
7.4	Migrations between W/t -bins.	82
7.5	Uncorrected FTT Efficiencies	84
7.6	FTT efficiency correction function	85
7.7	Corrected FTT Efficiencies	86
7.8	CIP trigger efficiency	87
7.9	FTT and CIP Trigger corrections.	87
7.10	LAr IF veto versus unassociated energy cut	88
7.11	Trigger efficiency	89
7.12	Overall Correction	90
8.1	Integrated Mass Spectra with fit results	92
8.2	Fit parameters of the ρ^0 for the Ross-Stodolsky model	93
8.3	Fit parameters of the ρ^0 for the Söding model	94
8.4	Tagged events	95

8.5	Tagging probabilities versus tagging fraction.	97
8.6	Differential cross sections	98
8.7	Differential cross sections	99
8.8	Differential cross sections	99
8.9	Systematic checks for the FTT Efficiencies	102
8.10	Systematic checks on elastic $d\sigma^{\gamma p}/dt$	103
8.11	Systematic class errors on elastic $d\sigma^{\gamma p}/dt$	105
8.12	Systematic error on elastic $d\sigma^{\gamma p}/dt$	106
9.1	Diffraction process $\gamma p \rightarrow \rho^0 Y$	108
9.2	Elastic process $\gamma p \rightarrow \rho^0 p$ for each t value	109
9.3	Proton-dissociative process $\gamma p \rightarrow \rho^0 Y$	110
9.4	Elastic $W_{\gamma p}$ slopes	111
9.5	Diffraction ρ^0 photoproduction	113
9.6	Proton-dissociative ρ^0 photoproduction	114
9.7	Systematic class errors for the energy dependence	115
9.8	Total systematic error for the energy dependence	116
9.9	Systematic class errors for the pomeron trajectory	117
11.1	Secondary vertices and impact parameters	123
11.2	Multiple coulomb scattering of charged particles in matter	124
11.3	CMS pixel barrel	125
11.4	Pixel Barrel Module	127
11.5	Overview of the PUC	128
11.6	Column drain mechanism	129
11.7	Analog readout of the ROC	130
11.8	PSI 43 ROC readout scheme	131
11.9	p-in-n sensor	132
11.10	Type inversion	132
11.11	n-in-n sensor	133
11.12	p-stop design for the PSI 43 module	134
11.13	Module sideview, narrow baseplate	134
11.14	HDI outline	135
11.15	Layout of the voltage distribution	137
11.16	Module Readout	138
11.17	Dual TBM Chip	139
11.18	Termination scheme	139
11.19	CLK simulation and measurement	140
11.20	Kapton cable	141
11.21	Setup for ROC testing	142
11.22	Internal reference voltage	144
11.23	DAC ranges for PSI 43 ROC	145
11.24	Assembly Overview	146
11.25	Bare wafer with bump-bonds	147

11.26	Photoresist is applied	147
11.27	Bump-bond openings	147
11.28	Under Bump Metal	147
11.29	Indium layer for ROC wafer	147
11.30	Photoresist lift-off for ROC wafer	147
11.31	Photoresist lift-off for sensor wafer	147
11.32	Second layer photoresist for sensor wafer	147
11.33	Second bump-bond openings for sensor wafer	147
11.34	Second layer of Indium for sensor wafer	147
11.35	Photoresist lift-off for sensor wafer	148
11.36	Reflow of sensor element	148
11.37	Bump-bonding ROC - sensor	148
11.38	Second reflow	148
11.39	Pull-Up test	149
11.40	HDI defect	150
11.41	Glue underfill	150
11.42	Prototype PSI 43 Module	151
11.43	Test setup for modules	152
11.44	A simple impedance match	153
11.45	A general impedance match	154
11.46	Voltage divider	154
11.47	Impeance Matching for the prototype module	155
11.48	Impeance Matching for CLK	155
11.49	Ultrablacks from the modules	156
11.50	Leakage current of two sensors	157

List of Tables

2.1	Trajectory Parameters	15
3.1	diffVM Generator Settings	21
3.2	Reweight Settings	24
4.1	Design parameters of HERA II	26
4.2	The three angular regions of the H1 detector	27
4.3	H1 detector components	28
4.4	H1 central tracker	31
4.5	CJC parameters	32
4.6	CIP parameters	33
5.1	FTT thresholds	42
5.2	Link quality	43
6.1	CJC Gain cuts	49
6.2	Track selection criteria	60
6.3	Analysis Bin in $W_{\gamma p} - t$	65
7.1	FTT reweight parameter settings	85
7.2	CIP reweight parameter settings	86
8.1	Fit results from the integrated mass spectra	91
11.1	CMS pixel parameters	126
11.2	Supply voltages for the ROC	130
11.3	Fill factors	135
11.4	Total radiation length for the HDI.	136
11.5	Current and Voltage drop on HDI	136
11.6	ROC test results	143
11.7	Operational ROCs for different values of R_X	144
A.1	Cross sections for $\langle t \rangle = -0.01 \text{ GeV}^2$	159
A.2	Cross sections for $\langle t \rangle = -0.03 \text{ GeV}^2$	160
A.3	Cross sections for $\langle t \rangle = -0.07 \text{ GeV}^2$	160
A.4	Cross sections for $\langle t \rangle = -0.12 \text{ GeV}^2$	161
A.5	Cross sections for $\langle t \rangle = -0.19 \text{ GeV}^2$	161

A.6	Cross sections for $\langle t \rangle = -0.26 \text{ GeV}^2$	162
A.7	Cross sections for $\langle t \rangle = -0.38 \text{ GeV}^2$	162
A.8	Cross sections for $\langle t \rangle = -0.58 \text{ GeV}^2$	162
A.9	Cross sections for $\langle t \rangle = -0.81 \text{ GeV}^2$	163
A.10	Cross sections for $\langle t \rangle = -1.16 \text{ GeV}^2$	163
A.11	Cross sections for $\langle t \rangle = -1.66 \text{ GeV}^2$	163
A.12	Cross sections for $\langle t \rangle = -2.23 \text{ GeV}^2$	164

Bibliography

- [1] H.R. Crouch et al., [Cambridge Bubble Chamber Group], “*Photoproduction on hydrogen of ρ^0 mesons between threshold and 6 BeV*”, Phys. Rev., **146** 994, 1966.
- [2] E. Erbe et al., [German Bubble Chamber Collaboration], “*Photoproduction of ω , ϕ , η and X^0 mesons at energies up to 5.8 GeV*”, Nuov. Cim., **46A** 795, 1966.
- [3] H. Blechschmidt et al., “*Photoproduction of ρ^0 mesons on hydrogen, carbon and aluminium with photons of known energy*”, Nuov. Cim., **52A** 1348, 1967.
- [4] Joseph Ballam et al., “*Bubble chamber study of photoproduction by 2.8 GeV and 4.7 GeV polarized photons. 1. cross-section determinations and production of ρ^0 and Δ^{++} in the reaction $\gamma p \rightarrow p\pi^+\pi^-$* ”, Phys. Rev., **D5** 545, 1972.
- [5] W. Struczinski et al., [Aachen-Hamburg-Heidelberg-Munich Collaboration], “*Study of photoproduction on hydrogen in a streamer chamber with tagged photons for $1.6 \text{ GeV} < E(\gamma) < 6.3 \text{ GeV}$: topological and reaction cross-sections*”, Nucl. Phys., **B108** 45, 1976.
- [6] P. Joos et al., “ *ρ production by virtual photons*”, Nucl. Phys., **B113** 53, 1976.
- [7] R. W. Clift et al., “*Backward photoproduction of ρ^0 and f between 2.8 GeV and 4.8 GeV*”, Phys. Lett., **B64** 213, 1976.
- [8] Robert L. Anderson et al., “*Measurements of exclusive photoproduction processes at large values of t and u from 4 GeV to 7.5 GeV*”, Phys. Rev., **D14** 679, 1976.
- [9] S. Bartalucci et al., “*Measurement of the photoproduction phases of the ρ , ω , and ϕ mesons*”, Nuovo Cim., **A44** 587, 1978.
- [10] R. M. Egloff et al., “*Measurements of elastic ρ and ϕ meson photoproduction cross-sections on protons from 30 GeV to 180 GeV*”, Phys. Rev. Lett., **43** 657, 1979.
- [11] Yu. A. Aleksandrov et al., “*Photoproduction of ρ^0 mesons on hydrogen at gamma quanta energies of 15 GeV - 30 GeV. (in Russian)*”, Yad. Fiz., **32** 651–658, 1980.
- [12] M. Atkinson et al., [Omega Photon Collaboration], “*Inclusive photoproduction of ρ and ω in the photon energy range 20 GeV To 70 GeV*”, Nucl. Phys., **B245** 189, 1984.

- [13] R.J. Apsimon et al., [OMEGA Photon Collaboration], “*Comparison of photon and hadron induced production of ρ^0 mesons in the energy range of 65 GeV to 175 GeV*”, Z. Phys. C, **53** 581, 1992.
- [14] M.R. Adams et al., [E665 Collaboration], “*Diffractive production of $\rho^0(770)$ mesons in muon proton interactions at 470 GeV*”, Z. Phys. C, **74** 237, 1997.
- [15] C. Wu et al., “*Photoproduction of ρ^0 mesons and Δ -baryons in the reaction $\gamma p \rightarrow p\pi^+\pi^-$ at energies up to $\sqrt{s} = 2.6$ GeV*”, Eur. Phys. J., **A23** 317–344, 2005.
- [16] M. Derrick et al., [ZEUS Collaboration], “*Measurement of total and partial photon proton cross- sections at 180 GeV center-of-mass energy*”, Z. Phys., **C63** 391–408, 1994.
- [17] M. Derrick et al., [ZEUS Collaboration], “*Measurement of elastic ρ^0 photoproduction at HERA*”, Z. Phys., **C69** 39–54, 1995.
- [18] S. Aid et al., [H1 Collaboration], “*Measurement of the total photon proton cross section and its decomposition at 200 GeV centre of mass energy*”, Z. Phys., **C69** 27–38, 1995.
- [19] S. Aid et al., [H1 Collaboration], “*Elastic Photoproduction of ρ^0 Mesons at HERA*”, Nucl. Phys. B, **463** 3, 1996.
- [20] E. Fermi, “*On the theory of the impact between atoms and electrically charged particles*”, Z. Phys., **29** 315–327, 1924.
- [21] C. F. von Weizsäcker, “*Ausstrahlung bei Stößen sehr schneller Elektronen (Radiation emitted in collisions of very fast electrons)*”, Z. Phys., **88** 612–625, 1934.
- [22] E. J. Williams, “*Nature of the high-energy particles of penetrating radiation and status of ionization and radiation formulae*”, Phys. Rev., **45** 729–730, 1934.
- [23] V. M. Budnev, I. F. Ginzburg, G. V. Meledin and V. G. Serbo, “*The two photon particle production mechanism. Physical problems. Applications. Equivalent photon approximation*”, Phys. Rept., **15** 181–281, 1974.
- [24] J. J. Sakurai, “*Theory of strong interactions*”, Annals Phys., **11** 1–48, 1960.
- [25] Murray Gell-Mann and Fredrik Zachariasen, “*Form-factors and vector mesons*”, Phys. Rev., **124** 953–964, 1961.
- [26] R. P. Feynman, “*Photon-hadron interactions*”. Benjamin, N.Y., 1972.
- [27] T. H. Bauer, R. D. Spital, D. R. Yennie and F. M. Pipkin, “*The hadronic properties of the photon in high-energy interactions*”, Rev. Mod. Phys., **50** 261, 1978, Erratum-ibid.51:407,1979.
- [28] Gerhard A. Schuler and Torbjorn Sjostrand, “*Towards a complete description of high-energy photoproduction*”, Nucl. Phys., **B407** 539–605, 1993.
- [29] S. D. Holmes, Won-Yong Lee and J. E. Wiss, “*High-energy photoproduction of charmed states*”, Ann. Rev. Nucl. Part. Sci., **35** 397–454, 1985.

-
- [30] A. Donnachie and G. Shaw, “*Electromagnetic interactions of hadrons. vol. 1*”, **1** 446, 1978, Plenum Press/New York 1978, (Nuclear Physics Monographs).
- [31] A. Donnachie and G. Shaw, “*Electromagnetic interactions of hadrons. vol. 2*”, **2** 574, 1978, Plenum Press/New York 1978, (Nuclear Physics Monographs).
- [32] I.Ya. Pomeranchuk and L.D. Landau, “*Emission of γ -quanta in collisions of fast π -mesons with nucleons*”, ZhETF, **24** 505, 1953.
- [33] I.Ya. Pomeranchuk and E.L. Feinberg, “*Inelastic diffraction processes at high energies*”, Nuovo Cim., **4** 652, 1956.
- [34] V. Barone and E. Predazzi, “*High-Energy Particle Diffraction*”. Springer-Verlag, 2002.
- [35] A. Donnachie and P. V. Landshoff, “*Total cross-sections*”, Phys. Lett., **B296** 227–232, 1992.
- [36] P. D. B. Collins, “*An introduction to Regge theory and high-energy physics*”. Cambridge University Press, 1977, Cambridge 1977, 445p.
- [37] T. Regge, “*Introduction to complex orbital momenta*”, Nuovo Cim., **14** 951, 1959.
- [38] T. Regge, “*Bound states, shadow states and Mandelstam representation*”, Nuovo Cim., **18** 947–956, 1960.
- [39] P. D. B. Collins and Alan D. Martin, “*Hadron reaction mechanisms*”, Rept. Prog. Phys., **45** 335, 1982.
- [40] A. V. Barnes et al., “*Pion charge exchange scattering at high-energies*”, Phys. Rev. Lett., **37** 76, 1976.
- [41] G. F. Chew and S. C. Frautschi, “*Regge trajectories and the principle of maximum strength for strong interactions*”, Phys. Rev. Lett., **8** 41–44, 1962.
- [42] Marcel Froissart, “*Asymptotic behavior and subtractions in the Mandelstam representation*”, Phys. Rev., **123** 1053–1057, 1961.
- [43] A. Martin, “*Unitarity and high-energy behavior of scattering amplitudes*”, Phys. Rev., **129** 1432–1436, 1963.
- [44] I.Ya. Pomeranchuk, “*Equality of the nucleon and antinucleon total interaction cross section at high energies*”, Sov. Phys. JETP, **7** 499, 1958.
- [45] S. Abatzis et al., [WA91], “*Observation of a narrow scalar meson at 1450 MeV in the reaction $pp \rightarrow p_f(\pi^+\pi^-\pi^+\pi^-)p_s$ at 450 GeV/c using the CERN Omega Spectrometer*”, Phys. Lett., **B324** 509–514, 1994.
- [46] S. J. Brodsky, V. S. Fadin, V. T. Kim, L. N. Lipatov and G. B. Pivovarov, “*The QCD pomeron with optimal renormalization*”, JETP Lett., **70** 155–160, 1999.

- [47] Marcello Ciafaloni and Gianni Camici, “*Energy scale(s) and next-to-leading BFKL equation*”, Phys. Lett., **B430** 349–354, 1998.
- [48] Victor S. Fadin and L. N. Lipatov, “*BFKL pomeron in the next-to-leading approximation*”, Phys. Lett., **B429** 127–134, 1998.
- [49] B. List and A. Mastroberardino, “*DIFFVM: A Monte Carlo generator for diffractive processes in ep scattering*”, DESY-PROC-1999-02, page 396, 1998, Prepared for Workshop on Monte Carlo Generators for HERA Physics (Plenary Starting Meeting), Hamburg, Germany, 27-30 Apr 1998.
- [50] Konstantin Goulianos, “*Diffractive interactions of hadrons at high-energies*”, Phys. Rept., **101** 169, 1983.
- [51] S. Eidelman et al., [Particle Data Group], “*Review of particle physics*”, Phys. Lett., **B592** 1, 2004.
- [52] Torbjorn Sjostrand, “*PYTHIA 5.7 and JETSET 7.4: Physics and manual*”, 1995.
- [53] J. Breitweg et al., [ZEUS Collaboration], “*Elastic and proton-dissociative ρ^0 photoproduction at HERA*”, Eur. Phys. J. C, **2** 247, 1998.
- [54] Marc Ross and Leo Stodolsky, “*Photon dissociation model for vector meson photoproduction*”, Phys. Rev., **149** 1172–1181, 1966.
- [55] M. G. Ryskin and Yu. M. Shabelski, “*Role of a nonresonance background in the diffractive electro- and photoproduction of ρ^0 mesons*”, Phys. Atom. Nucl., **61** 81–86, 1998.
- [56] H1 Collaboration, “*ep Physics beyond 1999*”, H1 internal report H1-10/97-531, October 1997.
- [57] U. Schneekloth, “*Recent HERA results and future prospects*”, DESY internal report 98-060, May 1998.
- [58] I. Abt et al., [H1 Collaboration], “*The H1 detector at HERA*”, Nucl. Instrum. Meth., **A386** 310–337, 1997.
- [59] I. Abt et al., [H1 Collaboration], “*The tracking, calorimeter and muon detectors of the H1 experiment at HERA*”, Nucl. Instrum. Meth., **A386** 348–396, 1997.
- [60] K. Müller et al., “*Construction and performance of a thin cylindrical multiwire proportional chamber with cathode pad readout for the H1 experiment*”, Nucl. Instrum. Meth., **A312** 457–466, 1992.
- [61] M. Cuje et al., “*H1 high luminosity upgrade 2000 CIP and Level 1 vertex trigger*”, DESY-PRC 98/02 and H1 internal note H1-01/98-535, 1998.
- [62] M. Urban, “*The new CIP2k z-vertex trigger for the H1 experiment at HERA*”, Dissertation, Universität Zürich, Zürich, 2004.

- [63] B. Andrieu et al., [H1 Calorimeter Group], “*Results from pion calibration runs for the H1 liquid argon calorimeter and comparisons with simulations*”, Nucl. Instrum. Meth., **A336** 499–509, 1993.
- [64] P. Biddulph et al., “*The H1 forward muon spectrometer*”, Nucl. Instrum. Meth., **A340** 304–308, 1994.
- [65] D. Müller and F. Sefkow, “*Improving the z-vertex trigger*”, H1 internal note H1-04/98-539, 1998.
- [66] A. Schweitzer, “*Optimierung eines z-Vertex-Triggers für den H1-Detektor bei HERA*”, Diplomarbeit, Ruprecht-Karls-Universität Heidelberg, Heidelberg, February 1999.
- [67] J. Becker, “*H1 CIP-Vertex-Trigger upgrade - Triggerhardware-Simulation*”, Internal note Physikalisches Institut, Ruprecht-Karls-Universität Heidelberg, March 1998.
- [68] A. Baird et al., “*A fast high resolution track trigger for the H1 experiment*”, IEEE Trans. Nucl. Sci., **48** 1276–1285, 2001.
- [69] H1 Collaboration, “*A Fast Track Trigger with high resolution for H1*”, Proposal submitted to the Physics Research Committee, DESY internal report PRC 99/06 and addendum PRC 99/07, 1999.
- [70] Niklaus Berger, “*Diffractional ϕ photoproduction using the Fast Track Trigger at H1*”, PhD thesis, ETH Zürich, 2006, [in preparation].
- [71] A. Schöning, “*The Topology Description Function*”, H1 internal document, January 2005.
- [72] I. P. Ivanov, N. N. Nikolaev and A. A. Savin, “*Diffractional vector meson production at HERA: From soft to hard QCD*”, 2004.
- [73] P. Söding, “*On the apparent shift of the ρ meson mass in photoproduction*”, Phys. Lett., **19** 702–704, 1966.
- [74] J. D. Jackson, “*Remarks on the phenomenological analysis of resonances*”, Nuovo Cim., **34** 1644–1666, 1964.
- [75] S.D. Drell, “*Production of particle beams at very high energies*”, Phys. Rev Lett., **5** 278, 1960.
- [76] A. Abele et al., [CRYSTAL BARREL], “ *4π decays of scalar and vector mesons*”, Eur. Phys. J., **C21** 261–269, 2001.
- [77] Arthur B. Clegg and A. Donnachie, “*Higher vector meson states produced in electron - positron annihilation*”, Z. Phys., **C62** 455–470, 1994.
- [78] R. Spital and D. R. Yennie, “ *ρ^0 shape in photoproduction*”, Phys. Rev., **D9** 126–137, 1974.
- [79] D. Aston et al., “*Photoproduction of ρ^0 and ω on hydrogen at photon energies of 20 GeV to 70 GeV*”, Nucl. Phys., **B209** 56, 1982.

- [80] A. Aktas et al., [H1], “*Measurement and QCD Analysis of the Diffractive Deep- Inelastic Scattering Cross Section at HERA*”, submitted to Eur. Phys. J., 2006.
- [81] J. Breitweg et al., [ZEUS Collaboration], “*Measurement of diffractive photoproduction of vector mesons at large momentum transfer at HERA*”, Eur. Phys. J., **C14** 213–238, 2000.
- [82] S. Chekanov et al., [ZEUS Collaboration], “*Measurement of proton-dissociative diffractive photoproduction of vector mesons at large momentum transfer at HERA*”, Eur. Phys. J., **C26** 389–409, 2003.
- [83] G. A. Jaroszkiewicz and P. V. Landshoff, “*Model for diffraction excitation*”, Phys. Rev., **D10** 170–174, 1974.
- [84] P. V. Landshoff, “*Diffractive processes*”, Nucl. Phys. Proc. Suppl., **12** 397–412, 1990.
- [85] Magnus Bodin, “*Helicity analysis of ρ^0 mesons from diffractive photoproduction at HERA*”, Diplomarbeit, ETH Zürich, 2006.
- [86] [The CMS Collaboration], “*Compact Muon Solenoid: Technical proposal*”, 1994, CERN-LHCC-94-38.
- [87] [LHC Study Group], “*The Large Hadron Collider: Conceptual design*”, 1995, CERN-AC-95-05-LHC.
- [88] Marlon Barbero, “*Development of a radiation-hard pixel read out chip with trigger capability*”, Dissertation, Universität Basel, 2003.
- [89] [The CMS Collaboration], “*Addendum to the CMS tracker TDR*”, 2000, CERN-LHCC-2000-016.
- [90] [The CMS Collaboration], “*The Tracker Project, Technical Design Report*”, 1998, CERN-LHCC-98-006.
- [91] F. Antinori et al., “*Experience with a 30 cm² silicon pixel plane in CERN experiment WA97*”, Nucl. Instrum. Meth., **A360** 91–97, 1995.
- [92] A. Andreazza et al., “*The DELPHI very forward tracker for LEP200*”, Nucl. Instrum. Meth., **A367** 198–201, 1995.
- [93] T. Rohe, “*Sensor concepts for pixel detectors in high energy physics*”, Prepared for PIXEL 2002: International Workshop on Semiconductor Pixel Detectors for Particles and X-Rays, Carmel, California, 9-12 Sep 2002.

Danksagung

Vor etwas mehr als zehn Jahren habe ich mein Studium der Physik in Zürich begonnen und beende nun meine Ausbildung hier an der ETH mit der vorliegenden Doktorarbeit. Ermöglicht hat mir dies mein Doktorvater Prof. Dr. Ralph Eichler, bei dem ich mich ganz herzlich bedanken möchte. Er gab mir die Chance, an zwei unterschiedlichen Experimenten mitzuwirken und sowohl das Paul Scherrer Institut in Villigen als auch das Deutsche Elektronen Synchrotron in Hamburg kennenzulernen.

In den zwei Jahren am PSI habe ich in der Gruppe von Dr. Roland Horisberger an der Entwicklung des CMS Pixel Detektors mitgearbeitet und danke ihm für die interessante Einführung in die Welt der Halbleiterdetektoren. Ich möchte auch Dr. Kurt Gabathuler, meinem direkten Vorgesetzten während der gesamten vier Jahre, für seine Hilfe bei allen administrativen Aufgaben danken sowie für die unkomplizierte Korrespondenz während meiner Zeit in Hamburg. Für seinen bevorstehenden Ruhestand wünsche ich ihm alles Gute. Des weiteren gilt mein Dank Dr. Wolfram Erdmann, der mich am PSI betreute und mir mit unzähligen Tipps und Tricks die Arbeit erheblich vereinfacht hat. Ebenso danke ich Beat Meier für die wertvolle Unterstützung in allen elektronischen Belangen sowie Silvan Streuli für die Hilfe bei den mechanischen Aspekten und ganz speziell für das ewige Erneuern der wire bonds bei den Prototyp Modulen.

Bei Tilman Rohe bedanke ich mich für seine Assistenz beim Ausmessen der Sensorelemente und meinem Mitdoktoranden Christoph Hörmann, mit dem ich viel Zeit verbrachte, danke ich ganz herzlich für seine Hilfsbereitschaft beim Bewältigen der alltäglichen Probleme. Unvergessen bleiben auch die zahlreichen Einsätze in der Experimentierhalle bei den diversen Strahltests der Auslese Chips. In diesem Zusammenhang seien auch noch Dr. Willy Bertl und Dr. Peter Robman verdankt.

Während meiner Analyse bei H1 wurde ich von Dr. Benno List betreut, bei dem ich mich ganz speziell bedanke für all die Unterstützung und Motivation, die er mir zukommen liess. Neben den theoretischen Aspekten der Vektor Meson Produktion war er auch eine schier unerschöpfliche Quelle, was die technischen Aspekte der Programmierung anging. So wurde die Analyse unter anderem mit dem Framework der Self-Filling Histograms, die er mit seiner Frau Jenny entwickelte, erfolgreich durchgeführt.

Dr. Andre Schöning und dem FTT Team danke ich für die vorbehaltlose Unterstützung in allen Belangen des Triggers. Spezieller Dank gebührt Dr. Christoph Wissing für seine unermüdliche Hilfe bei der Simulation der Monte Carlo Ereignisse und die immer wiederkehrende Suche nach den optimalen FTTEMU Simulations Parametern.

Meinen Doktorandenkollegen Marc Del Degan, Tobias Zimmermann und Michel Sauter sowie Dr. Guillaume Leibenguth sei ganz herzlich gedankt für die vielen hilfreichen Diskussionen inner- und ausserhalb des Büros. Einen besonderen Dank schulde ich meinem treuen Bürokollegen Nik Berger für seine unnachahmliche Unterstützung sowohl in unzähligen Gesprächen über Physik und die Welt als auch bei der Suche nach einem guten Restaurant. Die vielen Diskussionen mit ihm und sein Humor haben massgeblich zum Erfolg dieser Arbeit beigetragen.

Bei Dr. Christoph Grab bedanke ich mich ganz herzlich für seine Bereitschaft, bei technischen Fragen die nötige Hilfe zu leisten und meinem Vorgänger Dr. Simon Baumgartner danke ich für wertvolle Tipps zur Abgabe der Arbeit und die vielen gemeinsamen Erinnerungen aus der zweiwöchigen Sommerschule in Armenien.

Prof. Urs Langenegger danke ich für die Begutachtung der Arbeit und seine wertvollen Anmerkungen und Fragen.

Auch meinem persönlichen Umfeld gebührt grosser Dank für die schönen Erlebnisse und Momente neben der Arbeit, bei der ich wieder neue Energie tanken konnte. Besonderer Dank gilt dabei meiner Freundin Anke, die mit ihrer liebevollen Unterstützung und ihrer Geduld in schwierigeren Zeiten viel zum Gelingen der Arbeit beigetragen hat.

Bei Dr. Max Urban bedanke ich mich für die tolle Zeit in der gemeinsamen Wohnung an der Stresemannstrasse in Hamburg und für die unvergesslichen Grillabende am Elbstrand oder im Blauen Haus.

Meiner Familie möchte ich für die vorbehaltlose und fürsorgliche Hilfe danken, welche sie mir während meiner langen Ausbildung zukommen liess.

Abschliessend sei allen Personen die zum erfolgreichen Ende meiner Ausbildung direkt oder indirekt beigetragen haben, ein herzliches **”Dangge”** gesagt.

Curriculum Vitae

Persönliche Daten

Name	Ronald Mike Weber
Geburtsdatum	28. November 1974
Geburtsort	White Plains (USA)
Nationalität	CH, USA
Heimatort	Basel (BS)

Akademische Laufbahn

2002 – 2006	Doktorarbeit an der ETH Zürich in Zusammenarbeit mit dem PSI in Villgen und dem DESY in Hamburg
2001	Diplom in Physik an der ETH Zürich im Herbst 2001 Diplomarbeit in der Gruppe von Professor R. Eichler
1997 – 2001	Fachstudium Physik an der ETH Zürich
1995 – 1997	Grundstudium Physik an der ETH Zürich
1992 – 1993	Austauschjahr an der Springville High School in Utah, USA
1990 – 1994	Gymnasium in Münchenstein, BL Typus C, Matura im Dezember 1994
1986 – 1990	Sekundarschule in Reinach, BL
1981 – 1985	Primarschule in Reinach, BL